TECHNISCHE UNIVERSITÄT MÜNCHEN

FAKULTÄT FÜR ELEKTROTECHNIK UND INFORMATIONSTECHNIK

Kinetic Monte Carlo Investigation of Organic Solar Cell Architecture

Kashif Hussain

Vollständiger Abdruck der von der Fakultät für Elektrotechnik und Informationstechnik der Technischen Universität München zur Erlangung des akademischen Grades eines

Doktors der Ingenieurwissenschaften (Dr.-Ing.)

genehmigten Dissertation.

Vorsitzender:

Prof. Dr. rer. nat. Bernhard Wolfrum

Prüfende der Dissertation:

1. Prof. Dr. rer. nat. Alessio Gagliardi
2. Assoc. Prof. Aldo Di Carlo, Ph.D.

Die Dissertation wurde am 16.11.2021 bei der Technischen Universität München eingereicht und durch die Fakultät für Elektrotechnik und Informationstechnik am 02.06.2022 angenommen.

Dedicated to

My Family

Abstract

Energy harvesting directly from sunlight is an intriguing technique of energy production. The most recent scientific study has focused on photovoltaic technologies based on novel soft materials, such as dyes, perovskites, and organic. Organic solar cells (OSCs) comprising of organic semiconductors offer several benefits over other materials, including their flexibility, low weight, tunability, solution processability, and simplicity of synthesis. The processes governing charge generation, transport, and loss mechanisms in organic solar cells vary significantly from those in inorganic solar cells due to a general disordered molecular arrangement and a much lower permittivity of organic semiconductors. Therefore, a thorough knowledge of the physics of devices based on organic semiconductors is required.

Numerical simulation, in conjunction with experimental studies, can help understand exciton kinetics and charge carrier and dynamics at the molecular level. In the state of the art numerical tools such as drift-diffusion (DD), the complex bulk-heterojunction morphology is reduced by utilizing effective medium approximations. However, with increasing dimensionality, DD models face convergence issues and become very complex. More importantly, since DD models do not consider the non-equilibrium dynamics of charge carriers, they provide insufficient information on charge carrier dynamics in OSCs based on complex morphologies. Therefore, the kinetic Monte Carlo (kMC) method is a suitable tool for modelling the disordered arrangement of organic molecules and tracking the single-particle dynamics. This research study brings together different device aspects to better understand the physics of organic solar cells.

This thesis presents a three-dimensional (3D) kMC model to investigate different aspects of organic solar cells, from the role of interface disorder on cell performance to modelling high-efficiency multi-junction devices. At first, the device physics of bulk-heterojunction OSC is presented in Chapter 2. The importance of the implemented kMC model is highlighted along with the implemented processes, differentiating it from an effective medium approach in Chapter 3. Open-circuit voltage losses are common in OSCs and have been attributed to energetic disorder and recombination losses. In order to achieve high performance, these losses must be minimized along with the optimal control of the complicated bulk heterojunction morphology for efficient charge transport and extraction. Chapter 4 evaluates the influence of intermixed bulk-heterojunction morphology

and electronic density of states at the donor:acceptor (D:A) and extraction layer interfaces on the performance of OSC. The results show that the D:A interface significantly affects the device performance and needs to be controlled to achieve efficient OSCs. The role of morphology in charge transport mechanism for Dilute donor is presented in Chapter 5. The OSCs with low donor concentration (∼1 wt.%) represent the ideal test system for hole transport in isolated phases. The presented results show that even a minor amount of polymers forming percolation paths to the contact is sufficient to generate a substantial photocurrent and to obtain a high open-circuit voltage.

Furthermore, a combined study of kMC and DD is presented in Chapter 6 to model multi-junction hybrid perovskite-organic solar cells. Initially, tandem architecture using perovskite absorbers and organic blend is modelled to investigate the device performance of series-connected tandem solar cells. The results show that by proper combination of bandgap and thickness of the perovskite and organic layer, a high efficient hybrid tandem device can be obtained with an efficiency of 19.8%. This work further analyzes different perovskite cells in combination with the organic blend in a multi-junction configuration. Which gives a concrete model representation that can help to optimize the device architecture leading to high-efficiency hybrid perovskite-organic devices.

Zusammenfassung

Die direkte Energiegewinnung aus Sonnenlicht ist eine faszinierende Technik der Energieerzeugung. Die jüngsten wissenschaftlichen Studien konzentrieren sich auf photovoltaische Technologien, die auf neuartigen, weichen Materialien wie Farbstoffen, Perowskiten und organischen Materialien basieren. Organische Solarzellen (OSC), die aus organischen Halbleitern bestehen, bieten gegenüber anderen Materialien mehrere Vorteile, darunter ihre Flexibilität, ihr geringes Gewicht, ihre Abstimmbarkeit, ihre Verarbeitbarkeit in Lösung und ihre einfache Synthese. Die Prozesse der Ladungserzeugung, des Ladungstransports und der Verlustmechanismen in organischen Solarzellen unterscheiden sich erheblich von denen in anorganischen Solarzellen, da die Moleküle generell ungeordnet sind und die Permittivität organischer Halbleiter viel geringer ist. Daher ist eine gründliche Kenntnis der Physik von Bauelementen auf der Basis organischer Halbleiter erforderlich.

Numerische Simulationen können in Verbindung mit experimentellen Studien helfen, die Exzitonenkinetik und die Ladungsträgerdynamik auf molekularer Ebene zu verstehen. Bei den aktuellen numerischen Werkzeugen wie Drift-Diffusion (DD) wird die komplexe Morphologie der Bulk-Heteroübergänge durch durch Näherungsmethoden für effektive Medien reduziert. Mit zunehmender Dimensionalität haben die DD-Modelle jedoch Konvergenzprobleme und werden sehr komplex. Noch wichtiger ist, dass DD-Modelle die Nichtgleichgewichtsdynamik von Ladungsträgern nicht berücksichtigen und daher nur unzureichende Informationen über die Ladungsträgerdynamik in OSCs mit komplexen Morphologien liefern. Daher ist die kinetische Monte-Carlo-Methode (kMC) ein geeignetes Instrument, um die ungeordnete organische Strukturen zu modellieren und die Dynamik der einzelnen Teilchen zu verfolgen. In dieser Forschungsarbeit werden verschiedene Aspekte zusammengeführt, um die Physik organischer Solarzellen besser zu verstehen.

In dieser Arbeit wird ein dreidimensionales (3D) kMC-Modell vorgestellt, mit dem verschiedene Aspekte organischer Solarzellen untersucht werden. Von dem Einfluss der Unordnung an der Grenzfläche AUF die Leistung der Zelle bis hin zur Modellierung hocheffizienter Bauelemente mit mehreren Übergängen. Zunächst wird in Kapitel 2 die Bauteilphysik von Bulk-Heterojunction-OSCs vorgestellt. Die Bedeutung des implementierten kMC-Modells wird zusammen mit den implementierten Prozessen hervorgehoben,

wodurch es sich von einem Nährungsansatz für effective Medien in Kapitel 3 unterscheidet. Leerlaufspannungsverluste sind bei OSCs üblich und werden auf energetische Unordnung und Rekombinationsverluste zurückgeführt. Um eine hohe Leistung zu erreichen, müssen effizienter Ladungstransport und –extraktion gewährleistet werden. Um dies zu erreichen müssen die Verluste minimiert und die komplizierte Morphologie des Heteroübergangs optimal gesteuert werden. In Kapitel 4 wird der Einfluss der Morphologie des Bulk-Heteroübergangs und der elektronischen Zustandsdichte an den Grenzflächen zwischen Donor und Akzeptor (D:A) und der Extraktionsschicht auf die Leistung der OSC untersucht. Die Ergebnisse zeigen, dass die D:A-Grenzfläche die Leistung des Bauelements erheblich beeinflusst und kontrolliert werden muss, um effiziente OSCs zu erreichen. Der Einfluss der Morphologie auf den Ladungstransport in dilute donor OSCs wird in Kapitel 5 dargestellt. OSCs mit niedriger Donorkonzentration ($\sim$ 1 Gew.%) sind das ideale Testsystem für den Lochtransport in isolierten Phasen. Die vorgestellten Ergebnisse zeigen, dass bereits eine geringe Menge an Polymeren, die Perkolationspfade zum Kontakt bilden, ausreicht, um einen beträchtlichen Photostrom zu erzeugen und und eine hohe Zellspannung zu erhalten.

Darüber hinaus wird in Kapitel 6 eine kombinierte Studie von kMC und DD vorgestellt, um hybride Perowskit-organische Solarzellen mit mehreren Übergängen zu modellieren. Zunächst wird eine Tandem-Architektur aus Perowskit-Absorbern und einer organischen Mischung modelliert, um die Bauelementleistung von in Reihe geschalteten Tandem-Solarzellen zu untersuchen. Die Ergebnisse zeigen, dass durch die richtige Kombination von Bandlücke und Dicke der Perowskit- und organischen Schichten ein hocheffizientes hybrides-Bauelement mit einer Effizienz von 19,8% erzielt werden kann. In dieser Arbeit werden außerdem verschiedene Perowskit-Zellen in Kombination mit der organischen Mischung in einer Mehrfachübergangskonfiguration analysiert, um eine konkrete Modelldarstellung zu erhalten. Die bei der Optimierung der Bauteilarchitektur helfen kann, die zu hocheffizienten hybriden Perowskit-organischen Geräten führt.

List of Own Publications and Contributions

This dissertation is based on author's work conducted at the chair *Simulation of Nanosystems for Energy Conversion (SNE)*, Department of Electrical and Computer Engineering, Faculty of Electrical Engineering and Information technology, Technical University, Munich. Parts of the this dissertation have been published in peer-reviewed journals and conference proceeding as mentioned below.

Peer-reviewed journals

- K. Hussain, W. Kaiser, and A. Gagliardi, "Effect of Polymer Morphology on Dilute Donor Organic Solar Cells", *The Journal of Physical Chemistry C*, vol. 124, no. 6, pp. 3517–3528, 2020.

- K. Hussain, W. Kaiser, and A. Gagliardi, "Role of the Interafce and Extraction Layer Energetics in Organic Solar Cells", *The Journal of Physical Chemistry C*, vol. 125, no. 10, pp. 5447–5457, 2021.

- K. Hussain, A. Gagliardi, "Tandem/Multi-junction Modelling of Hybrid Perovskite-Organic Solar Cells: A kinetic Monte Carlo (kMC) and Drift-diffusion (DD) Study", *Solar Energy*, 243, 193-202, 2022.

Conference proceedings

- K. Hussain, W. Kaiser, and A. Gagliardi, "Role of Interface Energetics and Off-diagonal Disorder in Bulk-Heterojunction Organic Solar Cells", 2020 *IEEE 20th International Conference on Nanotechnology (IEEE-NANO)*, September 2020.

Conference presentations

- K. Hussain, W. Kaiser, and A. Gagliardi, "Role of Interface Energetics and Off-diagonal Disorder in Bulk-Heterojunction Organic Solar Cells", 2020 *IEEE 20th International Conference on Nanotechnology (IEEE-NANO: Virtual)*, Oral presentation, Montreal, Canada, Jul. 2020.

- K. Hussain, T. Albes, L. N. S. Murthy, L. Xu, J. W. P. Hsu, and A. Gagliardi, "Charge Transfer Mechanism in Dilute Donor Organic Solar Cells", *EMRS Spring Meeting 2019 Conference - ICAM International conference on Advanced Materials*, Poster Presentation, Nice, France, May 26-31, 2019.

International Summer School

- K. Hussain, A. Gagliardi, "Hole transport in Low-donor Content Organic Solar Cells", *International School on Hybrid and Organic Photovoltaics (ISOPHOS)*, Castiglione della Pescaia, Italy, September 2-6, 2019.

Contents

1 Introduction

Over the course of history, many technologies have been created to meet human requirements. These include providing light, heat, and mechanized work for houses, industrial and agricultural usage, transportation, and in general, making it easier to carry out a wide range of tasks in daily life. Several of these systems and technologies have similar features, and they all revolve around the concept of energy.

Energy, by definition, is the ability to perform a particular task, which refers to a force, that may cause an object to be displaced across a distance. However, in subsequent years, this is expanded to include a wide range of energies such as kinetic energy, which is associated with moving things; thermal energy, which is linked to heat; chemical energy, which is associated with electricity; and many more. Smil has provided a concise summary of the relationship between energy and the history of civilization [1]. While we live in a world where thermal energy is easily accessible, the kind of energy that we are interested in is one that we might use immediately for our wants and requirements. Ideally, we would be able to quickly direct this energy for activating a machine that would do the required job. The thermal energy that is now circulating in the environment is not helpful for these objectives. The energy that is capable of doing labor must be generated from readily accessible sources. It is also necessary to store usable energy when needed and transfer it to the location where it will be used.

Low-cost clean fuels and power affordability is essential for developing industry, transportation, lighting, and communication. Global population growth and growing living standards have exacerbated the need for a dependable, convenient, and flexible energy supply, which has risen to become a significant source of concern. Chemical energy is now the most practical and useful portable energy, which explains the world's reliance on fossil fuels as a source of energy (natural gas, petroleum, and coal). The widespread utilization of fossil fuels, on the other hand, has had a significant influence on the globe, especially in terms of environmental change and health consequences. According to many individuals, the production, distribution, and use of energy are all thought to need significant transformation. Another concern is the increasing need for various forms of energy storage and supply, which is needed to power portable devices and electric vehicles and ensure access to an uninterrupted supply of wind or solar power. The development of

new energy devices may fundamentally alter how energy is acquired and generated, with far-reaching consequences for both the environment and human needs.

1.1 Background

Harvesting energy directly from sunlight is an appealing method of energy production. The Sun provides a tremendous quantity of 1.75×10^{17} W energy to the Earth [2]. From this vast energy source, only approximately half of which reaches the earth's surface as usable energy [3]. Despite the development of the first photovoltaic device in 1954 Chapin *et al.* [4], the fossil fuels remains the primary source of energy for modern human civilization[1][2]. Unfortunately, these fossil fuels are also the biggest contributors to greenhouse emissions, specifically CO_2, amounting to about 34.0 billion tonne (BT) in the year 2019[3]. The global need for energy is increasing at an alarming pace. It has been driven primarily by two factors: the fast-growing world population and the expansion of the global economy. The global population is projected to be approximately 7.9 billion (B) people in 2021, and it is projected to reach almost 10B by 2050[4]. In terms of economic development, it is generally recognized that the expansion of the global middle class would result in increased worldwide energy consumption as more people will be accustomed to consumer electronics and their use in daily life. Growing energy needs and carbon emissions thus highlight the need for the energy transition of the power industry, and renewable technologies may play an important role in achieving this objective. As of 2020, renewables cover only 5% of global power generation, of which solar and wind power were two of the primary sources[3]. Although this is a small percentage of total energy production, it does seem that the world is more focused on the transition to clean energy, and solar power seems to be the most attractive option.

In addition, the significant price decrease in solar energy that has occurred in recent years is also an essential factor to consider. Within the past decade, the average selling price for multi-crystalline silicon solar modules has decreased by almost 15 times, making photovoltaics one of the most cost-effective alternatives for large-scale energy production [5]. The average power conversion efficiency of commercially available silicon-based PV modules is about 20% [6] and the recorded lab efficiency for multi and single-crystalline

[1] `https://www.eia.gov/totalenergy/data/browser/`, accessed 08.09.2021

[2] `https://www.iea.org/reports/world-energy-outlook-2020?mode=overview/`, accessed 08.09.2021

[3] `https://www.bp.com/content/dam/bp/business-sites/en/global/corporate/pdfs/energy-economics/statistical-review/bp-stats-review-2020-full-report.pdf`, accessed 08.09.2021

[4] `https://population.un.org/wpp/publications/Files/WPP2019_Highlights.pdf`, accessed 08.09.2021

silicon range from 23% to almost 27%, respectively [6]. However, the processing of Si crystals is expensive and requires high temperature and is not easily scalable. As a result of these limitations, Si solar cells have not been widely used, particularly in residential and private applications.

1.2 Motivation

The latest scientific research has concentrated on photovoltaic technologies based on new soft materials, including dyes, perovskites, and organic semiconductors. Several benefits to using this new generation of semiconducting materials, i.e. high absorption coefficients, coupled with their direct bandgaps, make them excellent candidates for thin-film solar cell applications. A low-temperature processing method, such as solution-based processing or roll-to-roll printing, provides for low-cost manufacturing. New research and development efforts in these photovoltaic technologies have resulted in improved power conversion efficiency (PCE) of 25.5% for perovskite solar cells, 18.2% for organic solar cells (OSCs), and even 29.5% for tandem perovskite/silicon solar cells, according to the National Renewable Energy Laboratory[5]. Although organic semiconductors and solar cells have advanced tremendously in recent years, they are not expressly regarded as a substitute for inorganic semiconductors but rather serve as alternate materials for new applications that complement inorganic photovoltaics (PV).

Compared to other technologies, the flexibility, low weight, tunability, and ease of manufacturing of OSCs are significant advantages [7]. Due to the high absorption coefficient of organic semiconductors, organic solar cells of active layers considerably thinner than 1 micron in thickness can absorb a significant amount of sunlight. When combined with low processing temperatures, these very thin films allow new device categories in shape, colour and flexible or semitransparent solar cells. Moreover, aesthetic effects and possible building integration of organic solar cells open a completely new dimension towards their commercialization.

Tang *et al.* published the first report on an organic photovoltaic (OPV) device with an efficiency of 1% in 1986 [8]. The device had two semiconductors: a phthalocyanine derivative as a *p*-type semiconductor and a perylene derivative as an *n*-type semiconductor, which were placed between two transparent conductive oxides and a semitransparent metal contact. The discovery of a photoinduced electron transfer from a conjugated polymer to the fullerene C60 opened the ground for the development of the donor-acceptor system (DAS) [9, 10]. In addition, the development of the bulk-heterojunction solar cell,

[5] `https://www.nrel.gov/pv/assets/pdfs/best-research-cell-efficiencies-rev210726.pdf`, accessed 08.09.2021

which formed an ambipolar interpenetrating system of the donor and acceptor phases, was another significant step forward [11]. A high interfacial area allowed for the effective separation of electron-hole pairs, and the percolation routes of relatively pure phases did not interfere with the charge transport [11]. Nowadays, efficiencies over 18% have been achieved[5], and accelerated ageing tests have shown that they have a potential long-term stability [6, 12].

Comparatively speaking, the knowledge of the physics of organic semiconductors is still in its evolution phase compared to the substantial experimental, analytical, and computational study on inorganic semiconductors conducted throughout the twentieth century. The two most significant distinctions between organic semiconductors and their inorganic counterparts are: 1) Organic semiconductors have a non-periodic arrangement of their components. The energy levels of their constituents are distributed in a spatially variable manner, which allows the localized charges to move using a thermally assisted hopping mechanism. 2) Electric charges are only weakly screened in organics since their permittivity is much lower than that of silicon, with values averaging about $\epsilon_r = 3$ to 5(as compared to Si $\epsilon_r = 11.7$). Because of the low permittivity, there is insufficient filtering of the electrostatic interaction, resulting in long-range Coulomb attraction. This has been shown to increase unwanted recombination [13, 14], and regulate the kinetics of charge carrier separation [15].

A detailed understanding of the physical processes occurring on the nanoscale is required due to the presence of charge carriers with low permittivity and strong interactions within complex bulk-heterojunction structures of spatially disordered molecules. This understanding will allow researchers to improve charge and exciton transport while reducing energy losses due to recombination. On the other hand, existing experiments are incapable of capturing both, particularly in the case of actual thin film devices in which the active layer is concealed behind selected transport layers and electrodes. Numerical simulation models may be used in conjunction with experimental analyses to link the experimental findings with the kinetics of charge carriers and excitons on a molecular level. In contrast to realistic morphologies, most current numerical tools like drift-diffusion (DD) models reduce the complicated bulk-heterojunction morphology by using effective medium approximations [16, 17]. Significant convergence problems, on the other hand, may occur when the dimensions are increased. Moreover, DD models do not include the non-equilibrium kinetics of charge carriers, which limits the insight to understand the detailed morphological effects in OSCs [17–19].

To address the complexity inherent in OSCs, numerical models, particularly simulations based on the kinetic Monte Carlo (kMC) technique, are an appropriate tool for investigating the mechanisms controlling OSC device operation. In recent decades, ki-

netic Monte Carlo (kMC) models have been effectively used to simulate charge carrier kinetics [20–22] and exciton dynamics [23, 24] in organic semiconductors recombination properties [14, 25–27], as well as complete OSC devices [28–32]. As a consequence, a diverse array of characteristics derived from the mobility of local charge carriers [33–35] up to the full current–voltage characteristics [30] can be examined. Thus, the use of kMC models enables the establishment of a link between molecular structures and complete device models.

1.3 Context and outline of thesis

The purpose of this study is to present a state-of-the-art, in-house implemented 3D kMC model for organic solar cells that is used to simulate a complete solar cell device under actual operating circumstances while taking into account morphological and particle-based effects on the nanoscale. The spatially and energetically disordered morphology of particles is implemented, with the set of main dynamic processes responsible for their time-dependent behavior. The developed kMC model is employed to explore a variety of features of OSCs, including charge transport and device morphology. Typical OSCs exhibit significant open-circuit voltage losses. Existing research has shown that the energetic disorder and the recombination losses mainly contribute to voltage loss. To get further insight, the main part of this study is focused to investigate the effect of the intermixed BHJ morphology and the electronic density of states at the interface of the acceptor, donor, and extraction layer. Besides typical OSC morphology with an equal ratio of donor and acceptor (mixed phases), there is also research inclination towards the origin of hole transport in isolated phases with low donor concentration, i.e. dilute donor OSCs. This work subsequently covers the examination of dilute donor OSCs as excellent test systems for examining the physical mechanisms behind hole transport in isolated phases.

Furthermore, the implemented kMC model is used in conjunction with another numerical simulation tool, Drift-diffusion (DD), to theoretically model tandem/multi-junction designs for high-efficiency hybrid perovskite-organic solar cells. While all-perovskite and all-organic tandem designs have been extensively explored, hybrid perovskite-organic devices are currently searching their ways towards higher efficiency by simplifying and optimizing the complicated fabrication processes. Simulation tools give possible pathways to help use simple fabrication materials and methods. Overall, this complete study focuses on the influence of critical factors like the energetic disorder and the active layer morphology on the charge transport mechanism and theoretical modelling of different solar cell architectures.

The outline of the thesis is as follows:

To begin with, Chapter 2 discusses the basics of solar cells — with an emphasis on organic materials as components, following a review of photovoltaic device operation and an overview of established and emerging solar cell technologies and state-of-the-art in general. This follows by discussing the evolution of OSC research from its inception till now. The unique properties of organic semiconductors are discussed, which differ significantly from those of inorganic semiconductors (particularly in terms of energetic disorder and permittivity). The following sections discuss the significance of active layer morphology to provide the required theoretical context for understanding the model implementations. Finally, briefly discussed are efficiency limits for OSCs.

The core of the kinetic Monte Carlo algorithm is presented in Chapter 3. A short overview of the evolution of kMC simulations and their wide range of applications provides the reader with an idea of the breadth of kMC simulations. It includes a mathematical representation of the algorithm and a model for the general flow of a sequential kMC method implementation.

Chapter 4 discusses the broader application of kMC implementation to investigate the impact of interface energetics and disorder at the donor:acceptor interface, and the interface between the photoactive layer and the extraction layer on OSC performance. We parameterize a moderately efficient OSC model to study both effects. Furthermore, we show that the losses owing to the disorder at the interface can be partially restored in the presence of energy cascades by mixed phases within the interface region. The contents of this chapter have been published in [36, 37].

Chapter 5 represents the novel architecture in the BHJ morphology, i.e. diluted donor organic solar cells. Organic solar cells with low donor content present an ideal test model to investigate the hole transport and isolated phases. We present a kMC study of the impact of the polymer morphology on the performance of organic solar cells with a donor content of 1wt.%. The photocurrent generation is investigated for different offsets between the acceptor and donor highest occupied molecular orbitals (HOMO) and morphologies. The results in this chapter are based on [38].

Chapter 6 focuses on the implementation of the tandem/multi-junction architecture for perovskite-organic tandem solar cells. Using a multiscale approach, a simulation tool addresses the many physical characteristics of the device while keeping computing cost low. We, in particular, model a multiscale tool that integrates the drift-diffusion model with the kMC model to help advance OPVs and organic semiconductor devices. In this study, we propose a tandem solar cell model using hybrid perovskite-organic solar cells. Initially, tandem architecture using perovskite and organic active layers is modelled to explore the series-connected tandem solar cell structure and analyze the

effect on the device performance. Further, this work examines different perovskite cells combined with the organic blend in a multi-junction configuration to give a concrete model representation. This is a unique way to simulate tandem/multi-junction solar cells in inorganic/organic configuration.

The research work for this thesis concludes with Chapter 7.

2 Organic Solar Cells

Since the invention of the first photovoltaic device many decades ago, organic solar cells (OSCs) have achieved a power conversion efficiency (PCE) exceeding 18%, according to the National Renewable Energy Laboratory (NREL). Over time, OSCs have developed rapidly due to multidisciplinary efforts, including novel materials synthesizing, device physics and engineering. These disciplines have made significant advances in recent years. This chapter provides an overview of solar cells in general and OSCs in specific. In the beginning, the fundamental operating principles of solar cells and the characteristic parameters used to quantify their performance are discussed. It follows the description of key processes in OSCs based on organic semiconductors. In the end, the possible challenges for efficient device operation and the outlook are presented concerning ongoing research.

2.1 Working mechanism of a solar cell

Solar cells use the photovoltaic effect to convert radiant energy into electrical energy. The photovoltaic effect is the voltage or current produced in a substance when exposed to light. A.H. Becquerel, a French scientist, discovered in 1839 that shining a bright light on an electrode submerged in conductive solution might generate an electric current [39]. In 1873, W. Smith discovered selenium's photo-conductivity, which led to the development of photovoltaic technology [40]. A. Einstein provided the first explanation of this effect in 1905 [41]. Semiconductors exposed to the light source (photons) with energies greater than their bandgap energy may exhibit this effect. A photon incident on the semiconductor material may transfer its energy and excite an electron from a bound state to an unoccupied state across the bandgap. This results in the formation of a hole state. After that, the charges may be collected at the respective electrodes to generate an electric current. A wide range of materials and methods can meet the criteria for photovoltaic energy conversion. However, in reality, semiconductor materials are used in almost all photovoltaic energy conversion applications. Since their bandgap energy is usually in the range of incoming photon energy from the solar spectrum (see Fig. 2.1)[1],

[1] https://www.nrel.gov/grid/solar-resource/spectra-am1.5.html

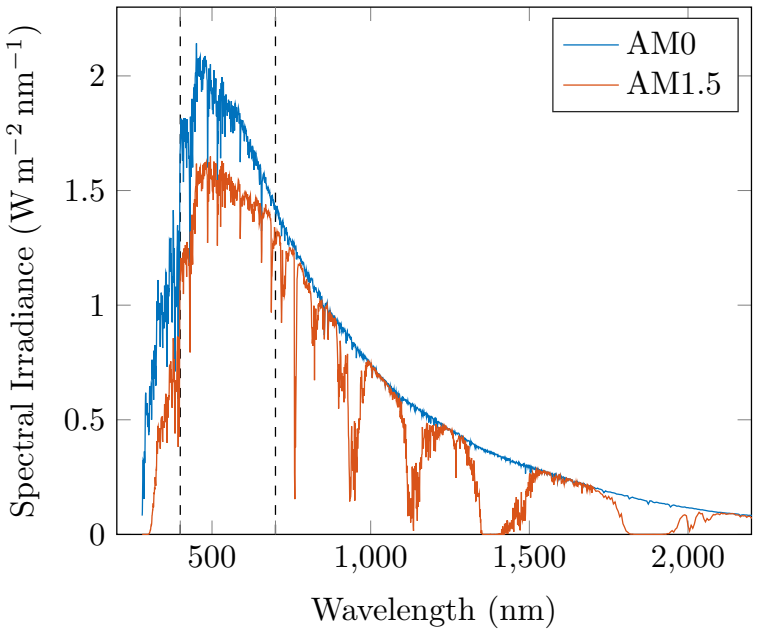

Figure 2.1: Spectral irradiance vs Wavelength. 'AM0' is the solar radiation under extraterrestrial conditions without absorption in the atmosphere. 'AM1.5G' spectrum is the industry standard for non-concentrated photovoltaic conversion, taking into account atmospheric light absorption and scattering. Data extracted from National Renewable Energy Lab[1].

thus allowing for photovoltaic effect to take place. The following are the fundamental processes in the solar cell operation:

- Formation of photo-generated carriers after the light absorption
- Dissociation of photo-generated carriers into free charge carriers
- Collection of the free charge carriers at the respective electrodes

The first step is the absorption of the incident light source in the form of photons. The most common method to characterize a light source is to measure its spectral irradiance as a function of photon wavelength (or energy). The photon flux and spectral irradiance are often required in the analysis of solar cells. Spectral irradiance may be calculated by converting photon flux at a particular wavelength to W m^{-2} and dividing by the wavelength as given by the equation[2]:

$$F(\lambda) = \Phi_{\mathrm{p}} \frac{E}{\Delta\lambda}\,, \tag{2.1}$$

where, $F(\lambda)$ is the spectral irradiance, λ and E are the wavelength and energy of the photon, while Φ_{p} is the photon flux. The standard solar irradiance spectrum is shown

[2]https://www.pveducation.org/pvcdrom/properties-of-sunlight/spectral-irradiance

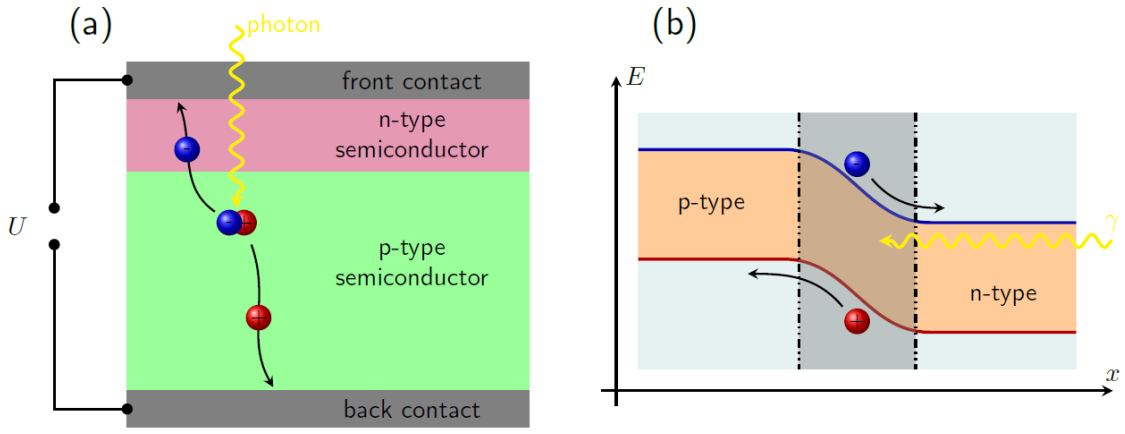

Figure 2.2: (a) Generic architecture of *p*-*n* junction solar cell (b) Movement of electrons and holes under *p*-*n* junction configuration. Reproduced with permission from [42].

in Figure 2.1. AM0 is the standard spectrum used for space applications with a combined power of 1366.1 $\mathrm{W\,m^{-2}}$, while AM1.5 is the Global spectrum, that reaches the surface of the earth with an integrated power of 1000 $\mathrm{W\,m^{-2}}$ (100 $\mathrm{mW\,cm^{-2}}$). The irradiance reaches its maximum value in the visible range sketched by vertical dotted lines in Figure 2.1. Exposure of semiconducting material to solar spectrum results in the formation of photo-generated carriers as electron-hole pairs. The solar cell can only produce electron-hole pair if the incident photon has more energy than the bandgap. Electrons and holes in *p*-type and *n*-type materials, respectively are meta-stable and only exist for a minority carrier lifetime before recombination. The charge carriers are lost if they recombine and no current can be extracted. The generic architecture of a *p*-*n* junction solar cell is represented in Figure 2.2. Standard *p*-*n* junction solar cells are fabricated using a material with highly doped *p*-layer as compared to an *n*-layer. A depletion layer forms at the interface between two oppositely doped materials. Since the light must be absorbed inside the depletion layer, the highly doped *p*-layer ensures excellent light absorption.

As shown in Figure 2.2(b), it is possible for holes from the p-doped region and electrons from the n-doped region to migrate to the region with opposite doping and partly recombine therein. This creates a positive (+) static charge on the n-side and a negative (-) charge on the *p*-side across the depletion region. The resultant static charge at the interface generates a field-effect within, accounting for the dissociation of electron-hole pairs into free charges during the dissociation process. Due to the internal field-effect in the depletion region, photo-generated electron–hole pairs are readily dissociated. As a result, electrons/holes are easily transported to the contacts through the *n*-layer/*p*-layer. It is possible to create a potential difference across a junction by the field-effect produced by the diffusion of majority charge carriers into the minority area. For photo-

generated charge carriers, the typical diffusion length is an essential parameter. That is how far charges travel on average before recombination happens. Only when the diffusion length is substantially higher than the active layer thickness it is possible to transport the charges via diffusion; if not, an internal electric field is required to to drive charge carriers towards the contacts successfully.

Lastly, an effective charge collection and extraction at electrodes is critical for efficient operation of any solar cell [43]. It has been reported that contacts with low sensitivity may significantly reduce the device efficiency [44]. To improve selectivity, electron and hole transport layers are often used in conjunction with one another to prevent the extraction of carriers at the wrong electrodes. Würfel *et al.* demonstrated the need for selectivity as the crucial condition for solar cell operation [45]. The conductivity of majority charge carriers on their route to the relevant contact must be considerably greater than the conductivity of minority charge carriers [45]. It is critical to note that this requirement must be met regardless of light or imposed bias. Furthermore, the development of Ohmic connections may restrict the charge extraction, as has been seen in silicon solar cells [46].

2.2 Figures of merit for solar cells

The current density-voltage J-V characteristic of a solar cell is the very first method to determine the efficiency of a solar cell, and an example of this characteristic is given in Figure 2.3. It is customary for this measurement to be performed under an AM1.5 solar spectrum. The output current of a solar cell is measured after it has been subjected to an external bias. The equivalent circuit diagram may be used to calculate p-n junction solar cell J-V characteristics (see Fig. 2.3(a)). A continuous current source J_{pv} represents the photocurrent produced by the incident light. A parallel resistance R_{sh} (shunt resistance) to the diode is assumed to account for leakage currents and R_{s}, the series resistance accounts for the contact resistance and losses at the interface. J-V characteristics can now be calculated as:

$$J = J_{pv} - J_0 \left[\exp\left\{ \frac{q(V + JR_{\mathrm{s}})}{nk_BT} \right\} - 1 \right] + \frac{V - JR_{\mathrm{s}}}{R_{\mathrm{sh}}} \,. \tag{2.2}$$

With J_0 being the saturation current, q is the electron charge, k_B is the Boltzmann's constant, T is the temperature, and n is the ideality factor. The equivalent circuit parameters must be adjusted to match the behavior of the equivalent circuit to the findings of the solar cell testing. In some cases, this adjustment can be performed numerically [47,48] or analytically [49–51]. In both the cases, it can be performed based on the data obtained

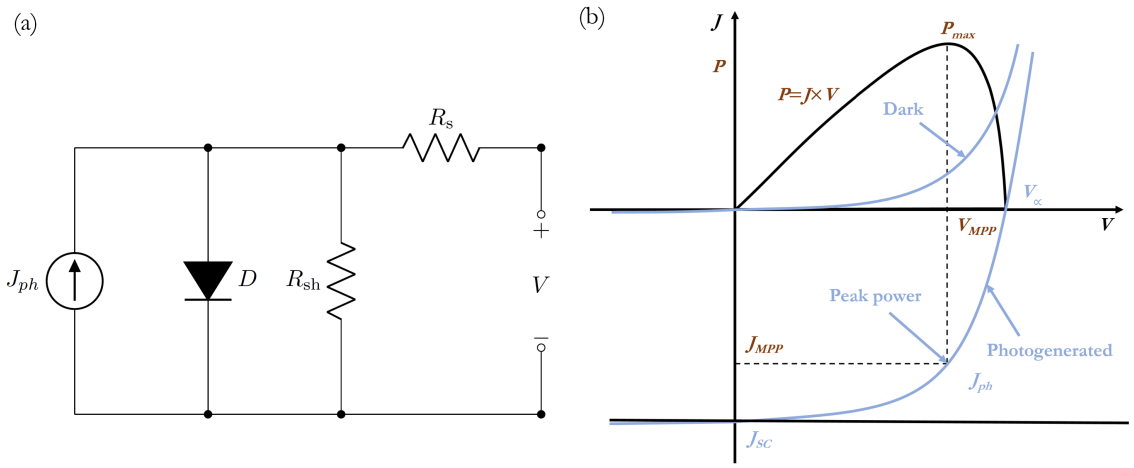

Figure 2.3: (a) Equivalent circuit diagram of a solar cell (b) J-V characteristic curve and figures of merit for solar cell.

from experimentally measured J-V curves or solely on the data obtained from the manufacturer's datasheets.

Based on the J-V curve, the following parameters may be used to calculate the figures of merit for a solar cell's performance:

Short circuit current (J_{sc})

The solar cell without any external bias ($V = 0$) is considered to be under short-circuit condition, and the current flowing through the cell is referred to as short-circuit current J_{sc} in this situation. J_{sc} may be improved in a variety of methods. These include increasing the light absorption via the use of narrow bandgap or high absorption coefficient materials, reducing non-radiative recombination, or increasing the charge carriers' mobilities [52].

Open circuit Voltage (V_{oc})

The V_{oc} is the voltage across the solar cell, at which the photo-generated current perfectly offsets the dark current, resulting in $J_{net} = 0$. This voltage is determined by the quasi-Fermi level splitting of holes and electrons after the absorption of incident photons [53,54]. Consequently, V_{oc} is linked to the relative energies of holes and electrons.

Fill Factor (FF)

The Fill Factor is essentially a quality indicator for solar cells. It is calculated by comparing the theoretical maximum power to the power output at both the open circuit voltage and short circuit current, such that,

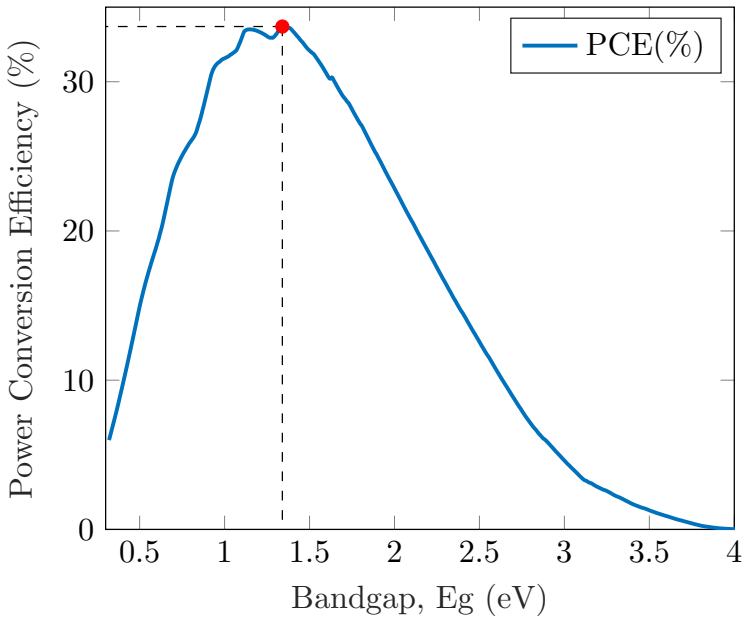

Figure 2.4: Shockley–Queisser limit for the PCE as function of the bandgap, E_g[3].

$$FF = \frac{P_{MPP}}{J_{sc}V_{oc}} = \frac{J_{MPP}V_{MPP}}{J_{sc}V_{oc}}. \tag{2.3}$$

Graphically, FF measures the squareness of the solar cell's J-V curve.

Power conversion efficiency (PCE)

The most common criterion for assessing solar cell performance is its efficiency. It is defined as the fraction of solar power produced to the power input from the solar spectrum. The percentage of incident power converted to electrical power determines a solar cell's efficiency as:

$$PCE = \frac{P_{MPP}}{P_{in}} = \frac{J_{MPP}V_{MPP}}{P_{in}} = \frac{FFJ_{sc}V_{oc}}{P_{in}}, \tag{2.4}$$

where, P_{in} is the power per unit area of the incident light spectrum. The conditions under which efficiency is assessed must be carefully regulated to compare one device's performance to another. Since solar cells should be as efficient as possible, it is necessary to simultaneously boost the fill factor, short circuit current, and open circuit voltage.

Detailed balance limit

The detailed balance method is used to determine the maximum achievable efficiency of the solar cell. Shockley and Queisser first presented the technique in 1961 [55]. Tiedje *et al.* released an extended version of the same in 1984 [56]. In its simplest and most frequent implementation, detailed balance assumes that electrons and holes are highly

mobile, allowing charge collection from any location irrespective of the origin they are generated from, and all the photons with energy above the bandgap of the material are absorbed. A photon absorbed by the cell results in the formation of one electron-hole pair, which in turn limits the maximum achievable current that can be extracted from the cell. We could, in theory, employ the semiconductors solely with a narrow bandgap to absorb solar radiation across a broad range of wavelengths.

Additionally, photon energies higher than the bandgap cause extra energy to be lost to the bandgap edges via thermal relaxation. This lowers the highest possible photovoltage; thus, the efficiency is similarly affected. Conversely, larger bandgaps lead to the absorption of fewer photons by the semiconductor, which decreases the photocurrent. Figure 2.4 shows the Shockley-Queisser limit for PCE as the function of the bandgap of semiconductors[3]. The Shockley and Queisser predicted that a single *p-n* (homo) junction might reach a thermodynamically feasible efficiency of approximately 33.7% at the optimal bandgap of 1.34eV as shown by the dotted lines in Figure 2.4[3]. PCE decreases due to reduced absorption for higher bandgaps, while lesser bandgap materials incorporate more losses. Their model has been explained for bulk-heterojunction OSCs, which are made up of a heterojunction, and have an inherent energy loss introduced by the energy offset [57–61].

2.3 Emerging photovoltaics

Emerging photovoltaics (PVs) are newly emerging technologies focused on a range of applications that may supplement large-scale power production. In addition to the National Renewable Energy Laboratory (NREL) chart[4], the most frequently used resources to record research cell efficiencies are the efficiency tables compiled by Martin Green, and his colleagues [6]. Both resources provide certification of the recorded efficiency for different photovolatic technologies, and serve as a bridge between research and industry. Figure 2.5 visualizes the reported efficiencies of different emerging Photovoltaic technologies by NREL and how these technologies have evolved in recent years.

Single-crystal silicon (Si) solar cells, introduced by Mobil Solar in the late 1970s reported to have an efficiency of around 14%. It rose in 1995 to 24%, but since then it has not really got the upward trend but a slight increase up to 26.1% to date. On the other hand, single-junction GaAs was reported as one of the efficient solar cells in the late 1970s by International Business Machines (IBM) with an efficiency of 22%. However, their efficiency has not been increased too much till now. The recorded efficiency for

[3]Reproduced from the data available at https://github.com/marcus-cmc/Shockley-Queisser-limit
[4]https://www.nrel.gov/pv/assets/pdfs/best-research-cell-efficiencies-rev210726.pdf

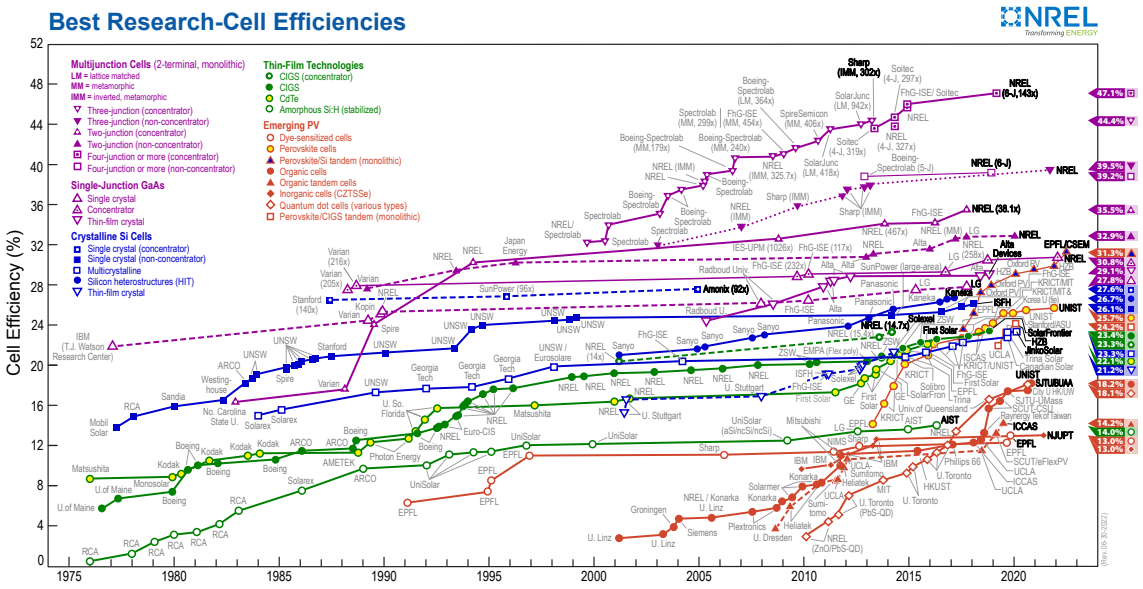

Figure 2.5: Efficiency chart of the reported cell efficiency of different Photovoltaic Systems by National Renewable Energy Laboratory (NREL)[4].

single-junction GaAs to date is around 27.8%. While using thin-film crystalline material, Si and GaAs have reported efficiency of 21.2% and 29.1%, respectively.

Multi-junction solar cells were introduced a little late as compared to crystalline and thin-film Si solar cells. In the early 1980s, North Carolina State University introduced two junction solar cells of concentrator type with a reported efficiency of about 16%. In the beginning, their efficiency was not that high, but with recent research, multi-junction solar cells with efficiency more than 47% are reported by National Renewable Energy Laboratory. Multi-junction solar cells are state of the art in space applications. In bad conditions like high temperature and low light conditions, multi-junction solar cells perform a bit better than crystalline silicon solar cells with decreased thermalization losses owing to their absorption of a broader spectrum. Two-junction (tandem), three-junction and four-junction (concentrated) solar cells are also reported to have a record efficiency of 35.5%, 44.4% and 47.1%, respectively.

Thin-film technologies have been recognized in the late 1970s. The earliest cells had very low efficiency. Solar cells like Cadmium Telluride (CdTe) and Copper-indium-gallium diselenide (CIGS), with recorded efficiency of 22.1% and 23.4%, respectively, now dominate the high-performance photovoltaic market, with substantial gains made in their efficiency over the last decade. Some of the benefits that emerging thin-film PVs bring to the table include their lightweight, semi-transparency, compatibility with roll-to-roll manufacturing techniques, and flexibility, which may help them carve out a place in the energy production industry in the near future.

There are numerous types of emerging photovoltaic technologies, including, but not limited to, organic solar cells (OSCs), dye-sensitive solar cells (DSSC), and perovskites (PSCs)These technologies typically do not use a single material but rather a family of materials. In certain instances, the device designs must account for the evolving scientific or technical design requirements. The study on emerging solar cell technologies also focuses on integrating flexible and semitransparent devices into buildings, greenhouses, aircraft, sails, cars, textiles, and interior applications. The state of the art devices in these settings would never make it into rankings of top research cells based on technology since they are still lacking the required efficiency and the stability for the commercial use [6].

Dye-sensitized solar cells (DSSCs) have been in the photovoltaic market for last 3 decades due to their excellent photovoltaic performance in low light, color and appearance versatility, ease of manufacture, and possible low cost. O'Regan and Grätzel fabricated the first efficient dye-sensitized solar cells (DSSCs) in the 1990s using mesoporous TiO_2 electrodes made from colloidal TiO_2 nanoparticles [62]. DSSCs have been the subject of considerable study for more than two decades due to their low cost, easy manufacturing technique, low toxicity, and simplicity of fabrication. Existing DSSCs have an efficiency of up to 13%, but this is still less than the efficiency of first- and second-generation solar cells, i.e., other thin-film solar cells and Si-based solar cells[4].

Due to their high power conversion efficiency, perovskite solar cells (PSCs) are the most rapidly developing field of research among the emerging photovoltaic technologies. As an active light-harvesting layer, the PSC makes use of the ABX3 crystal structure, also known as the perovskite structure. In contrast to silicon solar cells, PSCs are less costly, and their manufacturing may be accomplished via a simple wet chemical procedures. The technology has made significant strides in the last decade, with conversion efficiencies increasing from 3.8% in 2009 [63] to over 25% now. While perovskite solar cells have advanced to a high level of efficiency in a very short time, some challenges like hysteresis caused by ion migration, lead toxicity, and long-term stability must be overcome before they can be considered a viable commercial technology. A tandem architecture of perovskite with Si has also outperformed the single junction crystal Si solar cell with reported efficiency of 29.1%. However, the processing of such architectures involves high-temperature processing conditions and are typically costly [6]. The fabrication process sometimes contains hazardous chemicals and is not readily scalable. Because of these disadvantages, perovskite/Si based solar cells have not been widely adopted, particularly for residential and private applications.

During recent years, solar cells consisting of organic materials, so called organic solar cells (OSCs) have been subject of intense research. [13, 64–66]. OSCs consist of semicon-

ducting carbon-based molecules or polymers (malleable materials) that provide significant benefits including low-temperature high-throughput manufacturing (e.g. roll-to-roll printing) [67,68], a short energy payback time [69,70], and sustainability (i.e. availability and recyclability) [71]. Additional distinctive characteristics include mechanical flexibility, light weight, and semi-transparency enable a number of innovative applications, such as tiny, portable/wearable electronics or the integration of light harvesting devices onto building facades. Shaheen *et al.* reported the initial record PCE of 2.5% of organic photovoltaic devices based on a conjugated polymer/methanofullerene blend in 2001 [72]. Mitsubishi Chemical achieved a PCE of more than 9% for lab devices with an active surface of $< 1\,\mathrm{cm}^2$ around ten years later [73]. Efficiencies showed an increasing trend in the following years as a result of greater control over donor:acceptor morphologies and a better knowledge of the device physics. Operating efficiencies of up to 10% have been obtained in fullerene-based organic solar cells (OSCs). It has been more common in recent years to use non-fullerene acceptors instead of fullerene acceptors. Since 2015, the performance of non-fullerene acceptors has increased dramatically, and a verified PCE of 18.2% for single-junction solar cells has been achieved to date (see Fig. 2.5). Solar cells based on Si and thin-film are still more efficient than OSCs. However, the PCE of OSCs (organic semiconductors and the devices built from them) have fundamentally different charge generation, transport, and loss processes than inorganic semiconductors owing to their low permittivity and disordered structure. It is thus necessary to enhance their efficiency via optimization and as well as to gain a better understanding of their internal operations through experimental and theoretical studies.

2.3.1 State of the art

From the outset of the development of solar cells, there have been constant attempts to make them more efficient and reliable. The cost-effectiveness of solar energy generation has been a critical variable in its success. This resulted in the advancement of next-generations solar cells and the establishment of many photovoltaic businesses for their manufacture and development. Nonetheless, many new photovoltaic businesses are quickly emerging to maximize the use of this technology. Fraunhofer Institute for Solar Energy Systems (ISE) reported in their 2021 'Photovoltaics Report', the global photovoltaic market is dominated by mono and multi-crystalline Si solar cells with 80% and approximately 15% of the share respectively. Thin-film Si, CIGS, and CdTe solar cell technologies account for the remaining 5% [74].

Figure 2.6 visualizes the performance comparison of the cell to module ratio for different solar cell technologies. The record lab cell efficiency for mono-crystalline silicon wafer-based technology is 26.7%, while the record lab cell efficiency for multi-crystalline silicon

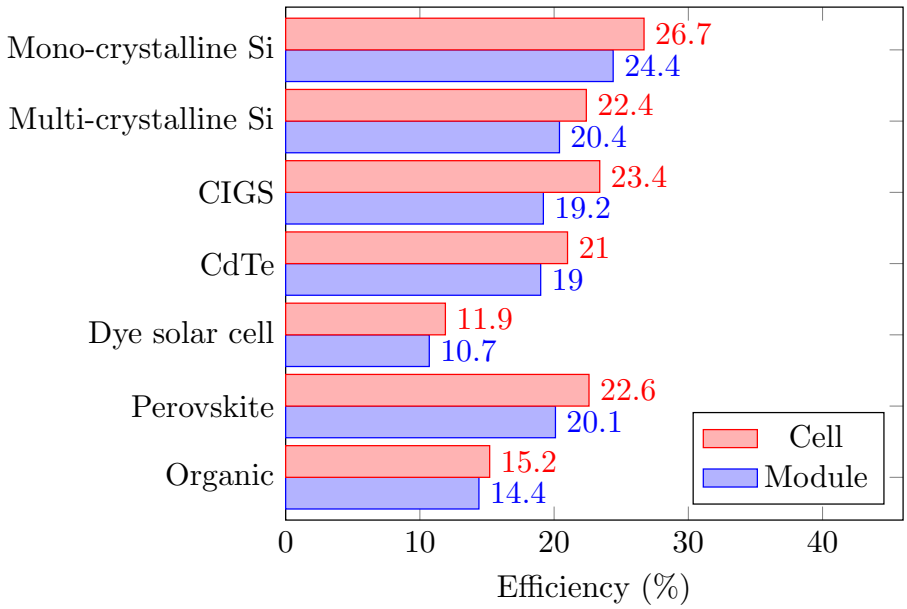

Figure 2.6: Cell to module ratio performance of different solar cell technologies. Data extracted from [6].

wafer-based technology is 22.4%. In the past decade, commercially available wafer-based silicon modules have improved from 15% to 20% efficiency. Meanwhile, CdTe modules have reached 19% efficiency from the initial efficency of 9% [74]. For CIGS solar cells, the lab efficiency is reported at 23.4%, whereas for CdTe solar cells, the best efficiency is 21.0%. Perovskite solar cells are the latest emerging technology with a reported module efficiency of 20.1% with organic solar cells to follow with 14.4% efficiency. The Cell-to-Module Ratio (CTM) in mass manufacturing has increased in recent years as a result of the reduction of losses and the use of potential benefits when integrating solar cells into modules for the mentioned technologies in Figure 2.6 [6].

When it comes to PV module manufacturing, Asia accounts for around 92% of the global production, while Europe accounts for 3%, USA/Canada 3%, and rest of the world accounts for remaining 2%. A total of 57 GW_p(8%) of the total PV capacity of 708 GW_p of the world was installed in Germany by 2021 [74]. Thin-film technologies are less developed than first-generation solar cells and account for a small proportion of the PV market. They face challenges related to material availability, long-term stability, cost and toxicity(except thin-film Si). Unfortunately, the total cost of energy generated by solar cells remains extremely expensive compared to fossil fuels. As a result, most of the research and development efforts are being directed toward the possibility of cost-effective organic and perovskite solar cell technologies. These technologies are still in the research and development stage and have not yet reached the commercialization stage.

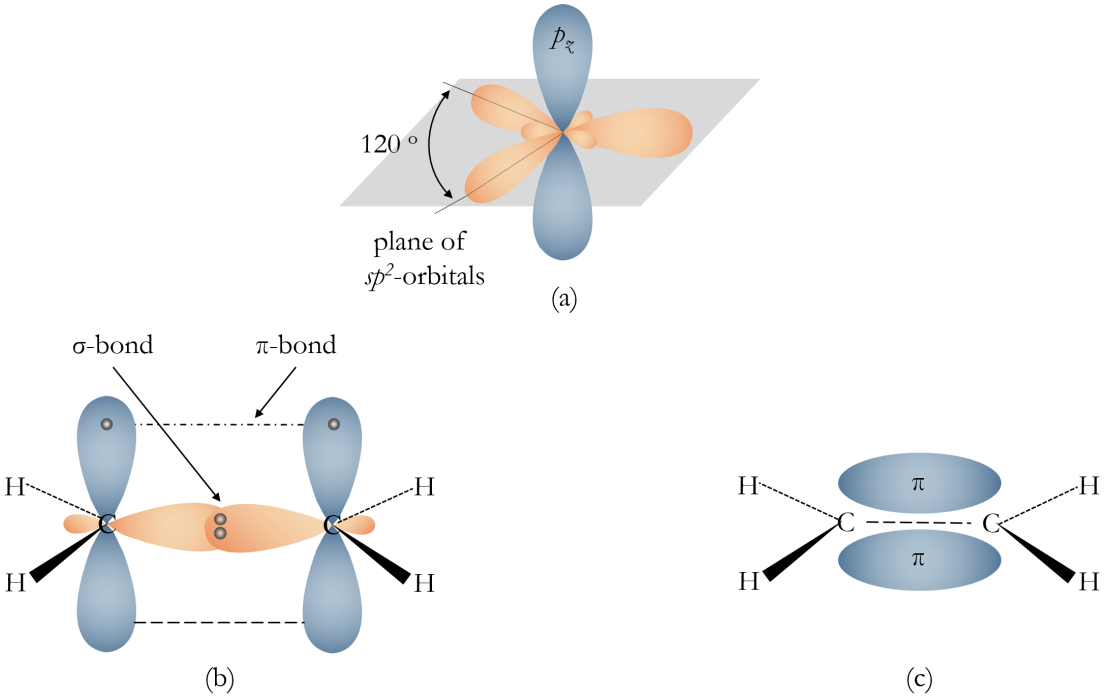

Figure 2.7: Schematic representation of π and σ bonds. Adapted from [79].

2.4 Organic Semiconductors

Organic (carbon-based) molecules dominate molecular semiconductor technology due to their incredible flexibility. Although some work on organic semiconductors had been done in the 1960's [75, 76], the discovery of conductive polymers in 1977 is widely regarded as the beginning of the research field in this area [77].

Organic semiconductors are a unique type of unsaturated hydrocarbons with a π-conjugated system and can readily be divided into two groups: conjugated small molecules and conjugated polymers. The so-called σ-bonds between sp^2-hybridized carbon atoms serve as the molecular backbone in both of these systems. The conjugated system is formed on the top of the backbone by the overlapping p_z orbitals of adjacent carbon atoms as shown in Figure 2.7. Since π-bonding is considerably weaker than σ-bonding, electronic transitions from bonding π-orbitals to antibonding π^*-orbitals are achievable by optical stimulation without causing the molecule to disintegrate completely as depicted in Figure 2.8 [78]. When atoms join together to create a molecule, bonding and antibonding orbitals are formed between them. Interaction between two π atomic orbitals leads to bonding when the interaction is in phase; otherwise, antibonding occurs, and the interaction results in antibonding orbitals.

In polymers, electrons are delocalized along the chain via unoccupied and occupied molecular orbitals. It is analogous to a one-dimensional electrical system, with charge

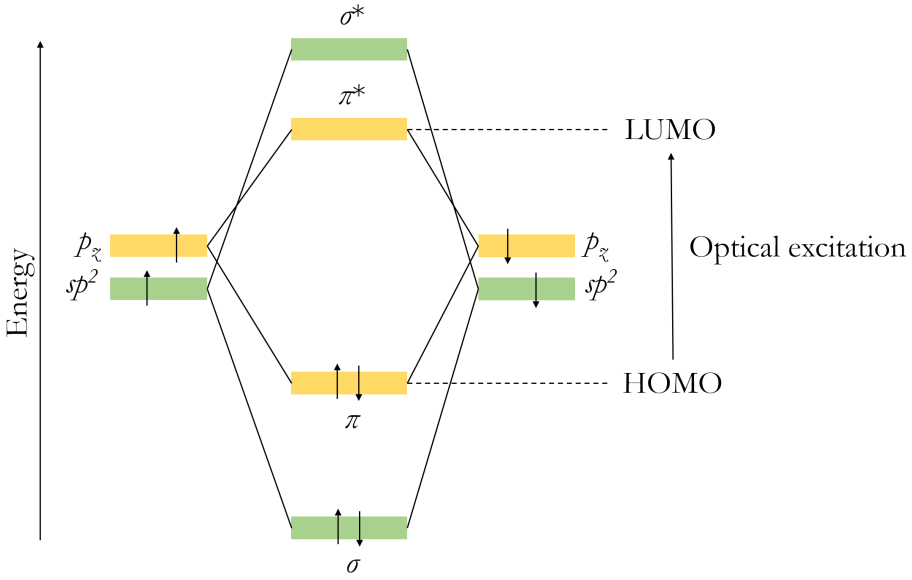

Figure 2.8: Energy level diagram of π and σ bonds of sp^2 hybridized carbon atoms. The lowest electronic excitation is shown from $\pi-$ to π^*- orbital. Adapted from [79].

transfer occurring through higher-occupied and lower-unoccupied molecular orbitals. The thermal-assisted hopping phenomena facilitate the charge transfer between chains. Two important energy levels distinguish the two distinct bands of occupied and unoccupied molecular orbitals, notably electron affinity (E_a) and ionization potential (I_p). E_a is the energy released from the vacuum level to the lowest energy level in the conduction band during an electronic transfer. On the other hand, I_p is the energy needed to liberate an electron from the highest energy level of the valence band. As a result, E_a is equal to the energy of the lowest conduction band state (π^* orbital) or the lowest unoccupied molecular orbital (LUMO), and I_p is the energy of the higher state of the valence band (π orbital), which corresponds to the highest occupied molecular orbital (HOMO). The bandgap (E_g) of a semiconductor is thus the distance between its LUMO and HOMO energy levels [80]. The energy gap for organic semiconductors typically lies in the range 1.5 - 3eV, which makes them useful for optoelectronic applications [78, 81]. The charge transfer in organic semiconductors occurs in π bonding and antibonding orbitals, or in other words, at the HOMO and LUMO energy levels. Individual HOMO and LUMO levels of molecules follow Gaussian distribution in the bulk of the semiconductor [80].

Organic semiconductors are inherently insulators, yet they are referred to as semiconductors because they have the ability to conduct electrical current if charge carriers can be injected or generated in them by field-effect, optical excitation, or injection from electrodes [78]. Organic semiconductors are mechanically extremely soft and have low melting temperatures, making them good candidates for use in wearable/flexible electronic devices. In inorganic semiconductors such as GaAs, Ge and Si, the adjacent atoms

in the lattice are tightly coupled together through covalent or ionic bonding in a long-range order, resulting in a significant electronic wave-function overlap over the individual atoms. The permissible conduction and valance bands are formed by the electronic wave-function overlap of the atoms [80]. The charge carriers can easily move from one atom to another because of the overlap of electronic wave-functions resulting from the delocalization of charge carriers within energy bands. This type of transport mechanism is referred to as the band transport. The charge carrier (wave-function) is delocalized throughout the whole molecule or system in the band transport regime. The delocalization of the system results in probability of finding the charge carrier in any location in the whole system. The band transport requires a highly ordered system that allows for large electronic coupling between neighboring sites on adjacent molecules or polymer repeat units resulting in coherent transport.On the other hand, organic semiconductors are disordered and include a large number of structural and chemical defects, and their intermolecular interactions are very weak compared to inorganic counterparts. The intramolecular bonds are mostly covalent, while the intermolecular interactions are primarily van-der-Waals and London forces [78]. The overlap of the molecular orbitals and the intermolecular electron exchange is minimal, and the energy levels in the conduction bands are discrete. The optical and electrical characteristics of semiconductors are directly affected by the weak electronic interaction between the molecules. Therefore, one must refer to the general notion of Density of States (DOS) instead of a band structure to describe the energetic landscape of such disordered materials. The distribution of DOS in a typical inorganic and organic semiconductor is shown in Figure 2.9. It is necessary to differentiate between the intrinsic DOS caused by the structural disorder and extrinsic DOS, caused by the defects located deep inside the bandgap and can be several hundred meV in magnitude. The following work will focus on the intrinsic DOS, a broadening effect around the LUMO/HOMO energy levels caused by the structural disorder. Gaussian or exponential DOS are frequently employed to statistically characterize the he distribution of the localized states around the corresponding LUMO and HOMO energies in order to quantitatively explain the disorder, introduced by Bässler [20]:

$$g(E) = \frac{N}{\sigma\sqrt{2\pi}} \exp\left(-\frac{(E - E_0^2)}{2\sigma^2}\right), \tag{2.5}$$

where, σ is the energetic disorder, N is the available DOS of the localized states, and E_0 is the energy level in the center of either the HOMO or LUMO energy levels.

According to Bässler, the movement of charge carriers in organic semiconductors mostly occur via a thermally-assisted hopping process [20]. In hopping mechanism, the charge carrier is localized on a single molecule, and the charge transport can be followed from

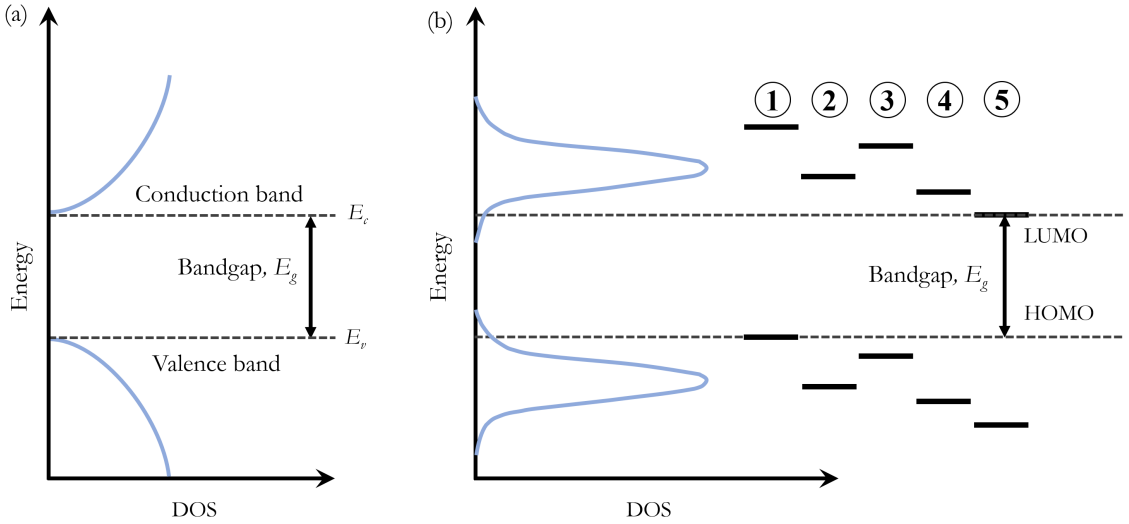

Figure 2.9: Density of states representation for (a) Inorganic (b) Organic semiconductors. Adapted from [80].

molecule to molecule or chain segment to chain segment. The hopping transport is incoherent because each hop is random and has no correlation to immediately preceding hop. Because hopping transport is a random process, the charge carrier mobilities in these materials are extremely low ($\mu << 1\,\mathrm{cm^2\,V^{-1}\,s^{-1}}$) and highly sensitive to temperature and electric field in comparison to band transport charge carrier mobilities of ($\mu \approx 100 - 10000\mathrm{cm^2\,V^{-1}\,s^{-1}}$) in inorganic semiconductors [78]. Miller Abaraham model describes hopping processes in disordered systems. [82] (see section3.3.2.1 for further details)

$$a_h = a_0 \cdot \exp(-2\gamma r) \begin{cases} \exp\left(-\frac{\Delta E_{a\to b}}{k_\mathrm{B}T}\right) & \text{if} \quad \Delta E_{a\to b} > 0 \\ 1 & \text{if} \quad \Delta E_{a\to b} \leq 0 \end{cases}, \tag{2.6}$$

where, a_0 is the hopping prefactor at room temperature, γ is localization length, r is the distance between localized states, and $\Delta E_{a\to b}$ is the molecular orbital energy difference. Bässler used the Miller-Abrahams model to study the effect of an applied electrostatic field, temperature, and Gaussian density of states on charge mobility using kMC simulations [56].

Experiments have shown that crystalline organic semiconductors have intrinsic charge transport, which is characterized by a negative temperature dependency of mobility in the 200 K to 300 K temperature range [83, 84]. It is widely accepted that this power-law dependency ($\mu \propto T^{-n}$) is a manifestation of coherent band-like transport, which arises from the contribution of Bloch electronic states and is analogous to the process of charge transport seen in their inorganic counterparts [85]. The electron-phonon coupling is often viewed as a perturbation, and the negative dependence of mobility is attributed to the

scattering of phonons. However, in crystalline semiconductors, this image is unclear since the mean free path of charges is found to be just a few lattice constants in this temperature range [86, 87]. On the other hand, at lower temperatures, when the mean free path is assumed to be larger, a positive temperature dependency of mobility is found [88–90]. In the case of disordered materials, the mean-free path before charges deviate from the periodic arrangement is short due to the lack of long-range order. Charges are restricted to localized states with a localization length of between 0.1 nm to 1 nm [91, 92]. In such case, the charge transport is frequently described by the traditional incoherent thermally activated hopping model [85].

Another popular framework for describing charge transfer through a mechanism involving molecule-to-molecule charge transfer is the Marcus model [93]. It is frequently used in the literature to determine the transfer rate of charge carriers between two molecules. Marcus Formula is derived from Fermi's golden rule and expresses the rate of an electron hopping from the electronic ground state of the initial molecule i to the electronic ground state of the final molecule j, always travelling along the lowest of the vibrational energy curves. The interaction of the charge with its surroundings is a major issue in electron transport within molecules [94]. In order to facilitate the charge transfer, the surrounding environment must be altered as the charges are being transferred. The charge distorts the molecular site and its surroundings, including other molecules and solvents, resulting in the stability of localized charges and distortion in the form of tiny polarons [95, 96]. A quasi-particle known as a polaron comprises the combination of a charge and its deformation on a molecule. The polaron serves to neutralize the increased charge via a lattice shift inside the molecule. Marcus theory accounts for this impact by including the reorganization energy of a molecule as a result of the charge transfer process. The reorganization energy provides the free energy necessary to reconfigure the initial system to conform to the final configuration. Though this study does not use the Marcus theory of charge transfer, it is stated at this point as a courtesy to our readers.

One of the most important characteristics that distinguish organic semiconductors from their inorganic counterparts is the dielectric constant ϵ_r. Most of the organic semiconductors have a dielectric constant in the range 3 , to 5 , while conventional semiconductor, e.g. Si has a dielectric constant of 11.7 [80]. Because of the low dielectric values, the photogenerated holes and electrons are subjected to a high coulomb interaction, resulting in substantial recombination losses [97]. This bound electron-hole pair is referred to as an exciton. Once generated, the hole and the electron are usually found on the same molecule, therefore within their respective Coulomb potentials. Such excitons with a larger binding energy of electron-hole pairs are referred to as Frenkel excitons, named after Yakov Frenkel. The strong binding energy of such excitons lies in the range 0.1–1 eV [98]. These

excitons are highly localized, typically occurring on a single molecule, and are produced in molecular solids such as organic semiconductors. The binding energy of the excitons is given as [80]:

$$E_B = \frac{q_1 q_2}{4\pi\epsilon_r\epsilon_0 r^2}\,, \tag{2.7}$$

where, q_1 and q_2 are the two opposing charges (identical in magnitude), ϵ_r is the dielectric constant of the semiconductor, and ϵ_0 is the permittivity of vacuum. The distance between the two charges is denoted by r. When an exciton with a diameter of 1 nm is placed in a medium with $\epsilon_r = 3$ (organic semiconductors), the binding energy is estimated to be $E_B = 0.5\,\text{eV}$ ($> 0.025\,\text{eV}$ thermal energy) at room temperature. In inorganic semiconductors, the binding energy, on the other hand, is found to be less than 0.01 eV in most cases. As a result, at ambient temperature (thermal energy 0.025 eV), the excitons in inorganic semiconductors dissociate into free electrons and holes, while the excitons in organic semiconductors are strongly bonded and do not dissociate. Increasing the temperature (which causes thermal instability) or increasing the exciton radius in single organic semiconductors may be used to dissociate the excitons in the material. With the introduction of the electron donor-acceptor idea in OSCs for effective separation of electron-hole pairs, two materials with distinct electron-donating and accepting characteristics were utilized to achieve efficient exciton dissociation [99]. The energy difference between the acceptor and donor interfaces generates enough force to separate the electron-hole pairs. This gives rise to the successful implementation of the heterojunction concept.

2.5 Organic Solar Cells

The progress of organic photovoltaics throughout its history is linked to the interdisciplinary breakthroughs, including the development of new OPV materials, electron donor (n-type) materials, electron acceptor (p-type), and interfacial materials. In addition, advancements in device architecture and device physics have been key for its recent progress [100–104]. The following sections provide an introduction to OSC research development, the device operation and the physical processes. Many reviews of the physics underlying organic solar cells may be found in the literature for further information [13, 64, 105–107].

2.5.1 Development of OSC research

Photoconductivity in organic compounds has been investigated for more than a century, with the first experiments on anthracene being carried out by Pochettino [108] and Volmer [109] in the early 1900s. However, the photo-conductivity of minerals such as

selenium, rather than their photovoltaic characteristics, drew the interest of researchers. In the late 1950s and early 1960s, researchers began to realize the potential for organic materials to be used as photoreceptors in imaging systems [110]. The growing scientific and commercial interest in photoconductivity has resulted in further research into these topics and beyond. Breakthrough research in the early 1960s reported that several popular dyes, such as methylene blue have semiconducting characteristics [111]. Following this discovery, these dyes were among the first organic compounds to show evidence of the photovoltaic effect [112]. The study of organic semiconductors saw a resurgence after Shirakawa *et al.* demonstrated the increased electrical conductivity in polyacetylene films by more than seven orders of magnitude after being exposed to halogens [77]. Their work on conductive polymers was recognized with the Chemistry Nobel Prize in 2000. However, despite these advances, single-layer photovoltaics based on merocyanine dyes as an active layer (see Fig. 2.10) showed very poor efficiency of less than 1% until the 1980s [113, 114]. The difference in work functions of the two electrodes serves as the driving factor for dissociation of exciton in these types of OSCs. The electron-hole pairs are unable to separate enough due to weak driving force. As a result, the reported PCEs at an early stage are usually very low. Following that, in 1986, Tang proposed a bi-layer heterojunction OSC structure with the reported efficiency of around 1% [8]. The donor and acceptors layers were placed between two electrodes as shown in Figure 2.10. The energy difference between the LUMO levels of the acceptors and donors result in efficient dissociation of the donor-acceptor (D/A) interface. Only excitons produced at the D/A interface could dissociate efficiently into free charges because of the higher absorption penetration depth than the exciton diffusion length (up to several orders of magnitude). As a consequence, the small interfacial area between the donor resulted in inadequate exciton dissociation, and high charge recombination [8].

Bulk-heterojunction (BHJ) has emerged as the dominant structure for fabricating organic photovoltaic (OPV) devices. The donor and acceptor materials are mixed and sandwiched between the two electrodes, as shown in Figure 2.10. The photoactive layer exhibits apparent phase separation, resulting in ambipolar networks and a significant D/A interface region when the donors and acceptors are mixed. The excitons produced may readily diffuse to the D/A interface and dissociate into free charges, which the electrodes can efficiently collect as compared to the bilayer OSCs [11, 115]. Heeger *et al.* fabricated a BHJ OSC by using MEH-PPV as a donor and C60 as an acceptor. The photoinduced electron transfer from the donor (MEH-PPV) to the acceptor (C60) as well as the ambipolar network of internal donor-acceptor heterojunctions were shown to be responsible for efficient charge dissociation and collection with a reported efficiency of 2.9%, which is more than two orders of magnitude better than the PCEs obtained with devices built

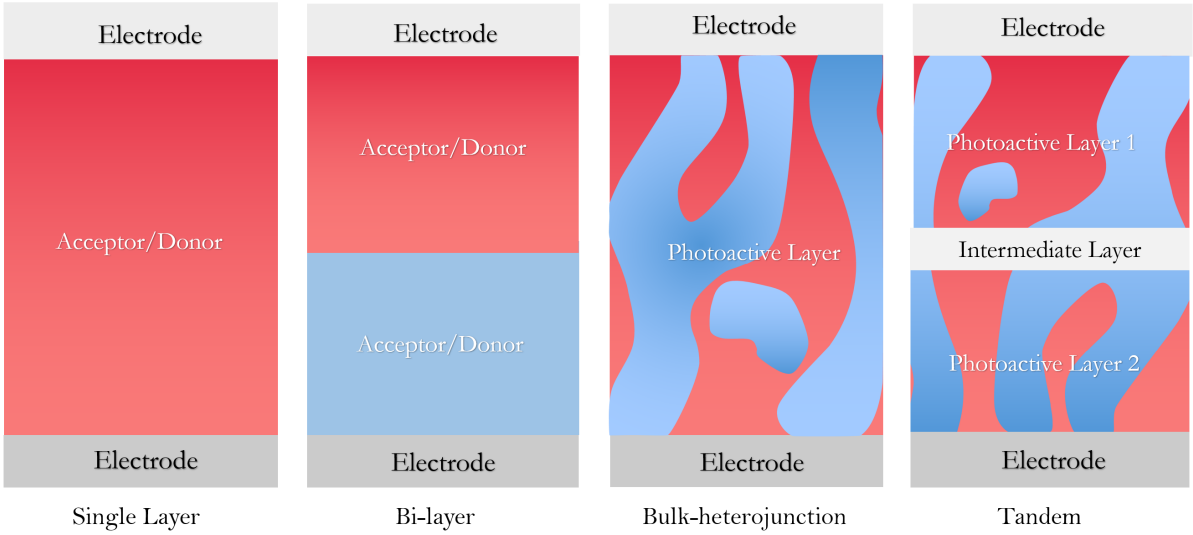

Figure 2.10: Schematic representation of different OSC architectures. Single-layer architecture with either Donor or Acceptor as active layer. Bi-layer with defined donor and acceptor layers. Bulk-heterojunction with an interface resulting from acceptor-donor blend. Tandem architecture with two active layers stacked using an intermediate layer.

with pure MEH-PPV [11]. The BHJ structure is then used to fabricate nearly all of the efficient single-junction OSCs. The precise internal structure of a BHJ is still a challenging task from an experimental perspective. Therefore, kinetic Monte Carlo (kMC) techniques were developed so that one may regulate the D/A blend in an OSC model (see section 3.3.1.2). The kMC method is an excellent tool for modeling the processes that are responsible for the operation of OSCs because it can account for both spatial and time-dependent variations in the charge separation process. Recent research has been focused on a new active layer morphology with a very low percentage of the donor material and has demonstrated good short circuit currents [116–119]. In such devices, a small wt% of the donor is distributed throughout the fullerene matrix. The donor creates isolated domains, obviating the need for successive percolation routes towards the contact electrodes for holes. This raises the question of whether the prevalent BHJ morphology, with percolation pathways within distinct phases, is required for the cell operation and, more specifically, demonstrates that the processes controlling photocurrent generation in OSCs remain poorly understood and further insight is required. The impact of blend morphology in low donor content bulk-heterojunction OSCs is discussed in Chapter 5.

Due to the restricted absorption spectrum of single-junction OSCs, only a fraction of incident light may be collected. Insufficient photon absorption may be addressed using tandem or multi-junction OSCs, which consist of two or more active layers stacked together with complementary absorption spectra (see Fig 2.10). Additionally, thermal

losses in OSCs may be reduced by absorbing higher energy photons in a broad bandgap cell, and lower energy photons in a narrower bandgap cell using a tandem or multi-junction approach [120, 121]. Hiramoto *et al.* reported the first tandem OSC in 1990, comprised of two identical sub-cells [122] with the V_{oc}, twice the magnitude of the single-junction solar cell. Forrest *et al.* demonstrated a multi-junction OPV device for the first time with a PCE of 2.5% and 2.3% for two-junction and three-junction OSC architecture, respectively [123, 124]. Since then, the performance of OSCs has considerably increased, reaching over 18% and more for both single-junction and tandem devices in recent years [125, 126]. Considerable effort has been put into developing novel absorbing materials and optimising device designs, including electron and hole transport layers.

2.5.2 Working mechanism of OSC

The geometric representation of the working principle of OSC and its energetic landscape is represented in Figure 2.11. The OSCs are bipolar devices that consist of two electrodes sandwiched together with active organic materials in between them(see Fig. 2.11a). The work functions of the two electrodes are different. The difference in work functions results in developing an electric field directed from a low work function (cathode) electrode to a high work function (anode) electrode. The transparent conducting oxide (TCO) such as fluorine-doped tin oxide (FTO) and indium tin oxide (ITO) are the best options for this purpose. ITO is the most commonly used TCO for organic semiconductors. For incident light to reach the light-absorbing organic semiconductors, top electrodes must be optically transparent. ITO has excellent optical transparency and excellent electrical conductivity. Using ITO substrates, it is possible to create OSCs in both the standard and inverted configurations. ITO is used as a hole-collecting electrode (anode) in the standard configuration, and an electron-collecting electrode (cathode) in inverted configuration.

A surface modifier or buffer layer is applied to the ITO-coated substrates in standard cell architecture to smooth the ITO interface for charge selectivity and enhance the overall effective work function of the anode. This buffer layer should have strong hole-transport characteristics and a work function that is higher than that of the ITO layer. Several materials, including poly(ethylene-dioxythiophene):polystyrene sulfonate (PEDOT:PSS), molybdenum trioxide (MoO_3), vanadium oxide (V_2O_5), and nickel oxide (NiO), have been used as a buffer layer [127–133]. PEDOT:PSS is a PEDOT polymer doped with PSS exhibiting excellent conductivity and work function characteristics.

Next, the active layer consisting of organic material is the part, which uses incident sunlight to generate charge carriers using photovoltaic effect. When it comes to deposition techniques of the active layer, the donor and acceptor materials can be evaporated together to produce an intermixed layer. However, the most typical approach is to dis-

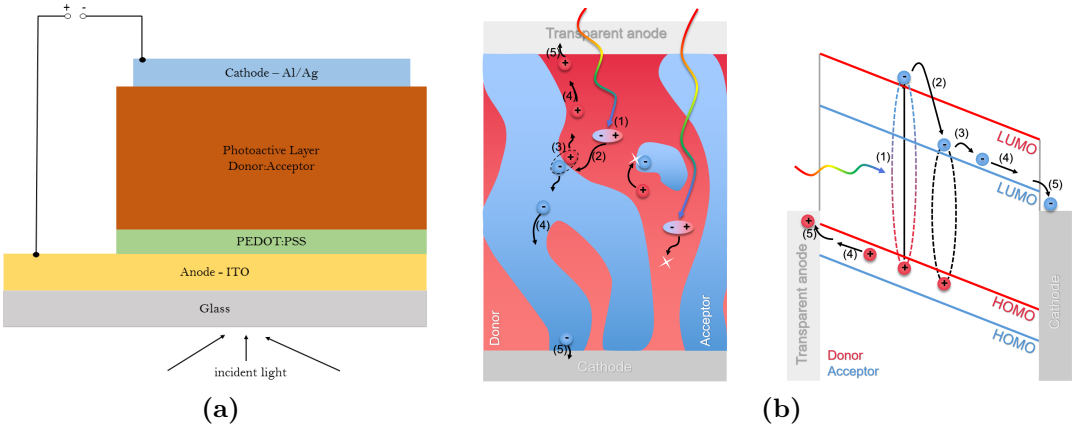

Figure 2.11: (a) Geometric representation of OSC and (b) energetic configuration with basic steps: 1) light absorption and exciton generation, 2) exciton diffusion, 3) exciton dissociation at acceptor-donor interface, 4) charge transfer towards respective electrodes, and 5) charge collection and extraction. Adapted from [13].

solve them together in one solution and then deposit them as a single layer from the liquid phase using deposition processes including spin-coating, inkjet printing, and slot-die coating, among others.

Finally, The active layer is coated with an electron-collecting top electrode (cathode) using an e-beam or thermal evaporation in a vacuum. Cathode materials are typically low work-function metals such as Ca, Mg, Al, and Ag, or their alloys. OSCs can include electron buffer layers such as LiF and $CsCO_3$ before the cathode [134]. Luminescent light absorption in the active layer produces electron-hole pairs, and the built-in electric field results in charge pair separation. These photo-generated charge carriers then move towards the appropriate electrodes where they will be collected and will contribute to electric current [135].

The operating mechanism of an OSC is shown in Figure 2.11(b) by using an energy level diagram. A representation of the transparent anode and cathode, and the electron acceptor (blue) and the donor (red) are shown. The charge pair separation is energetically favorable at the donor-acceptor interface and followed by charge transfer of the hole in the HOMO of the donor molecules or electron in the LUMO of the acceptor, respectively. Compared to the donor material, the acceptor is often engineered to have a lower HOMO and LUMO energetic level than the donor as shown in Figure 2.11(b). To provide sufficient hole extraction, the cathode work function(Φ_C) is selected to be lower than the acceptor LUMO energy level; for the anode, higher work function (Φ_A) than the donor HOMO is needed to ensure efficient electron collection and extraction. At zero bias, $\Delta\Phi = \Phi_C - \Phi_A$ creates an internal built-in field, which provides a driving force for electrons and holes to move towards respective electrodes.

2.5.3 Fundamental Processes in OSCs

The fundamental processes in the OSC, from light absorption to current generation, may be split into the following processes.

- Absorption of incident light and exciton generation
- Exciton diffusion
- Exciton dissociation
- Charge transport
- Charge extraction

These procedures are explained briefly as follows.

Absorption of incident light and exciton generation

To achieve high efficiency, the active layer of a solar cell must collect a significant proportion of the incoming solar light energy. The high absorption coefficient (about $1 \times 10^5\,\mathrm{cm}^{-1}$ of conjugated polymers allows them to absorb light very effectively [107]. Therefore, an active layer thickness of around 100 nm is sufficient to absorb the incident sunlight.

When photons with energy beyond the absorption edge are incident on a semiconducting polymer, a singlet exciton state is formed, with an electron and hole having an opposing spin and bound by Coulomb force. Unlike inorganic semiconductors, organic semiconductors have minimal coupling between adjacent molecules, which causes molecular excitations to be localized. As a result, there is no band to band transition in molecular solids. Further details on exciton generation are discussed in Section 3.3.2.5.

Exciton diffusion

Excitons have a very high binding energy and are relatively confined due to the low dielectric constant of organic semiconductors. Exciton is an electrically neutral entity that diffuses via a random thermal motion. Efficient OSCs use a D/A blend with a phase-separation to create a BHJ structure to overcome the exciton-binding energy and effectively generate free charge carriers [11]. The D/A interface provides an energetic driving force for exciton dissociation. After dissociation, electron remains in acceptor material and hole into the donor. However, charges are not free yet as the electron-hole pair is bound by Coulomb force. This state is often called as a charge-transfer (CT) state. The photo-generated excitons must reach D/A interface to produce free charge carriers by overcoming mutual interaction before returning to the ground state. Nevertheless, the

distance that an exciton may travel before recombining is limited by the diffusion length and give by:

$$L_D = \sqrt{ZD\tau_{\text{exc}}}\ , \tag{2.8}$$

with D being the diffusion constant, τ_{exc} is the exciton lifetime and Z refers to the dimensionality of exciton diffusion (1, 2, and 3 for 1-dimensional, 2-dimensional or 3-dimensional respectively) [136]. To dissociate excitons into free charge pairs, a charge distribution on a length scale equivalent to the exciton diffusion length is required, limiting the maximal domain size of the BHJ structure. For the bulk of amorphous materials, the diffusion length scale of singlet exciton is usually 5 nm to 10 nm and an exciton lifetime of 1 ns [136].

Exciton dissociation

As mentioned above, excitons in organic semiconductors have relatively short diffusion lengths.As a result, it is more likely to decay to ground state, if the exciton is produced far away from the D/A interface. When excitons reach the D/A interface, the possibility of exciton dissociation increases. The exciton can dissociate due to the difference in LUMO energies between the electron donor and the electron acceptor. Onsager [137], and Braun [138] described the amount of energy needed to overcome the Coulomb potential. In 2010, Marsh *et al.* [139] used transient absorption (TA) spectroscopy to get a direct measurement of electric field-assisted charge separation in polymer:fullerene solar cells. Similar results for field-dependent carrier dissociation were also reported by Veldman *et al.* [140] in 2008. Alternatively, charge-separated states create unbound charge carriers immediately. Evidence for field-independent ultrafast charge separation has been found by Howard *et al.* [141], Jamieson *et al.* [142], and Guo *et al.* [143] in field-dependent TA spectroscopy experiments.

Recent research on non-fullerene-based systems (NFAs) has shown that rapid and efficient charge separation is possible even with zero Ionization Energy (IE) and Electron Affinity (EA) offsets, in contrast to fullerene-based systems [144–146]. Furthermore, the minimal driving forces are often attributed to as the reduced energy losses seen in high-performance NFA systems [144, 147]. This debate regarding the charge separation in fullerene and non-fullerene systems as due to energy offset still needs further coherent study.

Charge transport

After the dissociation of the electron-hole pair (geminate pair), free charge carriers need to be collected at the respective electrode contact. Electrons must move towards the

cathode while holes towards the anode. The two primary transport mechanisms are drift and diffusion. The drift is mainly driven by choice of electrodes in the device. Since the difference of electrode work function causes the built-in potential (V_{bi}), which influences the V_{oc} of the solar cell. The charge carriers go towards their respective electrodes when the internal field is high in the solar cell. On the other hand, as the excitons dissociate at the donor-acceptor interface, the region immediately around it becomes highly charge concentrated. Electrons and holes tend to migrate away from the heterojunction as a result of this concentration gradient. This motion of charge carriers is called diffusion. When a bias and internal electric field are equal, diffusion is the dominant mechanism.

The charge transport in disorder semiconductor materials occurs via hopping between various localized states on separate molecules. Charges must be able to hop across molecules without being dispersed or trapped for efficient charge transfer. Numerous factors affect the charge transport, including molecular arrangement, defects, disorder, electric field, charge carrier density, and temperature [148]. The charge carrier mobilities are comparatively lower than the inorganic counterparts in the range $1 \times 10^{-2}\,\mathrm{m^{-2}\,V^{-1}\,s^{-1}}$ to $1 \times 10^{-6}\,\mathrm{m^{-2}\,V^{-1}\,s^{-1}}$ [149]. The balance between the hole and electron mobilities in OSCs is critical because imbalanced mobilities may result in the occurrence of the space charge limited current [150]. More specifically, when one kind of charge carrier has much more mobility than the other, the charge carriers will be able to reach their respective electrodes more effectively. However, since the opposite charge carriers are collected at a slower rate than the faster charge carriers, the faster charge carriers will accumulate, resulting in the formation of the so-called space charge, which will affect the current output from the device. Therefore, not only is it essential to consider the mobilities of the charge carriers in the solar cells, but also their balance with respect to each other.

Charge extraction

Once electron-hole pairs are separated, they move through through their respective phases, collected at the electrodes and consequently extracted in form of output current. The movement of charges across the donor and acceptor phases occurs only if they are able to overcome strong Coulomb binding energies. Charge extraction takes place if an appropriate energy alignment (HOMO, LUMO level and contact workfunction) is selected.

The recombination of the charge carriers, is one of the main loss mechanism for OSCs. Typically, recombination mechanisms are classified as geminate and non-geminate. The geminate recombination occurs when the geminate (electron-hole) pairs that originate from the same photon are recombined prior to their complete separation. While non-geminate recombination refers to the recombination of previously dissociated charge car-

riers irrespective of their origin [151]. This category encompasses a diverse range of recombination processes. Notable examples are direct recombination of two free charges, and trap-assisted recombination, which combines a free mobile charge carriers with an oppositely charged trapped carrier in an energetically deep, localized state. Non-geminate recombination include Auger type (trimolecular), which includes the transfer of energy produced by recombining two charge carriers to another charge carrier, as well as minority carriers surface recombination at the electrodes [54, 152].

2.5.4 Efficiency limits of OSC

The efficiency limits of OSCs are generally calculated using the Shockley-Queisser limit (a detailed-balance method) [55, 57]. To properly address the upper limit PCE of OSC, the thorough balancing method provides a rigorous estimation, considering ideal material properties. However, the ideality of materials is difficult to achieve in practice. Due to the energy level difference in acceptor and donor and the presence of a CT state that mediates recombination, BHJ OSC performance is limited by resultant voltage loss. The highest possible efficiency for BHJ OSC, according to Azzouzi et al., may be above 30% if the loss solely includes radiative recombination (SQ limit), for the non-radiative limit, it is around 25% in ideal case [153]. They predicted a more realistic limit of about 20% if 90% of external quantum efficiency (EQE) and 80% fill factor (FF) were considered. In addition, there are certain empirical techniques to obtain information on various possible improvements in the cell performance [154, 155].

3 The Kinetic Monte Carlo Algorithm

From Analytical methods, it has been observed that the electric charge transport is a complex phenomenon in amorphous organic systems. It has continuously been investigated whether there is a possibility of generating and developing a certain model, which can depict the system's dynamical behaviour. Various computational tools provide a possibility to get an insight into such disordered solids to an extent. Especially kinetic Monte Carlo (kMC) Simulation is one of the method to model such disordered systems to a advantageous extent compared to other numerical tools with a possibility to incorporate dynamic properties and to incorporate 3D morphologies on mesoscopic device scales. kMC uses quantum mechanical features like molecular orbital energy distributions or charge transfer integrals as input and calculates experimentally accessible device parameters like charge carrier mobility or complete solar cell device characteristics. Furthermore, kMC simulations can reveal the significance of local variations in morphology for solar cell efficiency. This allows us to connect the microscopic and macroscopic scales and customize the future evolution of materials and interfaces by bridging various length scales.

The presented thesis is based upon the kinetic Monte Carlo (kMC) tool developed within the group. Section 3.1 provides the advantageous perspective of the algorithm. The mathematical framework of the algorithm with the process flow is presented in section 3.2. The initial system setup, including discretization of the photoactive layer containing information about the structure and materials of organic semiconductors, is summarized in section3.3. Finally, the physical processes and the transition rates are presented in section 3.3. The basis for the kMC model was formed on the implementation of *Tim Albes*, TUM, presented in his dissertation [42].

3.1 Motivation and Advantages

Several modelling techniques are possible depending upon the time scale of the process to be analyzed and the structural dimension of the system. The models mainly focuses on the dynamic evaluation of the system of atoms to depict the behavioral approximation and its improvement. The trade-off arises between the accuracy of the system and the

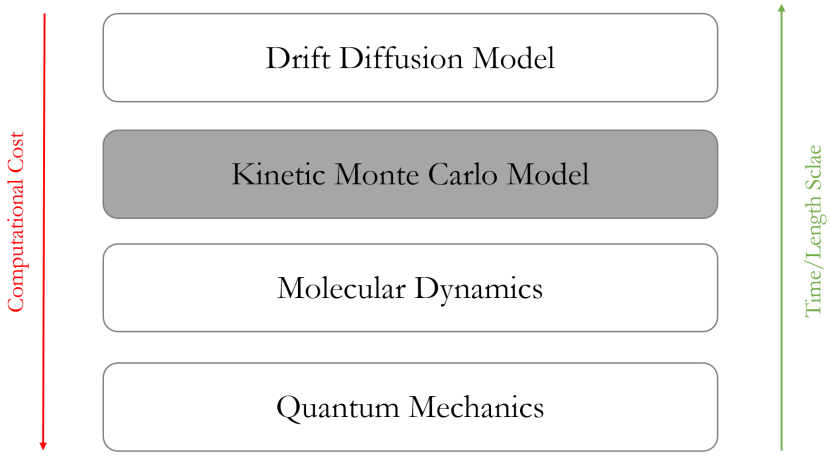

Figure 3.1: Overview of computational methods for different scales in time and dimension.

computational efforts involved. Typically, computational approaches are limited to a specific level of granularity and either concentrate on atomic qualities or directly evaluate device characteristics. This is owing to the high computational cost, which increases with atomic scale resolution. Figure 3.1 visualizes different simulation models and the associated trade-off with respect to time scale and computational cost.

Although the entire quantum mechanical method is extremely precise, it is not extremely practical for larger systems. Molecular Dynamics is a simulation approach that is used to analyze the physical motions of atoms and molecules in microscopic systems such as protein motion, exfoliation of few layers of graphene and carbon nanoscrolls [156]. MD simulation uses numerical methods to calculate the movement and vibration in molecular systems containing a vast number of particles on the scales of order 10^{-15} s. This results in the main limitation of the MD method as the accumulated time scale is too small (less than 1 microsecond) to observe the steady-state behavior of the system we wish to study, i.e. solar cell, which often requires much longer time scales [157].

Another macroscopic technique to model the system behavior is drift-diffusion (DD) equation model. This technique tends to resolve the DD equations to compute the new distribution of charge carriers and potential from an initially supposed charge carrier densities, electrostatic potential and current density till the convergence point is reached. larger time scale and large structure modelling are possible with the DD model as it is based on continuous quantities as spatial charge carrier density. The major limitation of this method comes from the fact that the accurate 3D morphology of the system under analysis, i.e. solar cell at the nanoscale, is difficult to incorporate in terms of charge carrier transport and recombination [158]. For spatially disordered BHJ systems, the DD equations become highly nonlinear, leading to a non-converging solution. Therefore, DD

models are restricted to an effective medium approach with lower dimensionality models with effective physical parameters.

In contrast, kinetic Monte Carlo is a widely used technique to explain a wide range of processes, including transport (diffusion), material structures and characteristics (e.g., crystal formation), and catalysis (non-equilibrium and equilibrium chemistry). KMC may be seen as a type of coarse-graining when it comes to atomistic simulations. This makes it particularly well suited to hierarchical multiscale modelling techniques, which combine data at several degrees of accuracy or detail to generate a more detailed description. In this context, KMC is a useful tool for bridging the macroscopic and microscopic approaches. The temporal evolution of a system is simulated using known transition rates between distinct states. The time scale problem of the MD approach is overcome by exploiting the fact that the system's long-term dynamics are made up of diffusive leaps from one state to another. This results in acquiring longer time scales because KMC characterizes the system with more underlying macroscopic states where even fast vibrational effects can occur. The dynamic evolution of the system can be seen by transitions between events (long time events). Such a system is called as an infrequent-event system [157]. Hence, sufficient processing time can be saved by neglecting underlying fast motion effects and considering event transitions. Thus overall simulation time is improved. On the other hand, to overcome the limitation of the DD approach, the KMC algorithm uses localized states where the hopping process of particles (excitons, electrons and holes in the case of a solar cell) can take place. To implement the nanoscale morphology, a discretized grid of localized states is implemented on the photoactive layer, where hopping can occur. This gives a better morphology as well as a dynamic process of individual particles at the nanoscale. This, in turn, is a great advantage over the DD continuum approach.

3.2 Kinetic Monte Carlo (kMC) Algorithm

The main objective of the Kinetic Monte Carlo approach is to characterize the dynamics of the system by specific long time states. Under dynamic evolution, the system tends to keep changing its state by different system-specific transitions and in turn hopping of particles from one state to another. It is necessary to identify all the important processes to depict the system behavior accurately. If small time scales are neglected and only long time states are considered, a trade-off between accuracy and high simulation times can be accomplished as described in section 3.1.

Assume that a certain system is in its initial state i. The transition from this initial state can be possible to one of the available states j. This transition from initial state

to the available final state happens at a certain rate i.e. $\{a_{i\to j}\}= \{a_{ij1}, ..., a_{ij\kappa}\}$ .These rate constants show the probability of transition from one state to another. It only depends upon the current state of the system, not the preceding one. This concept is evolved from Markov Chain theory and enables to determine the dynamic behavior of the system [159]. From statistical Physics [160, 161], the stochastic processes for the state to state transitions with certain rate constants is defined by the master equation:

$$\frac{dP_i(t)}{dt} = \sum_{j\neq\ i} a_{j\to i} P_j(t) - \sum_{j\neq\ i} a_{i\to j} P_i(t). \tag{3.1}$$

The change of probability $P_i(t)$ to find the system in state i at any instant t depends upon the probabilities of jumping out from the state i to final state j with rate constants a_{ij} and on the probability of jumping into state i from any other state j with rate constants a_{ji} $P_i(t)$. Analytical and numerical solution of the above equation is often complex and not feasible. This algorithm must determine which state the system should jump to next at each step along a state-to-state trajectory, and when this next leap should take place. KMC presents a numerical technique based on a stochastic framework for obtaining system dynamics based on state-to-state time-dependent transitions. This is accomplished by first selecting fundamental processes based on their rate constants and then updating the time. By selecting a transition path through a chain of subsequent states, dynamic system behavior is obtained. Taking an average over a large number of Markov chains results in system behavior that is identical to the master equation.

3.2.1 Probability density function

The early work of Gillespie [162] and Bortz et al. [163] is the foundation for modern kMC algorithms. The theoretical foundation of the kMC algorithm in the following sections is adapted from the work of Gillespie [162]. The Gillespie method is based on the capacity to characterize system events using a series of transitions R_κ with the total number of possible transitions κ=1,2,...,M. Depending on whatever events are enabled at a particular stage in the system's evolution, all transitions must explain unique processes. For each reaction R_κ, a transition probability reaction rate a_κ is introduced. The probability of R_κ to occur within the next time interval is defined by $a_\kappa \delta t$.

Instead of solving the master equation, the kMC approach relies on a function known as the Probability Density Function (PDF). Using random integers, the joint PDF function may be used to select a transition and its accompanying time step. This PDF is defined by $P(\tau, \kappa)d\tau$, which gives the probability at time t for the next transition to take place in the time intervals $(t + \tau, t + \tau + d\tau)$ and the reaction being R_κ. each transition is characterized by continuous-time variable $\tau(0 \leq \tau < \infty)$ and the integer variable

$\kappa(\kappa = 1, 2, ...M)$. Mathematically, the joint PDF can be constructed as the product of two independent probabilities as:

$$P(\tau, \kappa)\, d\tau = P_0(\tau) \cdot a_\kappa d\tau\,, \tag{3.2}$$

where $P_0(\tau)$ is the independent probability to have no transition in $(t, t+\tau)$ and $a_\kappa d\tau$ is the probability for a transition of type R_κ to occur in $(t+\tau, t+\tau+d\tau)$. In order to calculate the probability that none of the reaction of type R_κ occurs in the time interval $(t, t+\tau)$is further divided into L parts ($\epsilon = \frac{\tau}{L}$). The probability of no event κ in ϵ is $(1 - a_\kappa\epsilon)$. The combined probability can then be represented as:

$$\prod_{\kappa=1}^{M}(1 - a_\kappa\epsilon) = 1 - \sum_{\kappa=1}^{M} a_\kappa\epsilon + o(\epsilon)\,, \tag{3.3}$$

where $o(\epsilon)$ is the error term. As stated above, no reaction must occur in L sub-intervals. $P_0(\tau)$ is the probability of no transition in each of the sub-intervals combined, calculated as:

$$P_0(\tau) = \left(1 - \sum_{\kappa=1}^{M} a_\kappa\epsilon + o(\epsilon)\right)^L = \left(1 - \sum_{\kappa=1}^{M} a_\kappa\frac{\tau}{L} + o(\frac{\tau}{L})\right)^L . \tag{3.4}$$

For $L \to \infty$, $o(L^{-1})$ tends to be zero and

$$P_0(\tau) = \lim_{L\to\infty}\left(1 - \left[\frac{1}{L}\sum_{\kappa=1}^{M} a_\kappa\tau\right]\right)^L . \tag{3.5}$$

If we compare above equation with limit representation of an exponential term

$$\exp(x) = \lim_{n\to\infty}\left(1 + \frac{x}{n}\right)^n$$

, we can rewrite equation 3.5 as

$$P_0(\tau) = \exp\left(-\sum_{\kappa=1}^{M} a_\kappa\tau\right) . \tag{3.6}$$

Now, finally, the joint PDF expression can be given as

$$P(\tau, \kappa) = a_\kappa \cdot \exp\left(-\sum_{\mu=1}^{M} a_\mu\tau\right) . \tag{3.7}$$

For the dynamic evolution of the system, this function is the starting point for selecting a random number pair (τ, κ) that describes the next transition and time step.

3.2.2 Choosing time and transition for Monte Carlo Procedure

The main secret of KMC, as explained above, is to create stochastic trajectories in such a way that their proper averaging provides the temporal evolution of the probability $P_i(t)$ in the master equation 3.1. In the same context, our implementation of the Monte Carlo method is based on *Direct Method* as presented by Gillespie [162]. In this technique, the PDF is split into two PDFs with one variable each represented as:

$$P(\tau, \kappa) = P_1(\tau) \cdot P_2(\kappa|\tau)\,. \tag{3.8}$$

The probability density of any of the next possible transitions occurring in the interval $(t+\tau, t+\tau+d\tau)$ is represented by first part $P_1(\tau)d\tau$. Hence, $P_1(\tau)$ is the summation of the overall transition κ. Now, Equation 3.6 can be rewritten as:

$$P_1(\tau) = \sum_{\kappa=1}^{M} a_\kappa \exp\left(-\sum_{\kappa=1}^{M} a_\kappa \tau\right) = a_{\mathrm{T}} \exp(-a_{\mathrm{T}}\tau)\,, \tag{3.9}$$

where $a_T = \sum_{\kappa=1}^{M} a_\kappa$ with $0 \leq \tau < \infty$. The PDF $P_2(\kappa|\tau)$ represents the probability of reaction R_κ to occur next. Substituting the equation 3.9 in equation 3.8, $P_2(\kappa|\tau)$ can be represented as:

$$P_2(\kappa|\tau) = \frac{P(\tau,\kappa)}{P_1(\tau)} = \frac{a_\kappa}{a_{\mathrm{T}}}\,. \tag{3.10}$$

The direct method's premise is to use two random integers, ρ_1 and ρ_2, to compute the time step τ according to $P_1(\tau)$ and the reaction index κ according to $P_2(\kappa|\tau)$. The random numbers can be generated using the inversion method. For the Monte Carlo step, the generated random numbers must be distributed according to the PDFs (3.9) and (3.10). As they are unique functions, generating them from simpler distributions, such as a uniform distribution in the unit interval (0,1), necessitates the use of a method. Consider the probability distribution function

$$D(z) = \int_{-\infty}^{z} P(z').dz'\,. \tag{3.11}$$

The inversion method utilizes the uniformly generated random numbers to obtain z, which satisfies $D(z) = \rho$, such that,

$$z = D^{-1}(\rho)\,. \tag{3.12}$$

This ensures that the calculated values of z are distributed according to the distribution function from which D is derived. Using the inversion method and equation 3.9, the corresponding distribution function takes the form:

$$D(\tau) = \int_0^{\tau} a_{\mathrm{T}} \cdot \exp(-a_{\mathrm{T}}\tau')d\tau' = 1 - \exp(-a_{\mathrm{T}}\tau)\,. \tag{3.13}$$

Now, the continuous variable τ, the time span needed for one transition from ρ_1 can be given by the inverse function D_1

$$\tau = D_1^{-1}(\rho_1) = \frac{1}{a_{\mathrm{T}}} \ln\left(\frac{1}{\rho_1}\right) \qquad \rho_1 \in (0,1)\,. \tag{3.14}$$

On the other hand, as $P_2(\kappa|\tau)$ is the discrete probability density function, the probability can then be represented by:

$$D(i) = \sum_{v=-\infty}^{i} P(v)\,. \tag{3.15}$$

To choose a reaction R_i from set of events,

$$\sum_{v=1}^{i-1} P(v) < \rho_2 \leq \sum_{v=1}^{i} P(v)\,. \tag{3.16}$$

Introducing equation 3.10 in the above equation, we can get the form

$$\sum_{v=1}^{i-1} a(v) < \rho_2 a_{\mathrm{T}} \leq \sum_{v=1}^{i} a(v) \qquad \rho_2 \in (0,1)\,. \tag{3.17}$$

All transition probabilities are added up to an index for which the sum is higher than ρ_2. This index κ is set to the transition of choice.

3.2.3 Algorithm Implementation

A KMC trajectory comprises of series of discrete hops from one system state to another. The next probable state after which amount of time the next hop occurs is to be determined by calculating the probabilities shown in the master equation 3.1. KMC algorithm is fairly straightforward and can be described by following step by step procedure. Figure 3.2 also visualizes the important steps of the KMC loop in the shape of a flow chart.

Step 1: Initial Set up

Right at the start, the simulation setup requires all the system-specific parameters to calculate the transition rates. The initial time $t = 0$. The most important variable to

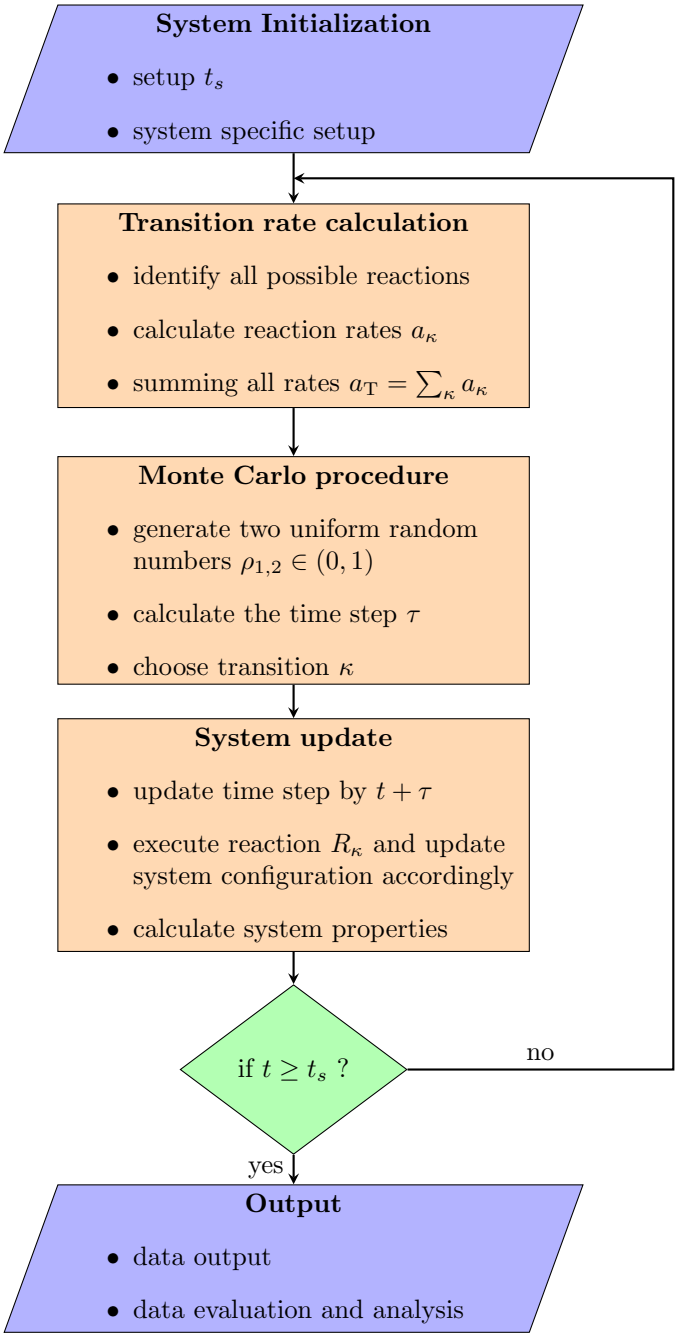

Figure 3.2: Flow chart of a general Kinetic Monte Carlo Algorithm.

consider here is simulation time t_s, which determines the total simulation time for a single run of dynamic evolution.

Step 2: Transition rate calculation

Generate the list of all the rates of possible transitions $R_{i\to j}$ in the system. KMC model is dependent upon the physical models for all the processes occurring in the system. As already discussed in section 3.2, the transitions only from the current state are activated,

the processes that can not occur during the current state are carefully deactivated. After all the rates are calculated, they sum up to give a total rate a_{T} as:

$$a_{\mathrm{T}} = \sum_{\kappa=1}^{M} a_{\kappa} \,. \tag{3.18}$$

Step 3: Monte Carlo Process

As discussed in Section 3.2, Monte Carlo process utilizes random numbers $\rho 1, 2$. A random number (ρ_1) is generated according to probability density function $P(\tau, \kappa)$. This calculates the accurate time step τ passed before the transition occurs. Here,

$$\tau = -\frac{1}{a_{\mathrm{T}}} \ln\left(\frac{1}{\rho_1}\right) \qquad\qquad \rho_1 \in (0,1)\,. \tag{3.19}$$

The random number ρ_2 identifies the transition κ which satisfies

$$\sum_{v=1}^{i-1} a(v) < \rho_2 a_{\mathrm{T}} \leq \sum_{v=1}^{i} a(v) \qquad\qquad \rho_2 \in (0,1)\,. \tag{3.20}$$

Step 4: System Updation

To update the system, the time t is incremented by τ and transition κ. Every update is dependent on a particular physical process. Once the system is updated, the simulation time t is compared with stopping time t_s. If $t < t_s$, the simulation will continue to step 2 and rates are recalculated. This continuous loop from steps 2-4 is called as *Monte Carlo Loop*. The simulation will stop once the termination condition is fulfilled.

Step 5: Data Output

Once the successive time advance t becomes greater than t_s. the MC loop is terminated, and variables tracking selected events can be evaluated.

The kMC technique is a straightforward algorithm that may be applied to a wide range of systems. An accurate physical rate description is essential for obtaining accurate system evolution dynamics.

3.3 Kinetic Monte Carlo Model of Organic Solar Cell

Organic solar cell modelling can be a useful tool for simulating various fabrication conditions and parameters, simplifying the manufacturing process and lowering material and fabrication costs. Partial differential equations and closed-form mathematical equations are extremely difficult to solve when simulating the complicated 3D shape of organic solar cells. As a result, the stochastic approach of Monte Carlo (MC) simulation is used to identify distinct characteristics of physical and chemical processes through repeated

random sampling. To create a simulation tool capable of reproducing the features of OSC devices under illumination, the physical mechanisms regulating the functioning of OSCs are combined with the kMC framework. KMC is well suited for modelling 3D donor-acceptor blend morphology because it can mimic the temporal development of processes. The earliest work describing the basic properties of the Monte Carlo method for Vacancy migration in binary ordered alloys was reported by Young *et al.* [164]. It was not until the late 1980s that the kMC technique was used to describe charge transport in disordered systems [165]. A pioneering study by Bässler revealed that the kMC technique is a useful tool for simulating charge carrier dynamics in disordered organic materials with a Gaussian DOS [20]. From that point on, kMC has been employed for many theoretical studies investigating charge carrier transport in disordered organic semiconductors [22, 33, 36, 166, 167].

The notion of acceptor and donor materials in the photoactive layer gave rise to the KMC model of bilayer systems [28,32,168]. Further study on the KMC model to recreate the intermixed structure of the donor-acceptor blend were reported after the introduction of the BHJ [11] to overcome the significant exciton decay in bilayer structures [169]. Watkins *et al.* did some MC simulation work on the morphology of organic solar cells [30]. They investigated the influence of morphology on internal quantum efficiency using Dynamic MC modelling of 3D organic solar cells. Meng *et al.* took into consideration all processes related to exciton and charge carrier transitions, including injection from electrodes, in order to integrate all prior models into one comprehensive model [29]. They were able to make predictions regarding the device's optimization in comparison to experimentally fabricated devices.

Further theoretical studies using KMC to organic photovoltaics have been carried out including the effect of morphology [170], charge carrier recombination [25, 171–174], exciton dynamics [24, 175], charge dissociation [15, 99, 176–178], charge mobility [31, 33, 179] and the effect of these processes on photocurrent generation [28,32,180].When it comes to whole devices such as BHJs, kMC simulations have been used a frequently in the past as well [14, 26, 28, 30, 31, 36]. kMC models for OSCs and OLEDs generally take into account either singlet [24, 29, 175] or triplet exciton dynamics [181, 182]. Singlet-triplet interactions can be used to control exciton lifetimes and diffusion periods in organic electronics and in turn the efficiency of the organic solar cells [183, 184]. More details about the kinetic Monte Carlo method and its applications to disorder systems can also be found elsewhere [22, 185, 186].

This work outlines a complete kMC model that takes advantage of the most modern techniques to simulate state-of-the-art OSC device composition in both bulk heterojunction and diluted donor configuration. If the material's particular properties, such as

HOMO and LUMO levels, hopping prefactors, and disorder are known, the model may be extended to various material configurations. A primary objective of this work is to fully implement all key dynamic processes during the solar cell operation.

3.3.1 System Setup

In order to set up a complete kMC device simulation, we will require the following components: 1) a simulation box with sites and species. 2) A collection of physical processes, as well as the rates at which they occur. 3) A decision-making algorithm that determines which events are selected. Detailed explanations of these components can be found further down in this section.

3.3.1.1 Simulation box

The simulation model represents the nanoscale structure of the solar cell in the form of the photoactive layer with a discrete set of sites and electrodes. Each node in the photoactive layer may be viewed as either monomers or small molecules. The active layer is commonly represented as a cubic lattice as evident in several existing kMC models [20, 28, 31, 177]. As a lattice constant, a node spacing of $a = 1\,\mathrm{nm}$ is set for most of the work in this thesis. This is comparable to the average hopping distance between two tiny molecules or along a polymer chain. Additionally, it allows analysis of local defects in bulk heterojunction and accounts for the separation of donor and acceptor materials into fine phases at the sub-nm scale.

Figure 3.3 visualizes the grid representation of the typical simulation box as a cubic lattice. The contact electrodes are placed at the bottom and top layers of the box as cathode ($z = 0$) and anode ($z = L_z a$) respectively and represent the real boundaries of the system. The spatial dimensions of the box are denoted by L_x, L_y and L_z. Due to equal spacing of nodes at $a = 1\,\mathrm{nm}$, the magnitude of L's signifies the solar cell dimensions in nm. The periodic boundary conditions are specified in x and y direction, while $L_z \cdot a$ determines the actual thickness of the box. In order to create unique settings for each node, all nodes have physical characteristics, such as kind of material, how much energy it has, whether it has hop prefactors and excitonic decay rates. The entire set of nodes with their current attributes represents the photoactive layer's current system state. The properties are summarized as:

- Every node is located at a fixed position in the assigned grid for the whole simulation time. This position explores the nearby localized states, enabling the identification of possible occurrences of different events and then calculating the respective rates.

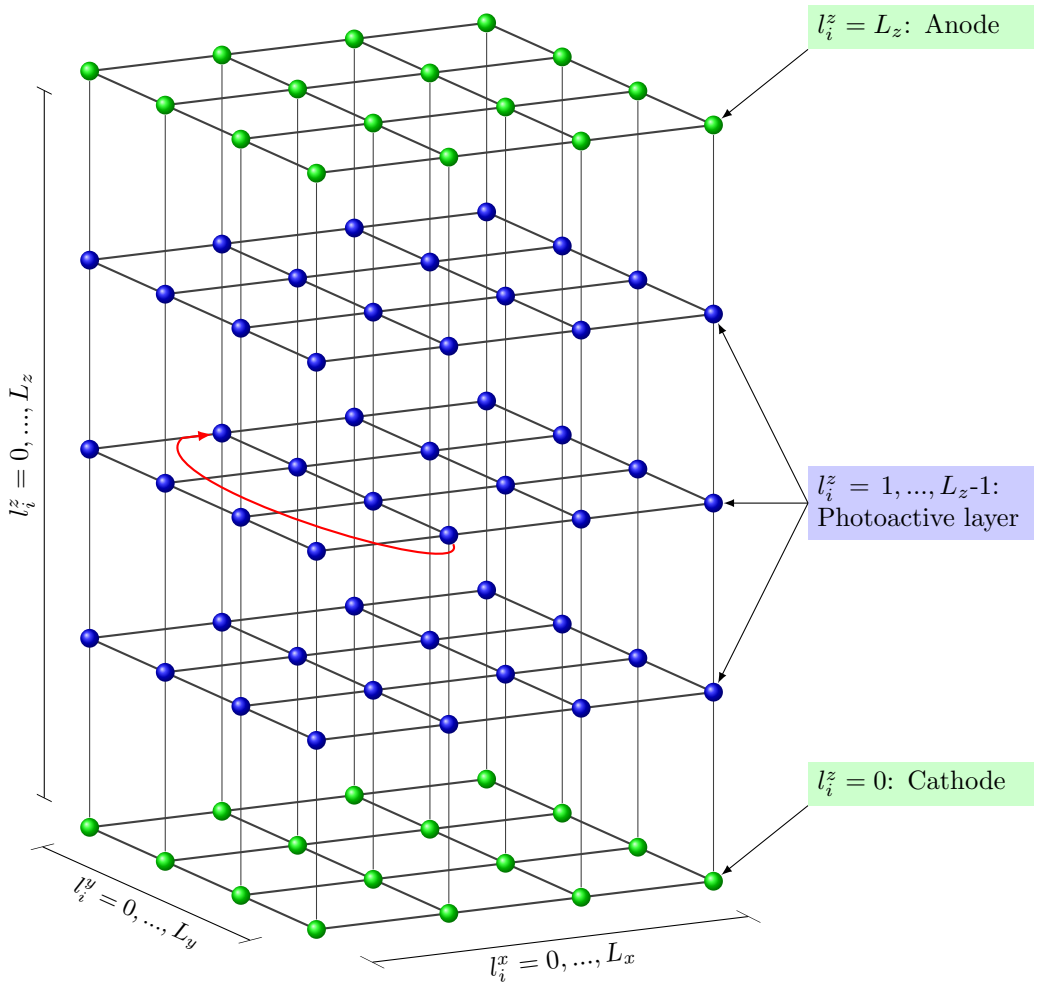

Figure 3.3: Grid representation of the Solar cell. The photoactive layer is represented in blue, anode and cathode in green. Adapted from [42]

The position is stored as:

$$r_i = (l_i^x a, l_i^y a, l_i^z a)\,, \tag{3.21}$$

with the integer values as mentioned in Figure 3.3.

- The nodes may be occupied by electrons, holes, singlet or triplet excitons. The processes that may occur in an operational device are dependent on the species that are being considered. The position is stored in the node occupation variable. It is pertinent to mention that a single node can not be populated by more than a single particle at a time because: When the node is occupied, the hopping rates are set to zero to prevent one from hopping into the occupied space. Charge recombination may occur only when an electron and a hole are adjacent. Exciton generation is also not allowed in an already occupied node.

- Each node in the photoactive layer either represents Donor or acceptor material. All material properties, including the HOMO and LUMO energy levels, localization radius, reorganization energies are stored within the node. Each node contains information allocated to it about whether or not an interface to another material is present, and the direction in which the interface is located. The location of exciton separation and charge recombination is critical for interface design.

- Finally, the event counters must be specified to track all node properties and event occurrences between neighboring nodes.

3.3.1.2 Morphology generation

OSCs have a complex morphology that must be controlled in order to achieve effective exciton dissociation at the donor-acceptor interface and charge transfer to the electrodes [29,187–189]. The active layer morphology must be implemented once the simulation box has been set up and the nodes have been assigned.

Bulk-heterojunction Morphology

In every BHJ morphology, the donor and acceptor molecules are interconnected phases with existing percolation routes [169]. A model based on the Kawasaki spin-exchange algorithm [30, 42, 190] is utilized to control the intermixing in the simulation. The method provides an efficient reproduction of the BHJ morphology. All nodes inside the photoactive layer are assigned a spin-up or spin-down at random with equal probability. The polarity of the material is represented by this flag. one may select their ratio of spin-up materials to spin-down materials in order to alter the donor-acceptor ratio.

Figure 3.4 visualizes the spin-exchange algorithm for Bulk-heterojunction morphology generation. Let us assume that the algorithm begins in the homogenized phase in which neighboring spins of the opposite polarity surround each node to the one in which it is starting. The method selects a random node i and one of its neighbors j from a pool of possible nodes. Node i is located in the middle of the dashed line diagram. During spin-up configuration, all neighbors j of node i have spin-up configuration [see Fig. 3.4 (left)], while site i is now in spin-down configuration. The magnetic interaction energy is estimated according to the Ising model [191]:

$$\epsilon_i = -J \sum_j (s_i s_j - 1) \ . \tag{3.22}$$

The interaction energy is J, and the summation index j spans all first and second neighbors. The spins may be either +1 (up) or -1 (down). The program now swaps site

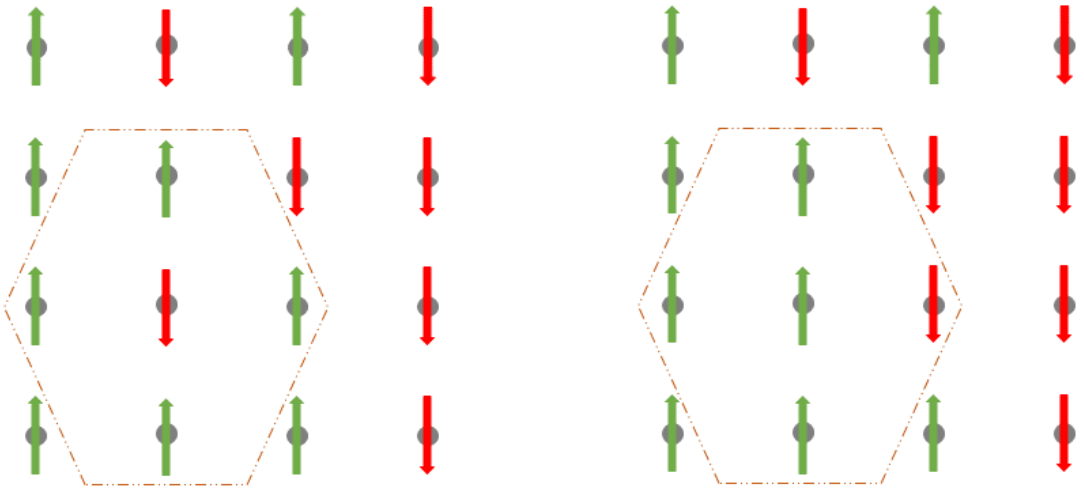

Figure 3.4: Visualization of spin-exchange algorithm for bulk-heterojunction morphology.

i's spin with that of a random neighbor j. The process comes to a halt and selects a new random site if the spins of sites i and j are equal. Otherwise, the spins are swapped [see Fig. 3.4 (right)], and the energy of the new configuration is recalculated. The overall change in energy of the system as a consequence of swapping them is then calculated and utilized to estimate the probability of swapping event

$$P(\Delta\epsilon) = \frac{\exp(-\Delta\epsilon/k_BT)}{1+\exp(-\Delta\epsilon/k_BT)}\,, \tag{3.23}$$

where total energy change $\Delta\epsilon = \epsilon_{i'} - \epsilon_i$ is the difference between initial (ϵ_i) and final ($\epsilon_{i'}$) swapped configurations. During a spin exchange, the total number of spins heading upwards or downwards remain same. The number of acceptor and donor nodes also does not change, they are just reallocated.

A random number generator is utilized to decide whether the sites are swapped or not once the likelihood of the swapping occurrence has been calculated. To keep the phase separation going, a suitable pair of sites is selected at random, and the procedure is repeated. Each iteration is tallied, and the evolution of the system is assessed by counting the number of Monte Carlo (MC) steps that have happened, whether the sites are swapped or not. The total number of iterations divided by the total number of sites in the lattice yields the number of MC steps $'N'$ [175]. This enables the development of the phase separation process to be described by a parameter that is independent of the lattice size.Figure 3.5 shows the 3D bulk-heterojunction morphology using 2000 MC steps.

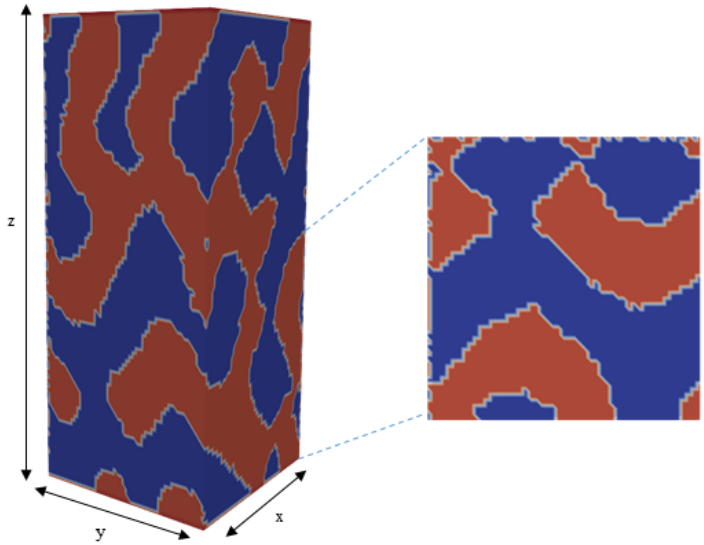

Figure 3.5: 3D bulk-heterojunction morphology and cross section along z-axis

Polymer Chains

In addition to bulk-heterojunction morphology generation, polymer chains can also be generated, in which the donor and acceptor areas are linked bulk regions. Pivot algorithm [192] is a simple way to generate polymer chains. This method has also been used to create polymers within dilute donor configuration of OSCs within a cubic lattice [38, 42, 116]. To generate polymer chains on regular lattices, the Pivot method uses the Metropolis Monte Carlo algorithm with a Self-Avoiding Walk (SAW). Let a be the lattice constant and $L = N \cdot a$ be the polymer chain length with N is the number of monomers. A second parameter specifies the number of pivot steps (kinks) n_s to be applied as input. In the beginning, the number of kinks performed is set to zero $k = 0$. The algorithm sequence is depicted in Figure 3.6 for $N = 7$ and the first four steps:

- Choose a 'pivot' location (red arrow) at random from the chain.
- Choose at random which part of the chain gets modified, i.e. whether it is above or below the pivot point.
- Apply a 90-degree rotation around the pivot site to all of the sites on the chosen chain component to get the desired result. Indicated with a black arrow, this rotation has an equal probability of occurrence in either direction.
- Check to see whether the chain is in contact with itself (self-avoidance). If it is, the rotation should be undone. If not, the rotation should continue.

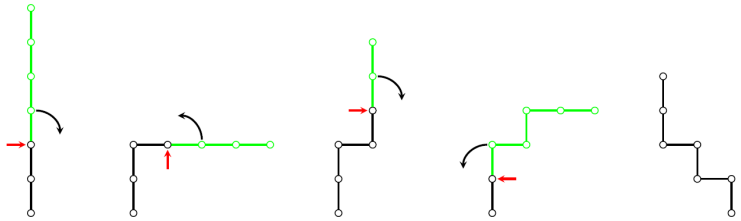

Figure 3.6: Generation of polymer chains using pivot algorithm. Reproduced with permission from [42].

- Increase the number of steps and end the program if $k = n_s$.

3.3.1.3 Energy level specification

The energy level allocated to each node accurately reproduces the potential landscape experienced by particles in the photoactive layer as a result of the interaction between them. The total energy at site i can be represented as:

$$E_i = E_{i,0} + E_{i,F} + E_{i,\sigma} + E_{i,C}\,, \tag{3.24}$$

where $E_{i,0}$ is the molecular orbital (MO) energy of the respective material, i.e. $E_{i,\mathrm{HOMO}}$ and $E_{i,\mathrm{LUMO}}$ for holes and electrons respectively. $E_{i,F}$ represents the electrostatic potential as a result of the external applied voltage across the device. $E_{i,\sigma}$ accounts for the energetic disorder and $E_{i,C}$ is Coulomb potential. The Coulomb interaction is a dynamic variable that is recalculated each time step of a simulation to account for the mobility of charges and their interaction.

Because of a significant energy barrier between the various organic materials, charge carriers can only be able to exist in one phase at a time, which is the acceptor for electrons and the donor for holes. At the same time, these D/A interfaces provide the energy required to dissociate an exciton into free charge carriers. The anode and cathode nodes are at $l_i^z = Lz$ and $l_i^z = 0$ respectively (see Fig. 3.3). The total potential energy drop from $l_i^z = 0$ to $l_i^z = L_z$ is made up of the contributions from the difference of electrode work functions ($\Delta\Phi = \Phi_{anode} - \Phi_{cathode}$) with $\Phi_{anode,cathode} < 0$, and the potential energy drop across the external load qV_{ext}. Now, the energy due to external field contribution from Eq.3.24 can be represented as:

$$E_{i,F} = \frac{l_i^z}{L_z}(qV_{ext} - \Delta\Phi)\,. \tag{3.25}$$

For every external field, the field effect is recalculated and adjusted to $E_{i,0}$. Further, we make use of Gaussian disorder model, where the site energies are sampled from a

Gaussian distribution of localized states (Gaussian Density of States (DOS) with certain width σ [20]. $E_{i,\sigma}$ is, the energetic disorder at node i for donor site ($E_{D,\sigma}$) and the acceptor site ($E_{A,\sigma}$), drawn by the Gaussian distribution of the form:

$$g(E) = \frac{N}{\sigma_i\sqrt{2\pi}}\exp\left(\frac{-(E-E_{i,0})^2}{2\sigma_i^2}\right), \tag{3.26}$$

with the available site density $N = l^{-3}$ and σ_i, the standard deviation (energetic disorder) of the Gaussian distribution in acceptor and donor material. The deviation varies depending on whether electrons or holes are present, reflecting the degree of energetic disorder in the system. The disorder may also be added for excitons, which have a smaller deviation than the charge carriers since they are less susceptible to electrostatic disorder as neutral objects. The HOMO and LUMO energy may also be correlated. The kMC simulations reported in this thesis do not utilize correlated energy levels. It is also possible for a charge carrier's on-site energy to be affected by Coulomb interactions with nearby charges, Coulomb interactions with image charges contained in an electrode, and the applied electric field, among other factors as represented in Eq.3.24. In OSC simulations, the Coulomb energy is computed using the Ewald summation method of calculation. A comprehensive explanation of the Ewald summation technique's implementation, as well as the basic theory behind it, can be found elsewhere [32, 42, 193].

3.3.2 Physical processes and rate equations

The transition rates for all processes involving charge carriers and excitons, as well as the specifics of their implementation, are outlined in the following section.

3.3.2.1 Charge carrier transport

A functional organic solar cell is one in which charge carriers move from sites inside the device to the electrodes while it operates. As previously stated, our kMC simulation box is made up of sites arranged in a basic cubic lattice pattern, and charge carriers can hop from site i to neighbouring site j. According to the Miller-Abrahams formalism [82], the hopping rate between two sites is dependent on the site energy ($E_{i,0}$, see Eq. 3.24), the distance between them, and can be calculated as:

$$a_{i\to j} = \sqrt{a_{0,i}a_{0,j}}\exp\left(-2\gamma r_{i\to j}\right)\begin{cases}\exp\left(-\frac{\Delta E_{i\to j}}{k_\mathrm{B}T}\right) & \text{if} \quad \Delta E_{i\to j} > 0\\ 1 & \text{elsewhere}\end{cases}, \tag{3.27}$$

where $\sqrt{a_{0,i}a_{0,j}}$ is the geometric mean of intrinsic attempt to hop frequencies of site i, and j, γ is the localization length, and $\Delta E_{i\to j} = E_j - E_i$ is the energy difference between

the sites, k_B is the Boltzmann's constant and T is the temperature. The attempt-to-hop rate may be calculated using an analogy to the random walk provided by:

$$a_0 = \frac{6\mu k_B T}{q \cdot l^2} \exp(2\gamma l)\,, \tag{3.28}$$

where μ is the mobility and l is the average site distance and γ is derived from the overlap integral between two adjacent wave functions. if just next neighbor hopping is considered, l is always equal to $r_{i\to j}$.

Eq. 3.27 serves as the basic foundation for the dynamic behavior of all charged particles in the solar cell. This equation may be used in either of two hopping types: nearest-neighbor or variable-range. High γ prevents variable-range hopping, while low γ may provide adequate variable-range hopping in ordered domains.

3.3.2.2 Charge carrier injection

To reflect the complete device properties, such as the relationship between current and voltage for OSCs, the charge injection from electrodes has to be taken into account. A model developed by Wolf *et al.* [194], based upon thermionic injection is used in this work, that injects charge carriers from electrodes into adjacent the organic materials. It is essentially a particular instance of charge transfer in which electrons or holes are produced in the first layer of sites immediately next to the electrode. The rate at which charge carriers are injected to a site i can be represented as an analogy to Miller Abraham equation (Eq: 3.27):

$$a_{inj,i} = \sum_{i}^{n} a_{0,i} \exp\left(-2\gamma r_{c\to i}\right) \exp\left(-\frac{E_{b,n} - \frac{q^2}{16\pi\epsilon_r\epsilon_0 r_{c\to i}}}{k_{\mathrm{B}}T}\right)\,, \tag{3.29}$$

where $E_{b,n} = E_n - \Phi$ is the injection barrier from electrode at $l_z^n = 0$ for cathode ($l_z^n = L_z$ for anode) into the neighboring organic node at $l_z^n = 1$ ($l_z^n = L_z - 1$ for anodic injection). $\sum_i^n a_{0,i}$ denotes summation index for the entire metal-semiconductor contact area. $r_{c\to i}$ is the distance between the contact layer and the organic site. Using the term $\frac{q^2}{16\pi\epsilon_r\epsilon_0 r_{c\to i}}$, we can account for the decrease in barrier height caused by an induced mirror charge [194].

To determine injection rates, the injection model takes into account the static energy distribution in the active layer; however, it does not take into account the dynamic fluctuations produced by charges in the system. To create a more sophisticated contact model, it is necessary to update the computation of injection rates and to consider particular nodes for the injection process (rather than arbitrarily selecting a node) while considering the internal electrostatic potential. However, since it is not possible to do so in every simulation step due to computing constraints, approximations must be used to accomplish

a compromise between simulation time and physical accuracy to achieve a reasonable time-to-market.

3.3.2.3 Charge carrier collection

Extracting current requires that the collection rate of electrons and holes at nodes close to the electrodes ($l_i^z = 1$ and $l_i^z = L_z - 1$) be enabled. Charge collection at the electrodes (anode and cathode) is enabled if a charge carrier is present on a site near the contact layer. It is essential to consider the energy barrier that exists at the interface. Because the collection of a charge is the reversal of the injection process, the same analogy to Miller Abraham rate [82] is utilized with an inverse energy barrier as:

$$a_{inj,i} = \sum_{i}^{n} a_{0,i} \exp\left(-2\gamma r_{c\to i}\right) \exp\left(-\frac{\frac{q^2}{16\pi\epsilon_r\epsilon_0 r_{c\to i}} - E_{b,n}}{k_{\mathrm{B}}T}\right) . \tag{3.30}$$

A collection procedure removes a particle from the photoactive layer that contributes to the photocurrent retrieved from the cell.

3.3.2.4 Charge carrier recombination

One of the main loss processes in OSCs is charge recombination. Two oppositely charged particles may recombine at a recombination rate of a_{ehr} if they are placed on neighboring sites (with a distance of 1nm). It denotes the rate at which a bonded electron-hole pair undergoes direct recombination. Activation of recombination is only possible in the kMC simulations if both an electron and a hole are located on nearest-neighbor sites. In organic solar cells, it is usually necessary to differentiate between several kinds of recombination that may occur. For instance, *geminate recombination*, where electron and hole originate from the same source and *non-geminate recombination*, where both the charge carriers have different origin. KMC model keeps the track of the charge origin. Therefore, the recombination channels can easily be identified. Recombination can often be described by the form:

$$R = \beta \cdot np\,, \tag{3.31}$$

where R is volume recombination rate, n and p are charge carrier densities for electron and hole respectively. The parameter β from Langevin model [195] is given as:

$$\beta = \frac{q}{\epsilon_0\epsilon_r}\left(\mu_n + \mu_p\right) , \tag{3.32}$$

where μ_n and μ_p are charge carrier mobility for electrons and holes respectively. β is a characteristic of the materials, rather than a characteristic of the device operation

(i.e. n and p). However, its predictions are not always in accordance with the observed recombination rate in OPVs, β_{eff}. It is generally stated to be lower than the predictions made by the Langevin equation [196–199] and to be depending on the charge density of the electrons [197, 200, 201]. Marsh *et al.* reported a recombination rate to $5 \times 10^5\,\text{s}^{-1}$ to achieve good agreement with the experimental data [180]. It was noted, however, that the rate may vary by many orders of magnitude depending on the materials used and the specific molecular interaction occurring at the contact layer. The $j - V$ characteristics have been fitted using recombination rates ranging between $1 \times 10^4\,\text{s}^{-1}$ to $1 \times 10^6\,\text{s}^{-1}$ [197]. The constant recombination rate in this case is given by the inverse of recombination time constant τ_{ehr},

$$a_{\text{ehr}} = \frac{1}{\tau_{\text{ehr}}}\,. \tag{3.33}$$

Models with constant recombination rates are often used to restrict the CT state lifetime [14, 99, 197, 202]. When doing kMC investigations, the typical rates utilized are in the range of $1 \times 10^5\,\text{s}^{-1}$ to $1 \times 10^9\,\text{s}^{-1}$. With a constant recombination model, we are unable to differentiate between the several recombination channels. The recombination rate increases if an electron and a hole are found on neighboring sites, regardless of where they are located within the active layer of the semiconductor.

3.3.2.5 Exciton generation

Excitons are produced in the photoactive layer when it is illuminated. To count the number of excitons produced per unit time and volume at node i, A generation profile, measured in $\text{nm}^{-1}\,\text{s}^{-1}$ to characterize the exciton generation is used. It is important to mention that the attenuation of light intensity inside the photoactive layer and reflection at interfaces between the photoactive layer and the extraction layers must be taken into consideration when calculating the exciton generation rate. Therefore, for a comprehensive treatment of optical effects, Transfer Matrix Model (TMM) [203, 204] is used to describe the exciton generation rate a_{op} with respect to the penetration depth z,

$$G(x_i, y_i, z_i) = a_{\text{op}}(z_i)\,. \tag{3.34}$$

The TMM model is a more advanced model that uses the unique complex wavelength dependent refraction indices $\bar{n}(\lambda) = n(\lambda) + ik(\lambda)$ of the active layer materials, where $n(\lambda)$ is the refractive index and $ik(\lambda)$ is the extinction coefficient, to compute the generation profile with respect to AM1.5 solar spectrum. The TMM assumes that the layers are completely homogeneous and that they are perpendicular to the light direction. The generation rate is therefore determined for each z-layer. Choosing a certain z-coordinate for generation results in a random selection of both the x and y-positions of the photon absorb-

ing site [31]. One such generation profile for ITO/PEDOT:PSS/PTB7:$PC_{71}BM$/Ca/Al device architecture using TMM model is shown in Figure A.1. Alternatively, exciton generation can also be specified as a constant rate, where node materials do not affect the generation rate; thus, exciton production occurs with the same probability in both donor and acceptor materials, independent of the node materials. The constant generation model contains no information on the external illumination intensity. Therefore, the generation rate must either be modified to the AM1.5 solar spectrum or fitted to experimental data. The constant generation rate can then be represented as:

$$G(x_i, y_i, z_i) = a_{\mathrm{g}} = a_{\mathrm{g},0} \cdot \nu_{\mathrm{box}}\,, \tag{3.35}$$

where $a_{g,0}$ is the constant rate and ν_{box} is the volume of the simulation box.

3.3.2.6 Exciton diffusion

Excitons are zero-charge particles, indicating that they are neutral. They diffuse across the organic semiconductor as a result of energy transfer between sites in the semiconductor. In this work, exciton diffusion using either Förster resonance energy transfer (FRET) [24] or based on a random walk [23] is implemented.

Exciton diffusion based on random walk

The use of a constant diffusion rate is a simple and efficient approach for include exciton diffusion in a model [32, 42, 172]. When there is no energetic disorder, and the primary emphasis is on the characteristics of free charge carriers or CT states, this model is adequate for capturing the exciton properties in most cases. The diffusion constant as an analogy to 3D random walk can be given by:

$$D = \frac{L_D^2}{6\tau_{exc}}\,, \tag{3.36}$$

with average diffusion length L_D and τ_{exc} being the lifetime of an exciton before decay. The diffusion rate then between adjacent sites i and j can be given as:

$$a_{\mathrm{diff}} = \frac{1}{\tau_{\mathrm{ediff}}} = \frac{6D}{r_{i\to j}^2}\,, \tag{3.37}$$

with $r_{i\to j}$ being the distance between the adjacent sites i and j.

Exciton diffusion by Förster Resonant Energy Transfer (FRET)

Exciton diffusion happens as a result of Förster resonant energy transfer (FRET), which transfers energy from an excited donor site to an empty exciton acceptor site [205]. FRET efficiency η_{FRET} is the percentage of energy transfer events that occur for every excitation event. It is dependent on a variety of physical factors, including: 1) the distance between the donor and acceptor molecules; and 2) the temperature of the donor and acceptor molecules. 2) Aspects of the donor emission spectrum that coincide with those of the acceptor absorption spectrum 3) The direction of the donor emission dipole moment with relation to the acceptor absorption dipole moment. Using non-radiative dipole-dipole coupling, a virtual photon is exchanged, resulting in the formation of Förster transfer. η_{FRET} depends upon distance between donor-acceptor as:

$$\eta_{\mathrm{FRET}} = \frac{1}{1 + \left(\frac{r_{i\to j}}{r_{\mathrm{FRET}}}\right)}\,, \tag{3.38}$$

where r_{FRET} is Förster radius, $r_{i\to j}$ is the distance between two adjacent sites. At $r_{\mathrm{FRET}} = r_{i\to j}$, the efficiency of the energy transfer becomes 50% [206]. The spectral overlap integral of the donor and acceptor is used to calculate r_{FRET} experimentally.In our kMC model, Förster energy transfer between ajacent sites i and j is calculated as:

$$a_F = \Gamma \left(\frac{r_{FRET}}{r_{i\to j}}\right)^6 \begin{cases} \exp\left(-\frac{\Delta E_{i\to j}}{k_{\mathrm{B}}T}\right) & \text{if} \quad \Delta E_{i\to j} > 0 \\ 1 & \text{elsewhere} \end{cases}, \tag{3.39}$$

where Γ is the exciton decay rate.

3.3.2.7 Exciton decay

If an exciton does not reach a donor/acceptor heterojunction before decaying radiatively, it will decay after its average lifetime if not dissociated. As a result, the decay rate may be stated as the inverse of the lifetime as:

$$a_{exd} = \frac{1}{\tau_{exc}}\,, \tag{3.40}$$

Singlet excitons decay radiatively within a nanosecond or even a picosecond time span. Exciton decay is believed to be irreversible, which means that once it has happened, the excitation energy has been lost and cannot be used to contribute to any other processes.

3.3.2.8 Exciton dissociation

When operating at the donor-acceptor interface, it is critical for OSCs to produce free charge carriers from excitons in order to function properly. The treatment of charge transfer differs depending on whether the exciton was located in a donor or acceptor material at the time of dissociation. If the exciton was located in a donor, an electron transfer to the acceptor is performed, and the hole remains in the donor. In the event that the exciton was on an acceptor, a hole transfer to the donor is conducted, and the electron stays on the acceptor. Exciton dissociation process has been reported to have very fast timescales in the range of $\approx$ fs [9, 207, 208]. The exciton dissociation rate can be defined as the inverse of the dissociation time constant,

$$a_{\text{sep}} = \frac{1}{\tau_{\text{sep}}} \,. \tag{3.41}$$

Alternatively, existing kMC studies [182, 209] have reported that dissociation rate can also be modelled as analogy to charge carrier hopping using Miller Abraham transfer rate using Eq. 3.27, where the energy difference is given by:

$$\Delta E_{i\to j} = E_j - E_i + E_{CT} - E_b \,. \tag{3.42}$$

BHJ organic solar cells have a high LUMO offset between the donor (D) and acceptor (A) materials compared to the exciton binding energy (E_b), which guarantees that exciton dissociation is more likely to occur at the D-A interface.

3.3.3 Data Evaluation

3.3.3.1 Charge carrier density calculation

We utilize the average occupancy by electrons and holes, separately, of each node i, to calculate the local particle densities for electrons, n_e and holes n_h. we track the occupancy $\chi_{k,i} \in (0, 1)$ at site i for each time step τ_k during simulation time t_s. This gives the charge density,

$$n_{i,e/h} = \frac{\sum_k \chi_{k,i} \cdot \tau_k}{t_s \cdot \nu_i} \,, \tag{3.43}$$

with volume of site i, $\nu_i = a^3$. Total density is calculated by taking the average across all sites inside the photoactive layer.

3.3.3.2 Current density calculation

The current density is defined as the amount of net charge flowing through the organic/electrode contact per unit area and unit time of the electrode. The current density is measured at both the bottom and top contacts. For the cathode, the current density can be given as:

$$j = 10^{17} \cdot \frac{-q(N_{ec,c} - N_{ei,c} + N_{hi,c} - N_{hc,c})}{A \cdot t_s}, \tag{3.44}$$

where $N_{ec,c}$ and $N_{hc,c}$ are electron and holes collected at the cathode, while $N_{ei,c}$ and $N_{hi,c}$ are the electron and holes injected at the cathode respectively. $A = a^2.l_x l_y$ is the electrode area and t_s is the simulation time. The vice versa can be calculated for anode current density. Further details on the parameter evaluation can be found in Chapter 4 and 5.

4 Role of Energetics on the Device Performance of Organic Solar cells

Interface engineering plays a very critical role for performance improvement of bulk-heterojunction organic solar cells (OSCs). The energetic landscape and charge carrier dynamics near the interface can strongly differ from the rest of the active layer. This is especially important for OSC performance when the interface is very disordered or nanostructured. In this work, we present a kinetic Monte Carlo (kMC) model to investigate the impact of interface energetics and disorder at the donor:acceptor interface, as well as the interface between the photo-active layer and the extraction layer, on OSC performance. We parameterize a moderately efficient OSC model to study both effects. Our findings show that the disorder at the donor:acceptor interface influences overall device performance, whereas the disorder at the extraction layer primarily influences open-circuit voltage. The D:A interface has a significant impact on the device performance and need to be controlled to achieve efficient OSCs. Furthermore, we show that the losses owing to the disorder at the interface can be partially restored in the presence of energy cascades by mixed phases within the interface region.

The content of this chapter is adapted with permission from:

1) K. Hussain, W. Kaiser,and A. Gagliardi, "Role of the Interface and Extraction Layer Energetics in Organic Solar Cells", *The Journal of Physical Chemistry C*, vol. 125, no. 10, pp. 5447–5457, 2021.

2) K. Hussain, W. Kaiser, and A. Gagliardi, "Role of Interface Energetics and Off-diagonal Disorder in Bulk-Heterojunction Organic Solar Cells", 2020 *IEEE 20th International Conference on Nanotechnology (IEEE-NANO)*, September 2020.

4.1 Background

There is an increased research trend towards the study of interfaces in organic electronics that involve organic semiconductors, metals, electrolytes, as well as ferroelectrics and biological organisms [210]. These interfaces play a crucial role in the function of organic electronic devices, especially OSCs. Two types of interfaces are present: The interface either consists of two different organic semiconductors, an electron acceptor (A) and an electron donor (D), or the semiconductor-metal contact. The molecular arrangement at the D:A interface affects the energy alignment due to local defects as well as the energetic disorder and crucial for exciton dissociation and separation of the photo-generated charge carriers [211, 212]. The energetics of these interfaces influences the charge transfer and charge separation properties in the OSC and thus strongly impacts the device performance. To make the most of the solar spectrum, research has been progressing on multi-junction architectures, where number of interfaces further increase [213]. This highlights the critical importance of optimizing interfaces for optimum device efficiency. In the same context, utilizing new materials as hole transport layer (HTL) and electron transport layer (ETL) within OSCs has been pursued [214, 215]. Interfacial engineering either uses an appropriate interfacial layer to improve charge collection [216] or alters the interface energetics by passivating bulk defects by chemical processing of the active layer [217]. The most well studied strategy nowadays is the use of new and well-designed materials. Organic molecules and conductive polymers, [218, 219], fluorides, [220], hybrid oxide-organic materials, [221], and graphene and graphene oxide derivatives, among others, have been incorporated at the organic contacts to improve device performance and the stability. These research trends highlight the need to optimize interfaces for optimum device efficiency.

The energetic disorder at the D:A interface is a major cause of open-circuit voltage V_{oc} losses. Changes in conjugation length and interactions with neighboring molecules cause the energetic disorder, which results in a random electrostatic landscape. This disorder, which is represented by the Gaussian distribution of the highest occupied molecular orbital (HOMO) and lowest unoccupied molecular orbital (LUMO) energies, is decisive in all electronic processes in Organic semiconductors with localized charge carriers and excitons [106, 222–225]. An increase in energetic disorder can significantly reduce open-circuit voltage due to induced tail states in the density of states [185, 226]. Photogenerated charging carriers move between localized quantum states with extremely disordered molecular orbital energies by incoherent hopping [223, 227]. Thus, the energy loss by thermalization highly depends on the width of the DOS. Due to the finite size of the photoactive layer, however, the thermalization of charge carriers before reaching the contacts is not com-

plete [228]. Transient nonequilibrium effects need to be included to fully understand the physics of electronic and excitonic processes within disordered semiconductors [228, 229]. Furthermore, it is widely understood that a significant energetic disorder impedes charge transfer and hence reduces mobility [230]. In addition, the interface morphology is important for losses in the V_{oc} [212]. Azzouzi *et al.* emphasized the relevance of charge transfer (CT) states, specifically the CT-oscillator strength, for non-radiative energy losses [153]. Few important factor affecting V_{oc} losses are recombination, light intensity, temperature and illumination intensity, carrier density, work function of electrodes, as reviewed by Uddin *et al.* [231].

Different numerical models, especially drift-diffusion (DD) [226, 232–236] and kinetic Monte Carlo (kMC) [185, 229] studies have been used to study the effect of the interface energetics and contact layers on open-circuit voltage. DD simulations showed that the energetic disorder can cause a loss in V_{oc} and account for intensity-dependent recombination rates [226]. Sandberg *et al.* observed S-shaped J-V characteristics in presence of imperfect contacts and a strong connection of the injection barrier on V_{oc} [232]. Unlike BHJ solar cells, flat heterojunction solar cells have no dependency on the injection barrier for V_{oc} [235]. For significant work function differences, Zampetti *et al.* proved the presence of a saturation regime, with maximum V_{oc} substantially dependent on the DOS [237]. Most DD simulations describe the complex active layer architecture as an effective medium in 1D, limiting the study to bulk characteristics only. The effective medium approximation does not take into account accurate exciton and charge carrier dynamics in the complex three-dimensional (3D) morphology and can not discriminate molecular orbital energies at interfaces from bulk. Only a handful DD investigations of OSCs have reached greater dimensionality to yet. Buxton *et al.* used two-dimensional DD to investigate structure-property relationships in OSCs [238]. Furthermore, two-dimensional DD was used to investigate the influence of mid-gap states at interfaces on the vacuum level landscape in BHJ solar cells [239]. Three-dimensional DD models have been employed to investigate the impact of charge carrier mobility, [18], but they ignore local changes in energetics. Most importantly, DD models assume instantaneous charge carrier equilibration and cannot correctly represent transient effects. As an alternative numerical tool, kMC models offer full device simulations incorporating local variations in morphology and energetic structure. Most importantly, kMC captures the nonequilibrium properties of charge carriers [28, 185, 240]. kMC studies underline that CT electroluminescence at disordered organic hetero interfaces can only be accurately described if nonequilibrium charge carrier dynamics is included [241]. Further experimental studies indicate that the occupancy of CT states under steady-state conditions is insufficient, and hence cannot be represented by the "equilibrium" Boltzmann distribution [242]. This observation is

also corroborated by earlier kMC studies [185]. Furthermore, kMC studies have provided significant insight into charge separation, [15,177,243,244] charge recombination, [27,245] as well as charge carrier transport in OSCs [28,116,223,240,246]. kMC has an edge over DD and other numerical tools because of the importance of detailed morphology and the non-equilibrium characteristics of charge carrier dynamics.

In order to achieve efficient OSCs, the function of interfaces in all device properties, such as j_{sc}, V_{oc}, and FF, must be understood. In this particular work, we present a kMC study on the effect of interface and extraction layer energetics on the device performance of bulk-heterojunction OSCs. This study aims to understand to how much extent the energetics at donor:acceptor interface and the extraction layer energetics affect the photovoltaic properties of OSCs. The relation between energetic disorder and open-circuit voltage and that between the contact energetics and V_{oc} has already been known from the experimental perspective and DD simulations as summarized above. However, the effect of the combined disorders on the device performance still needs investigation to reveal the dominant mechanism. We explore 3D kMC model capabilities to include both the energetics for the bulk-heterojunction morphology. Our results demostrate that the disorder at the D:A interface mostly affects J_{sc} and FF, whereas the extraction layer disorder has a negative influence on V_{oc}. The cumulative effect of both disorders has a significant detrimental effect on the device efficiency. We also show that energy cascades at the D:A interface, which are frequently assumed in mixed phases, can overcome the negative consequences of interface disorder. This might explain why, despite the presence of energetic disorder at the interface, conventional BHJ solar cells show reasonable performance.

4.2 Computational Model

All the calculations are performed using kMC model explained in Section3. The rate models used in the kMC simulations and the system configuration for this particular work are briefly summarized below. A cubic lattice with constant lattice spacing l represents the active layer. Only the nearest neighbors, i.e. six neighbors at each site, are considered in all charge transport processes. In both the x and y directions, periodic boundaries are used. Contacts terminate the cell in the z direction. A bulk-heterojunction morphology is generated using spin exchange algorithm presented by Watkins *et al.* [30] looped over 400 Monte Carlo steps [31], which gives a cluster size of 16.1 nm.

Within the active layer, singlet excitons are generated using a generation profile $a_{\mathrm{gen}}(z)$ computed using the transfer matrix method [203] for the layer combination of ITO/PEDOT:PSS/PTB7:I as an example device architecture. Figure A.1, represents the generation profile. A con-

stant decay rate $a_{\mathrm{exd}} = \tau_{\mathrm{ex}}^{-}1$ is incorporated in the finite singlet lifetime, τ_{ex}. Singlet diffusion is modelled as a long-range Förster resonant energy transfer, given by [24].

$$a_{\mathrm{exh},i\to j} = \tau_{\mathrm{ex}}^{-1}\left(\frac{r_{\mathrm{F}}}{r_{i\to j}}\right)^{6}\begin{cases}\exp\left(-\frac{\Delta E_{\mathrm{ex},i\to j}}{k_{\mathrm{B}}T}\right) & \text{if} \quad \Delta E_{\mathrm{ex},i\to j} > 0\\ 1 & \text{else}\end{cases}, \tag{4.1}$$

with Förster radius r_{F} and difference in energy $\Delta E_{\mathrm{ex},i\to j}$ modeled by

$$\Delta E_{\mathrm{ex},i\to j} = E_j^{\mathrm{LUMO}} - E_i^{\mathrm{LUMO}} - E_j^{\mathrm{HOMO}} + E_i^{\mathrm{HOMO}}\,. \tag{4.2}$$

Final sites are defined as all j sites with a distance of $r_{i\to j} < r_{\mathrm{F}}$. At the D:A interface, singlet dissociation is represented as a constant dissociation rate a_{diss} from the excited donor to the acceptor site. The dissociation rate is only activated if a singlet is located at the D:A interface [14, 32].

Charge carrier transport is modeled by the Miller-Abrahams hopping rate [82]:

$$a_{i\to j} = a_{0,\mathrm{hop}}\begin{cases}\exp\left(-\frac{\Delta E_{i\to j}}{k_{\mathrm{B}}T}\right) & \text{if} \quad \Delta E_{i\to j} > 0\\ 1 & \text{else}\end{cases}, \tag{4.3}$$

where $a_{0,\mathrm{hop}}$ is the attempt-to-hop rate, k_{B} is the Boltzmann constant, T is the temperature , and $\Delta E_{ij} = E_j - E_i$ is the energetic difference between the sites i and j. The potential at site i is calculated as

$$E_i = E_i^{\mathrm{MO}} + E_i^{C} + E_i^{F}\,, \tag{4.4}$$

where E_i^{MO} is the molecular orbital energy (MO $\in$ HOMO/LUMO) derived from a Gaussian variance σ^2 distribution. The Coulomb energy is E_i^{C}, while the potential owing to the external bias voltage V is E_i^{F}. The Coulomb interaction is included by the Ewald summation, which accounts for all charge carrier interactions, including their periodic replica and image charges owing to contacts [32]. Recombination can occur if an electron and a hole reside on adjacent sites. For simplicity, we use a constant recombination rate a_{ehr}.

Charge carriers can be produced by singlet dissociation and by injection from contacts, as previously stated. The charge injection rate is implemented as a Miller-Abrahams hopping from anode/cathode with work function $\phi_{\mathrm{a/c}}$ onto an adjacent site with attempt-to-hop rate a_0, cont. The collection of charge carriers is accomplished as a Miller-Abrahams hopping from the photoactive layer into the contact with an attempt-to-hop frequency a_0, cont, which is activated if the charge is located near the contact.

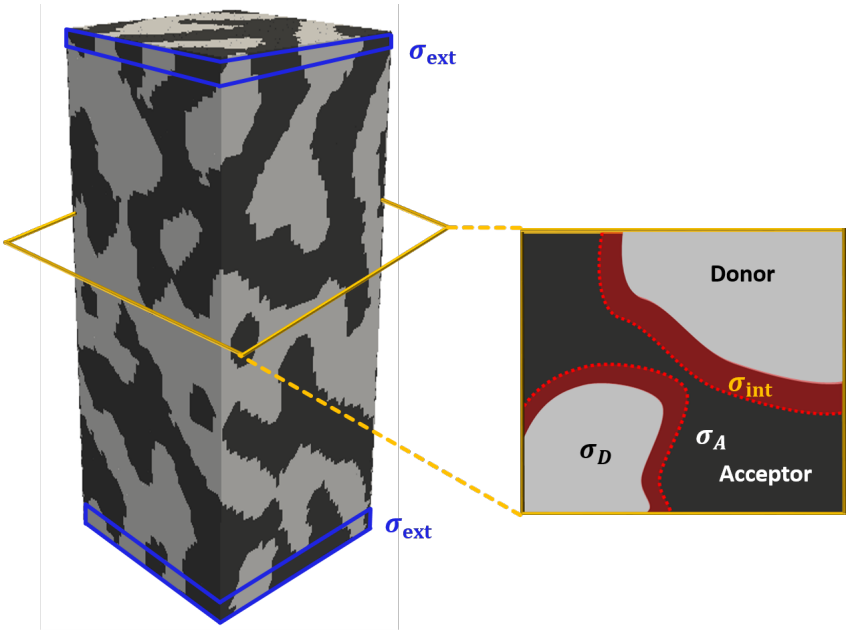

Figure 4.1: Schematic representation of the BHJ morphology. We set different energetic disorder within the bulk, $\sigma_{\mathrm{A/D}}$, at the donor:acceptor interface, σ_{int}, and at the extraction layer to the anode and cathode, σ_{ext}.

Organic Blend	τ_{ex}(ps)	μ_{h} (cm^2/(Vs))	μ_{e} (cm^2/(Vs))	V_{oc}(V)	J_{sc}(mA/cm^2)	FF (-)	PCE (%)	Reference
PCPDTBT:PC$_{71}$BM	78	2.6×10^{-5}	3.8×10^{-4}	0.62	16.2	0.55	5.5	[247–249]
PSBTBT:PC$_{71}$BM	810	3×10^{-3}	1.2×10^{-3}	0.68	12.7	0.55	5.1	[250–252]
P3HT:PC$_{60}$BM	422	5.1×10^{-5}	1.1×10^{-4}	0.61	10.6	0.67	4.4	[247, 253]
PCDTBT:PC$_{60}$BM	463	2.4×10^{-3}	1.5×10^{-4}	0.89	6.92	0.63	3.6	[247, 254, 255]
PTB7:PC$_{71}$BM	93	8.3×10^{-4}	3×10^{-4}	0.72	18.1	0.71	9.25	[247, 256, 257]
PTB7-Th:PC$_{71}$BM	220	2.3×10^{-4}	2×10^{-3}	0.78	18.95	0.72	10.95	[258, 259]
PBnDT-FTAZ:PC$_{71}$BM	300	6.2×10^{-3}	5.9×10^{-4}	0.75	13.7	0.68	7.0	[260]

Table 4.1: Device parameters for different fullerene-based organic solar cells.

Figure 4.1 depicts the bulk-heterojunction morphology as well as the various types of energetic disorders that are studies in this work. We differentiate between energetic disorder in the bulk, $\sigma_{\mathrm{A}} = \sigma_{\mathrm{D}} = \sigma_{\mathrm{bulk}}$, energetic disorder at the donor:acceptor interface, σ_{int}, and energetic disorder in the organic layer next to the anode and cathode, σ_{ext}. Each site that has a neighbor of a different phase is referred to as an interface site. All energetic disorders mentioned here are assumed to follow a Gaussian distribution.

4.2.1 Model Parametrization

To achieve simulation results covering a wide range of OSCs, we must properly parameterize the material properties. This is based on a literature review on several fullerene-based OSCs, which is summarized in Table 4.1. These devices have efficiencies ranging from

Parameter	Value
Simulated volume	$40 \times 40 \times 80$ sites
Lattice parameter, l	1.8 nm
Dielectric constant, ϵ_r	4.0
Thermal energy, $k_\mathrm{B}T$	25 meV
HOMO energy of donor, E_HOMO	−5.1 eV
LUMO energy of acceptor, E_LUMO	−3.7 eV
Holes attempt-to-hop frequency, $a_{0,\mathrm{h}}$	$2 \times 10^9\,\mathrm{s}^{-1}$
Electrons attempt-to-hop frequency, $a_{0,\mathrm{e}}$	$2 \times 10^9\,\mathrm{s}^{-1}$
Exciton lifetime, τ_ex	500×10^{-12} s
Exciton dissociation rate, a_diss	$1 \times 10^{12}\,\mathrm{s}^{-1}$
Förster radius, r_F	3.5 nm
Electron-hole recombination rate, a_ehr	$1 \times 10^6\,\mathrm{s}^{-1}$
Anode work function, ϕ_a	−4.8 eV
Cathode work function, ϕ_c	−4.0 eV
Contact attempt-to-hop frequency, $a_{0,\mathrm{c/a}}$	$2 \times 10^9\,\mathrm{s}^{-1}$

Table 4.2: Key parameters used in the kMC model.

≈ 3 to 10 %, with a wide range in J_sc, FF, and V_oc. We briefly discuss the model OSC's parametrized values. Table 4.2 summarizes the kMC parameters used in this work.

Charge carrier mobilities vary from $10^{-5}\,\mathrm{cm}^2\,\mathrm{V}^{-1}\,\mathrm{s}^{-1}$ to $10^{-3}\,\mathrm{cm}^2\,\mathrm{V}^{-1}\,\mathrm{s}^{-1}$. The electron mobility differs by at least one order of magnitude even when the same acceptor materials are used. This is due to the fact that charge transfer is highly dependent on the energetic disorder [230] and local morphological features such as mixed donor:acceptor phases [21]. Furthermore, charge carrier mobility imbalance can have a significant influence on device efficiency [18]. We assume identical attempt-to-hop rates for charge carriers of $a_{0,\mathrm{h}} = a_{0,\mathrm{e}} = 2 \times 10^9\,\mathrm{s}^{-1}$ to keep the focus on interface characteristics. According to Pasveer *et al.* [230], this corresponds to a charge carrier mobility of $2.4 \times 10^{-4}\,\mathrm{cm}^2\,\mathrm{V}^{-1}\,\mathrm{s}^{-1}$. We also computed the charge carrier mobility inside the 3D BHJ morphology at the applied bias voltage $V_\mathrm{ext} = 0.6$ volt, with all σ set to 50 meV. We set the lattice constant to 1.8 nm in agreement with the earlier kMC study on TQ1:$PC_7$1BM solar cells, [229]. Figure A.2, visualizes a variety of mobilities as well as a Gaussian fit. The average mobility is $1.5 \times 10^{-4}\,\mathrm{cm}^2\,\mathrm{V}^{-1}\,\mathrm{s}^{-1}$, which is somewhat lower than the prediction made by [230]. This value is consistent with the results of the summarized experimental studies. We choose an electron-hole recombination rate of $10^6\,\mathrm{s}^{-1}$, which is in the range of values used within previous kMC studies [27, 32, 99, 229].

Experimentally measured exciton lifetimes range from tens to hundreds of picoseconds. In this case, we estimate an exciton lifespan of 500 ps. The inverse of the exciton lifetime is directly included into the Förster resonant energy transfer rate. Exciton diffusion lengths of less than 10 nm are seen in the majority of organic semiconductors [136].

We set the Förster radius to $r_{\mathrm{F}} = 3.5\,\mathrm{nm}$ to parametrize the exciton diffusion length. Figure A.3, depicts the distribution of exciton diffusion lengths when exciton dissociation is supressed. The average exciton diffusion length obtained is 7.2 nm. Once excitons reach the donor:acceptor interface, they dissociate at a rate of $10^{12}\,\mathrm{s}^{-1}$. This value is consistent with prior theoretical studies [261].

4.3 Results and discussion

4.3.1 Role of Energetic Disorder

We begin our comprehensive study by analyzing the influence of the energetic disorder at the donor:acceptor interface, σ_{int}, and at the extraction layer, σ_{ext}. The levels of both sources of energetic disorder range from 50 meV to 125 meV. The bulk disorder is kept constant at 50 meV.

First, σ_{int} is varied while σ_{ext} is kept constant at 50 meV. Figure 4.2a depicts the J-V characteristics with varying σ_{int}. Table 4.3 summarizes the extracted device characteristics. The model OSC has a PCE of 4 %, a fill factor of 0.56, a J_{sc} of $10.2\,\mathrm{mA\,cm^{-2}}$, and a V_{oc} of 0.8 V at $\sigma_{\mathrm{int}} = 50\,\mathrm{meV}$ (treated as as reference hereafter). At maximum power point, the device shows an exciton dissociation efficiency, i.e. the percentage of excitons that reach and dissociate at the D:A interface, of 88.9 % and an internal quantum efficiency of 73.2 %. We further calculate the geminate (nongeminate) volume recombination rate, given by [116]

$$R_{\mathrm{gem(nongem)}} = \frac{\#N_{\mathrm{gem(nongem)}}}{t_{\mathrm{sim}}}\,, \tag{4.5}$$

where $\#N_{\mathrm{gem,nongem}}$ is the number of geminate (nongeminate) recombination events and t_{sim} simulation time. The reference OSC shows $R_{\mathrm{gem}} = 1 \times 10^{4}\,\mathrm{s}^{-1}$ ($R_{\mathrm{nongem}} = 3.5 \times 10^{4}\,\mathrm{s}^{-1}$). Photo-generated charger carriers are therefore able to quickly escape their Coulomb attraction and then collected at respective electrodes. The advantage of the kMC model is that it allows us to distinguish between charge carrier behavior in the bulk and that at the D:A interface. We achieve this by calculating the charge carrier density at each j location in bulk (at the interface) by

$$n_{\mathrm{bulk(int)}} = \left\langle \sum_{j\in\{\mathrm{bulk(int)}\}} \frac{\tau_{j,\mathrm{occ}}}{t_{\mathrm{sim}} V_j} \right\rangle_{j\in\{\mathrm{bulk(int)}\}} \tag{4.6}$$

where j represents all sites in bulk (at the interface), V_j represents the volume of site j, and $\tau_{j,\mathrm{occ}}$ represents the amount of time that site j is occupied by a charge carrier. The interface and bulk density in the reference OSC are $2.4 \times 10^{16}\,\mathrm{cm^{-3}}$ and $2.1 \times 10^{16}\,\mathrm{cm^{-3}}$,

	σ (meV)	V_{oc} (V)	J_{sc} (mA cm^{-2})	FF (-)	PCE (%)	n_{int} (cm^{-3})	n_{bulk} (cm^{-3})	R_{gem} (s^{-1})	R_{nongem} (s^{-1})
σ_{int}	50	0.80	10.1	0.56	4.5	2.4×10^{16}	2.1×10^{16}	1.0×10^{4}	2.5×10^{4}
	62.5	0.79	10.2	0.55	4.4	6.9×10^{16}	2.1×10^{16}	3.1×10^{4}	1.3×10^{5}
	75	0.79	10.1	0.46	3.7	1.8×10^{17}	2.3×10^{16}	7.5×10^{4}	6.0×10^{5}
	87.5	0.78	8.8	0.37	2.6	3.8×10^{17}	1.4×10^{16}	1.3×10^{5}	1.4×10^{6}
	100	0.77	7.0	0.33	1.8	6.3×10^{17}	1.2×10^{16}	2.0×10^{5}	1.8×10^{6}
	125	0.73	3.7	0.30	0.8	1.4×10^{18}	4.9×10^{15}	3.3×10^{5}	2.2×10^{6}
σ_{ext}	50	0.80	10.1	0.56	4.5	2.4×10^{16}	2.1×10^{16}	1.0×10^{4}	2.5×10^{4}
	62.5	0.78	10.0	0.56	4.4	2.5×10^{16}	2.4×10^{16}	1.8×10^{4}	2.7×10^{4}
	75	0.76	9.8	0.57	4.3	2.5×10^{16}	2.5×10^{16}	1.3×10^{4}	2.5×10^{4}
	87.5	0.73	9.6	0.59	4.1	4.0×10^{16}	3.8×10^{16}	1.8×10^{4}	3.7×10^{4}
	100	0.66	9.6	0.58	3.7	5.7×10^{16}	5.2×10^{16}	1.2×10^{4}	6.2×10^{4}
	125	0.50	9.7	0.67	3.3	1.5×10^{17}	1.4×10^{17}	1.2×10^{4}	7.8×10^{4}

Table 4.3: Device characteristics (V_{oc}, J_{sc}, FF, PCE) of the model OSC with different σ_{int} and σ_{ext}. Charge carrier densities in bulk (n_{bulk}) and at the interface (n_{int}) at maximum power point. Geminate (R_{gem}) and nongeminate recombination (R_{nongem}) at maximum power point.

respectively. In the presence of equal disorder at the interface and within the bulk, a similar charge carrier density is found. This was observed in a previous kMC study by Albes *et al.* [14], for high ϵ_r and energetic disorder smaller than 50 meV. In contrast to the previous work, the present study's Coulomb attraction between electron-hole pairs on neighboring sites is less due to a higher lattice parameter (1.8 nm versus 1 nm). This is an efficient method of simulating a greater delocalization of charge carriers and excitons within kMC.

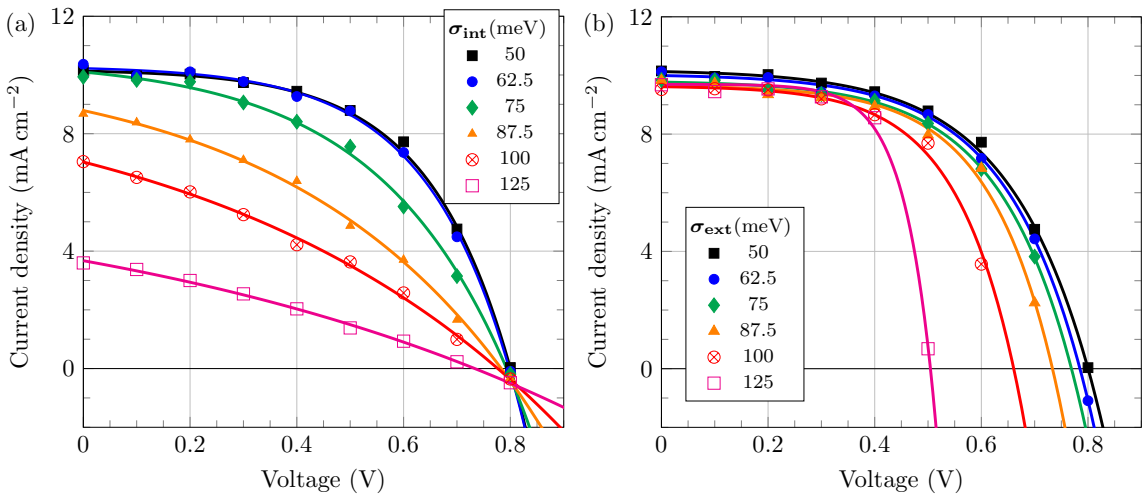

Figure 4.2: J-V characteristics of the model OSC with (a) different σ_{int} at $\sigma_{ext} = 50$ meV, and (b) different σ_{ext} at $\sigma_{int} = 50$ meV. Solid lines show fits obtained by the Shockley equation.

As σ_{int} is increased, PCE drops monotonically to a minimum of 0.8 %. At the highest interface disorder, the shape of the *J-V* characteristic curve becomes linear, as indicated by the low fill factor of 0.30. Up to $\sigma_{int} = 75$ meV, J_{sc} is generally constant. At increasing

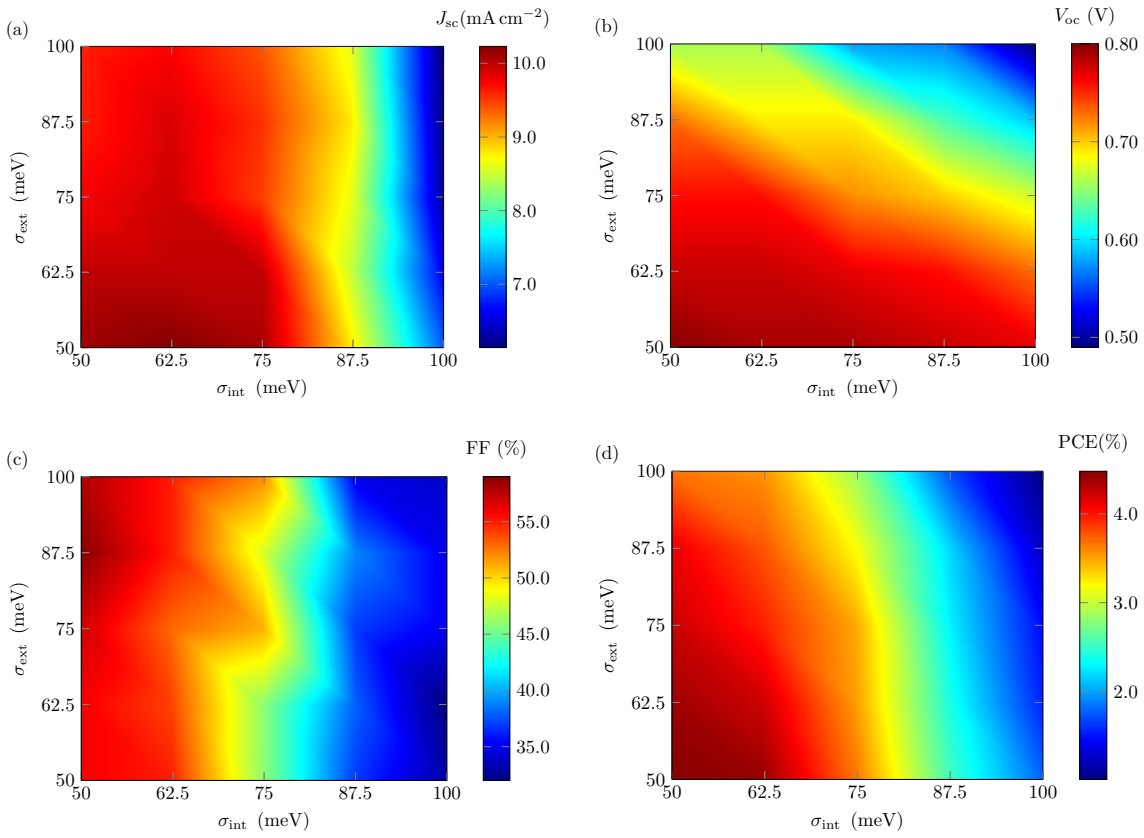

Figure 4.3: Device characteristics of the model OSC for $\sigma_{\text{int}}, \sigma_{\text{ext}} \in \{50\,\text{meV} \ldots 100\,\text{meV}\}$: (a) short-circuit current density, J_{sc}, (b) open-circuit voltage, V_{oc}, (c) fill factor, FF, and (d) power conversion efficiency, PCE. Raw data is shown in Tables A.1-A.4.

disorder, J_{sc} falls to $3.7\,\text{mA}\,\text{cm}^{-2}$. Interestingly, increasing interface disorder only results in a slight drop in V_{oc} to $0.73\,\text{V}$. The patterns in the simulated J-V characteristics are consistent to earlier DD simulation results for'high' intensity ($G = 10^{22}\,\text{cm}^{-3}\,\text{s}^{-1}$) and field-independent generation and recombination rates (see [226], Figure 4.3). The average generation rate used in our study ($G \approx 5 \times 10^{21}\,\text{cm}^{-3}\,\text{s}^{-1}$) is comparable to aforementioned DD study; additionally, even at $\sigma_{\text{int}} = 75\,\text{meV}$, the recombination rate only varies by less than a factor of 2 ($2.28 \times 10^{6}\,\text{s}^{-1}$ at $V_{\text{ext}} = 0\,\text{V}$ and $3.01 \times 10^{6}\,\text{s}^{-1}$ at $V_{\text{ext}} = 0.7\,\text{V}$). Despite the fact that the disorder is only modified at the interface, our findings are consistent with a σ change within effective medium DD models [226]. It is worth noting that the trends concur, but the quantitative influence on the J-V features is considerably larger in the effective medium DD model. With increasing disorder, tail states in the Gaussian DOS act as local trapping sites for charge carriers, leading to higher densities overall. At $\sigma_{\text{int}} = 125\,\text{meV}$, the charge carrier density in the bulk falls to $4.9 \times 10^{15}\,\text{cm}^{-3}$, while the interface density increases by nearly two orders of magnitude $1.4 \times 10^{18}\,\text{cm}^{-3}$. The increase in charge carrier density at the interface significantly

enhances the recombination. The rate of geminate recombination is enhanced by one order of magnitude ($R_{\mathrm{gem}} = 3.3 \times 10^5\,\mathrm{s}^{-1}$), while the rate of nongeminate recombination is increased by nearly two orders of magnitude ($R_{\mathrm{nongem}} = 2.2 \times 10^6\,\mathrm{s}^{-1}$).

We now analyze the effect of the extraction layer disorder σ_{ext} on device performance while keeping σ_{int} at 50 meV. The influence of σ_{ext} on the PCE is less significant when compared to σ_{int}. PCE still amounts to 3.3 % at $\sigma_{\mathrm{ext}} = 125\,\mathrm{meV}$. With an increase in σ_{ext}, only a minor reduction in J_{sc} is observed; the fill factor is nearly constant for $\sigma_{\mathrm{ext}} \leq 100\,\mathrm{meV}$; and an increase in FF of 0.67 is recorded for $\sigma_{\mathrm{ext}} = 125\,\mathrm{meV}$. The reason of the PCE decrease is in the reduced V_{oc}. In contrast to σ_{int}, increasing disorder at the extraction layer is detrimental to the V_{oc}. A higher σ_{ext} causes the increase in n_{bulk} (n_{int}) to $1.4 \times 10^{17}\,\mathrm{cm}^{-3}$ ($1.5 \times 10^{17}\,\mathrm{cm}^{-3}$). This also results in a significant rise in nongeminate recombination ($R_{\mathrm{nongem}} = 7.8 \times 10^4\,\mathrm{s}^{-1}$), but no change in geminate recombination is observed. Interestingly, the V_{oc} values at $\sigma_{\mathrm{ext}} = 75\,\mathrm{meV}$ and 100 meV are quantitatively comparable to the quasi-Fermi level splitting, $\Delta E_{\mathrm{F,q}}$, for different bulk disorder reported by Kaiser *et al.* [185]: $V_{\mathrm{oc}} = 0.76\,\mathrm{V}$ and $\Delta E_{\mathrm{F,q}}/e = 0.766\,\mathrm{V}$ at 75 meV; $V_{\mathrm{oc}} = 0.66\,\mathrm{V}$ and $\Delta E_{\mathrm{F,q}}/e = 0.697\,\mathrm{V}$ at 100 meV. While $\Delta E_{\mathrm{F,q}}$ increased for even lower σ [185], the complete device simulations show a saturation of the V_{oc} at 0.8 V, equal to the difference in contact work functions.

Moving our analysis forward, we will look at the combined effect of interfacial and extraction layer disorder. Figure 4.4 visualizes the device characteristics of the model OSC for $\sigma_{\mathrm{int}}, \sigma_{\mathrm{ext}} \in \{50\,\mathrm{meV} \ldots 100\,\mathrm{meV}\}$ - (a) J_{sc}, (b) V_{oc}, (c) FF, and (d) PCE. J_{sc} drops significantly by about 40 % from the reference value of from the reference value of $10.1\,\mathrm{mA\,cm}^2$ to $6.14\,\mathrm{mA\,cm}^2$ at $\sigma_{\mathrm{int}} = \sigma_{\mathrm{ext}} = 100\,\mathrm{meV}$. The drop in J_{sc} is mostly due to an increase in the interface density n_{int} (see Figure 4.4b) and, as a result, an increase in nongeminate recombination (see Figure 4.4d) is observed. Increase in σ_{ext} at constant σ_{int} induces a small drop in J_{sc}, which is rather insignificant in contrast to σ_{int}. V_{oc} also decreases significantly from the reference value of 0.80 V to 0.49 V at the highest disorder of $\sigma_{\mathrm{int}} = \sigma_{\mathrm{ext}} = 100\,\mathrm{meV}$. Both σ_{int} and σ_{ext} have a substantial influence on the open-circuit voltage, but the extraction layer's contribution is the most dominant. The decrease in V_{oc} is due to a rise in bulk density n_{bulk} and n_{int}, as well as restricted charge extraction at contacts in the presence of low energy tail states in the Gaussian DOS [185].

As we recall from our study of extraction layer disorder with a minimum V_{oc} of 0.66 V at $\sigma_{\mathrm{ext}} = 100\,\mathrm{meV}$, the existence of both sources of disorder further decreases the achievable V_{oc} by 150 mV. The fill factor of the OSC is mostly influenced by σ_{int}. Due to the substantial increase in nongeminate recombination towards the maximum power point, the device displays essentially linear behavior with FF close to 34 % at the highest disorder values (see Figure 4.4d). Finally, PCE is observed to be strongly influenced by σ_{int},

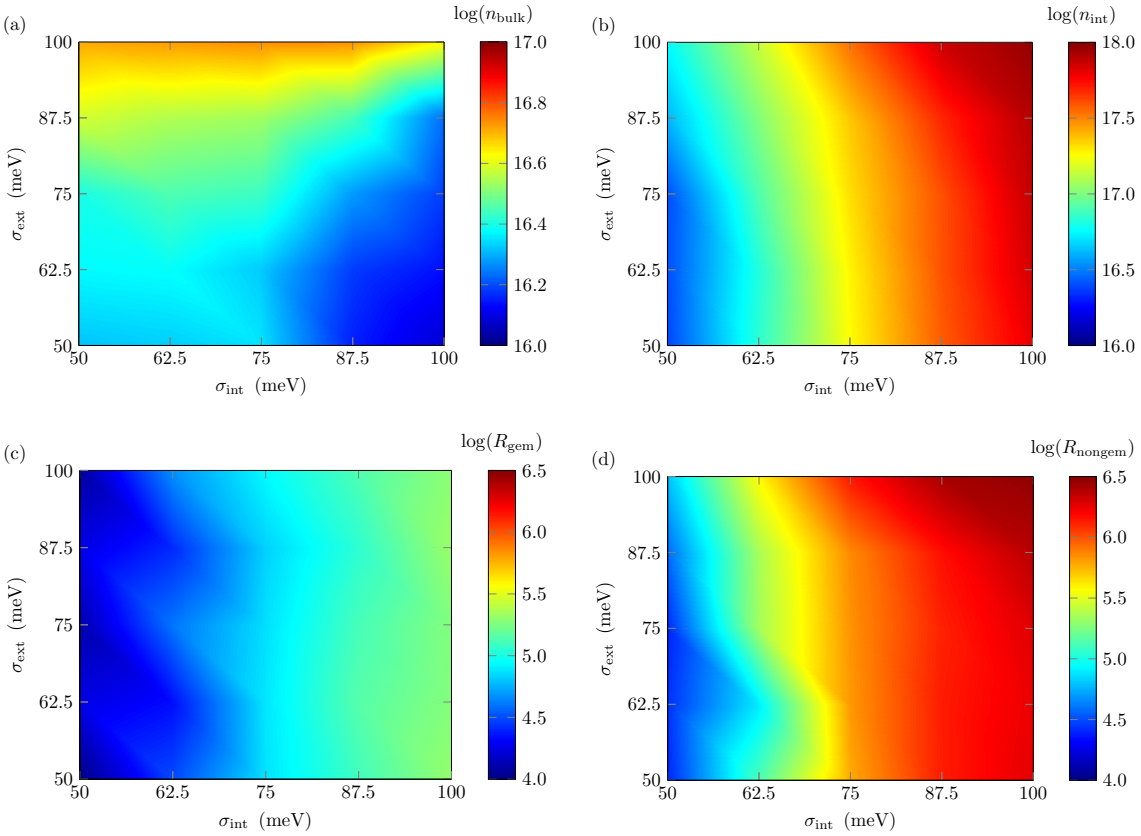

Figure 4.4: Charge carrier density (a) within the bulk, n_{bulk} and (b) at the donor:acceptor interface, n_{int}. (c) Geminate, R_{gem}, and (d) nongeminate volume recombination rate, R_{nongem}. All properties were extracted at at maximum power point. Raw data is shown in Tables A.5-A.8, Supporting Information.

but σ_{ext} has a lesser impact. If we increase both the disorder levels to 100 meV, PCE falls to 1.01 %. The major influence of σ_{ext} stays on lowering the open-circuit voltage, whereas σ_{int} degrades overall device performance. As a result, it is critical to decrease interface disorder in order to obtain highly efficient OSCs. Controlling interfaces between extraction layers and the photoactive layer is required to increase V_{oc}.

4.3.2 Role of Energy Cascades at Donor-Acceptor Interface

Previous research studies have suggested that mixed phases might be beneficial in the interface region between donor and acceptor aggregates. The mixed interface is mainly amorphous, with a larger HOMO-LUMO gap than the aggregates [229]. Experimental studies have revealed, for example, that disordered regiorandom P3HT has a HOMO energy 300 meV lower than ordered regioregular P3HT [262], but the LUMO energy in PCBM decreases following crystallization [263]. Groves proposed that, in the presence of mixed phases or ternary-blends, cascaded energy heterojunctions can enhance efficient

charge separation and supress geminate charge recombination. Burke *et al.* showed that, reducing the optical gap between the donor and acceptor by 200 meV with respect to the mixed interface may significantly improve photocurrent without reducing V_{oc} [264]. However, the summarized studies do not account for variations in the energetic disorder within such mixed phases and often do not simulate entire device characteristics.

To simulate the energy broadening in mixed phases with respect to aggregates in our kMC model, we introduce a Δ increase in the HOMO-LUMO gap at interface sites. For simplicity, as shown in Figure 4.5a, Δ is equally distributed between HOMO and LUMO, thereby performing electrons and holes. $\sigma_{int} = 100\,\text{meV}$ and $\sigma_{ext} = 50\,\text{meV}$ have been fixed for the following study. *J-V* curves with Δ ranging from 0 meV to 300 meV are simulated using kMC. Figure 4.5b visualizes the device characteristics *J*sc, V_{oc}, FF and PCE as a function of Δ. All properties are normalized with respect to their values at $\Delta = 0\,\text{eV}$, i.e.

$$\delta_x = \frac{x - x(\Delta = 0)}{x(\Delta = 0)}\,. \tag{4.7}$$

All reference values can be found in Table 4.3.

For $0 < \Delta \leq 100\,\text{meV}$, J_{sc} increses by 30 % from $7.03\,\text{mA}\,\text{cm}^{-2}$ to $9.11\,\text{mA}\,\text{cm}^{-2}$. At higher Δ, J_{sc} reduces down to $4.72\,\text{mA}\,\text{cm}^{-2}$. The energy cascade at the interface has a contentious effect on both charge carriers and excitons. Charge carriers benefit from a rise in Δ because the shift in HOMO and LUMO energies produces a driving force that supports charge separation, as demonstrated by Groves previously [171]. This is reflected in the lower interface density (see Figure 4.5c) and, as a result, a much reduced (non)geminate recombination (see Figure 4.5d). The reduction in J_{sc} is caused by a decrease in exciton dissociation, which is studied by the exciton dissociation probability η_{diss}, as illustrated in Figure 4.5b. Exciton diffusion occurs via Förster resonant energy transfer, which is proportional to the difference in molecular orbital energies between the initial and final sites. Excitons encounter an energy barrier for migration to the interface as the HOMO-LUMO gap at the interface is raised with Δ. As a result, the number of excitons reaching the interface decreases, and η_{diss} decreases as well. η_{diss} drops from 92.6 % to 42.9 % as Δ varies from 0 eV to 300 meV.

An rise in Δ causes a substantial increase in fill factor from 0.33 ($\Delta = 0\,\text{eV}$) to 0.56 ($\Delta = 0.3\,\text{eV}$) due to a tremendous two to three order of magnitude drop in geminate and nongeminated recombination rates, respectively. Saturation in FF is seen above $\Delta \approx 225\,\text{meV}$. The increase in FF implies that the OSC has shifted from an interface-dominated to a bulk-dominated OSC. This is seen in Figure 4.5c, which demonstrates a significant reduction in charge carrier densities at the D: A interface with higher Δ and a little increase in n_{bulk} simultenousöy. For higher $\Delta > 250\,\text{meV}$, the interface

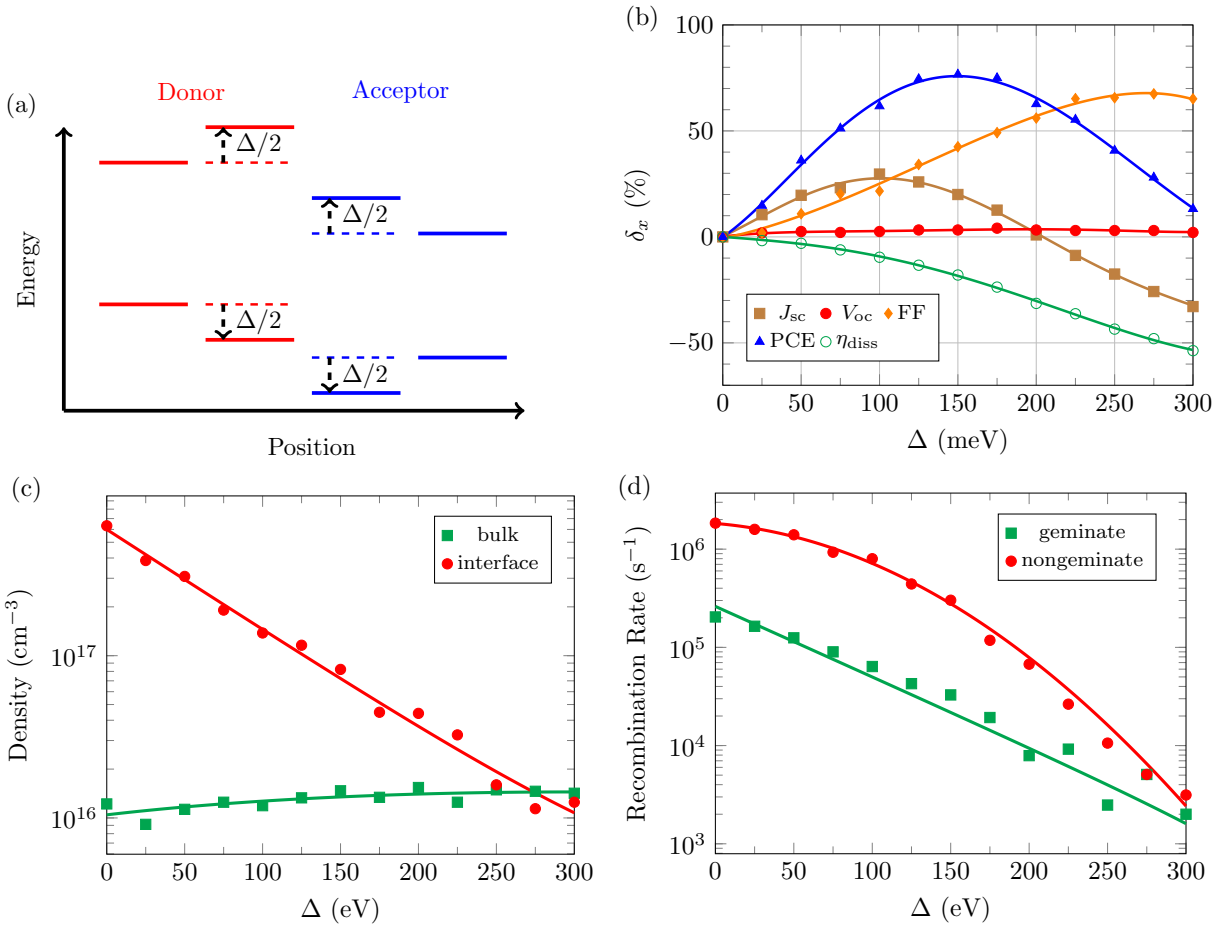

Figure 4.5: (a) Schematic of the energy levels at the donor:acceptor interface with increased HOMO-LUMO gap by Δ at the interface. (b) Device characteristics - normalized to their values at $\Delta = 0\,\text{eV}$ - as function of the HOMO-LUMO gap increase of Δ. (c) Charge carrier density in bulk and at the interface as function of Δ. (d) Geminate and nongeminate recombination rates as function of Δ.

density decreases even below the bulk density. Due to lower geminate and nongeminate recombination, V_{oc} increases by 30 meV with increasing Δ. The PCE of the OSC increases from 1.8 % to 3.2 % for $0 < \Delta \leq 150\,\text{meV}$ owing to increases in J_{sc} and FF with Δ. PCE decreases when Δ increases due to a reduction in exciton dissociation. At $\Delta = 0\,\text{eV}$, PCE is only 2.0 %, which is close to the reference value.

The existence of Δ in the HOMO-LUMO gap at the interface can partially restore FF and V_{oc} in contrast to device simulations at $\sigma_{int} = \sigma_{ext} = 50\,\text{meV}$ (see Table 4.3). $\Delta = 100\,\text{eV}$ can partially restore J_{sc} ($9.1\,\text{mA}\,\text{cm}^{-2}$ with Δ compared to $10.1\,\text{mA}\,\text{cm}^{-2}$), but too large Δ can be detrimental to photocurrent generation. Mixed phases can also have an influence on optical absorption owing to a change in the optical gap, however this is outside the scope of this study.

4.3.3 Role of Off-diagonal Disorder

The primary goal of improving the working mechanism of Bulk Heterojunction OSCs is to regulate the charge carrier interaction at the electron-donor interface as well as charge separation. The generation of charge carriers and their transmission to the respective electrodes has been quite efficient, as evident by an internal quantum internal efficiency of 100 percent [265], although low V_{oc} remains a key issue for increased efficiency in OSCs. Diluted donor organic solar cells have also been investigated in order to overcome the trade-off between J_{sc} and V_{oc} in order to achieve efficient device performance [38, 116]. There is now a significant push to investigate the impact of energy disorder [266] , charge delocalization [267] , and entropy [268] as important variables determining efficient exciton dissociation. For practical device applications, the contribution of diagonal (energetic) and off-diagonal (structural) disorder to charge transport is most important. Diagonal or energetic disorder refers to the distribution of hopping site energy levels in amorphous aggregates, whereas off-diagonal or structural disorder refers to the distribution of amorphous aggregates in terms of intermolecular distance and relative orientation between neighboring molecules [269]. It is a widely studied that energetic disorder limits charge carrier mobility [185]. When considering structurally disordered systems, diagonal and off-diagonal, both kinds of disorder are commonly utilized [269]. Off-diagonal disorder describes variations in the coupling of transport molecules, while on-diagonal disorder describes variation in one-site parameters (energies of electronic atom levels, random magnetic or electric field on the atom, etc.).

The influence of energy disorder and delocalization on hopping transport of electron-hole pairs at organic surfaces has been explored by Athanasopolus et al. [266]. The charge transport across a disordered lattice with on-diagonal as well as off-diagonal disorder between the two sites was discussed using the Monte Carlo approach in another work by Bässler [20]. The role of energetic disorder and the nearest neighbor hopping mechanism with localized particles has been demonstrated by numerous numerical simulations. However, research into off-diagonal disorder in the case of delocalized particles needs further insight. Using our previously established kMC model [185] , we explore the combined influence of interface disorder and off-diagonal disorder on the device properties of bulk heterojunction OSC. As shown in Fig.1, the model is configured for a 50 x 50 x 50 nm device structure with a 1 nm spacing and periodic boundary conditions in the x and y directions. This study shows that V_{oc} and recombination efficiency are strongly influenced by interface and off-diagonal disorders. Charge hopping mechanism is implemented by using Miller Abraham hopping model [82] as

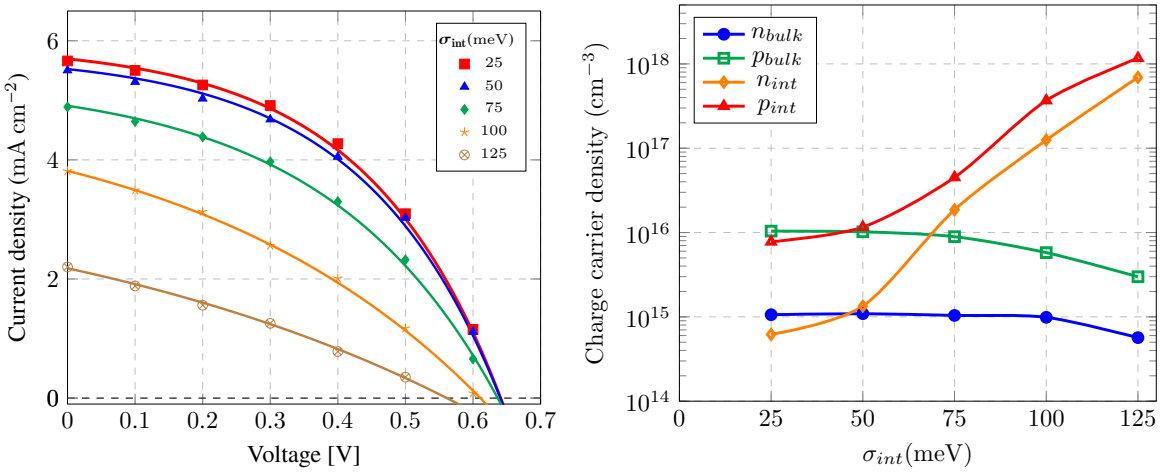

Figure 4.6: (a) *J-V* characteristics and (b) Charge carrier density of the OSC with different σ_{int} at $\sigma_{\text{bulk}} = 50\,\text{meV}$ and $\Sigma = 0$. Solid lines in (a) show fits obtained by the Shockley equation.

$$v_{i\to j} = v_0 \exp\left(-2\gamma r_{i\to j}\right) \begin{cases} \exp\left(-\frac{(E_j - E_i)}{k_B T}\right) & \text{for} \quad E_j \geq E_i \\ 1 & \text{for} \quad E_j \leq E_i \end{cases}, \tag{4.8}$$

where v_0 is the hopping rate, γ is inverse localization constant, $r_{i\to j}$ is the hopping distance and E_i is the energetic landscape modelled by equation 4.4 with energetic disorder E^σ is modelled using literature [20, 227]:

$$g(E) = \frac{N}{\sigma\sqrt{2\pi}} \exp\left(\frac{-(E - E_i^0)^2}{2\sigma^2}\right) \tag{4.9}$$

After a normalized Gaussian distribution, the disorder for each site i is chosen separately. Aside from on-diagonal disorder (Eq. 4.9), our model also accommodates for off-diagonal disorder by assuming $\Gamma_{i\to j} = 2r_{i\to j}$ from equation. 4.8. Where $\Gamma_{i\to j}$ is the random function for each site using a Gaussian distribution and a standard deviation $\delta\Gamma$ of width Σ [270]. This Σ occurs as a result of random variations in intersite coupling between the molecules.

First, we compute the effect of interface disorder on device characteristic parameters and electron density at the interface n_{int}, in the bulk n_{bulk}, hole density at the interface p_{int} and in the bulk p_{bulk}. Figure 4.6a shows the *J-V* characteristic curve for $\sigma_{\text{int}} \in \{25,\ 50,\ 75,\ 100,\ 125\}\,\text{meV}$ and a fixed bulk disorder. $\sigma_{\text{int}} = 25\,\text{meV}$ represents minimum disordered interface while that of 125 meV shows the strongly disordered interafce. Figure 4.6b visualizes the corresponding charge carrier densities at the interface ($n_{\text{int}}/p_{\text{int}}$) and within the bulk ($n_{\text{bulk}}/p_{\text{bulk}}$). In the second part of the analysis, the effect of off-diagonal disorder on device properties and average electron and hole densities at

	σ (meV)	V_{oc} (V)	J_{sc} (mA cm^{-2})	FF (-)	PCE (%)	η_{rec}(%)	η_{gem}(%)
σ_{int}	25	0.64	5.7	0.46	1.67	0.65	99.56
	50	0.64	5.52	0.45	1.61	3.26	97.63
	75	0.63	4.91	0.42	1.29	13.65	94.50
	100	0.61	3.81	0.34	0.79	30.97	77.33
	125	0.56	2.18	0.30	0.36	56.99	57.02

Table 4.4: Device characteristics (V_{oc}, J_{sc}, FF, PCE) of OSC with different σ_{int}, σ_{bulk} = 50 meV and $\Sigma = 0$.

the interface and in the bulk is investigated. As σ_{int} approaches ≥ 75 meV, the average n_{int}/p_{int} surpass the average n_{bulk}/p_{bulk} due to strong coulomb binding energies. As the σ_{int} rises, so does the number of sites with low level energy; these energy levels tend to function as local trapping sites, allowing charges to collect in these levels, resulting in increased charge densities.

For an interface disorder of 25 meV, the bulk densities overcome the interface densities, while at $\sigma_{int} = \sigma_{bulk} = 50$ meV, the averge charge carrier densities are almost teh same. At $\sigma_{int} = 100$ meV, the electron and hole density at the interface is calculated to be 1.2×10^{17} cm^{-3} and 3.7×10^{17} cm^{-3}, respectively, whereas the bulk density is 9.8×10^{14} cm^{-3} and 5.7×10^{15} cm^{-3}. The equivalent electron and hole densities at considerably higher $\sigma_{int} = 125$ meV are 6.9×10^{17} cm^{-3} and 1.1×10^{15} cm^{-3} at the interface and 5.6×10^{14} cm^{-3} and 2.9×10^{15} cm^{-3} in the bulk, as shown in Figure 4.6b. Charge carriers are more evenly distributed and almost uniform in respective phases when the interface disorder is smaller. Due to the flat energetic landscape, the charges are generated at the interface and then move away. The role of interface energetics is less prominent at lower σ_{int}. As a result of the increased interface densities at high σ_{int}, the maximum Voc drops from 0.64 V at 25 meV to 0.64 V at 25 meV interfacial disorder, as seen in Fig 1. J_{sc} also drops from 5.7 mA cm^{-2} to 2.1 mA cm^{-2}. The FF and PCE both follow the same decreasing trend, as can be seen, with the device exhibiting virtually resistive behavior at maximum $\sigma_{int} = 100$ meV (Figure 4.6a). Maximum V_{oc} and PCE are attained at $\sigma_{int} = 25$ meV. The overview of device characteristic parameters is shown in Table 4.4.

Figure 4.7 visualizes the effect of off-diagonal disorder (ranging from 0 to 2) on the device performance parameters. As average charge densities are computed at $\sigma_{int} = \sigma_{bulk} = 50$ meV, Σ has no effect on them. Off-diagonal disorder, on the other hand, has significant role in the device performance parameters. Because increasing Σ affects the intersite distance in the material, affecting the molecule coupling, the recombination yield drops considerably for $\Sigma \geq 1$. This also leads to a 6 % increase in FF and a 7 % increase in PCE. The short circuit current J_{sc} slightly increases by 1 %, whereas V_{oc} falls by ~ 3 %. The maximum PCE is attained at $\Sigma = 2$. This demonstrates that, even in the presence

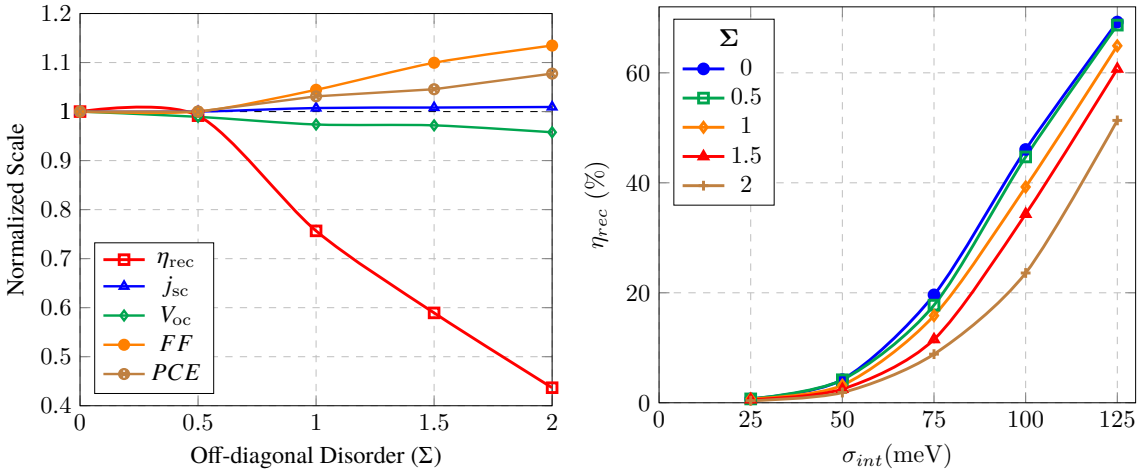

Figure 4.7: (a) Device performance parameters at $\sigma_{\text{int}} = \sigma_{\text{bulk}} = 50\,\text{meV}$ for different Σ, (b) Recombination yield at

of high structural disorder, our model represents efficient charge carrier separation in the device.

Finally, when the combined effect of the interfacial and off-diagonal disorders is examined, we can infer that the interfacial disorder outperforms the off-diagonal disorder in defining device characteristic performance. The J-V characteristic curves for $25\,\text{meV} \leq \sigma_{\text{int}} \leq 125\,\text{meV}$ at $\Sigma = 1$ and 2 are shown in Figure 4.8a. It can be shown that the open circuit voltage has not changed significantly in either instance, ranging from 0.55 V for higher $\sigma_{\text{int}} = 125\,\text{meV}$ to 0.62 V for lower $\sigma_{\text{int}} = 25\,\text{meV}$. This was equally true for the V_{oc} without off-diagonal disorder, as seen in Figure 4.6a. This demonstrates that our simulation model has efficient exciton dissociation even at higher Σ. Figure 4.8b shows the average charge carrier densities at the interface and in the bulk. Charge carrier densities for both off-diagonal and interfacial disorder are roughly the same upto $\sigma_{\text{int}} = 50\,\text{meV}$. While for $\sigma_{\text{int}} \geq 75\,\text{meV}$, the charge carrier densities at the interface and in the bulk for both electrons and holes follow the same pattern for $\Sigma = 1$ and 2. To put it another way, the bulk densities stay roughly constant while the interface densities overcome the bulk densities. This means that the charges accumulated at the interface account for the overall charge density in the active layer. Higher the interfacial disorder, higher will be the charge accumulation. The function of interface energetics becomes more significant at increasing σ_{int}. If we increase Σ, as seen in Figure 4.7b, the recombination efficiency significantly increases. The efficiency rises considerably as we go beyond $\sigma_{\text{int}} \geq 50\,\text{meV}$, from 4 % at 50 meV to 68 % at 125 meV. However, as we move from $\Sigma = 0$ to 2, the recombination yield drops from a high of 68 % $\Sigma = 0$ to 51 % $\Sigma = 0$. This is due to the fact that increased structural disorder affects the coupling force between molecules inside the material.

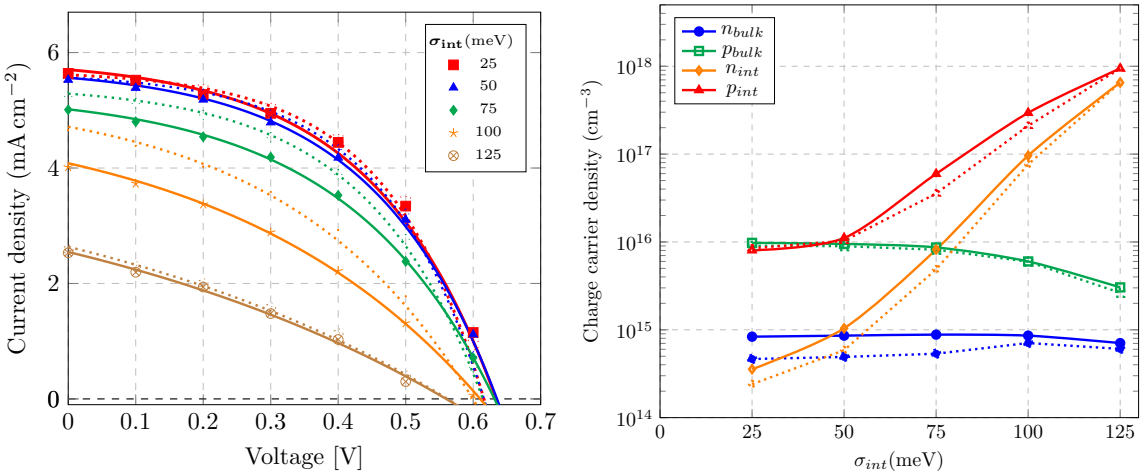

Figure 4.8: (a) J-V characteristics and (b) Charge carrier density of the OSC with different σ_{int} and $\Sigma = 0$ at $\sigma_{\text{bulk}} = 50\,\text{meV}$. Solid lines in (a) show fits obtained by the Shockley equation. The smooth lines shows the analysis for $\Sigma = 1$ and dotted line shows for $\Sigma = 2$

4.4 Conclusion

In conclusion, this study provides an analysis of the impact of the interface and extraction layer energetics on the device performance of bulk-heterojunction organic solar cells using kinetic Monte Carlo simulations. The results represent the significant degradation of the device performance with increasing interface disorder. At higher disorder, the interface charge densities exceed the bulk densities, significantly increasing nongeminate recombination owing to tail states in the Gaussian density of states. As a result, the fill factor and short-circuit current density are significantly reduced. For energetic disorder levels less than 100 meV, the interface has little influence on V_{oc}. Our results for varying extraction layer disorder indicate a substantial effect on the maximum achievable V_{oc}, whereas FF and J_{sc} are only slightly affected. The combined effect of the interface and the extraction layer order results in substantially linear J-V characteristics with a low fill factor and PCE. Our findings show that the interface disorder has a more detrimental role than the extraction layer and requires careful optimization.

Furthermore, by increasing the HOMO-LUMO gap at the D:A interface, we investigate the effect of energy cascades at the D:A interface on device performance. We demonstrate that energy cascades, which are frequently assumed in mixed phases, may overcome the negative impacts of the interface disorder on fill factor and PCE. For a small increase in the HOMO-LUMO gap, J_{sc} increases significantly. However, the rise in current density is restricted by a decrease in exciton dissociation. While the energy cascade promotes charge separation, it also functions as an energy barrier for exciton diffusion from the bulk to the mixed interface. Overall, the effect on device efficiency is advantageous for

device performance throughout a large range of Δ. This might explain why, despite the presence of amorphous phases at the donor:acceptor interface, conventional BHJ solar cells show reasonable performance.

Finally, as the structural order of the device film evolves into an amorphous state with increased on-diagonal disorder, we infer that increasing interfacial disorder is not advantageous for efficient device performance. With the help of experimental investigations, this loss in device performance may be prevented by choosing materials with greater molecular packing and less flexibility. The molecular coupling gains directionality as a result of the off-diagonal disorder. It has an impact on the characteristics of a material with varying crystallographic orientations and intersite distance. The geometry of the system, with dependence of both the distance and orientation on the component molecules, causes the off-diagonal disorder. This model helps to analyze a system with strong delocalization.

5 Charge Tansport and Impact of Morphology in Dilute Donor Organic Solar Cells

Fullerene-based dilute donor organic solar cells with a minute donor content provide a promising alternative to overcome the trade-off between j_{sc} and V_{oc} by allowing a high open-circuit voltage, theoretically being limited by the electrical bandgap of the acceptor molecules. The main challenge of such an architecture is to realize hole extraction pathways. Due to the reduced donor content, there are negligible percolation paths toward the contacts for the photogenerated holes. Charge transport toward the contacts can either happen by tunneling between the diluted polymers, hole back transfer to the acceptor, and rarely percolation to the contacts along polymers. However, the detailed morphology of the polymer chain network strongly controls which is the dominant mechanism and its impact on solar cell performance. We present a kMC study of the impact of the polymer morphology on the performance of organic solar cells with a donor content of 1 wt.% . The photocurrent generation is investigated for different offsets between the acceptor and donor highest occupied molecular orbitals (HOMO) and different morphologies. Due to the low donor concentration used, we only consider hole back-transfer and percolation along polymer networks. We analyze three different morphologies: isolated polymer chains (SAW), polymer chain networks touching the contacts (NTC), and polymer networks not touching the contact (NNTC). Our results show that even a minor amount of polymers forming percolation paths to the contact is sufficient to generate a substantial photocurrent and keep a high V_{oc}. Polymer chains with longer chain length provide substantial short-circuit current from the hole back-transfer to the acceptor even at high HOMO offsets of 0.6 eV.

The content of this chapter is adapted with permission from K. Hussain, W. Kaiser,and A. Gagliardi, "Effect of Polymer morphology on dilute donor organic solar cells", *The Journal of Physical Chemistry C*, vol. 124, no. 6, pp. 3517–3528, 2020.

5.1 Background

In recent years, there has been a great effort to develop and optimize the photo-active material. A large set of organic semiconductor have been exploited to engineer the optimal charge separation and transport properties. The introduction of non-fullerene acceptors has also motivated the research activities to enhance the performance of OSCs further. Many additional strategies have been used to improve the device efficiency and stability: new semiconductor materials [271], ternary blending [272], device interface engineering [273], choice of solvent additives [274–276], thermal annealing [277], polymer self aggregation and crystallinity [278]. Improved materials and blend control have led to record efficiencies beyond 18%. It can thus be expected that further material synthesis and blend morphologies can lead to further improvement in the efficiency and stability of organic solar cells [11, 279].

One major research trend focuses on an alternative to the traditional bulk- heterojunction (BHJ) morphology, which is the standard morphology for high-efficiency OSCs. BHJs are composed of a complex intermixing of a donor (D) and an acceptor (A) semiconductor. The D:A blend obtains phase separation distances in the range of singlet diffusion lengths to improve the exciton separation yield and to avoid exciton decay [99]. Due to the large interface area, high short-circuit current densities and internal quantum efficiencies close to 100 % have been observed [265], but the open-circuit voltage V_{oc} is very low and mainly controlled by the charge transfer (CT)-state which is present at the D:A interface [100, 280]. A drawback of the standard BHJ morphologies is the substantial recombination at the interfaces [14] and charge extraction at the "wrong" electrodes [281, 282]. Besides, low-temperature processing technologies such as solution processing can only provide limited control of the nanostructured morphology.

In standard BHJ OSCs, optimal tuning of donor and acceptor molecular orbital energy levels is needed to optimize the exciton dissociation; however, it comes with the trade-off of losses in the open-circuit voltage. Donors with lower bandgap allow a large absorption of the solar spectrum and enhance the j_{sc}, however, they show a significant reduction in the quasi-Fermi level splitting of the charge carriers, thus limiting the V_{oc}. Fullerene-based dilute donor organic solar cells with a minute donor content provide a promising alternative to overcome the trade-off between j_{sc} and V_{oc} by allowing a high open-circuit voltage, theoretically being limited by the electrical bandgap of the acceptor molecules [283–286]. The V_{oc} in such a dilute framework is supposed to be dominated by the Schottky junction between the acceptor and the anode and can be increased due to the reduced recombination of the free charge carriers [116, 117, 284]. Larger V_{oc} was initially observed in intrinsic fullerene-based devices; however, this comes with a low short-circuit

current [287]. Adding a minute donor content $5 - 9\,\text{wt.\%}$ showed a multifold increase in the short-circuit current. This increase is predominantly considered to arise from an improved exciton dissociation at D:A interface, thus increasing the overall device performance [117, 288, 289].

Important questions within the dilute donor OSCs are (i) what is the main aspect controlling for an increased V_{oc} and (ii) what is the charge transport mechanism for the hole extraction? Several studies have investigated these questions. The V_{oc} was reported to increase for a reduced D:A interface area within BHJ morphologies due to reduced non-radiative recombination [284]. On the other hand, Zhang *et al.* showed that the performance in OSCs with reduced donor content is strongly dependent on the presence of a Schottky barrier between the acceptor and the anode. [286]

Melianas *et al.* studied the generation of the photocurrent for a $4-7\,\text{wt.\%}$ dilute donor without consistent percolation pathways within the donor, forming a fully dispersed and discontinued network. [21] For such low concentration, they suggested hole transfer to occur by long-range tunneling between donor molecules with an average tunneling distance of about 4 nm. However, for donor concentrations below 4 wt.%, in particular at $\sim 1\,\text{wt.\%}$ and below, the proposed tunneling mechanism is unlikely. Although, a substantial photocurrent can be observed even in systems with 0.1% donor concentration [116]. Another proposed mechanism of the hole transport in dilute donor OSCs has been presented by Spoltore *et al.* [290]. Their study suggests that the hole transport is accomplished by long-range Fowler-Nordheim tunneling through several fullerene molecules at $\sim 6\,\text{mol\%}$ of donor content. Collado-Fregoso *et al.* studied the performance of BHJ morphologies with a systematic variation of the energetics through chemical modification. [291] They demonstrated a strong sensitivity of the V_{oc}, j_{sc}, and fill factor (FF) depending on the donor used. This, in turn, indicates that the performance of the system is a function of the energetics of the donor-acceptor morphology. Albes *et al.* observed a good agreement between experiment and theory for a fullerene-based OSC with a 1 vol% concentration of P3HT assuming that holes escape the donor chains due to a high Coulomb repulsion between holes within the donor chains [116]. Additionally, due to the less ordered structure compared to the BHJ morphology, the change in the HOMO level for the strongly disordered donor chains is considered to enable the efficient back transfer. Other studies associate the charge transport with the formation of donor columns [292], hole extraction via the acceptor phase under operating conditions [293], or continuous percolation paths by planar donor molecules [294].

The primary remaining mechanisms of the current generation are the back-transfer of holes [116], and percolation as in the case of BHJ morphologies [295]. One powerful way to distinguish between both is given by kinetic Monte Carlo (kMC) models. [116, 296]

Detailed polymer morphologies can be generated within the fullerene matrix with any desirable structure. In a previous study, [116] the donor (P3HT) polymer chains were distributed in a fully dispersed arrangement. The generation of charge carriers in such an architecture is assumed to occur in the same way as in BHJs [117]: excitons generated in the acceptor diffuse to the D:A interfaces and are dissociated by hole-transfer towards the donor. As Albes *et al.* argued, a substantial photocurrent can arise caused by the Coulomb repulsion between holes accumulating on the donor chains, which then leads to a hole back transfer to the fullerene matrix. [116] However, in the mentioned study, fully isolated polymer chains were considered, which may not be the case within dilute donor cells. Moreover, the question arises on how polymer chains that provide a percolation to the anode modify the observations.

Within the recent years, experimental techniques have been developed to study and to control the morphology formation and the alignment of polymers. Molina-Lopez and coworkers have tuned the crystal packing of solution-coated thin films by using an electric field during processing [297]. This method led to a threefold improvement in mobilities within diketopyrrolopyrrole with stronger anisotropy of charge transport [298]. Similar methods have been applied to tailor the nanoscale morphology within polymer:fullerene blends with enhanced device performance. [299] The electric field is affecting both the morphology and the crystal orientations. Also annealing and the cooling rate have been shown to modify polymer stratification and interfacial structure. [300] Fibrous morphologies with improved charge transport have been engineered within polymer/fullerene blends by a modification of the solubility of the polymer and the fullerene using the additive 1,8-diiodooctane (DIO). [301,302] Additionally, improved fine-tuning of the polymer aggregation have been achieved within molecular engineering strategies using compact bulky side-chains. [303] Similar strategies might be of interest to control the polymer network within dilute donor solar cells.

In this work, we present a kMC study of the effect of the polymer morphology in dilute donor organic solar cells. We focus on the effect of different polymer chain lengths and different polymer networks to analyze the dominant mechanism for the generation of the photocurrent. First, we analyze the impact of the polymer chain length on the photocurrent by hole back transfer from the donor to the fullerene matrix. Three different morphologies are then generated to determine the impact of the polymer arrangement on the solar cell characteristics. We distinguish between (i) entirely dispersed and unconnected polymers, (ii) polymer networks that are not connected to the contacts, and thus provide no percolation paths, (iii) polymer networks connected to the contacts. Finally, a comparison to the standard BHJ morphology is reported.

5.2 Computational Model

To analyze the photocurrent generation by hole back transfer and the subsequent charge transport through the fullerene phase, a kinetic Monte Carlo (kMC) method has been implemented. kMC is a powerful method to investigate the charge transport in organic semiconductors [20, 28, 33, 304], and full solar cell device characteristics [26, 31, 282, 296]. The kMC method used, accounts for exciton generation, exciton and charge carrier dynamics. Generation of excitons is modelled using a z-dependent generation rate $G(z)$, which is determined using a transfer matrix method [203]. Exciton diffusion is implemented using a random walk model [24]. A constant exciton decay rate $a_{\mathrm{dec}} = \tau_{ex}^{-1}$ given by the inverse of the lifetime τ_{ex} is used. Exciton dissociation is initiated at the interface if the target site isn't occupied by using constant dissociation rate a_{exd}. Once the exciton dissociation occurs, we place an electron in the appropriate acceptor and a hole in the donor site. The generated charge carriers can now move through a hopping mechanism under the influence of the energetic disorder, the electric field and the Coulomb potential caused by other charges. Hopping between neighboring sites i and j is described based on the Miller-Abrahams hopping mechanism [82]:

$$a_{i\to j} = a_0 \exp\left(-2\gamma r_{i\to j}\right) \begin{cases} \exp\left(-\frac{\Delta E_{i\to j}}{k_{\mathrm{B}}T}\right) & \text{for} \quad \Delta E_{i\to j} > 0 \\ 1 & \text{for} \quad \Delta E_{i\to j} \leq 0 \end{cases}, \tag{5.1}$$

where i and j are the neighbor sites, $r_{i\to j}$ is the hopping distance between the sites, a_0 is the attempt-to-hop rate, γ is the inverse localization length, and $\Delta E_{ij} = E_j - E_i$ is the energetic difference between the system states if the charge is at site i or at site j. The potential energy at site i is calculated as [14]

$$E_i = E_i^0 + E_i^\sigma + E_i^C + E_i^F \,, \tag{5.2}$$

where E_i^0 is the average energy level of the molecular orbital, E_i^σ is the energetic disorder chosen from a Gaussian distribution of variance σ^2, E_i^C is the Coulomb energy, E_i^F is the energy from external potential.

Recombination of the charges on neighboring sites can take place with a rate a_{ehr}. For this particular analysis, a constant $a_{\mathrm{ehr}} = 1 \times 10^9\,\mathrm{s}^{-1}$ is used. Charge recombination accounts for major losses mechanism in organic solar cells apart from exciton decay. Recombination allows the particle to be lost and make respective sites free of charges again. Charges next to the extraction layer can be collected by electron collection rate a_{elec} and a_{holc}, leading to generation of photocurrent. In this particular work, we use two mechanisms for the generation of photocurrent: (i) hole back transfer from the isolated

polymer chains into the fullerene matrix; (ii) percolation along polymer chains. The onset for hole tunneling between donor molecules has been shown to occur at $5.3-3.4\,\text{nm}$ for α-6T, corresponding to a molar weight percentage of $1.5\,\%$ to $5.7\,\%$ [21]. However, Albes *et al.* showed that even for donor concentrations as low as 0.1 wt% of F4-TCNQ a significant photocurrent is produced [116].

Our model consists of simulation box of fullerene molecules ($PC_{71}BM$) with a volume 50 x 50 x 50 nm between anode and cathode contacts [116]. The donor molecules are then distributed in the form 180, 48, 30 ans 18 polymer chains with varying chain length of 10 nm, 40 nm, 70 nm, and 100 nm, respectively, to represent the fixed $\sim$ 1 wt% of donor molecules in the active layer [305]. We use th epivot algorithm in the form of self avoiding random walk (SAW) to generate the polymer chains [306]. The algorithm allows polymer chains to be isolated from each other. Figure 5.1 shows the morphology generation at different polymer chain lengths using the SAW. We investigate four polymer chain lengths to study the effect of polymer chain length on the current generation.

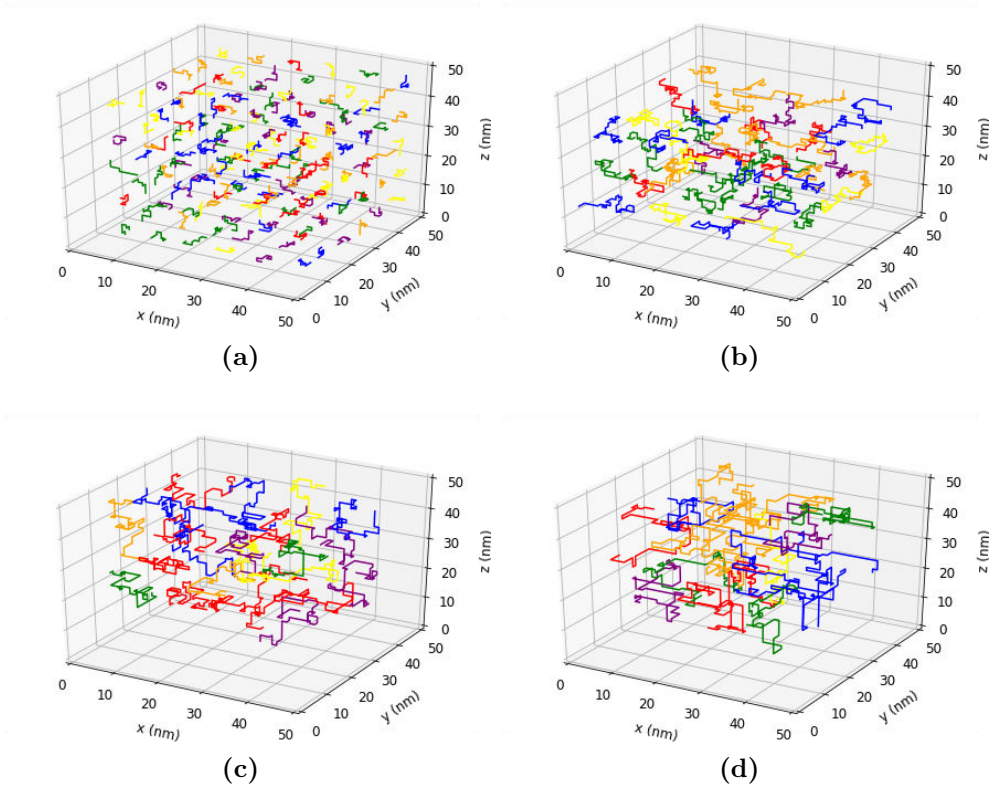

Figure 5.1: Chain morphologies generated by the self avoiding random walk (SAW) algorithm at polymer chain lengths of (a) 10 nm, (b) 40 nm, (c) 70 nm and (d) 100 nm.

In order to analyze the effect of different polymer morphologies on the current generation in the device, we further model three different morphologies: (i) Isolated polymer chain network without percolation paths towards the contacts (SAW); (ii) polymer chain

network with percolation paths towards contacts being allowed to occupy sites next to anode or cathode, termed as network touching the contacts (NTC); (iii) polymer chain network with percolation pathways, but not touching the contacts, termed as network not touching the contact (NNTC). In all three cases, donor molecules are distributed in the form of 18 polymer chain lengths with length of 100 nm as shown in Fig. 2.

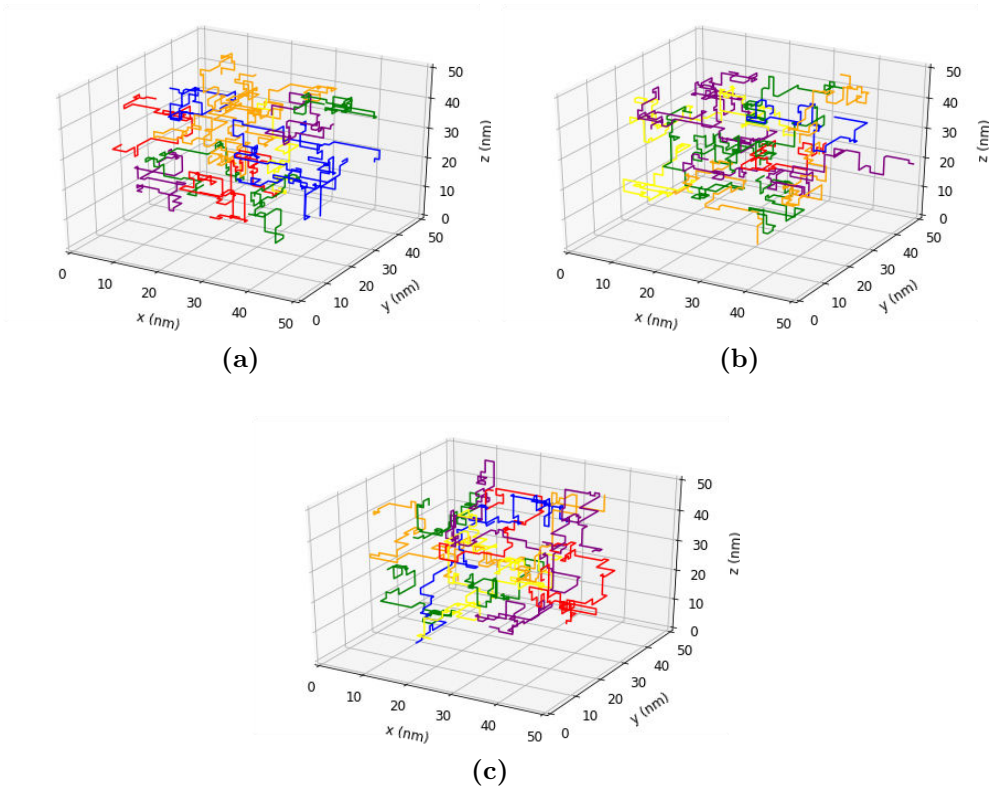

Figure 5.2: Morphology generation for a) SAW, (b) NNTC and (c) NTC at polymer chain length of 100 nm.

The performance of all the morphologies and different chain lengths is analyzed for different HOMO energy level offsets by keeping HOMO level of fullerene constant and varying the HOMO level of the donor. The major advantage of kMC is that, it keeps the track of time-dependent trajectories of all the charges. The characteristic parameters can then be computed and averaged over time using these trajectories [307]. The net hole-escape current density $j_{\mathrm{esc}}^{\mathrm{h}}$ is calculated by the net number of holes N_{h} leaving the donor region per D:A interface area A of the heterojunction and the simulation time t_s [116]:

$$j_{\mathrm{esc}}^{\mathrm{h}} = \frac{q \cdot N_{\mathrm{h}}}{A \cdot t_{\mathrm{s}}} \,. \tag{5.3}$$

During the simulation time t_{s}, the kMC model counts the number of charges participating in geminate $N_{\mathrm{rec}}^{\mathrm{gm}}$ and nongeminate $N_{\mathrm{rec}}^{\mathrm{ngm}}$ recombination based on the origin of

recombination partners. This helps to calculate recombination current density at the interface. If a recombination occurs, we differentiate between geminate recombination, if both charge carriers origin from the same exciton, and non-geminate recombination, if they origin from different excitons. The recombination ratio of the photogenerated charges is calculated as

$$\eta_{\mathrm{rec}} = \frac{N_{\mathrm{rec}}^{\mathrm{ngm}} + N_{\mathrm{rec}}^{\mathrm{gm}}}{2 \cdot N_{\mathrm{gen}}}\,, \tag{5.4}$$

where N_{gen} is the number of excitons separated into electrons and holes during t_{s}. The volume recombination rate is then defined by

$$R = \frac{N_{\mathrm{rec}}^{\mathrm{ngm}}}{t_{\mathrm{s}}}\,. \tag{5.5}$$

The used parameters are summarized in Table 5.1 and 5.2.

Parameter	Symbol	Values	Reference
Size in x-direction	l_{x}	50 nm	-
Size in y-direction	l_{y}	50 nm	-
Size in z-direction	l_{z}	50 nm	-
Lattice constant	l_{c}	1 nm	-
Inverse localization length	γ	$2\,\mathrm{nm}^{-1}$	[31]
Relative permittivity	ϵ_{r}	3.5	[308]
Energetic disorder	σ	30 meV	-
Cathode work function	ϕ_{cathode}	−4.30 eV	[308]
Anode work function	ϕ_{anode}	−5.50 eV	-
Acceptor (PCBM) HOMO level	$E_{\mathrm{A}}^{\mathrm{HOMO}}$	−6.0 eV	[31]
Acceptor (PCBM) LUMO level	$E_{\mathrm{A}}^{\mathrm{LUMO}}$	−4.25 eV	[31]
Donor (P3HT) HOMO level	$E_{\mathrm{D}}^{\mathrm{HOMO}}$	[-5.2 to -5.8]eV	-
Donor (P3HT) LUMO level	$E_{\mathrm{D}}^{\mathrm{LUMO}}$	−3.0 eV	[31]
Temperature	T	298 K	-
Simulation time	t_{s}	1 ms	-

Table 5.1: System Setup parameters used in kinetic Monte Carlo simulations.

Parameter	Symbol	Values	Reference
Electron-hole recombination	a_{rec}	$1 \times 10^{9}\,\mathrm{s}^{-1}$	[116]
Exciton hopping	a_{exh}	$2 \times 10^{11}\,\mathrm{s}^{-1}$	[116]
Exciton decay	a_{exd}	$2 \times 10^{9}\,\mathrm{s}^{-1}$	[116]
Exciton Seperation	a_{exs}	$2 \times 10^{13}\,\mathrm{s}^{-1}$	[116]
Electron attempt-to-hop rate in acceptor	$a^{\mathrm{A}}_{0,\mathrm{eh}}$	$3 \times 10^{12}\,\mathrm{s}^{-1}$	[116]
Electron attempt-to-hop rate in donor	$a^{\mathrm{D}}_{0,\mathrm{eh}}$	$3 \times 10^{12}\,\mathrm{s}^{-1}$	[116]
Hole attempt-to-hop rate in acceptor	$a^{\mathrm{A}}_{0,\mathrm{hh}}$	$6 \times 10^{11}\,\mathrm{s}^{-1}$	[116]
Hole attempt-to-hop rate in donor	$a^{\mathrm{D}}_{0,\mathrm{hh}}$	$6 \times 10^{11}\,\mathrm{s}^{-1}$	[116]
Electron collection	a_{ec}	$1 \times 10^{10}\,\mathrm{s}^{-1}$	[116]
Hole collection	a_{hc}	$1 \times 10^{10}\,\mathrm{s}^{-1}$	[116]

Table 5.2: Rate parameters used in the kinetic Monte Carlo simulations.

5.3 Results and discussion

This section is further devided into two sub sections. In the first subsection, we analyze the impact of varying polymer chian lengths $N \in \{10\,\mathrm{nm},\ 40\,\mathrm{nm},\ 70\,\mathrm{nm},\ 100\,\mathrm{nm}\}$ on photocurrent generation at different HOMO energy levels ΔE_{HOMO} ranging from 0.2 eV to 0.6 eV. In the second subsection, we study the impact of three different polymer morphologies i.e. SAW, NTC and NNTC on photocurrent generation and full jV-characteristics.

5.3.1 Impact of polymer chain length

To provide a realistic image of the working mechanism of our model, three morphologies are created for each of the four chain lengths 10 nm, 40 nm, 70 nm, and 100 nm. Figures 5.3 and 5.4 illustrate the steady-state mean values of the short-circuit and hole escape current densities, respectively. The error bars represent the standard deviation.

The short-circuit current density j_{sc} is representative of the whole device, whereas the hole escape current density j^{h}_{esc} describes the escape properties with respect to the donor-acceptor interface region. Figure 5.4 shows (a) average hole densities and (b) recombination efficiency for all the configurations. We adjust the HOMO level offset from 0.2 eV to 0.6 eV for each setup. It should be noted that, as demonstrated experimentally, the HOMO level inside disordered P3HT is about 0.3 eV deeper than the HOMO level of ordered regioregular P3HT, [116, 262], which represents the shift in the HOMO level offset, considered for this work.

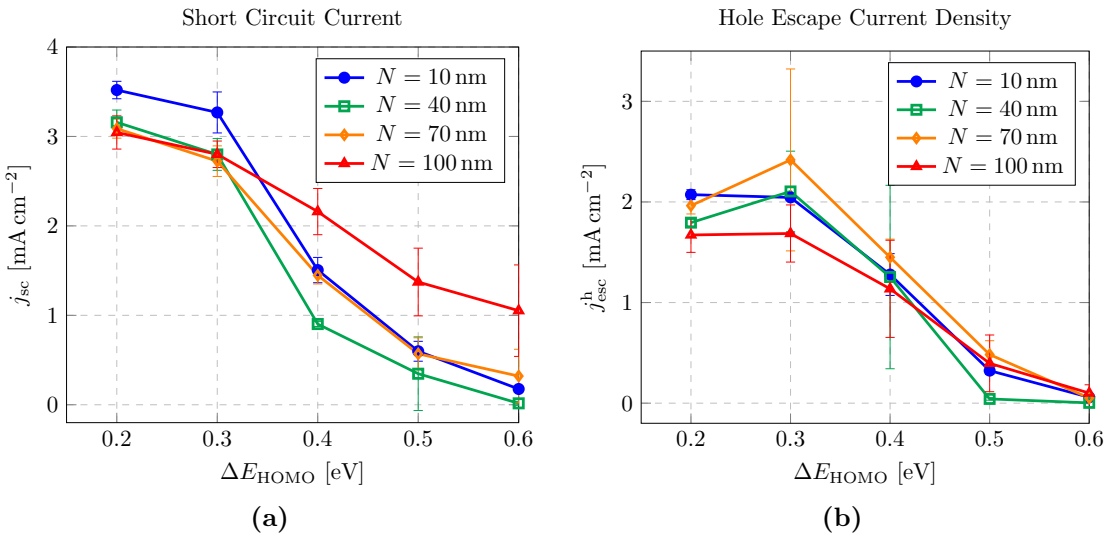

Figure 5.3: (a) Short-circuit current density j_{sc} and (b) hole escape current density $j^{\mathrm{h}}_{\mathrm{esc}}$ at various polymer chain lengths N for different HOMO level offset ΔE_{HOMO}.

We find a substantial j_{sc}, from $3.1\,\mathrm{mA\,cm^{-2}}$ to $3.6\,\mathrm{mA\,cm^{-2}}$ for $N = 10\,\mathrm{nm}$ to $N = 100\,\mathrm{nm}$, respectively towards low ΔE_{HOMO}. Holes escape from the donor through back transfer to the acceptor and travel to the contact, resulting in a significant j_{esc} up to a maximum of $\approx 1.65\,\mathrm{mA\,cm^{-2}}$ for a polymer chain length of 100 nm.A higher amount of short-circuit current and hole escape density is produced for the shorter lengths of 10 nm to 70 nm.

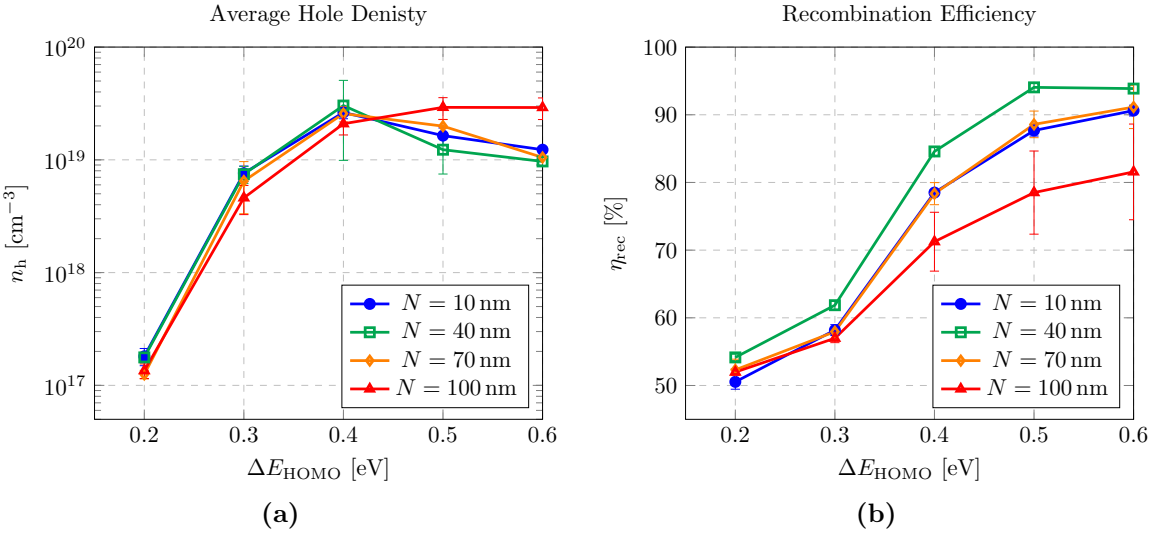

Figure 5.4: (a) Average Hole Density and (b) recombination efficiency at various polymer chain lengths for different HOMO level offset.

We notice an exponential drop in the hole densities in the OSC for $\Delta E_{\mathrm{HOMO}} < 0.4\,\mathrm{eV}$. The reason being, the hole escape occurs as a result of thermally activated Miller-

Abrahams hopping.The escape gets more evident as the rate grows exponentially with the energy barrier to overcome throughout the hopping process. As a result, holes can escape the polymer chains and enter the fullerene matrix. When the offset is reduced to 0.3 eV, the hole density also reduces to $n_h = 7 \times 10^{18}\,\mathrm{cm}^{-3}$. When the HOMO level offset is reduced further to 0.2 eV, a small hole density $n_\mathrm{h} \approx 1 \times 10^{17}\,\mathrm{cm}^{-3}$ is built-up, since the hole escape becomes exceedingly simple at ambient temperature. For this offset, all the charges either recombine at the interface or transferred to the contacts contributing to j_sc.

Due to the large energy barrier for hole escape at a HOMO level offset beyond 0.5 eV, holes are trapped within the isolated polymer chains. This results in high hole densities of up to $n_\mathrm{h} > 3 \times 10^{19}\,\mathrm{cm}^{-3}$ and recombination efficiency of over 90 %. A saturation is observed When all of the polymer sites are filled with holes and no further exciton dissociation is possible. At steady state, electron surround the positively charge polymer chains due to high Coulomb attraction resulting in a high recombination efficiency. The average hole density for smaller polymer chains is around $n_\mathrm{h} \approx 2 \times 10^{19}\,\mathrm{cm}^{-3}$. In the steady-state, a small short-circuit current is obtained as a result of suppressed hole current towards the contacts. The current density drops below $0.5\,\mathrm{mA\,cm}^{-2}$ in short chains with $N \leq 70\,\mathrm{nm}$. A considerably higher current density of $1.05\,\mathrm{mA\,cm}^{-2}$ is observed for the longest chain lengths.

To assess the origin of the efficient hole escape current at low HOMO level offsets, the average electron and hole potentials are analyzed. We plot (a) the molecular orbit energy and coulomb potential ϕ_C and (b) the electron and hole densities as shown in Figure 5.5. We refer to Albes *et al.* [116] for further information on the calculation of coulomb potential. The plots in (a) are extracted along the dashed line shown in the right plot. We observe a minimal Coulomb potential in the donor region of less than 10 meV. The sum of MO energies and the Coulomb potential (solid lines) overlap the molecular orbital energies (dashed lines). We observe a substantial hole density all across the cell despite the low Coulomb repulsion (see Fig.5.5b). This shows that the hole can easily cross the HOMO energy barrier between the donor and acceptor. Most of the time, the Coulomb interaction between the geminate electron-hole pair is enough to create a efficient hole back transfer. We can see a significantly higher hole density in regions of polymer chains.

The current density is higher for lower chain length when $0.2\,\mathrm{eV} \leq \Delta E_\mathrm{HOMO} \leq 0.3\,\mathrm{eV}$. The average distance between the tortuous polymer chains increases for longer chains, when the volume concentration is held constant for each chain length. As a result, fewer excitons dissociate in larger polymer chain length configuration. This in turn gives rise to higher exciton dissociation efficiency for chain length of $N = 10\,\mathrm{nm}$ as compared to

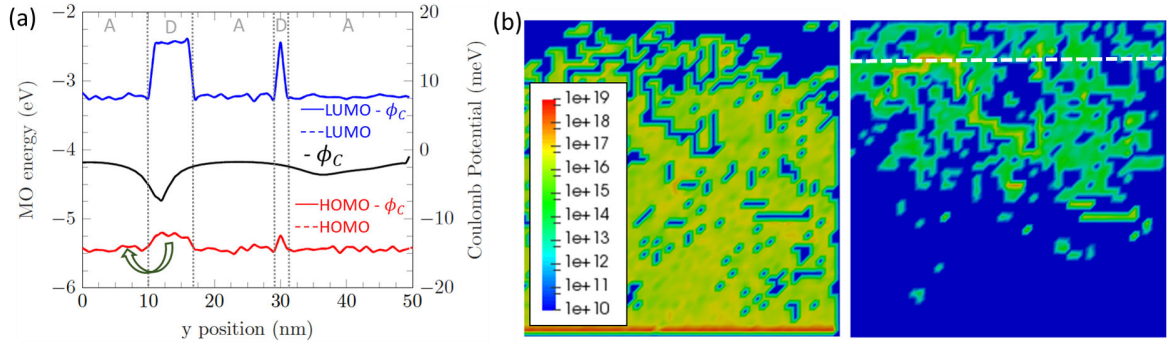

Figure 5.5: (a) Molecular orbital (MO) energies (dotted) and the Coulomb potential (black line), as well as the sum of MO energies and Coulomb potential (b) electron (left) and hole (right) densities. The colorbar shows the density in unit cm^{-3}.

$N = 40\,\mathrm{nm}$ to $N = 100\,\mathrm{nm}$, as shown in Figure 5.6. The current density for $N = 10\,\mathrm{nm}$ to 70 nm drops faster than for the longest polymer chains of 100 nm for $\Delta E_{\mathrm{HOMO}} > 0.3\,\mathrm{eV}$.

Figure 5.7 shows the molecular orbital energies, the Coulomb potential and the charge carrier densities for the polymer chains of length (bottom) 100 nm and (top) 10 nm. The left side of the figure shows MO energies through the active layer and the Coulomb potential (ϕ_{c}). In combination with the charge densities, we can explain the difference in the charge density for long and short chain lengths in terms of the escaping and trapping of the charge carriers from the donor phase. We find a minimum Coulomb potential of $-0.74\,\mathrm{eV}$ at the position of the polymer chains for longer polymer chain lengths (Fig. 5.7a). We observe an enhanced Coulomb potential of up to $-0.1\,\mathrm{eV}$ outside of the chains, i.e. in the acceptor area. As a result, the effective energy barrier is reduced significantly, and holes have a larger chance of escaping. Furthermore, as holes leave the chain, the shape of the Coulomb potential, particularly the repulsion from the chain's large hole density of $> 10^{19}\,\mathrm{cm}^{-3}$, induces a substantial driving force away from the chain.

We also observe a substantial Coulomb potential down to $-0.14\,\mathrm{eV}$ for a shorter chain length of 10 nm at high ΔE_{HOMO}, as shown in Figure 5.7c and d), shifting the donor HOMO level downwards in energy. However, we can notice that, the distance between the Coulomb potential within and outside of the chain is reduced with respect to longer chains. A significant Coulomb repulsion arises as a result of smaller distance between short polymer chains within this model, and if all holes fill the chains. The interaction between the holes of nearby chains, on the other hand, significantly lowers the difference between the Coulomb potential on and off the chain, resulting in a lower driving force for hole escape. As a result, the current density is reduced significantly.

Now we study the effect of chain length on device performance. For both 10 nm and 100 nm chain lengths, jV-characteristics are computed at HOMO levels offsets of 0.2 eV and 0.5 eV, respectively. The typical jV-curves for $\Delta E_{\mathrm{HOMO}} = 0.2\,\mathrm{eV}$ and $\Delta E_{\mathrm{HOMO}} =$

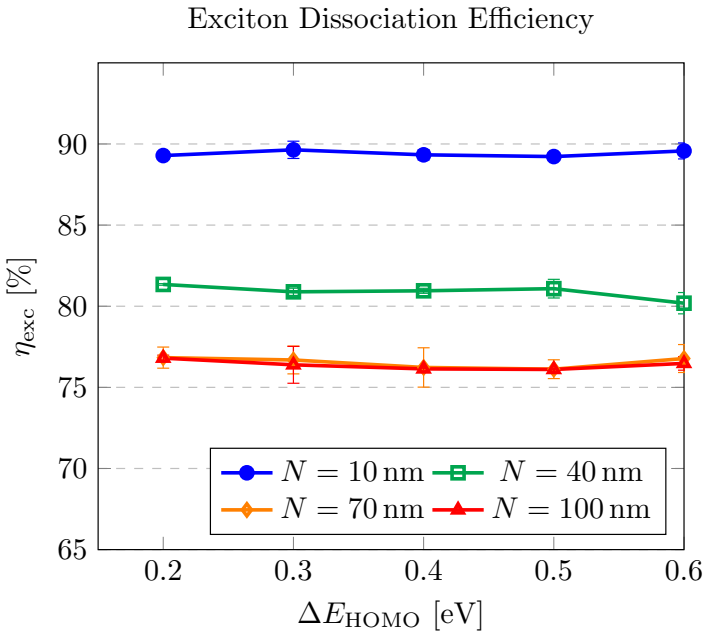

Figure 5.6: Exciton dissociation efficiency for the polymer chain lengths of 10 nm, 40 nm, 70 nm and 100 nm

0.5 eV, respectively, are shown in Figure 5.8(a) and (b). The characteristic performance parameters are summarized in Table A.9. For low HOMO offset, holes can easily escape from the polymer chain and be effectively collected at the contacts. A slightly higher power conversion efficiency (PCE) of 0.71% is observed for $N = 10\,\mathrm{nm}$ compared to 0.69% for $N = 100\,\mathrm{nm}$.

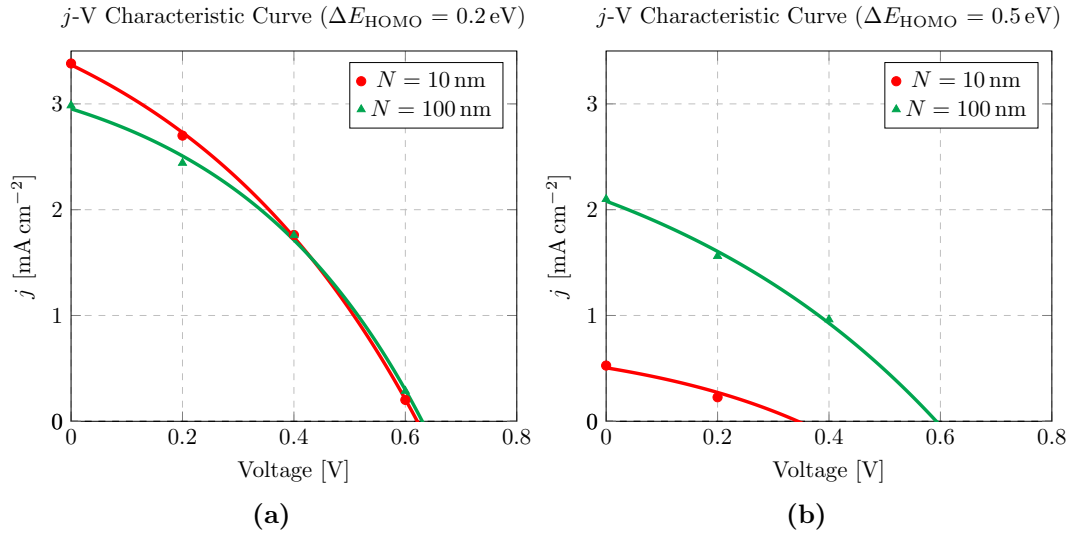

Figure 5.8: jV-characteristics at (a) 0.2 eV, (b) 0.5 eV for polymer chain lengths of 10 nm and 100 nm. Solid lines show fits obtained using the Shockley equation.

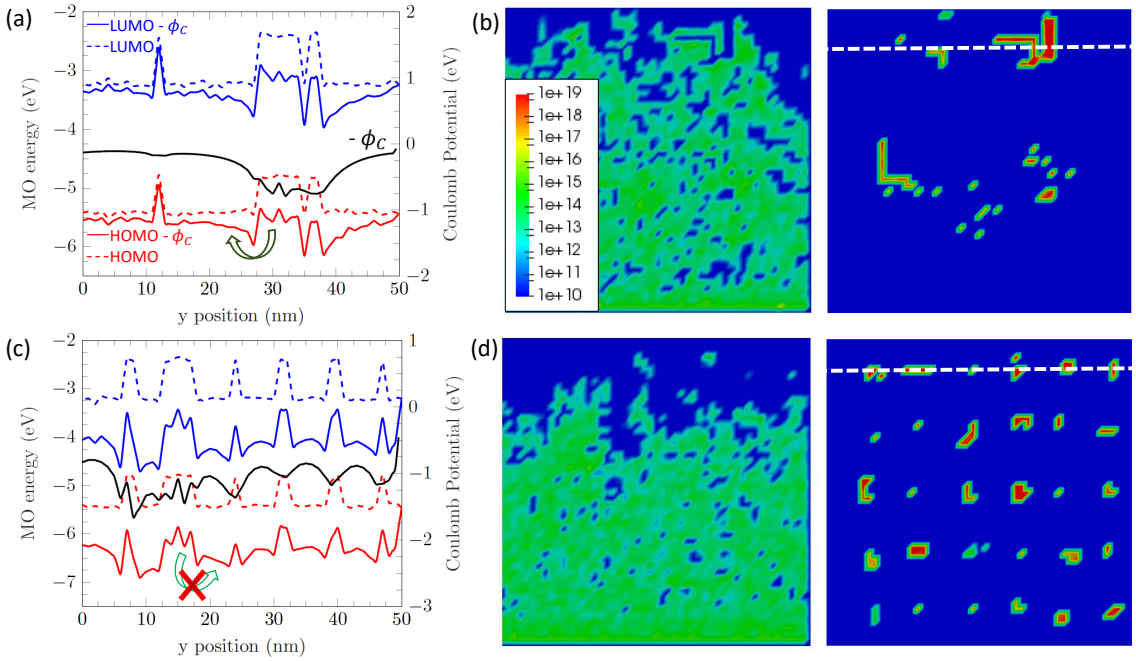

Figure 5.7: (a,c) Molecular orbital (MO) energies (dashed) and the Coulomb potential (black line), as well as the sum of MO energies and Coulomb potential (b,d) electron (left) and hole (right) densities. (a) and (b) show the results for chain length $N = 100\,\text{nm}$, and (c) and (d) represent $N = 10\,\text{nm}$. The colorbar shows the density in unit cm^{-3}.

The enhanced exciton dissociation (Figure 5.6) results in a higher j_{sc} of $3.37\,\text{mA}\,\text{cm}^{-2} > 2.95\,\text{mA}\,\text{cm}^{-2}$, resulting in a larger PCE. Due to the high energy barrier at high HOMO level offset (0.5 eV), holes are trapped in the polymer chain for shorter chain lengths of $N = 10\,\text{nm}$, which may be lowered by using longer polymer chain lengths at the same concentration, as mentioned above. This leads to a higher j_{sc} of $2.01\,\text{mA}\,\text{cm}^{-2} > 0.51\,\text{mA}\,\text{cm}^{-2}$, a higher V_{oc} ($0.59\,\text{V} > 0.34\,\text{V}$) and especially an increased PCE ($0.39\,\% > 0.05\,\%$) for long polymer chains. The reduced V_{oc} for short chains is caused by high recombination losses as hole back transfer is suppressed.

5.3.2 Impact of different morphology

This section focuses on the effect of the three distinct morphologies SAW, NTC, and NNTC on the photovoltaic performance of diluted donor OSCs. Figure 5.2 shows the three morphologies SAW, NTC, and NNTC, as explained in section 5.2. All morphologies are generated with a fixed polymer chain length of 100 nm. Alike the preceding subsection, we compute the short-circuit and hole escape current densities. We also look at the complete jV-characteristics, particularly the V_{oc}, for three distinct HOMO level offsets of 0.3 eV, 0.4 eV, and 0.7 eV.

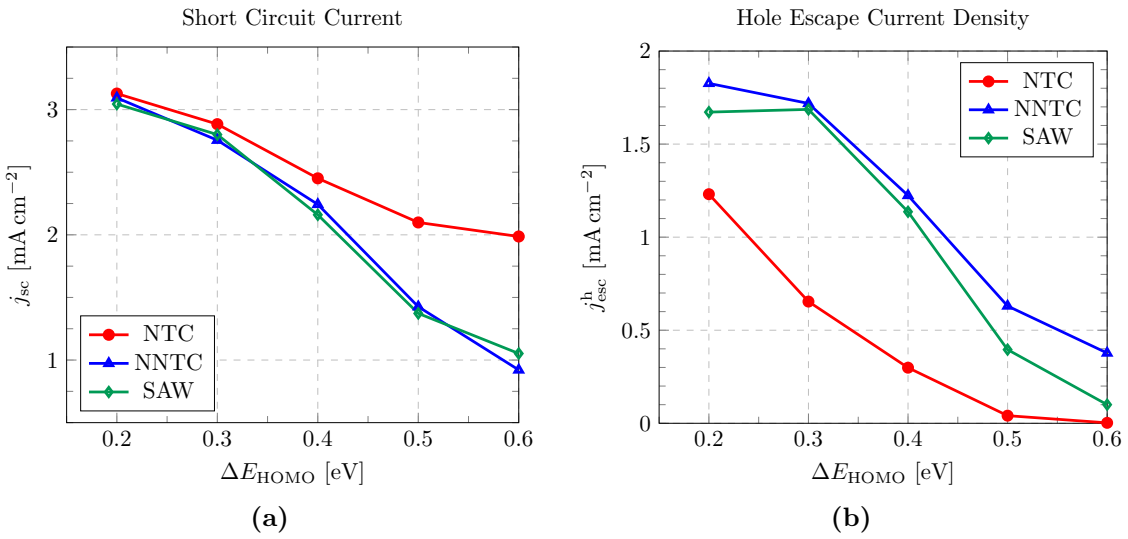

Figure 5.9: (a) Short-circuit current density j_{sc} and (b) hole escape current density j^{h}_{esc} for the SAW, NTC and NNTC morphologies at different HOMO level offset ΔE_{HOMO}.

Figure 5.9 visualizes (a) short circuit current and (b) hole escape current density for the three morphologies. For a small HOMO level offset, holes have a low barrier to leave the donor. Thus they are transferred to the acceptor molecules where they move towards the contacts. This results in a large hole escape current as well as a large short-circuit current density. At the lowest HOMO level offset, a j_{sc} of $\approx 3\,\mathrm{mA\,cm^{-2}}$ is attained for all the three morphologies. Because both the NNTC and the SAW configurations lack percolation pathways towards the contacts, identical values are found over the whole range of HOMO level offsets. They show a maximum hole escape current of $\approx 1.8\,\mathrm{mA\,cm^{-2}}$. At low HOMO level offsets, we notice a similar j_{sc} for the NTC morphology. The hole escape current density, on the other hand, is just $\approx 3\,\mathrm{mA\,cm^{-2}}$. The holes moving through the percolation pathways of the few chains connected to the contacts are responsible for the remaining current. This percolation current contributes to 35 % of the total short-circuit current density.

Both the NNTC and SAW morphologies exhibit a considerable drop in short-circuit and hole escape current density as the HOMO level offsets increase. The j^{h}_{esc} also drops substantially for the NTC, but the j_{sc} remains constant at $2\,\mathrm{mA\,cm^{-2}}$ beyond $\Delta E_{HOMO} = 0.5\,\mathrm{eV}$. The NTC offers a sufficient percolation path for the holes to move along the polymer chains and does not require any back-transfer to the acceptor to generate a sufficient current density. This morphology is comparable to the conventional BHJ morphology, but with significantly less donor material. This makes it more essential to control the polymer network as the charge transport mechanism, and performance depends heavily on morphology.

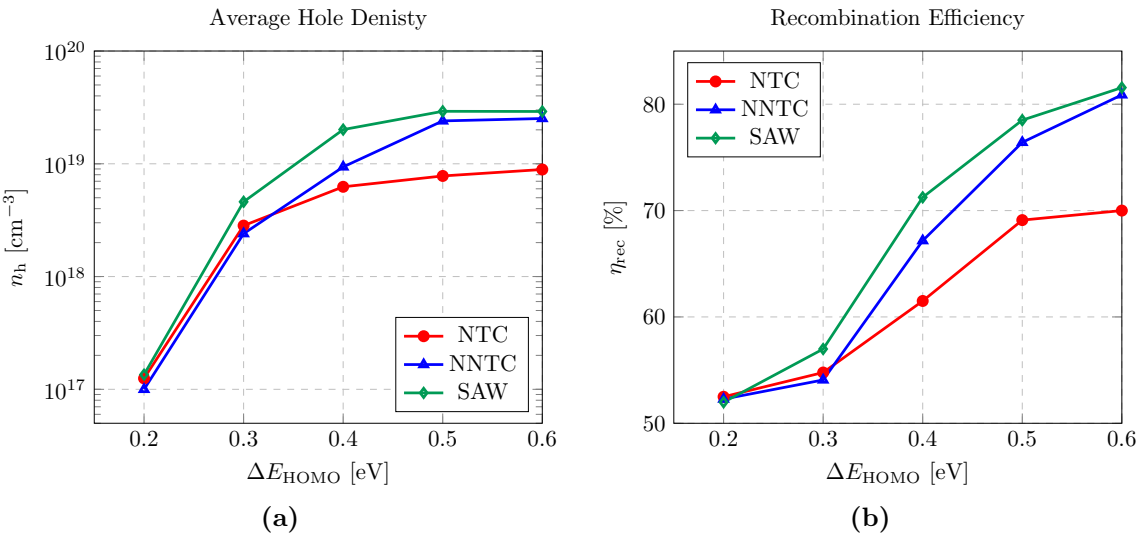

Figure 5.10: (a) Average hole density n_h and (b) recombination efficiency η_{rec} for SAW, NTC and NNTC morphologies at different HOMO level offset.

Figure 5.10 sums up (a) the average hole densities n_h and (b) the recombination efficiency η_{rec} for different polymer networks. The average hole density rises exponentially with increasing HOMO level offset. The hole density saturates for the NTC and the SAW configuration at a maximum value of $n_h =\approx 5 \times 10^{19}\,\mathrm{cm}^{-3}$, whereas it is reached at $n_h =\approx 9 \times 10^{18}\,\mathrm{cm}^{-3}$ for NTC network. For all three morphologies as mentioned in the preceding section, the smaller barrier allows the holes to easily escape towards the contacts, resulting in a lower hole density. For all the networks, holes accumulate on the polymer chain at higher barriers and cannot be transferred back to the fullerene matrix. The difference with the NTC morphology is that there is adequate hole transport towards contacts, resulting in a shorter average duration for holes to reside within the polymer network.

The short-circuit current must be inversely related to the recombination current. The trend is shown in 5.10(b) to corroborate the preceding conclusion. At higher HOMO offset, all the photo-generated charges recombine and no escape current is observed as a result the average hole density is higher. Beyond the HOMO level offset of 0.5 eV, the recombination efficiency for the SAW and NNTC morphologies saturates for larger barriers at $\eta_{rec}\approx 80\%$, while it stays constant for the NTC morphology at $\eta_{rec} = 70\,\%$. SAW and NNTC, in comparison, provide better results for j^{h}_{esc} with a HOMO level offset of 0.2 eV to 0.6 eV. The findings for j_{sc} are almost same for all three morphologies up to the HOMO level offset of 0.2 eV to 0.4 eV, but NTC has an advantage for the offset beyond 0.4 eV due to unique percolation pathways.

We now analyze at the complete jV-characteristics for the three distinct morphologies at the HOMO level offsets of $\Delta E_{\mathrm{HOMO}} = 0.3\,\mathrm{eV}$, $0.4\,\mathrm{eV}$, and $0.5\,\mathrm{eV}$. Figure 5.11(a)-(c) shows the jV-characteristics. To evaluate the highest possible open circuit voltage, the work functions of the anode and cathode were selected to be $-5.5\,\mathrm{eV}$ and $-5.5\,\mathrm{eV}$, respectively, for this specific analysis. There is no difference between the jV-curves of the different morphologies at $\Delta E_{\mathrm{HOMO}} = 0.3\,\mathrm{eV}$. The observed device characteristic parameters are summarized in Table 5.3, which reports higher V_{oc}, j_{sc} and PCE for the three morphologies at $0.3\,\mathrm{eV}$ as compared to the earlier study for $\sim 1\%$ dilution by Xu *et al.* [117]. For modest HOMO level offsets of $0.3\,\mathrm{eV}$ and $0.3\,\mathrm{eV}$, the devices show a similar Fill Factor (FF) for all the three morphologies. The difference in FF at the maximum HOMO level offset of $0.3\,\mathrm{eV}$ is related to the fact that the SAW and NNTC devices have resistive jV-characteristics owing to suppressed back transfer, whilst the NTC morphology shows effective current flow along the percolation pathways formed by polymer chains.

ΔE_{HOMO} (eV)	SAW				NNTC				NTC			
	$j_{\mathrm{sc}}(\mathrm{mA\,cm^{-2}})$	V_{oc}(V)	FF	PCE (%)	$j_{\mathrm{sc}}(\mathrm{mA\,cm^{-2}})$	V_{oc}(V)	FF	PCE(%)	$j_{\mathrm{sc}}(\mathrm{mA\,cm^{-2}})$	V_{oc}(V)	FF	PCE(%)
0.3	4.16	1.21	0.33	1.64	4.04	1.22	0.32	1.60	4.29	1.27	0.31	1.69
0.4	3.11	1.17	0.32	1.15	3.29	1.16	0.31	1.19	3.48	1.28	0.28	1.26
0.7	0.94	0.57	0.25	0.13	1.15	0.56	0.25	0.17	2.53	1.26	0.37	1.18

Table 5.3: Device characteristic parameters for SAW, NNTC and NTC morphologies.

The trend within the jV-characteristic for $\Delta E_{\mathrm{HOMO}} = 0.4\,\mathrm{eV}$ is similar at low voltages, while the NTC exhibits a larger current density towards the V_{oc}. As a result, the NTC morphology has a higher maximum V_{oc} than the other two networks. The open-circuit voltage for SAW and NNTC morphologies at the maximum HOMO level offset is $V_{\mathrm{oc}} \approx 0.57\,\mathrm{volt}$ and $V_{\mathrm{oc}} \approx 0.56\,\mathrm{volt}$, respectively, whereas the NTC has a higher V_{oc} of $1.26\,\mathrm{V}$. The drop in V_{oc} for the SAW and NNTC morphologies at larger HOMO level offsets is owing to the substantially enhanced recombination. Charges may still be collected at the contacts due to percolation paths inside the NTC network, and recombination is stays low, as reflected by the higher V_{oc}.

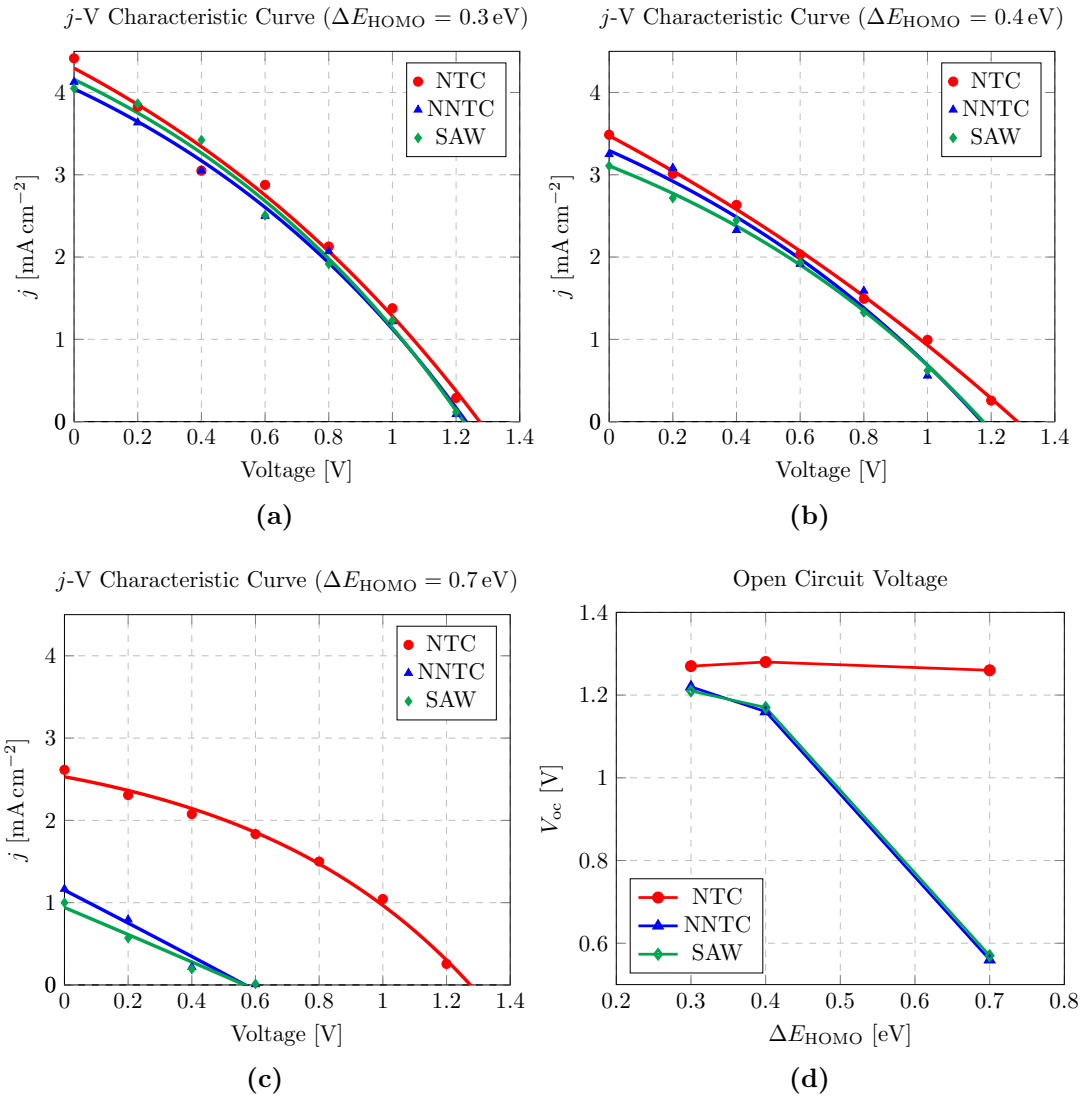

Figure 5.11: jV-characteristics at (a) 0.3 eV, (b) 0.4 eV, (c) 0.7 eV and (d) Open-circuit voltage for SAW, NTC and NNTC morphologies at different HOMO level offset.Solid lines in (a)-(c) show fits obtained using the Shockley equation.

Popp *et al.* [282] demonstrated higher $j_{sc} = 9.1\,\mathrm{mA\,cm^{-2}}$ within standard P3HT:PCBM bulk-heterojunction solar cell. The open-circuit voltage, however, was restricted to $V_{oc} = 0.67\,\mathrm{V}$. The diluted donor OSC provides a significant improvement in terms of V_{oc} as charge carriers are extracted via the fullerene matrix, the intrinsic limit of the V_{oc} is increased to the difference between the HOMO and LUMO levels of the acceptor molecules, resulting in a substantial improvement in terms of V_{oc}. Furthermore, charge extraction at the wrong contacts is substantially suppressed, which is one promising technique to significantly increase the V_{oc} despite utilizing the same material system. [281,282]

5.4 Conclusion

In conclusion, we examine the effect of the polymer network on photocurrent generation in dilute donor organic solar cells. First, the morphologies of isolated polymer chains were studied for various chain lengths and HOMO level offsets between the donor chains and the fullerene acceptor. Our findings demonstrate that a significant hole current may be generated as a result of hole back transfer towards the fullerene matrix. This occurs without the necessity for donor material percolation pathways towards the contacts. Larger polymer chain lengths exhibit improved behavior at high HOMO level offsets ($\geq 0.3\,\mathrm{eV}$), but smaller polymer chain lengths exhibit significantly decreased performance. Even in the absence of a significant Coulomb repulsion, substantial back transfer is possible 1t short polymer chain lengths. The major source of loss in current density is the loss of excitons that do not reach the donor/acceptor interface and are thus not separated. Strong Coulomb repulsion exists for all chain lengths at large HOMO offsets. However, for large chain lengths, there is a higher current density, but for shorter chains, there are reduced current values. We demonstrated that the chain length may significantly affect the shape of the Coulomb repulsion, which, even for HOMO level offsets more than $0.5\,\mathrm{eV}$, produces a substantial driving force pushing holes towards the fullerene phase for long chains. This provides a better understanding of how the donor semiconductor's molar weight affects the performance of the dilute donor cells.

In the second part of the study, SAW morphology was compared to the NTC and NNTC networks to further support the dominating transport mechanism, as well as the significant observation of V_{oc}. In terms of current generation, even at the higher HOMO level offsets, a small fraction of polymer chains connected to the contact is sufficient to provide a substantial current density. However, no variation in jV-characteristics is found for low HOMO level offsets. While the SAW and NNTC morphologies are solely based on hole-back transfer, the NTC exhibits a significant degree of percolation current despite the low donor concentration. Thus, controlling the donor network has the potential to change the main transfer mechanism and might provide a transition between back-transfer. This is accomplished through the use of an acceptor-controlled device or a percolation-dominated solar cell in which the donor itself controls hole transport.

6 Tandem/Multi-junction Modelling of hybrid perovskite-organic device

Hybrid Organic-inorganic semiconductors are an excellent option for developing photovoltaic devices because of their broad range of bandgaps, inexpensive deposition techniques, and broad solar spectrum absorption. Perovskite-organic tandem solar cells with two terminals (2T) have emerged as the potential architectures to reach high efficiency. Several device characteristics like thickness and bandgaps of the sub-cells must be optimized to maximize solar spectrum utilization in a 2T tandem cell. In this study, we propose a tandem solar cell model using hybrid perovskite-organic solar cells. Initially, tandem architecture using perovskite absorbers and organic blend is modelled to explore the series-connected tandem solar cell structure and analyze the effect on the device performance. Furthermore, this work analyzes different perovskite cells in combination with the organic blends in a multi-junction configuration to give a concrete model representation that can help to optimize the device architecture leading to high-efficiency hybrid perovskite-organic devices.

6.1 Introduction

Solar cells are widely recognized as an essential tool to overcome environmental pollution and the use of renewable energy. As a result, a variety of solar cell types have been developed. Thin-film solar cells, such as organic solar cells (OSCs) and perovskite solar cells (PSC) have piqued the interest of researchers owing to their benefits in terms of ease of manufacturing, low weight, and solution processing, among other factors. The maximum certified power conversion efficiency (PCE) of single-junction PSC and OSCs has been determined to be 25.7% and 18.2%, respectively [6]. The PCE of single-junction PSC is approaching the PCE (26.1%) of mono-crystalline silicon solar cells, bringing it

closer to the Shockley-Queisser limit [6, 55]. Solar cells based on stacked architecture are being developed to enhance the overall device efficiency to overcome the limitations of thermodynamic principles. The stacked architecture comprises two or more sub-cells that have distinct absorption spectra from one another. A tandem architecture is created by joining two cells (top and bottom) together, and a recombination layer in the middle. The stacked architecture can be connected in series and parallel configurations. The top cell (larger bandgap) absorbs high-intensity light, while the bottom cell (smaller bandgap) absorbs low-intensity light, thus allowing broader use of the solar spectrum. While the tandem design may improve solar cell PCE, it requires a recombination layer between the two sub-cells, which involves considering sub-chemical and physical characteristics, complicating the production of stacked solar cells. Additionally, the current output of the two sub-cells should be closely matched for optimal efficiency.

Two-terminal (2T) perovskite-perovskite tandem cells have been reported to have PCE of 24.9% [309], while that for 2T organic tandem cells PCE is reported to be 17.3% PCE recently [310]. These tandem architectures do, however, require solvents with comparable characteristics to process the top and bottom cells, which makes it challenging to achieve reproducible high performing tandem devices [311]. As reported in the literature, a PSC cell is more sensitive to aqueous/polar solvents and employ an organic hole (electron) transport layer in standard(inverse) configuration to reduce recombination and efficient charge extraction [312]. Therefore, it is challenging to fabricate a recombination layer and subsequently a second PSC absorber layer through a solution process. The use of orthogonal solvents to dissolve organic and perovskite materials has facilitated the fabrication of hybrid tandem cells [313]. The high carrier mobility and absorption coefficient of the perovskites allow efficient conversion of high-energy solar spectrum to useful energy. Furthermore, the recent fast development of low-band-gap organic semiconductors with near-infrared light absorption properties offer a variety of good options for use as bottom cells in the tandem architecture [314–316].

Chen *et al.* developed an effective hybrid 2T tandem cell by placing a PSC sub-cell on the top of an OSC sub-cell with an alcohol/water processed recombination layer in between [317]. They reported that the low-bandgap organic bulk-heterojunction systems show great potential as complementary spectral absorbers in 2T hybrid tandem structures. However, molecular design and structural modification still have space for development. The tandem design must handle the photons converted by specific sub-cells in the most effective manner possible. As previously stated, this tandem architecture is challenging to build owing to the multi-solution procedures required. Solution treatments with an aqueous layer of PEDOT:PSS, for example, may harm the PSC layer, even if it is covered by an organic layer(e.g. PCBM). Due to these difficulties, despite their

significance, there are yet very few reports on such 2T hybrid architectures, and the understanding of how to optimize the recombination layer is still progressing [312,318–322].

Hybrid tandem devices have shown better reproducibility than all-perovskite tandem devices, but with a lower PCE, which remains at 24% as reported by Brinkmann *et al.* [323]. They demonstrated a highly efficient perovskite-organic tandem device with a J_{sc} of 14 mA cm^{-2}, V_{oc} of 2.15 V and 80 % fill factor (FF). The reduction in electrical and optical losses in the interconnecting layer (ICL) were reported to be as a result of using ultra-thin metal-like indium oxide (InOx) layer. Furthermore, Chen *et al.* also reported a perovskite-organic tandem solar cell with 23.6% efficiency for small area devices [324]. First, they demonstrated the reduction in V_{oc} losses of the wide bandgap perovskite (top cell) by passivating NiOx HTL surface with Benzylphosphoric acid (BPA), which in turn significantly improves the PCE of single-junction devices. In addition, They have also reported the minimization of optical and electrical losses and excellent near-infrared transmittance in the ICL consisting of indium zin oxide (IZO) between bathocuproine (BCP) and molybedenum oxide (MoOx). The optimized ICL resulted in J_{sc} of 14.87 mA cm^{-2}, V_{oc} of 2.06 V and 77.2 % fill factor (FF). The low photovoltaic performance of the OSC layer in the stack may be reasonably ascribed to the reduced PCE of hybrid tandem systems. The high efficiency of a single-junction OSC ($> 18\%$) also suggests that the lower efficiency of a tandem device is related to additional complicated considerations including the intensity of light for the single-junction and multi-junction architecture, unfavorable active layer morphology, misaligned materials for transport layers and recombination, and the energy level offset between the HOMO (highest occupied molecular orbital) and LUMO (lowest unoccupied molecular orbital level) of the organic blend [325]. Most research on hybrid tandem devices has concentrated on high device performance, with little information on device photovoltaic characteristics and design concepts. Further research is needed to improve device design principles for perovskite-organic tandem devices, particularly PCE loss.

Theoretical studies have been conducted to examine tandem cell efficiency using perfect absorbers and ideal device designs [326–329]. The majority of these research studies have relied on either a certain set of thicknesses or bandgaps. Here, we present a modelling technique to simulate perovskite-organic hybrid multi-junction architecture. The consistent electro-optical simulations are presented to account for exciton states, contact properties, the internal geometry of the compound semiconductors, and the charge transport in the organic materials. For this reason, kinetic Monte Carlo (kMC) simulation is a suitable tool for implementing the required design strategies for organic photovoltaics. Regardless of how well experimental data are reproduced, the kMC approach has a very high computing cost and does not appear to be suitable for simulating complex device

architectures. In fact, kMC can handle devices in the range of 200 nm, while in tandem cells, OSC can be coupled to inorganic solar cells that can be in the range of microns. This means that kMC is the correct modelling for the OSC part but cannot describe the entire tandem cell. The likely answer to this problem is a simulation tool that applies different models for different regions/aspects of the device to address all the most important physical aspects, keeping the computational cost low.

In particular, for OSCs and, more generally, organic semiconductor devices, we develop a model which combines the drift-diffusion model with the kMC model. This innovative approach simulates tandem solar cells in perovskite-organic configurations. Therefore, the perovskite-organic multi-junction architecture simulations are carried out using kMC and Drift Diffusion (DD) studies. We use the one-dimensional (1D) DD model for the perovskite cell (top), and the three-dimensional (3D) kMC model for the organic cell (bottom) in a 2T configuration, analogous to two series-connected cells. The bandgap of perovskite absorbers for this work range from 1.5 eV to 2.3 eV and that for OSC includes 1.14 eV to 1.64 eV. While selecting materials for our theoretical calculations, we look for commercially accessible and widely utilized materials to address the viability and dependability of our proposed structures. We use the transfer matrix model (TMM) to calculate the optical model for the said architecture accounting for the optical losses to achieve the optical coupling. The generation profile obtained from the TMM calculation for each cell is then fed as an independent input to the top and bottom cells, and J-V characteristic curves are obtained. The output current of an ideal system will be the lower of the two cell currents, due to the recombination of charge carriers entering the low-current cell from the high-current cell. Compared to a series-connected voltage source, the voltage output is the sum of the two cell voltages. This work analyzes the overall performance of the tandem/multi-junction architecture by parameterizing the characteristics of one sub-cell at a time.

6.2 Computational Model

6.2.1 Optical Modelling

Optimizing hybrid tandem solar cells is not a simple task since each layer affects the final device's performance. Optical modelling is a successful approach for creating multilayer architecture for solar cells. The optical modelling of the multi-junction hybrid perovskite-organic is carried out using the Transfer Matrix Model (TMM) inspired by Burkhard *et al.* [203] to calculate the spatial distribution of photogenerated charge carriers for different perovskites, and the organic blends to take into account the spatial profile of the optical

generation rate and its fluctuation with layer thickness. The optical transfer matrix theory describes the optical processes occurring within a thin film layer stack and calculates the power conversion efficiency. The transfer matrix method used in this work calculates the attenuation, reflection and transmission based on the n and k optical constants of the selected material. The theory of the calculation has been explained in detail in the literature [204, 330].

The charge carrier generation rate $G(z, \lambda)$ is given by:

$$G(z, \lambda) = 2\pi \cdot \frac{Q(z, \lambda)}{h\omega}, \tag{6.1}$$

where, h is the plank constant, ω is the angular frequency of the striking photon and $Q(z)$ is the local energy dissipated the device and given by:

$$Q(z) = \frac{1}{2}\epsilon_0 c\alpha n|\mathrm{E}(z)|^2, \tag{6.2}$$

where, ϵ_0 is the permittivity of the vacuum, c is the speed of the light, $\alpha(\alpha = 4\pi k/\lambda)$ is the absorption coefficient, n and k are the real and complex part of the refraction index. λ is the wavelength, and E is the optical electric field at point z.

Finally, the generation rate can be obtained by summing $G(z, \lambda)$ over the range of wavelength:

$$G(z) = \sum_{\lambda=300}^{\lambda=1200} G(z, \lambda) \tag{6.3}$$

The TMM calculates the generation rate (G) for the AM1.5 illumination spectrum (assuming 100% internal quantum efficiency) at all wavelengths using Equations (1) to (3). We can determine the amount of light absorbed and reflected by a cell using the input n and k refraction index data for all the materials utilized in the cell throughout a wavelength range. The n and k values of the active layers used in this work are shown in the Appendix, Figure A.4 [203, 331–337].

6.2.2 Drift-Diffusion Modelling

To simulate perovskite device, we use the finite element drift-diffusion (DD) method implemented in TiberCAD [338, 339]. The model has successfully been implemented to simulate organic semiconductors [340], organic solar cells [18, 341, 342], perovskite solar cell [343, 344] and dye-sensitized solar cells (DSSCs) [345, 346]. The model is based on Drift-diffusion and Poisson equations to solve the electron, hole, and trap drift-diffusion problems simultaneously. The model considers light absorption, the production of electron-hole pairs in the perovskite absorber, and the recombination processes. We

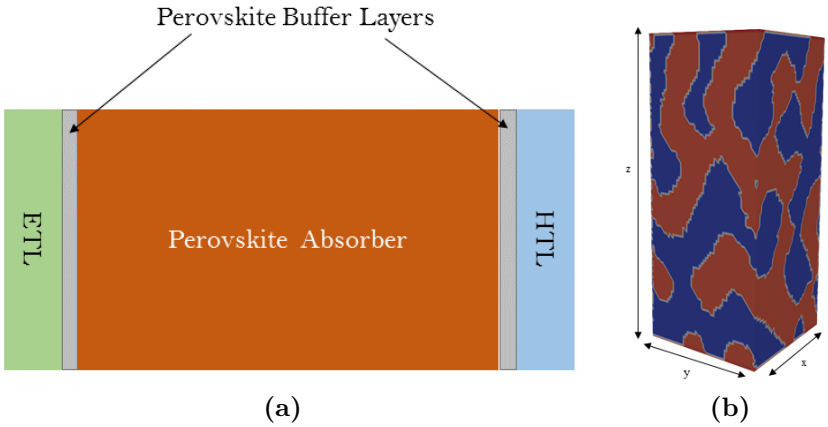

Figure 6.1: (a) Schematic diagram of a perovskite sub-cell and (b) schematic of the organic sub-cell.

solve the perovskite cell independently in a 1D space. To account for the traps at the interface, the hole transport layer (HTL) and the electron transport layer (ETL) are coupled to two 2 nm buffer layers on either side of the perovskite layers as shown in Figure 6.1(a). These buffer layers are thought to accumulate interface traps. The electrons and holes produced in the bulk perovskite are transported to the electron transport and hole transport layers, respectively. The transport of these charge carriers is governed by diffusion and electrically induced drift. As variables, the electrochemical and the electrostatic potential are used. The entire set of equations are given as:

Poisson Equation

$$\vec{\nabla} \cdot \vec{\nabla}\Phi = -\frac{q}{\epsilon}(p - n + N_D - N_A + \rho_p - \rho_n)\,, \tag{6.4}$$

Continuity equations

$$\vec{\nabla} \cdot \mu_n n(\vec{\nabla}\Phi_n) = G - R\,, \tag{6.5}$$

$$\vec{\nabla} \cdot \mu_p p(\vec{\nabla}\Phi_p) = -(G - R)\,, \tag{6.6}$$

where, Φ is the electrochemical potential, q is the electron charge, ϵ is the material permittivity, p and n is the hole, and electron density, respectively, N_D and N_A are the donor and acceptor impurities, ρ_p and ρ_n are the trap density for donor and acceptor respectively. μ_p and μ_n are hole and electron mobility, while Φ_p and Φ_n are the electrochemical potentials for hole and electrons, respectively. R and G represent the net recombination and generation rates.

Table 6.1: Simulation parameters for 1D drift-diffusion model.

Parameter	Values	Units	Reference
Perovskite mobility (electron)	5	cm^2/Vs	[329, 347]
Perovskite mobility (hole)	5	cm^2/Vs	[329, 347]
Perovskite relative permitivity	20	—	[329, 348–350]
Bandgap (PCBM)	1.8	eV	[351]
PCBM HOMO	-5.9	eV	[329]
Electron mobility in PCBM	1	cm^2/Vs	[352]
Hole mobility in PCBM	$1x10^{-5}$	cm^2/Vs	[329]
PCBM relative permitivitty	3.9	—	[353]
Spiro-OMeTAD bandgap	3.17	eV	[354]
Spiro-OMeTAD valence band	-5.22	eV	[354]
Electron mobility in Spiro-OMeTAD	$1x10^{-5}$	cm^2/Vs	fit.
Hole mobility in Spiro-OMeTAD	$1x10^{-3}$	cm^2/Vs	[355]
Spiro-OMeTAD relative permitivitty	3.53	—	[329]
Cathode fermi level	-5.1	eV	[344]
Anode fermi level	-4.3	eV	fit
Bimolecular recombination constant	$1x10^{-10}$	$cm^3\ s^{-1}$	[329]
Trapping time for electron and hole	$1x10^{-7}$	s	[344]

The ETL and HTL mobilities have been used as fitting factors to ensure that the perovskite cell is not constrained by charge transfer in the collection layers. The mobility has been selected so that the ETL has a fivefold increase in electron mobility and a fivefold increase in hole mobility compared to their equivalents (electrons in the HTL and holes in the ETL). The anode and cathode energy levels are used based on the workfunctions of commonly accessible contact metals (Au, Ag). The majority of hybrid perovskites exhibit comparable ambipolar mobilities [356, 357], the perovskite material was chosen to have the same mobility value of $5\,\mathrm{cm\,V^{-1}\,s^{-1}}$ and for the inorganic perovskite, the mobility was chosen to be $25\,\mathrm{cm\,V^{-1}\,s^{-1}}$ [358].

Recombination rates in the perovskite are modelled using; first, the direct recombination, given by:

$$R_d = C(np - n_i^2)\,, \tag{6.7}$$

Where C is the bi-molecular rate constant, and n_i is the carrier density at equilibrium ($n = p$). The second recombination rate is modelled by Shockley-Read-Hall (SRH) recombination model given by:

$$R_s = \frac{np - n_i^2}{(n + n_i \exp\{E_t/k_B T)\tau_p\} + (p + p_i \exp\{-E_t/k_B T)\tau_n\}}\,, \tag{6.8}$$

where, $E_t = E_{trap} - (E_c + E_v)/2$ is the trap energy with respect to midband energy level. τ_n and τ_p are the electron and hole trapping times respectively and defined as:

$$\tau_{n,p} = \frac{1}{N_t C_{p,n}}\,, \tag{6.9}$$

where, N_t is the trap density, and $C_{n,p}$ is the probability of the charge particle to be trapped. The simulation model uses midgap traps, as they are demonstrated to be most effective [359]. The simulation parameters for drift-diffusion analysis are summarized in Table 6.1.

6.2.3 Kinetic Monte Carlo Modelling

The organic cell in the multi-junction architecture is simulated by the kinetic Monte Carlo (kMC) model. The kmC simulation model has been successfully implemented to analyze the role of energetics and permittivity on the charge separation efficiency [14] and dynamics, [15] tuning the exciton dynamics using phosphorescent sensitizers, [282] the role of interface energetics on the open-circuit voltage, [36, 185] and the origin of charge transport and the importance of the morphology in dilute donor organic solar cells. [38, 116].

The active layer is represented by a cubic lattice with size $50 \times 50 \times z\,\mathrm{nm}^3$ and lattice spacing with lattice constant 1 nm. Where z corresponds to thickness in the z-direction as shown in Figure 6.1. For all transport processes, only nearest neighbors are considered, i.e. 6 neighbors for each site. Periodic boundaries are applied in x- and y-direction. In z-direction, contacts terminate the cell. A bulk-heterojunction morphology is generated using a spin-exchange algorithm presented by Watkins *et al.* [30]. The bulk-heterojunction morphology used within this study is computed with the spin-exchange algorithm looped over 2,000 Monte Carlo steps [31], which gives a cluster size of 13.9 nm. We use poly[[2,5-bis(2-hexyldecyl-2,3,5,6-tetrahydro-3,6 dioxopyrrolo[3,4-c] pyrrole-1,4-diyl]-alt-[3',3"-dimethyl 2,2':5',2"-terthiophene]-5,5"-diyl] (PMDPP3T), poly[[4-(2-ethylhexyl)-4Hdithieno [3,2-b:2',3'-d]pyrrole-2,6-diyl]-alt-2,5-selenophenediyl [2,5-bis (2 ethylhe-xyl)-2,3,5,6-tetrahydro-3,6-dioxopyrrolo[3,4-c]-pyrr-ole-1,4-diyl] -2,5 -selenophenediy (PDPP-STDTPS), and poly[[4,8-bis[(2-ethylhexyl)-oxy]benzo[1,2-b:4,5-b0] dithiophene-2,6-diyl][3-fluoro-2-[(2-ethylhexyl) carbonyl] thieno[3,4-b] thioph-enediyl]] (PTB7) as donors, and PCBM as acceptor, to be used as sub-cells in multi-junction architecture. For the calculations in section 6.3, the organic blends may be considered as: PMDPP3T:PC_{60}BM, PDPPSTDTPS:PC_{60}BM, and PTB7:PC_{71}BM.

Singlet excitons are generated within the active layer either using a generation profile $G(z)$ calculated from the transfer matrix method [203]. Singlet diffusion is modelled by

Parameter	Symbol	Values	Reference
Size in x-direction	l_{x}	50 nm	-
Size in y-direction	l_{y}	50 nm	-
Size in z-direction	l_{z}	80 nm to 100 nm	-
Lattice constant	l_{c}	1 nm	-
Inverse localization length	γ	$2\,\mathrm{nm}^{-1}$	[31]
Relative permittivity	ϵ_{r}	3.5	[308]
Energetic disorder	σ	30 meV	-
Cathode work function	ϕ_{cathode}	−4.30 eV	[308]
Anode work function	ϕ_{anode}	−5.0 eV	-
Acceptor ($PC_{71}BM$) HOMO level	$E_{\mathrm{A}}^{\mathrm{HOMO}}$	−6.0 eV	[36]
Acceptor ($PC_{71}BM$) LUMO level	$E_{\mathrm{A}}^{\mathrm{LUMO}}$	−4.25 eV	[36]
Acceptor ($PC_{60}BM$) HOMO level	$E_{\mathrm{A}}^{\mathrm{HOMO}}$	−5.8 eV	[31]
Acceptor ($PC_{60}BM$) LUMO level	$E_{\mathrm{A}}^{\mathrm{LUMO}}$	−3.7 eV	[31]
Donor (PMDPP3T) HOMO level	$E_{\mathrm{D}}^{\mathrm{HOMO}}$	−5.10 eV	[360]
Donor (PMDPP3T) LUMO level	$E_{\mathrm{D}}^{\mathrm{LUMO}}$	−3.50 eV	[360]
Donor (PDPPSDTPS) HOMO level	$E_{\mathrm{D}}^{\mathrm{HOMO}}$	−4.84 eV	[360]
Donor (PDPPSDTPS) LUMO level	$E_{\mathrm{D}}^{\mathrm{LUMO}}$	−3.50 eV	[360]
Donor (PTB7) HOMO level	$E_{\mathrm{D}}^{\mathrm{HOMO}}$	−5.80 eV	[360]
Donor (PTB7) LUMO level	$E_{\mathrm{D}}^{\mathrm{LUMO}}$	−3.7 eV	[360]
Temperature	T	298 K	-
Simulation time	t_{s}	1 ms	-

Table 6.2: System Setup parameters used in kinetic Monte Carlo simulations for organic subcell.

a constant diffusion rate $a_{\mathrm{exh}} = 6D/l^2$, with the diffusion constant D and the lattice spacing l. The finite lifetime is singlet is included by a constant decay rate $a_{\mathrm{exd}} = \tau_{\mathrm{ex}}^{-1}$. Singlet dissociation at the donor-acceptor interface is modelled as a constant electron transfer rate a_{exs} from the excited donor to the acceptor site. The dissociation rate is only activated if the singlet is located at the interface [14,32]. Charge carriers can be generated from singlet dissociation, as explained above, and by injection from contacts. The charge injection rate is implemented following the thermionic injection model presented by Wolf *et al.* [194]. Collection of charge carriers is implemented by a constant collection rate a_{col}, which is activated if the charge is located next to the contact.

Charge carrier transport is modelled by the Miller-Abrahams hopping rate [82]:

$$a_{i\to j} = a_0 \exp\left(-2\gamma r_{i\to j}\right) \begin{cases} \exp\left(-\frac{\Delta E_{i\to j}}{k_{\mathrm{B}}T}\right) & \text{for} \quad \Delta E_{i\to j} > 0 \\ 1 & \text{for} \quad \Delta E_{i\to j} \leq 0 \end{cases}, \tag{6.10}$$

where $r_{i\to j}$ is the hopping distance between neighbor sites i and j, a_0 is the attempt-to-hop frequency, γ is the inverse localization constant, Boltzmann constant k_{B}, temperature T,

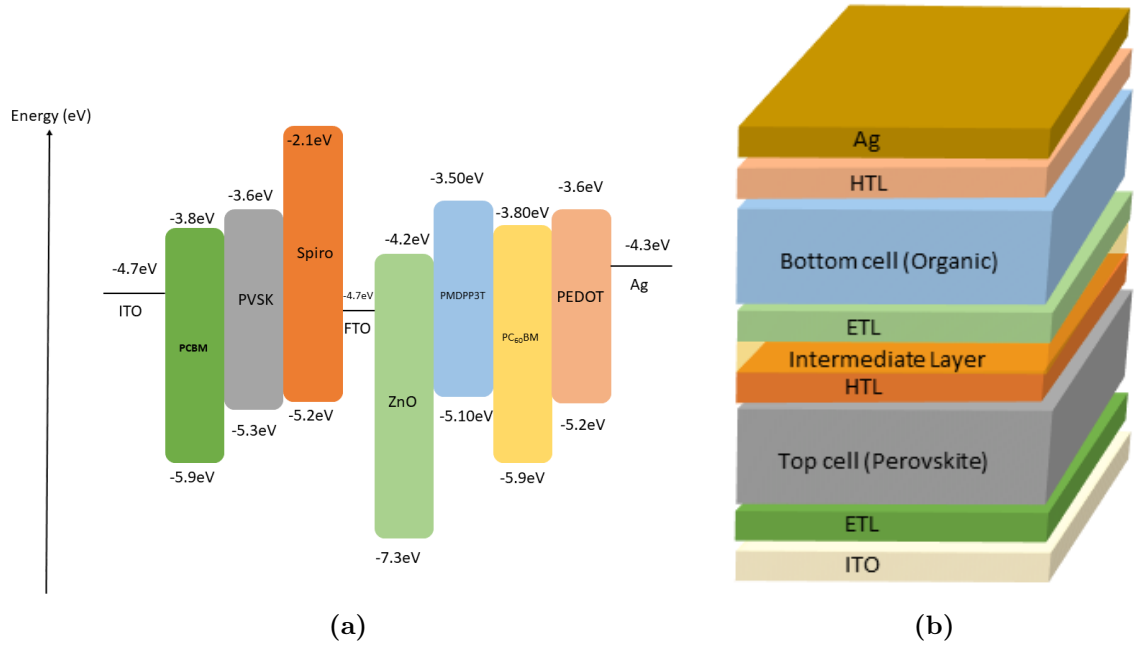

Figure 6.2: (a) Energy level diagram of the hybrid tandem architecture and (b) schematic of the tandem stack with perovskite (Top) and organic (bottom) cell.

and $\Delta E_{ij} = E_j - E_i$ is the energetic difference between the states i and j. The potential at site i is calculated as [14]

$$E_i = E_i^{\mathrm{MO}} + E_i^C + E_i^F \,, \tag{6.11}$$

where, E_i^{MO} is the molecular orbital energy (HOMO/LUMO) drawn from a Gaussian distribution of variance σ^2. E_i^C is the Coulomb energy, and E_i^F is the potential due to the external bias voltage V. The Coulomb interaction is included by the Ewald summation, which accounts for the interaction between all charge carriers, their periodic replica and image charges due to the contacts [32]. Recombination can occur if an electron and a hole reside on adjacent sites. For simplicity, we use a constant recombination rate $a_{\mathrm{ehr}} = 1 \times 10^6\,\mathrm{s}^{-1}$. The charge carrier Charge mobilities used for the mentioned blends are in the range of $1 \times 10^{-4}\,\mathrm{cm}^2\,\mathrm{V}^{-1}\,\mathrm{s}^{-1}$ to $1 \times 10^{-2}\,\mathrm{cm}^2\,\mathrm{V}^{-1}\,\mathrm{s}^{-1}$ [36]. Details on the Monte Carlo algorithm based on the Gillespie method can be found elsewhere [361, 362]. The system setup parameters for the kMC are summarized in Table 6.2.

Configuration	Bandgap (eV)	Cell	Thickness (nm)	J_{sc} (mA cm^{-2})	V_{oc} (V)	FF(-)	PCE (%)
$MAPbI_3$/ PDPPSDTPS:PCBM	1.5/1.14	Top	340	18.12	1.18	0.82	17.6
		Bottom	100	12.86	0.53	0.68	4.73
		Tandem		**12.86**	**1.71**	**0.71**	**15.85**
$CsFAMABr_2I$/ PDPPSDTPS:PCBM	1.63/1.14	Top	270	19.06	1.32	0.79	20.03
		Bottom	100	12.62	0.53	0.69	4.68
		Tandem		**12.62**	**1.85**	**0.73**	**17.14**
$CsPbI_3$/ PDPPSDTPS:PCBM	1.7/1.14	Top	300	15.21	1.36	0.81	16.77
		Bottom	100	13.86	0.54	0.69	5.23
		Tandem		**13.86**	**1.90**	**0.75**	**19.81**
$MACsPbI_2Br$/ PDPPSDTPS:PCBM	1.75/1.14	Top	300	15.63	1.37	0.74	16.10
		Bottom	100	14.17	0.54	0.70	5.38
		Tandem		**14.17**	**1.91**	**0.72**	**19.50**
$CsPbI_2Br$/ PMDPP3T:PCBM	1.92/1.3	Top	400	12.27	1.58	0.71	13.89
		Bottom	100	11.61	0.67	0.71	5.59
		Tandem		**11.61**	**2.25**	**0.71**	**18.81**
$MAPbBr_3$/ PTB7:PCBM	2.3/1.64	Top	450	7.15	1.82	0.60	7.87
		Bottom	80	9.10	0.77	0.56	3.94
		Tandem		**7.15**	**2.59**	**0.62**	**11.50**

Table 6.3: Performance parameters of hybrid tandem architecture with respect to different perovskite absorbers.

6.3 Results

6.3.1 Tandem architecture

We first study the hybrid perovskite-organic tandem architecture, where perovskite is used as the top cell and organic as the bottom cell as shown in Figure 6.2. The low-bandgap organic sub-cell used for this work are fullerene-based PMDPP3T:PCBM, PDPPSDTPS:PCBM and PTB7:PCBM, which have shown promising results in multi-junction architecture [360]. The perovskite absorbers used for this work are: Methylammonium lead iodide ($MAPbI_3$), cesium formamidinium methylammonium lead Bromide iodide ($CsFAMAPbBr_2I$), Cesium lead iodide ($CsPbI_3$), methylammonium cesium lead iodide bromide ($MACsPbI_2Br$), cesium lead iodide bromide ($CsPbI_2Br$), and methylammonium lead bromide ($MAPbBr_3$). The bandgap combination for each perovskite absorber as a top cell and organic active layer as a bottom cell are shown in Table 6.3. The thickness of both cells has been selected for optimum efficiency calculations. Table 6.3 shows the calculated performance parameters for different sub-cell combinations. The corresponding $J-V$ characteristic curves for the single junction as well as tandem and multi-junction configurations are shown in Figure S2 and S3 along with the reflection and transmission profile (at the interface) in Figure S4 and S5 of the supporting information.

For series-connected cells, assuming negligible losses at the interface, the output current is limited by the lowest of the two cell currents. The cell dimensions are described as follows: Glass/ITO (100 nm)/PCBM (20 nm)/Perovskite (300 nm to 450 nm)/Spiro-OMeTAD (20 nm)/FTO (100 nm)/ZnO (10 nm) / OSC (80 nm to 100 nm) /PEDOT:PSS (10 nm)/Ag (100 nm). The efficiency first tends to increases as we increase the bandgap to 1.75 eV, but it tends to decrease as the bandgap increases beyond 1.75 eV. The stack covers the the wavelength range of 300 nm to 1150 nm from the solar spectrum with light intensity of $\approx$ 70%. The fraction of light intensity absorbed by each active layer in tandem configuration is shown in supporting information, Figure S6.The maximum efficiency is observed for the thicknesses of $\approx$ 300 nm and $\approx$ 100 nm for the top and bottom cell, respectively, and for the bandgap combination of $E_g = 1.75$ eV for the top cell and $E_g = 1.14$ eV for the bottom cell. From the calculations shown in Table 6.3, we may also conclude that the efficiency of the 2T tandem solar cell is limited by the thickness of the current-limiting sub-cell.

For the bandgap combination of 1.5 eV and 1.14 eV for the top and bottom cell, respectively, the output current is matched for both the cells at the maximum power point. The PCE is calculated to be 15.85% with a fill factor (FF) of 0.71. The open-circuit voltage (V_{oc}) and the short circuit density (J_{sc}) is calculated to be 1.71 V and 12.86 mA cm^{-2}, respectively. The J_{sc} is limited by the lowest current from the sub-cell, as mentioned earlier. The bandgap combination of 1.63 eV (top cell) and 1.14 eV (bottom cell) gives the PCE of 17.14% with FF of 0.73. The J_{sc} and the V_{oc} of a tandem cell is calculated to be 12.62 mA cm^{-2} and 1.85 V. The bandgap combination of 1.75 eV and 1.14 eV for top and bottom cell, respectively, achieve second-best achievable efficiency PCE = 19.50% in this work. The corresponding V_{oc} and J_{sc} come out to be 1.91 V and 14.17 mA cm^{-2}, respectively. Beyond the top cell bandgap of 1.92 eV, the efficiency of the tandem cell is decreased to 11.50% with a FF of 0.62 as shown in Table 6.3. The efficiency trend increases from 15.85% to 19.81% and then decreases to 11.50% for the highest bandgap combination of hybrid perovskite-organic combination.

6.3.2 Multi-junction architecture

Further, we investigate three different types of multi-junction solar cells. The stacked active layers comprise of perovskite-organic-perovskite (POP) configuration, perovskite-organic-organic (POR) configuration and perovskite-perovskite-organic (PPO) configuration. The variation of the light intensity and J-V characteristics were analyzed, and power conversion efficiency was calculated. The three configurations studied are:

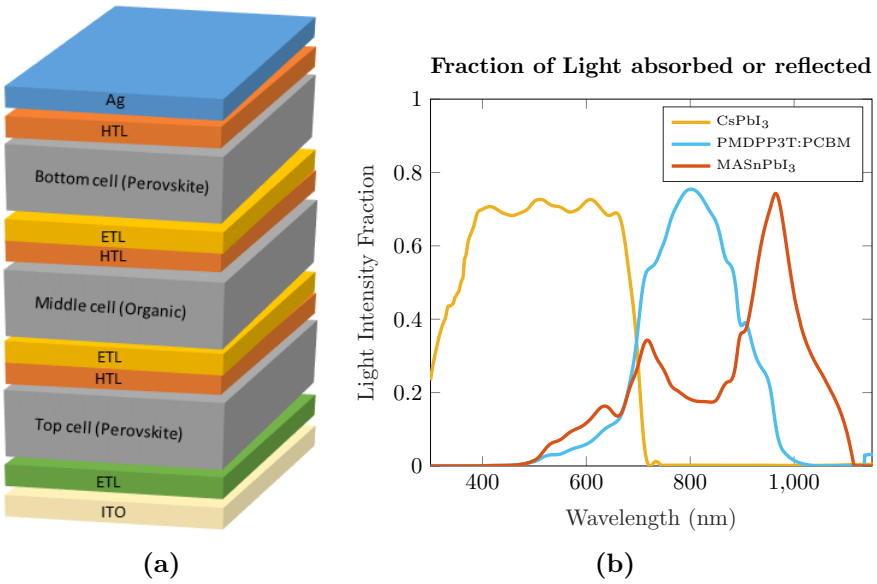

(a) **(b)**

Figure 6.3: (a) Stack diagram of a perovskite-organic-perovskite (POP) configuration, (b) Fraction of light absorbed by each active layer in the stack.

Perovskite-organic-perovskite (POP) Configuration

The three-junction architecture for POP configuration was modelled by using high(1.7 eV), medium (1.3 eV) and low (1.17 eV) bandgap materials. For this hybrid multi-junction architecture three active layers were stacked together as shown in Figure 6.3(a). We calculated the optical properties of the stack using the TMM method having the dimensions: Glass/ITO (100 nm)/C60 (20 nm)/$CsPbI_3$ (300 nm)/Spiro-OMeTAD (20 nm)/ZnO (10 nm)/ PMDPP3T: PCBM (200 nm) /PEDOT:PSS (10 nm)/C60 (10 nm)/$MASnPbI_3$ (320 nm)/Spiro-OMeTAD (20 nm)/Ag (100 nm). The thickness of the active layers have been optimized to give maximum device performance. For the three series-connected junctions, the maximum output current is limited by the cell with lowest current. The current matching is done at maximum power point, so that same amount of current flows across the stack.

We can see from Figure 6.3(b) that the three-junction configuration covers the solar spectrum in the range of 300 nm to 1150 nm and the light intensity of $\approx$ 70%. The J_{sc} for POP configuration was calculated to be 8.7 mA cm^{-2}, with a V_{oc} of 2.89 V. The PCE of 16.8 % was achieved with FF of 0.71.

Perovskite-organic-organic (POR) Configuration

The three-junction solar cell architecture was modelled using high (1.7 eV), medium (1.3 eV) and low (1.13 eV) bandgap materials as shown in Figure 6.4(a). The cell has

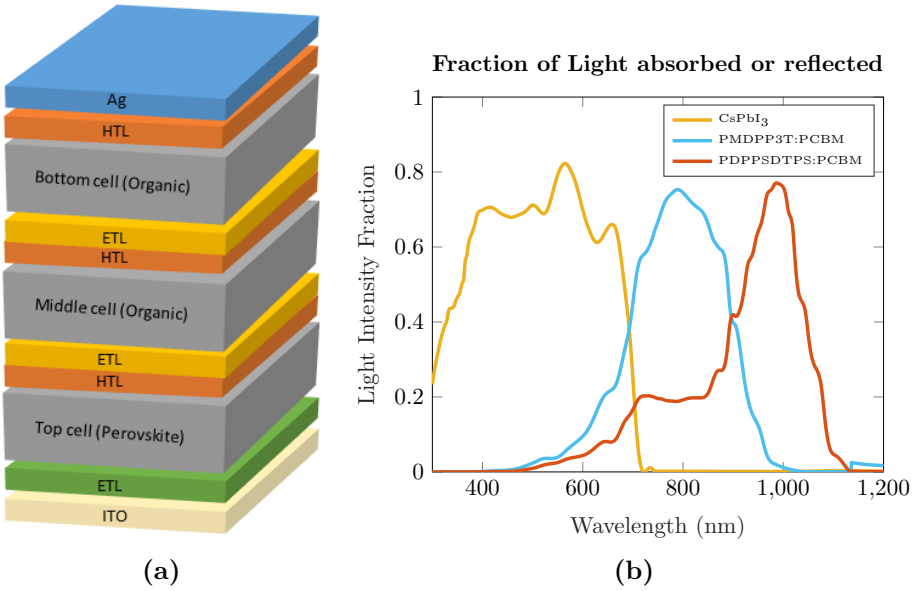

(a) **(b)**

Figure 6.4: (a) Stack diagram of a perovskite-organic-organic (POR) configuration, (b) Fraction of light absorbed by each active layer in the stack.

the following dimensions: Glass/ ITO (100 nm)/ C60 (20 nm)/ $CsPbI_3$ (270 nm)/ Spiro-OMeTAD (20 nm)/ ZnO (10 nm)/ PMDPP3T: PCBM (200 nm)/ PEDOT:PSS (10 nm)/ ZnO (10 nm)/ PDPPSDTPS:PCBM (100 nm)/ PEDOT:PSS (10 nm)/ Ag (100 nm). As the output current is affected by the thickness of each cell, so the thicknesses are determined to give optimum device performance. The light intensity absorbed by each active layer is shown in Figure 6.4(b) corresponds to $\approx$ 80% and covers the solar spectrum wavelength from 300 nm to the near-infrared range of 1150 nm as shown Figure 6.4(b).

The J_{sc} for POR configuration is limited to 7.40 mA cm^{-2}, by the low bandgap organic cell. The V_{oc} is calculated to be 2.55 V with PCE of 14.25% and fill factor of 0.69. The decrease in device performance of POR configuration compared to the POP configuration can be attributed to the organic sub-cells, which limit the device's short circuit density and PCE.

Perovskite-perovskite-organic (PPO) Configuration

The third type of multi-junction architecture was modelled using high 1.92 eV, medium 1.5 eV and low 1.14 eV bandgap materials as shown in Figure 6.5(a). The stacked cell has the following dimensions: Glass/ ITO (100 nm)/ C60 (20 nm)/ $CsPbI_2Br$ (300 nm)/ Spiro-OMeTAD (20 nm)/ C60 (10 nm)/ $MAPbI_3$ (290 nm)/ Spiro-OMeTAD (10 nm)/ ZnO (10 nm)/ PDPPSDTPS:PCBM (120 nm)/ PEDOT:PSS (10 nm)/ Ag (100 nm). We can see from Figure 6.5(b) that the three active layers of PPO configuration covers the wavelength range in the near-infrared region from 300 nm to 1150 nm. The fraction of

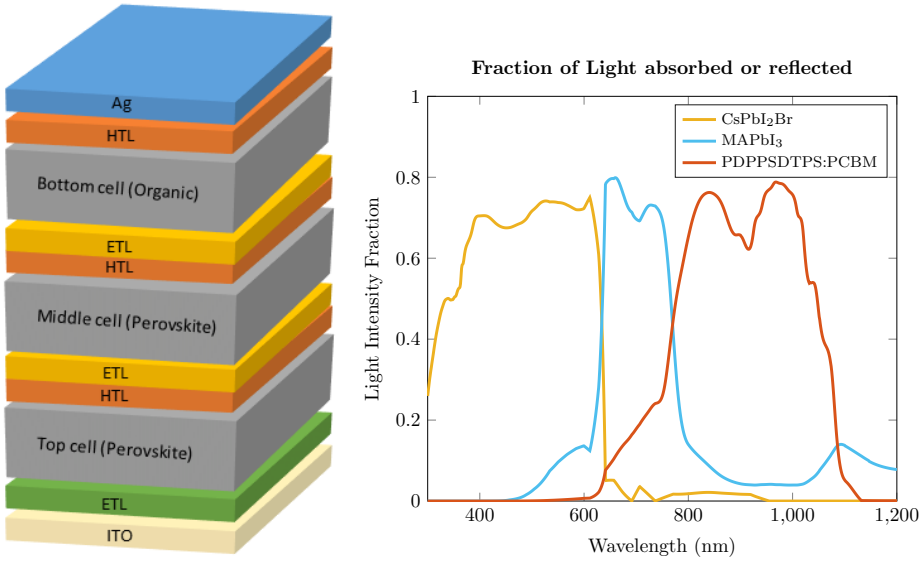

(a) **(b)**

Figure 6.5: (a) Stack diagram of a perovskite-perovskite-organic (PPO) configuration, (b) Fraction of light absorbed by each active layer in the stack.

the light intensity absorbed in this case is ≈ 70%. The PPO configuration shows much improved performance as compared to POP and POR configuration, the calculated J_{sc} equals 10.67 mA cm^{-2}. The overall device efficiency is the highest among the three configurations and calculated to be 25.2% with an FF of 0.82. The V_{oc} is also calculated to as much high as 3.26 V.

6.4 Discussion

For the various bandgap combinations of hybrid perovskite-organic tandem architecture, we observe from Table 6.3 that the efficiency of all the simulated models achieve efficiency of $>$ 10% and approaching ≈ 20%. The maximum J_{sc} is achieved from the bandgaps of 1.75 eV and 1.14 eV for the top and bottom cell, respectively. While the largest bandgap material combination of 2.3 eV for top cell and 1.64 eV for bottom cell achieve highest V_{oc} of 2.59 V with lowest-performing efficiency of 11.5%. The optimum PCE of 19.81% is approaching the already reported efficiency of 24% for perovskite-organic tandem architecture [323]. The optimal bandgap combination for our study is calculated to be 1.7 eV and 1.14 eV for the top and bottom cell, respectively. With further optimization and tuning of organic sub-cell and the inclusion of high performing non-fullerene acceptors, the efficiency is promising to be surpassing the maximum efficiency reported in the literature.

Figure 6.6 shows the PCE compared to FF and J_{sc} vs V_{oc} for the three multi-junction hybrid configurations. We observe that all three kinds of multi-junction configurations

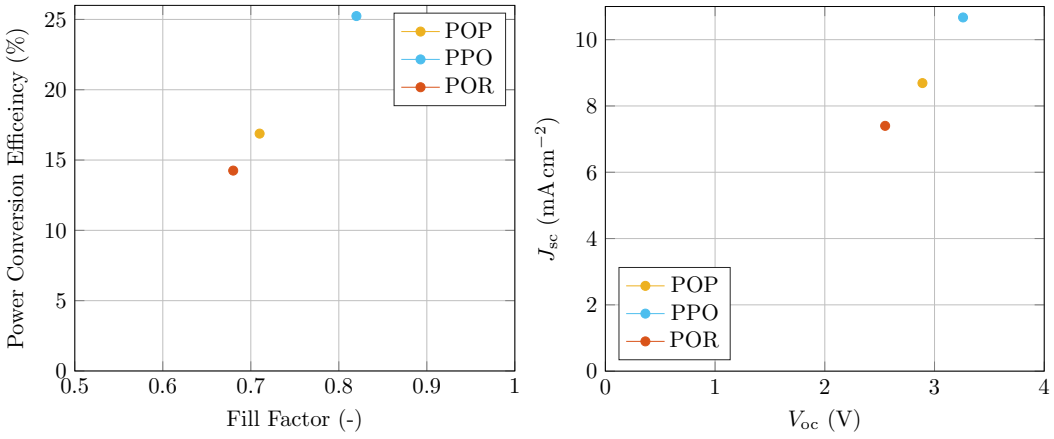

(a) **(b)**

Figure 6.6: (a) Power conversion efficiency vs. fill factor, and (b) J_{sc} vs. V_{oc} for multi-junction solar cells for three configurations POP, PPO and POR.

achieve more than 14% efficiency. However, the PPO configuration has a maximum efficiency of 25.2%. The short circuit density for all the three configurations is in the range of 7 mA cm^{-2} to 11 mA cm^{-2}. It is evident from Figure 6.6 that maximum PCE, V_{oc}, and FF is achieved from PPO configuration with calculated values of 25.2%, 3.26 V, and 0.82, respectively. While, POR configuration has the minimum V_{oc}, PCE and FF. This reduction in the overall performance is due to the moderate to low performance of the organic blends in sub-cell configuration. Therefore, It can be implied that the position of the organic sub-cell has a substantial impact on the device performance of multi-junction hybrid solar cells.

6.5 Conclusion

In conclusion, this work provides a theoretical setting for modelling hybrid perovskite-organic tandem and multi-junction architectures. We showed how kinetic Monte Carlo (kMC) and drift-diffusion tools could be combined to model efficient multi-junction devices in connection with the optical TMM method. The junctions are connected in series in a two-terminal (2T) multi-junction configuration. The individual cells are simulated independently using a generation profile from the optical modelling. The recombination layer is assumed to have minimum/negligible losses, already calculated as a part of optical modelling to simplify the analysis. Our simulation results showed that the hybrid tandem cells could provide high efficiencies if the bandgaps of the sub-cells are tuned optimally. The maximum efficiency of 19.81% was observed for the tandem architecture, $CsPbI_3$ and PDPPSDTPS:PCBM with the bandgap combination of 1.7 eV and 1.14 eV for the

top and the bottom cell, respectively. This tandem configuration is a promising device with the near-infrared absorbance of the solar spectrum. From the multi-junction architecture, $CsPbI_2Br$, $MAPbI_3$, and PDPPSDTPS:PCBM, a perovskite-perovskite-organic (PPO) configuration was observed to achieve the highest efficiency and V_{oc} of 25.2% and 3.26 V. The bandgap combination for the PPO architecture used was 1.92 eV, 1.5 eV, and 1.14 eV for top, middle and bottom sub-cell, respectively. Further optimization of cell bandgaps and high-performance non-fullerene acceptors for organic sub-cells can further enhance the device performance of the modelled architectures.

7 Conclusion

This thesis addresses the different aspects of organic solar cells using 3D kinetic Monte Carlo simulations. The kMC method is well suited to describe the disordered arrangement of organic molecules and track single-particle dynamics for complex bulk-heterojunction morphology. The physical processes governing the device physics of organic solar cells are mapped in the rate equations for kMC, allowing the time-dependent evolution of the solar cell operation. The presented work provides insight into the role of disorder at different interfaces, charge transfer mechanism in dilute donor organic solar cells and a novel multi-scale modelling of hybrid perovskite-organic multi-junction architecture.

The combined role of disorder at donor:acceptor interface and extraction layer has been presented by using kMC simulations. The presented results show the significant degradation of the device performance with increasing interface disorder. At higher disorder, the interface charge densities exceed the bulk densities, significantly increasing nongeminate recombination owing to tail states in the Gaussian density of states. As a result, the fill factor and short-circuit current density are significantly reduced. The combined effect of the interface and the extraction layer order results in substantially linear J-V characteristics with a low fill factor and PCE. Our findings show that the interface disorder has a more detrimental role than the extraction layer. Furthermore, the presented results demonstrate that the energy cascades, which are frequently assumed in mixed phases, may overcome the negative impacts of the interface disorder on the fill factor and PCE. While the energy cascade promotes charge separation, it also functions as an energy barrier for exciton diffusion from the bulk to the mixed interface. Overall, the effect on device efficiency is advantageous for device performance.

Recently, the research focus has been on the charge transport mechanism in a novel active layer morphology, known as dilute donor organic solar cell. The morphology contains a small amount of donor content without any percolation paths for holes towards the contacts. Therefore, how the polymer morphology affects the hole transport needed further insight. The effect of polymer morphology on charge transport mechanism within dilute donor OSCs has been presented. The results demonstrate that a significant hole current may be generated as a result of hole back transfer towards the fullerene matrix. This occurs without the necessity for donor material percolation pathways towards the

contacts. Larger polymer chain lengths exhibit improved behavior at high HOMO level offsets, but smaller polymer chain lengths exhibit significantly decreased performance. The presented results thus highlight the importance of controlling polymer morphology in dilute donor organic solar cells.

Finally, a theoretical modelling of hybrid perovskite-organic tandem and multi-junction architectures is presented. The presented results demonstrate how kinetic Monte Carlo (kMC) and drift-diffusion tools could be combined to model efficient multi-junction devices in connection with the optical Transfer-Matrix method (TMM). The simulation results showed that the hybrid tandem cells could provide high efficiencies if the bandgaps and the thicknesses of the sub-cells are tuned optimally. This tandem/multi-junction configuration is a promising approach to absorb the solar spectrum in a wider region.

Overall, the presented kMC model is a powerful to understand the fundamental processes in an organic solar cell. The work covers broad aspects of the working mechanism in organic solar cells. Investigation of loss mechanisms due to interface and extraction layer energetics is presented. A new insight has been presented to understand the role of polymer morphology in dilute donor organic cells. Finally, by combining kMC and DD models, an optimum design is presented to obtain high-efficiency hybrid perovskite-organic tandem/multi-junction cells.

A Appendix

A.1 Role of Energetics on the Device Performance of Organic Solar Cell

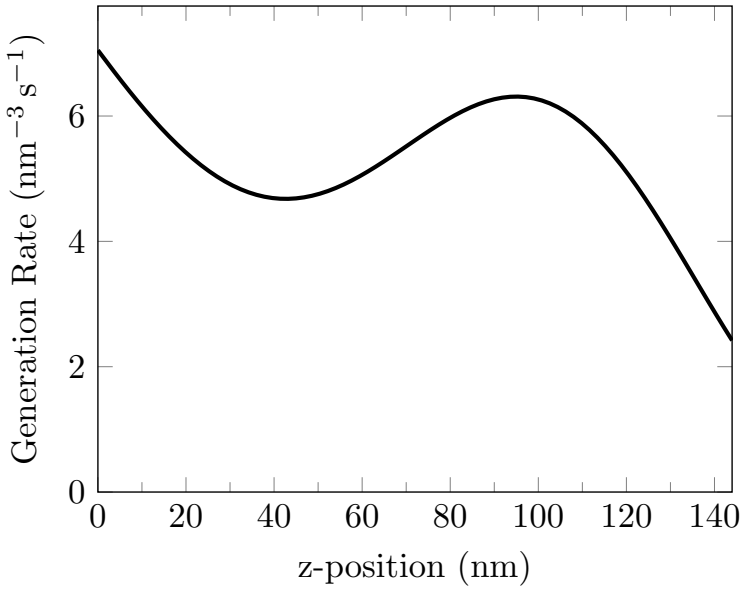

Figure A.1: Generation profile as function of the z-position in the photoactive layer calculated by the transfer matrix method. [203] The generation profile has been calculated exemplary for a ITO/PEDOT:PSS/PTB7:$PC_{71}BM$/Ca/Al device architecture. The optical refractive index of PTB7:$PC_{71}BM$ has been extracted from [363] This generation profile gives a maximum photocurrent density of 12.3 mA cm^{-2}.

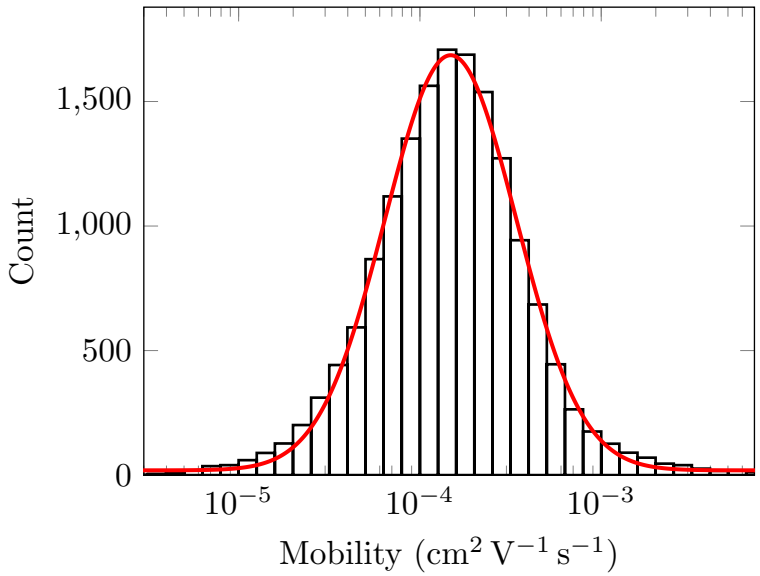

Figure A.2: Distribution of mobility of photo-generated charge carriers in the bulk-heterojunction morphology at maximum power point. The mobility is evaluated using Einstein-Smoluchowski relation $\mu = e/(k_\mathrm{B}T)\cdot\langle z^2\rangle/(2t)$, with electron charge e, thermal energy $k_\mathrm{B}T$, distance z that the charge carrier has traveled in time t before being extracted at the electrodes. The red curve depicts a Gaussian fit of the mobility data with center $1.5 \times 10^{-4}\,\mathrm{cm^2\,V^{-1}\,s^{-1}}$.

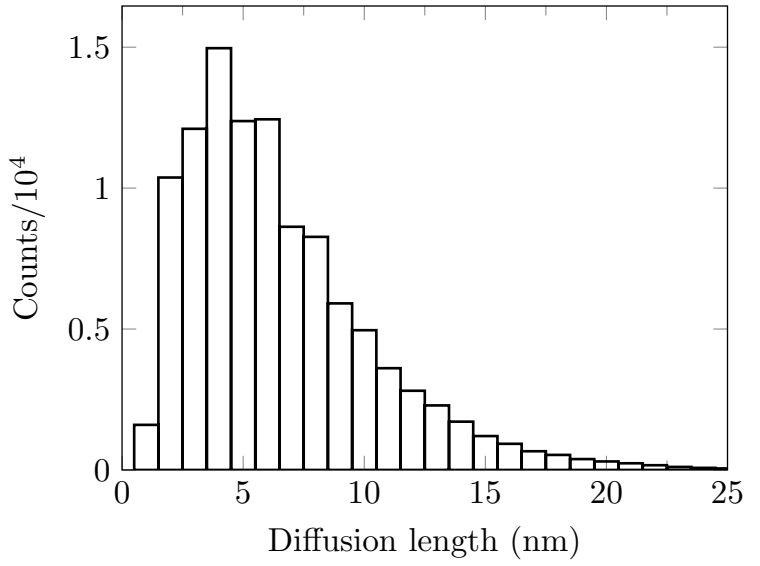

Figure A.3: Distribution of exciton diffusion lengths. The diffusion length is taken as the Euclidean distance between the spot of generation and the spot of decay. Dissociation and other exciton quenching processes were suppressed during this simulation.

		σ_{int}(meV)				
		50	62.5	75	87.5	100
σ_{ext}(meV)	50	10.13	10.23	10.10	8.79	7.03
	62.5	10.00	10.00	10.00	8.48	6.62
	75	9.77	9.94	9.50	8.63	6.28
	87.5	9.63	9.89	9.55	8.79	6.18
	100	9.62	9.75	9.41	8.60	6.14

Table A.1: Short-circuit current density J_{sc} (mA/cm^2) of the model OSC with different σ_{int} and σ_{ext}.

		σ_{int}(meV)				
		50	62.5	75	87.5	100
σ_{ext}(meV)	50	0.80	0.79	0.79	0.78	0.77
	62.5	0.78	0.78	0.77	0.76	0.73
	75	0.76	0.76	0.72	0.70	0.67
	87.5	0.73	0.69	0.69	0.63	0.59
	100	0.66	0.66	0.58	0.57	0.49

Table A.2: Open-circuit voltage V_{oc} (V) of the model OSC with different σ_{int} and σ_{ext}.

		σ_{int}(meV)				
		50	62.5	75	87.5	100
σ_{ext}(meV)	50	0.56	0.55	0.46	0.37	0.33
	62.5	0.56	0.54	0.46	0.38	0.32
	75	0.57	0.53	0.51	0.37	0.35
	87.5	0.59	0.55	0.48	0.39	0.35
	100	0.58	0.55	0.52	0.35	0.34

Table A.3: Fill factor of the model OSC with different σ_{int} and σ_{ext}.

		σ_{int}(meV)				
		50	62.5	75	87.5	100
σ_{ext}(meV)	50	4.48	4.42	3.66	2.55	1.80
	62.5	4.40	4.23	3.52	2.41	1.56
	75	4.25	3.96	3.48	2.29	1.47
	87.5	4.13	3.78	3.18	2.19	1.25
	100	3.68	3.56	2.86	1.72	1.01

Table A.4: Power conversion efficiency (%) of the model OSC with different σ_{int} and σ_{ext}.

σ_{ext}(meV) \ σ_{int}(meV)	50	62.5	75	87.5	100
50	2.09×10^{16}	2.14×10^{16}	2.25×10^{16}	1.43×10^{16}	1.22×10^{16}
62.5	2.37×10^{16}	2.41×10^{16}	2.13×10^{16}	1.53×10^{16}	1.38×10^{16}
75	2.52×10^{16}	2.85×10^{16}	2.74×10^{16}	1.91×10^{16}	1.53×10^{16}
87.5	3.84×10^{16}	3.56×10^{16}	3.44×10^{16}	2.81×10^{16}	1.71×10^{16}
100	5.17×10^{16}	5.32×10^{16}	5.49×10^{16}	5.44×10^{16}	4.25×10^{16}

Table A.5: Charge density in the bulk $n_{\text{bulk}}\,(\text{cm}^{-3})$ of the model OSC with different σ_{int} and σ_{ext}.

σ_{ext}(meV) \ σ_{int}(meV)	50	62.5	75	87.5	100
50	2.43×10^{16}	6.88×10^{16}	1.80×10^{17}	3.79×10^{17}	6.32×10^{17}
62.5	2.53×10^{16}	6.60×10^{16}	1.88×10^{17}	3.98×10^{17}	7.03×10^{17}
75	2.53×10^{16}	8.10×10^{16}	2.07×10^{17}	4.03×10^{17}	7.52×10^{17}
87.5	4.04×10^{16}	1.02×10^{17}	2.32×10^{17}	4.86×10^{17}	8.11×10^{17}
100	5.65×10^{16}	1.39×10^{17}	3.45×10^{17}	7.20×10^{17}	9.41×10^{17}

Table A.6: Charge density at the interface $n_{\text{int}}\,(\text{cm}^{-3})$ of the model OSC with different σ_{int} and σ_{ext}.

σ_{ext}(meV) \ σ_{int}(meV)	50	62.5	75	87.5	100
50	1.00×10^{4}	3.10×10^{4}	7.50×10^{4}	1.27×10^{5}	2.04×10^{5}
62.5	1.80×10^{4}	2.20×10^{4}	7.70×10^{4}	1.43×10^{5}	1.87×10^{5}
75	1.30×10^{4}	4.00×10^{4}	7.40×10^{4}	1.31×10^{5}	1.85×10^{5}
87.5	1.80×10^{4}	2.60×10^{4}	6.80×10^{4}	1.14×10^{5}	2.11×10^{5}
100	1.20×10^{4}	4.70×10^{4}	8.70×10^{4}	1.37×10^{5}	1.96×10^{5}

Table A.7: Geminate recombination rate $R_{\text{gem}}(\text{s}^{-1})$ of the model OSC with different σ_{int} and σ_{ext}.

σ_{ext}(meV) \ σ_{int}(meV)	50	62.5	75	87.5	100
50	2.50×10^{4}	1.34×10^{5}	6.01×10^{5}	1.36×10^{6}	1.84×10^{6}
62.5	2.70×10^{4}	8.00×10^{4}	6.65×10^{5}	1.37×10^{6}	1.78×10^{6}
75	2.50×10^{4}	2.20×10^{5}	6.86×10^{5}	1.32×10^{6}	1.90×10^{6}
87.5	3.70×10^{4}	2.28×10^{5}	7.22×10^{5}	1.47×10^{6}	2.39×10^{6}
100	6.20×10^{4}	3.83×10^{5}	1.41×10^{6}	2.64×10^{6}	2.97×10^{6}

Table A.8: Nongeminate recombination rate $R_{\text{nongem}}(\text{s}^{-1})$ of the model OSC with different σ_{int} and σ_{ext}.

A.2 Charge Transport and Impact of Morphology in Dilute Donor OSCs

ΔE_{HOMO} (eV)	10 nm				100 nm			
	j_{sc}(mA cm^{-2})	V_{oc}(V)	FF	PCE (%)	j_{sc}(mA cm^{-2})	V_{oc}(V)	FF	PCE(%)
0.2	3.37	0.62	0.34	0.71	2.95	0.62	0.37	0.69
0.5	0.51	0.34	0.32	0.05	2.01	0.59	0.32	0.39

Table A.9: Device performance parameters for polymer chain lengths of 10 nm and 100 nm at 0.2 eV and 0.5 eV.

A.3 Tandem/Multi-junction Modelling of hybrid perovskite-organic Device

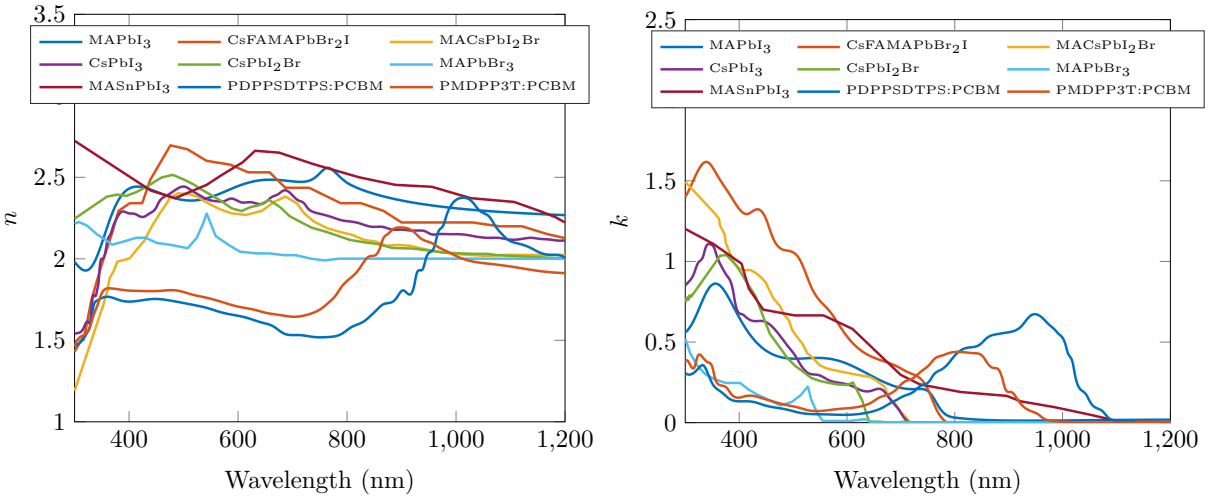

(a) (b)

Figure A.4: The refraction index n and k values for the active layers used for tandem/multi-junction modelling.

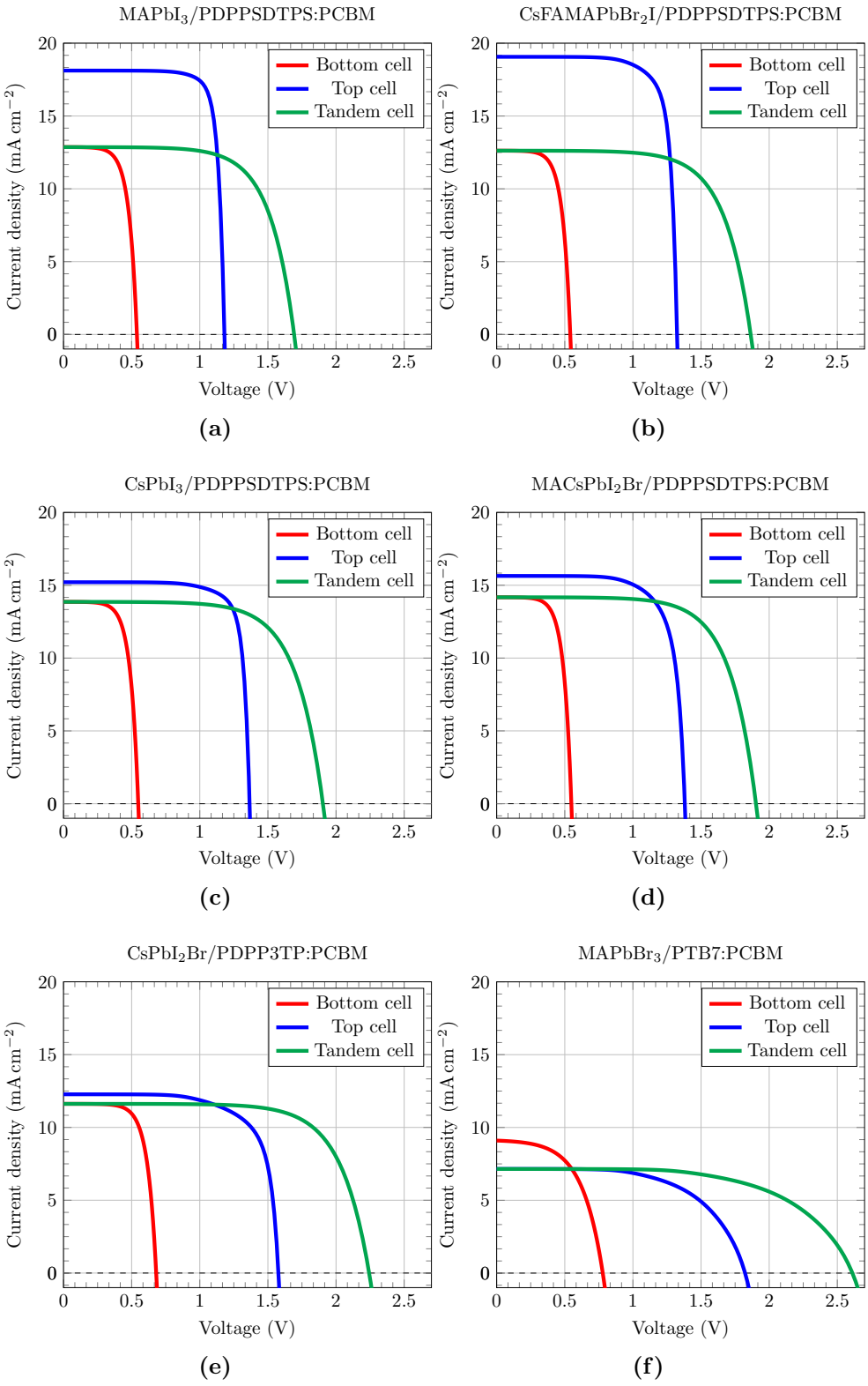

Figure A.5: $J - V$ Characteristic curves for all the tandem configurations.

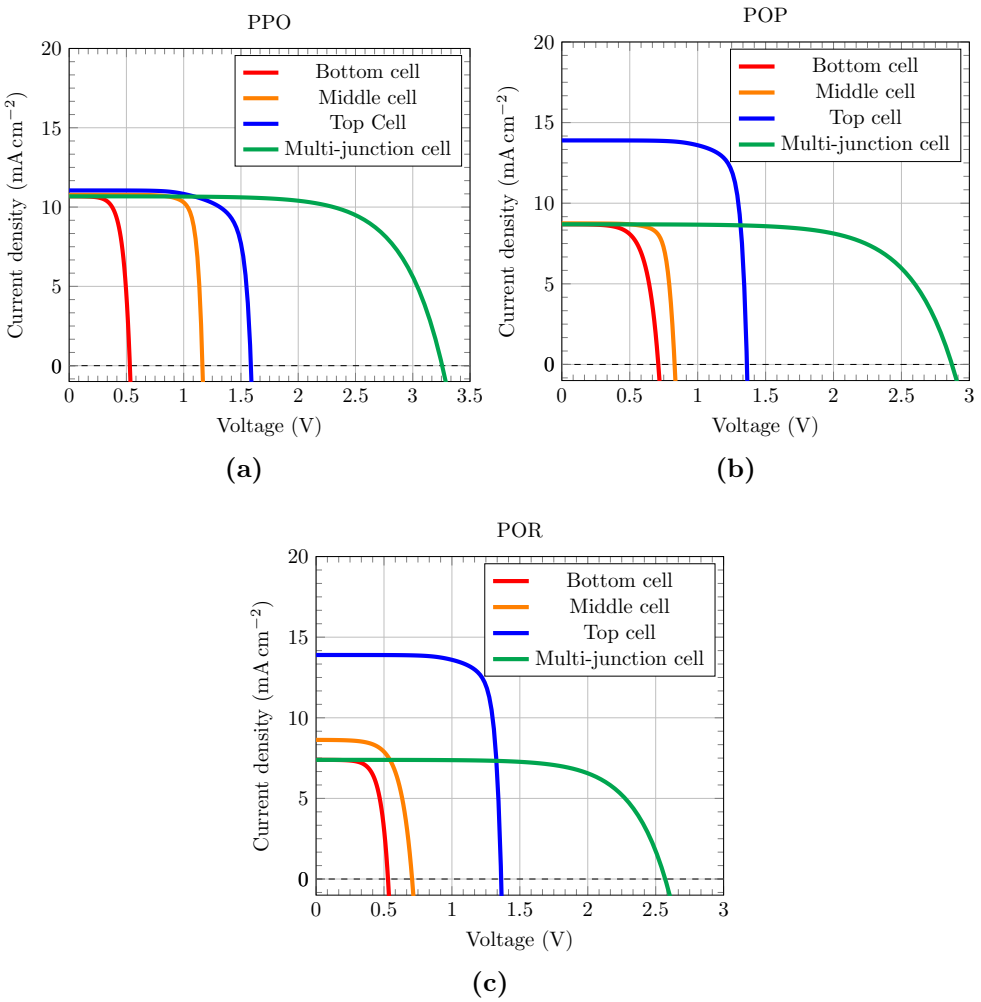

Figure A.6: $J - V$ Characteristic curves for all the multi-junction configurations.

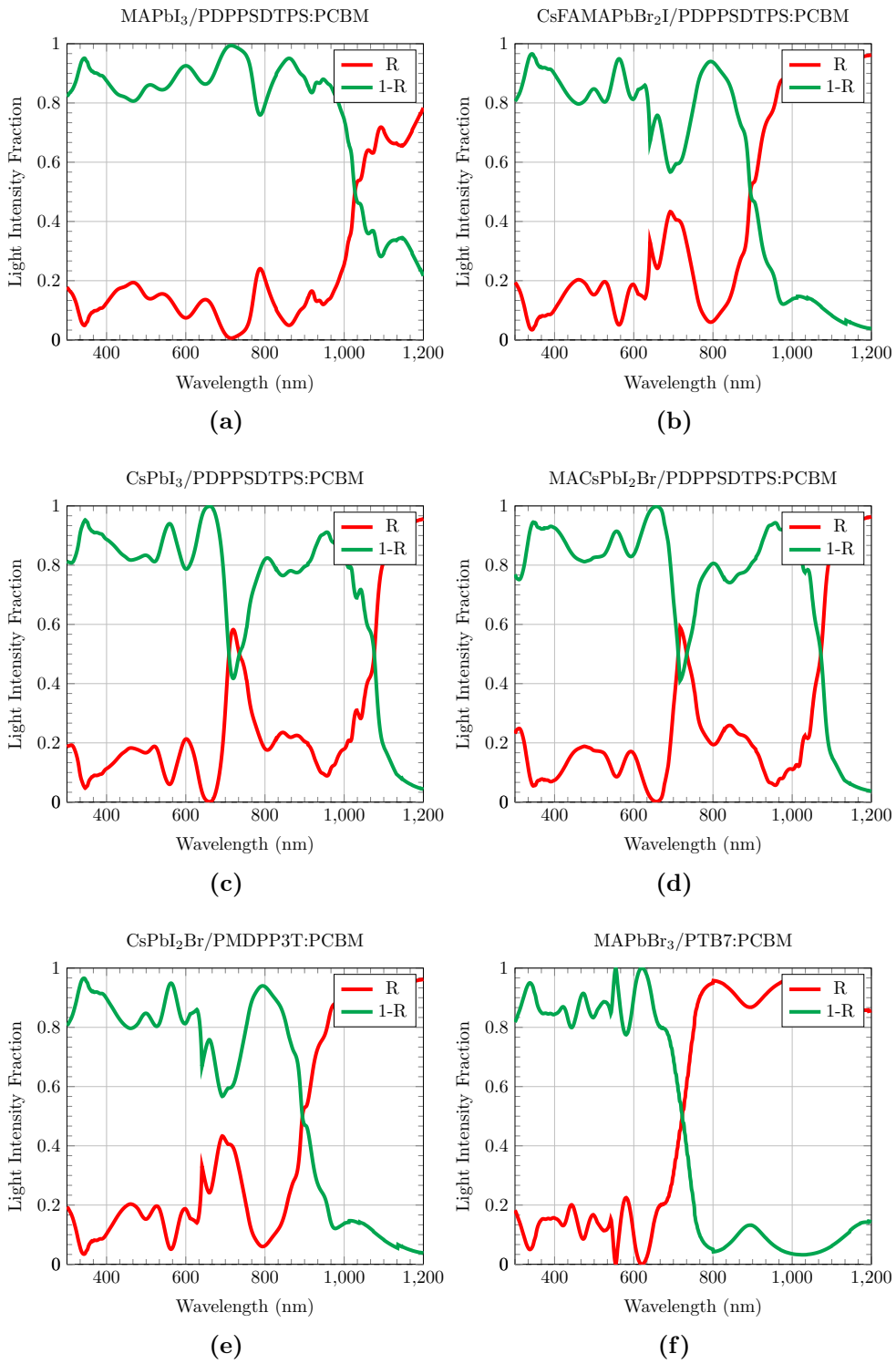

Figure A.7: Reflection (R) and transmission (1-R) spectrum at the interface for all the tandem configurations.

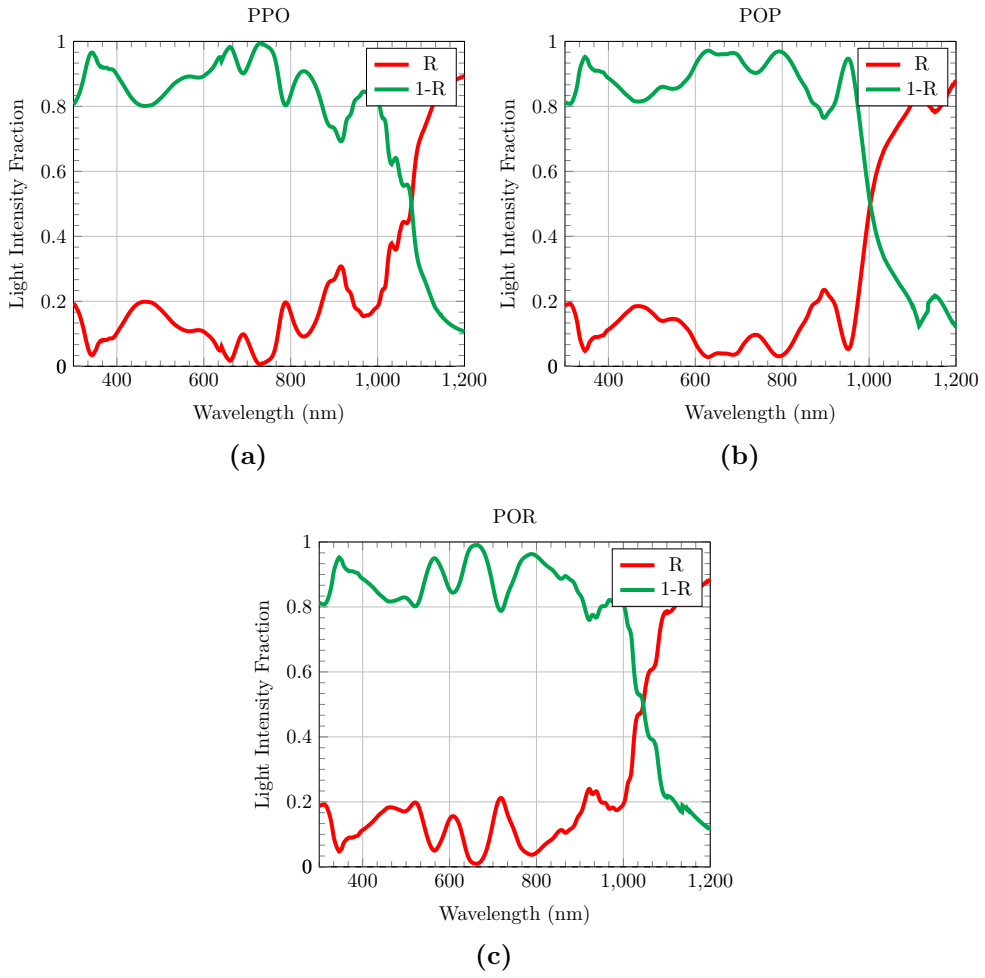

Figure A.8: Reflection (R) and transmission (1-R) spectrum at the interface for all the tandem configurations.

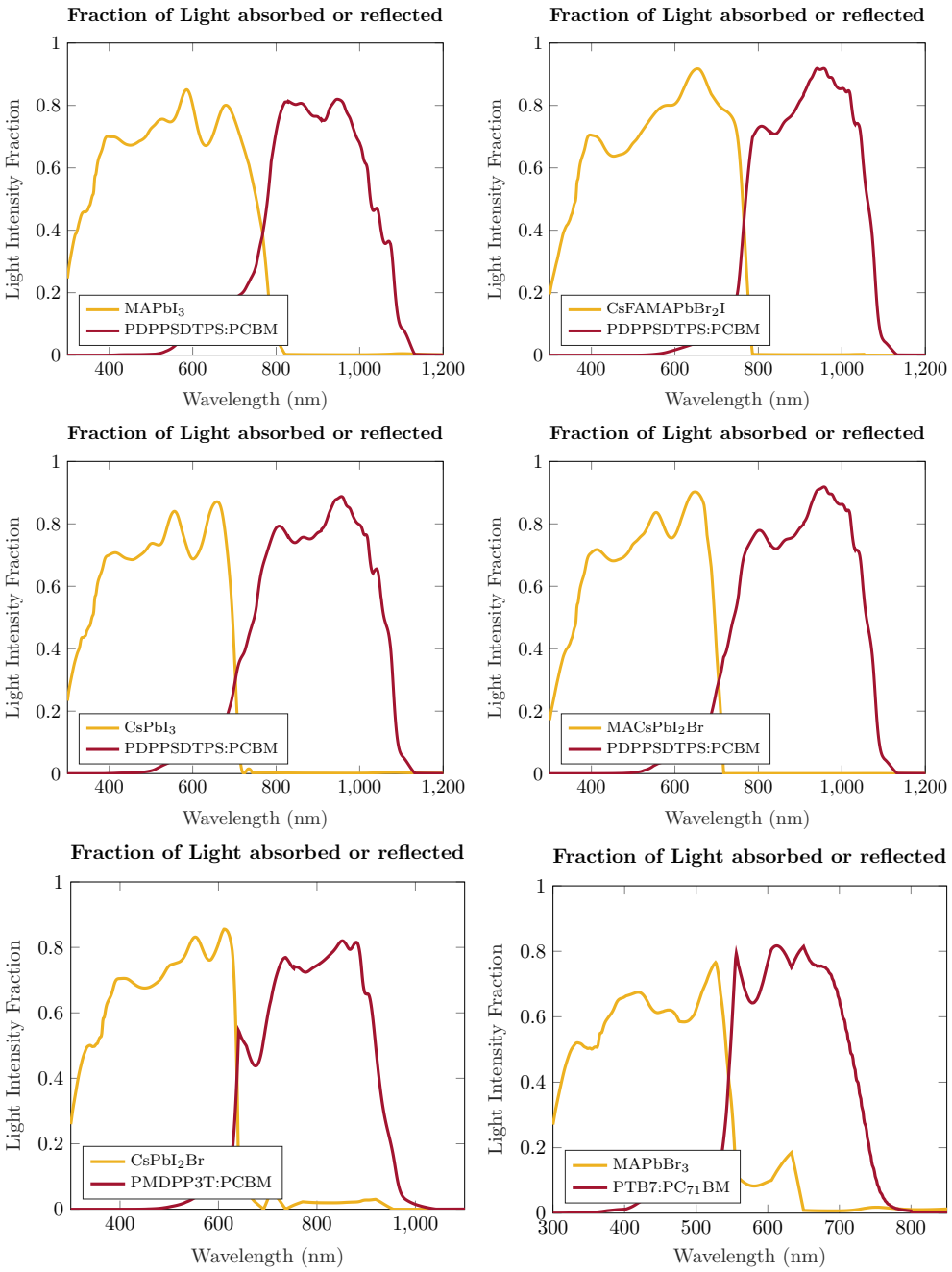

Figure A.9: Fraction of light intensity absorbed by hybrid tandem cell configurations.

List of Figures

List of Tables

Bibliography

[1] V. Smil, *Energy and Civilization* (The MIT Press, 2017).

[2] C. Brabec, V. Dyakonov, and U. Scherf, eds., *Organic Photovoltaics* (Wiley, 2008).

[3] W. HERMANN, "Quantifying global exergy resources," Energy **31**, 1685–1702 (2006).

[4] D. M. Chapin, C. S. Fuller, and G. L. Pearson, "A new silicon p-n junction photocell for converting solar radiation into electrical power," J. Appl. Phys. **25**, 676–677 (1954).

[5] M. A. Green, "How did solar cells get so cheap?" Joule **3**, 631–633 (2019).

[6] M. A. Green, E. D. Dunlop, J. Hohl-Ebinger, M. Yoshita, N. Kopidakis, and X. Hao, "Solar cell efficiency tables (version 58)," Progress in Photovoltaics: Research and Applications **29**, 657–667 (2021).

[7] W. Yang, Z. Luo, R. Sun, J. Guo, T. Wang, Y. Wu, W. Wang, J. Guo, Q. Wu, M. Shi, H. Li, C. Yang, and J. Min, "Simultaneous enhanced efficiency and thermal stability in organic solar cells from a polymer acceptor additive," Nat. Commun. **11** (2020).

[8] C. W. Tang, "Two−layer organic photovoltaic cell," Appl. Phys. Lett. **48**, 183–185 (1986).

[9] N. S. Sariciftci, L. Smilowitz, A. J. Heeger, and F. Wudl, "Photoinduced electron transfer from a conducting polymer to Buckminsterfullerene," Science **258**, 1474–1476 (1992).

[10] L. Smilowitz, N. S. Sariciftci, R. Wu, C. Gettinger, A. J. Heeger, and F. Wudl, "Photoexcitation spectroscopy of conducting-polymer–c60composites: Photoinduced electron transfer," Phys. Rev. B **47**, 13835–13842 (1993).

[11] G. Yu, J. Gao, J. C. Hummelen, F. Wudl, and A. J. Heeger, "Polymer photovoltaic cells: Enhanced efficiencies via a network of internal donor-acceptor heterojunctions," Science **270**, 1789–1791 (1995).

[12] S. B. Sapkota, A. Spies, B. Zimmermann, I. Dürr, and U. Würfel, "Promising long-term stability of encapsulated ITO-free bulk-heterojunction organic solar cells under different aging conditions," Sol. Energy Mater. Sol. Cells **130**, 144–150 (2014).

[13] C. Deibel and V. Dyakonov, "Polymer−Fullerene bulk heterojunction solar cells," Rep. Prog. Phys. **73**, 096401 (2010).

[14] T. Albes and A. Gagliardi, "Influence of permittivity and energetic disorder on the spatial charge carrier distribution and recombination in organic bulk-heterojunctions," Phys. Chem. Chem. Phys. **19**, 20974 (2017).

[15] T. Albes and A. Gagliardi, "Charge pair separation dynamics in organic bulk-heterojunction solar cells," Adv. Theory Simul. **1**, 1800032 (2018).

[16] U. Würfel, D. Neher, A. Spies, and S. Albrecht, "Impact of charge transport on current–voltage characteristics and power-conversion efficiency of organic solar cells," Nat. Commun. **6** (2015).

[17] N. Felekidis, A. Melianas, and M. Kemerink, "Nonequilibrium drift-diffusion model for organic semiconductor devices," Phys. Rev. B **94** (2016).

[18] A. Gagliardi, S. Wang, and T. Albes, "Simulation of charge carrier mobility unbalance in organic solar cells," Org. Electron. **59**, 171–176 (2018).

[19] D. Rossi, F. Santoni, M. A. D. Maur, and A. D. Carlo, "A multiparticle drift-diffusion model and its application to organic and inorganic electronic device simulation," IEEE Trans. Electron Devices **66**, 2715–2722 (2019).

[20] H. Bässler, "Charge transport in disordered organic photoconductors: A Monte Carlo simulation study," Phys. Status Solidi B **175**, 15 (1993).

[21] A. Melianas, V. Pranculis, D. Spoltore, J. Benduhn, O. Inganäs, V. Gulbinas, K. Vandewal, and M. Kemerink, "Charge transport in pure and mixed phases in organic solar cells," Adv. Energy Mater. **7**, 1700888 (2017).

[22] C. Groves, "Simulating charge transport in organic semiconductors and devices: a review," Rep. Prog. Phys. **80**, 026502 (2016).

[23] S. Athanasopoulos, E. V. Emelianova, A. B. Walker, and D. Beljonne, "Exciton diffusion in energetically disordered organic materials," Phys. Rev. B **80** (2009).

[24] K. Feron, X. Zhou, W. Belcher, and P. Dastoor, "Exciton transport in organic semiconductors: Förster resonance energy transfer compared with a simple random walk," J. Appl. Phys. **111**, 044510 (2012).

[25] C. Groves, R. A. Marsh, and N. C. Greenham, "Monte Carlo modeling of geminate recombination in polymer-polymer photovoltaic devices," J. Chem. Phys. **129**, 114903 (2008).

[26] C. Groves, R. G. Kimber, and A. B. Walker, "Simulation of loss mechanisms in organic solar cells: A description of the mesoscopic Monte Carlo technique and an evaluation of the first reaction method," J. Chem. Phys. **133**, 144110 (2010).

[27] C. Groves, "Developing understanding of organic photovoltaic devices: Kinetic Monte Carlo models of geminate and non-geminate recombination, charge transport and charge extraction," Energy Environ. Sci. **6**, 3202–3217 (2013).

[28] R. G. E. Kimber, E. N. Wright, S. E. J. O'Kane, A. B. Walker, and J. C. Blakesley, "Mesoscopic kinetic Monte Carlo modeling of organic photovoltaic device characteristics," Phys. Rev. B: Condens. Matter Mater. Phys. **86**, 235206 (2012).

[29] L. Meng, Y. Shang, Q. Li, Y. Li, X. Zhan, Z. Shuai, R. G. E. Kimber, and A. B. Walker, "Dynamic Monte Carlo simulation for highly efficient polymer blend photovoltaics," J. Phys. Chem. B **114**, 36–41 (2009).

[30] P. K. Watkins, A. B. Walker, and G. L. Verschoor, "Dynamical Monte Carlo modelling of organic solar cells: The dependence of internal quantum efficiency on morphology," Nano Lett. **5**, 1814–1818 (2005).

[31] T. Albes, P. Lugli, and A. Gagliardi, "Investigation of the blend morphology in bulk-heterojunction organic solar cells," IEEE Trans. Nanotechnol. **15**, 281–288 (2016).

[32] M. Casalegno, G. Raos, and R. Po, "Methodological assessment of kinetic Monte Carlo simulations of organic photovoltaic devices: The treatment of electrostatic interactions," J. Chem. Phys. **132**, 094705 (2010).

[33] W. Kaiser, T. Albes, and A. Gagliardi, "Charge carrier mobility of disordered organic semiconductors with correlated energetic and spatial disorder," Physical Chemistry Chemical Physics **20**, 8897–8908 (2018).

[34] N. Vukmirović and L.-W. Wang, "Charge carrier motion in disordered conjugated polymers: A multiscale ab initio study," Nano Lett. **9**, 3996–4000 (2009).

[35] M. Rinderle, W. Kaiser, A. Mattoni, and A. Gagliardi, "Machine-learned charge transfer integrals for multiscale simulations in organic thin films," J. Phys. Chem. C **124**, 17733–17743 (2020).

[36] K. Hussain, W. Kaiser, and A. Gagliardi, "Role of the interface and extraction layer energetics in organic solar cells," J. Phys. Chem. C **125**, 5447–5457 (2021).

[37] K. Hussain, W. Kaiser, and A. Gagliardi, "Role of interface energetics and off-diagonal disorder in bulk heterojunction organic solar cells," in "2020 IEEE 20th International Conference on Nanotechnology (IEEE-NANO)," (IEEE, 2020).

[38] K. Hussain, W. Kaiser, and A. Gagliardi, "Effect of polymer morphology on dilute donor organic solar cells," J. Phys. Chem. C **124**, 3517–3528 (2020).

[39] A. Becquerel, "Memoire sur les effects d'electriques produits sous l'influence des rayons solaires," Annalen der Physick und Chemie **54**, 35–42 (1841).

[40] W. Smith, "Effect of light on selenium during the passage of an electric current*," Nature **7**, 303–303 (1873).

[41] A. Einstein, "Über einen die erzeugung und verwandlung des lichtes betreffenden heuristischen gesichtspunkt," Annalen der Physik **322**, 132–148 (1905).

[42] T. Albes, "Kinetic Monte Carlo simulations of organic solar cells," Dissertation, Technical University of Munich (2019).

[43] U. Rau and T. Kirchartz, "Charge carrier collection and contact selectivity in solar cells," Adv. Mat. Interfaces **6**, 1900252 (2019).

[44] R. Brendel and R. Peibst, "Contact selectivity and efficiency in crystalline silicon photovoltaics," IEEE J. Photovolt. **6**, 1413–1420 (2016).

[45] U. Wurfel, A. Cuevas, and P. Wurfel, "Charge carrier separation in solar cells," IEEE J. of Photovolt. **5**, 461–469 (2015).

[46] B. Lim, T. Brendemuhl, T. Dullweber, and R. Brendel, "Loss analysis of n-type passivated emitter rear totally diffused back-junction silicon solar cells with efficiencies up to 21.2%," IEEE J. Photovolt. **6**, 447–453 (2016).

[47] K. Kennerud, "Analysis of performance degradation in CdS solar cells," IEEE Trans. Aerosp. Electron. Syst. **AES-5**, 912–917 (1969).

[48] T. Easwarakhanthan, J. Bottin, I. Bouhouch, and C. Boutrit, "Nonlinear minimization algorithm for determining the solar cell parameters with microcomputers," Int. J. Sol. Energy **4**, 1–12 (1986).

[49] D. Chan and J. Phang, "Analytical methods for the extraction of solar-cell single- and double-diode model parameters from i-v characteristics," IEEE Trans. Electron Devices **34**, 286–293 (1987).

[50] A. K. Das, "Analytical derivation of explicit j–v model of a solar cell from physics based implicit model," Sol. Energy **86**, 26–30 (2012).

[51] M. Villalva, J. Gazoli, and E. Filho, "Comprehensive approach to modeling and simulation of photovoltaic arrays," IEEE Trans. Power Electron. **24**, 1198–1208 (2009).

[52] A. D. Printz and D. J. Lipomi, "Competition between deformability and charge transport in semiconducting polymers for flexible and stretchable electronics," Appl. Phys. Rev. **3**, 021302 (2016).

[53] S. Sze and K. K. Ng, *Physics of Semiconductor Devices* (John Wiley & Sons, Inc., 2006).

[54] P. Würfel, *Physics of Solar Cells* (Wiley, 2005).

[55] W. Shockley and H. J. Queisser, "Detailed balance limit of efficiency of p-n junction solar cells," J. Appl. Phys. **32**, 510–519 (1961).

[56] T. Tiedje, E. Yablonovitch, G. Cody, and B. Brooks, "Limiting efficiency of silicon solar cells," IEEE Trans. Electron Devices **31**, 711–716 (1984).

[57] T. Kirchartz, K. Taretto, and U. Rau, "Efficiency limits of organic bulk heterojunction solar cells," J. Phys. Chem. C **113**, 17958–17966 (2009).

[58] T. Kirchartz, J. Mattheis, and U. Rau, "Detailed balance theory of excitonic and bulk heterojunction solar cells," Phys. Rev. B **78** (2008).

[59] N. C. Giebink, G. P. Wiederrecht, M. R. Wasielewski, and S. R. Forrest, "Thermodynamic efficiency limit of excitonic solar cells," Phys. Rev. B **83** (2011).

[60] L. J. A. Koster, S. E. Shaheen, and J. C. Hummelen, "Pathways to a new efficiency regime for organic solar cells," Adv. Energy Mat. **2**, 1246–1253 (2012).

[61] M. Gruber, J. Wagner, K. Klein, U. Hörmann, A. Opitz, M. Stutzmann, and W. Brütting, "Thermodynamic efficiency limit of molecular donor-acceptor solar cells and its application to Diindenoperylene/C_{60}-based planar heterojunction devices," Adv. Energy Mat. **2**, 1100–1108 (2012).

[62] B. O'Regan and M. Grätzel, "A low-cost, high-efficiency solar cell based on dye-sensitized colloidal TiO2 films," Nature **353**, 737–740 (1991).

[63] A. Kojima, K. Teshima, Y. Shirai, and T. Miyasaka, "Organometal halide perovskites as visible-light sensitizers for photovoltaic cells," J. Am. Chem. Soc. **131**, 6050–6051 (2009).

[64] L. Lu, T. Zheng, Q. Wu, A. M. Schneider, D. Zhao, and L. Yu, "Recent advances in bulk heterojunction polymer solar cells," Chem. Rev. **115**, 12666 (2015).

[65] S. Günes, H. Neugebauer, and N. S. Sariciftci, "Conjugated polymer-based organic solar cells," Chem. Rev. **107**, 1324–1338 (2007).

[66] G. Dennler, M. C. Scharber, and C. J. Brabec, "Polymer−Fullerene bulk-heterojunction solar cells," Adv. Mater. **21**, 1323–1338 (2009).

[67] R. Søndergaard, M. Hösel, D. Angmo, T. T. Larsen-Olsen, and F. C. Krebs, "Roll-to-roll fabrication of polymer solar cells," Mater. Today **15**, 36–49 (2012).

[68] Y.-J. Heo, Y.-S. Jung, K. Hwang, J.-E. Kim, J.-S. Yeo, S. Lee, Y.-J. Jeon, D. Lee, and D.-Y. Kim, "Small-molecule organic photovoltaic modules fabricated via Halogen−Free solvent system with roll-to-roll compatible scalable printing method," ACS Appl. Mater. Interfaces **9**, 39519–39525 (2017).

[69] J. Kalowekamo and E. Baker, "Estimating the manufacturing cost of purely organic solar cells," Sol. Energy **83**, 1224–1231 (2009).

[70] N. Espinosa, M. Hösel, D. Angmo, and F. C. Krebs, "Solar cells with one-day energy payback for the factories of the future," Energy Environ. Sci. **5**, 5117–5132 (2012).

[71] S. Lizin, S. V. Passel, E. D. Schepper, W. Maes, L. Lutsen, J. Manca, and D. Vanderzande, "Life cycle analyses of organic photovoltaics: a review," Energy Environ. Sci. **6**, 3136 (2013).

[72] S. E. Shaheen, C. J. Brabec, N. S. Sariciftci, F. Padinger, T. Fromherz, and J. C. Hummelen, "2.5% efficient organic plastic solar cells," Appl. Phys. Lett. **78**, 841–843 (2001).

[73] R. F. Service, "Outlook brightens for plastic solar cells," Science **332**, 293–293 (2011).

[74] F. I. for Solar Energy Systems (ISE), "Photovoltaic report," `https://www.ise.fraunhofer.de/content/dam/ise/de/documents/publications/studies/Photovoltaics-Report.pdf` (2021).

[75] O. H. LeBlanc, "Hole and electron drift mobilities in anthracene," J. Chem. Phys. **33**, 626–626 (1960).

[76] M. Pope, H. P. Kallmann, and P. Magnante, "Electroluminescence in organic crystals," J. Chem. Phys. **38**, 2042–2043 (1963).

[77] H. Shirakawa, E. J. Louis, A. G. MacDiarmid, C. K. Chiang, and A. J. Heeger, "Synthesis of electrically conducting organic polymers: halogen derivatives of polyacetylene, (CH)x," J. Chem. Soc., Chem. Commun. **.**, 578 (1977).

[78] W. Brütting, ed., *Physics of Organic Semiconductors* (Wiley, 2005).

[79] U. Hörmann, "Voc from a morphology point of view: On the open circuit voltage of polycrystalline organic heterojunction solar cells," Dissertation, Universität Augsburg (2014).

[80] P. Kumar, ed., *ORGANIC SOLAR CELLS: Device Physics, Processing, Degradation, and Preventions* (CRC Press, Taylor & Francis Group, 2017).

[81] H. Naito, ed., *Organic Semiconductors for Optoelectronics* (Wiley, 2021).

[82] A. Miller and E. Abrahams, "Impurity conduction at low concentrations," Phys. Rev. **120**, 745–755 (1960).

[83] V. Podzorov, E. Menard, J. A. Rogers, and M. E. Gershenson, "Hall effect in the accumulation layers on the surface of organic semiconductors," J. Chem. Phys. **95** (2005).

[84] C. Liu, T. Minari, X. Lu, A. Kumatani, K. Takimiya, and K. Tsukagoshi, "Solution-processable organic single crystals with bandlike transport in field-effect transistors," Adv. Mater. **23**, 523–526 (2010).

[85] J. Dong and C. Wu, "Crossover from hopping to band-like transport in crystalline organic semiconductors: The effect of shallow traps," J. Chem. Phys. **150**, 044903 (2019).

[86] Y. C. Cheng, R. J. Silbey, D. A. da Silva Filho, J. P. Calbert, J. Cornil, and J. L. Brédas, "Three-dimensional band structure and bandlike mobility in oligoacene single crystals: A theoretical investigation," J. Chem. Phys. **118**, 3764–3774 (2003).

[87] K. Marumoto, S. ichi Kuroda, T. Takenobu, and Y. Iwasa, "Spatial extent of wave functions of gate-induced hole carriers in pentacene field-effect devices as investigated by electron spin resonance," Phys. Rev. Lett. **97** (2006).

[88] V. Podzorov, E. Menard, A. Borissov, V. Kiryukhin, J. A. Rogers, and M. E. Gershenson, "Intrinsic charge transport on the surface of organic semiconductors," Phy. Rev. Lett. **93** (2004).

[89] O. Ostroverkhova, D. G. Cooke, F. A. Hegmann, J. E. Anthony, V. Podzorov, M. E. Gershenson, O. D. Jurchescu, and T. T. M. Palstra, "Ultrafast carrier dynamics in pentacene, functionalized pentacene, tetracene, and rubrene single crystals," Appl. Phys. Lett. **88**, 162101 (2006).

[90] S. P. Senanayak, A. Z. Ashar, C. Kanimozhi, S. Patil, and K. S. Narayan, "Room-temperature bandlike transport and hall effect in a high-mobility ambipolar polymer," Phys. Rev. B **91** (2015).

[91] O. Rubel, S. D. Baranovskii, P. Thomas, and S. Yamasaki, "Concentration dependence of the hopping mobility in disordered organic solids," Phys. Rev. B **69** (2004).

[92] W. S. C. Roelofs, S. G. J. Mathijssen, R. A. J. Janssen, D. M. de Leeuw, and M. Kemerink, "Accurate description of charge transport in organic field effect transistors using an experimentally extracted density of states," Phys. Rev. B **85** (2012).

[93] R. Marcus and N. Sutin, "Electron transfers in chemistry and biology," Biochimica et Biophysica Acta (BBA) - Reviews on Bioenergetics **811**, 265–322 (1985).

[94] H. Oberhofer, K. Reuter, and J. Blumberger, "Charge transport in molecular materials: An assessment of computational methods," Chem. Rev. **117**, 10319–10357 (2017).

[95] G. Kemeny and B. Rosenberg, "Small polarons in organic and biological semiconductors," J. Chem. Phys. **53**, 3549–3551 (1970).

[96] H. Tamura, M. Tsukada, H. Ishii, N. Kobayashi, and K. Hirose, "Roles of intramolecular and intermolecular electron-phonon coupling on the formation and transport of large polarons in organic semiconductors," Phys. Rev. B **86** (2012).

[97] M. Knupfer, "Exciton binding energies in organic semiconductors," Appl. Phys. A **77**, 623–626 (2003).

[98] B. Zakharchenya and S. Permogorov, "Excitons in crystals," in "Encyclopedia of Condensed Matter Physics," (Elsevier, 2005), pp. 171–179.

[99] C. Deibel, T. Strobel, and V. Dyakonov, "Origin of the efficient polaron-pair dissociation in Polymer−Fullerene blends," Phys. Rev. Lett. **103**, 036402 (2009).

[100] S. M. Menke, N. A. Ran, G. C. Bazan, and R. H. Friend, "Understanding energy loss in organic solar cells: Toward a new efficiency regime," Joule **2**, 25–35 (2018).

[101] P. Bi and X. Hao, "Versatile ternary approach for novel organic solar cells: A review," Sol. RRL **3**, 1800263 (2018).

[102] H. Sun, X. Guo, and A. Facchetti, "High-performance n-type polymer semiconductors: Applications, recent development, and challenges," Chem **6**, 1310–1326 (2020).

[103] Z. He, H. Wu, and Y. Cao, "Recent advances in polymer solar cells: Realization of high device performance by incorporating water/alcohol-soluble conjugated polymers as electrode buffer layer," Adv. Mat. **26**, 1006–1024 (2013).

[104] G. Xu, H. Rao, X. Liao, Y. Zhang, Y. Wang, Z. Xing, T. Hu, L. Tan, L. Chen, and Y. Chen, "Reducing energy loss and morphology optimization manipulated by molecular geometry engineering for hetero-junction organic solar cells," Chinese J. Chem. **38**, 1553–1559 (2020).

[105] G. Li, R. Zhu, and Y. Yang, "Polymer solar cells," Nat. Photonics **6**, 153 (2012).

[106] T. M. Clarke and J. R. Durrant, "Charge photogeneration in organic solar cells," Chem. Rev. **110**, 6736–6767 (2010).

[107] P. Blom, V. Mihailetchi, L. Koster, and D. Markov, "Device physics of Polymer:Fullerene bulk heterojunction solar cells," Adv. Mater. **19**, 1551–1566 (2007).

[108] A. Pochettino, "Sul comportamento foto-elettrico dell'antracene," Acad. Lincei Rend **15**, 355 (1906).

[109] M. Volmer, "Die verschiedenen lichtelektrischen erscheinungen am anthracen, ihre beziehungen zueinander, zur fluoreszenz und dianthracenbildung," Annalen der Physik **345**, 775–796 (1913).

[110] P. M. Borsenberger, *Organic Photoreceptors for Imaging Systems* (CRC Press, 1993).

[111] R. H. Bube and S. A. Rice, "Photoconductivity of solids," Phys. Today **14**, 54–54 (1961).

[112] G. Chamberlain, "Organic solar cells: A review," Sol. Cells **8**, 47–83 (1983).

[113] D. L. Morel, A. K. Ghosh, T. Feng, E. L. Stogryn, P. E. Purwin, R. F. Shaw, and C. Fishman, "High-efficiency organic solar cells," Appl. Phys. Lett. **32**, 495–497 (1978).

[114] A. K. Ghosh and T. Feng, "Merocyanine organic solar cells," J. Appl. Phys. **49**, 5982–5989 (1978).

[115] M. Hiramoto, H. Fujiwara, and M. Yokoyama, "Three-layered organic solar cell with a photoactive interlayer of codeposited pigments," Appl. Phys. Lett. **58**, 1062–1064 (1991).

[116] T. Albes, L. Xu, J. Wang, J. W. P. Hsu, and A. Gagliardi, "Origin of photocurrent in Fullerene-based solar cells," J. Phys. Chem. C **122**, 15140–15148 (2018).

[117] L. Xu, J. Wang, M. d. A. Villa, T. B. Daunis, Y.-J. Lee, A. V. Malko, and J. W. P. Hsu, "Quantitative analyses of competing photocurrent generation mechanisms in fullerene-based organic photovoltaics," J. Phys. Chem. C **120**, 16470–16477 (2016).

[118] Y. qiong Zheng, W. J. Potscavage, T. Komino, M. Hirade, J. Adachi, and C. Adachi, "Highly efficient bulk heterojunction photovoltaic cells based on C_{70} and tetraphenyldibenzoperiflanthene," Appl. Phys. Lett. **102**, 143304 (2013).

[119] B. Yang, F. Guo, Y. Yuan, Z. Xiao, Y. Lu, Q. Dong, and J. Huang, "Solution-processed fullerene-based organic schottky junction devices for large-open-circuit-voltage organic solar cells," Adv. Mater. **25**, 572–577 (2012).

[120] T. Ameri, N. Li, and C. J. Brabec, "Highly efficient organic tandem solar cells: a follow up review," Energy Environ. Sci. **6**, 2390 (2013).

[121] A. Hadipour, B. de Boer, and P. Blom, "Organic tandem and multi-junction solar cells," Adv. Funct. Mater. **18**, 169–181 (2008).

[122] M. Hiramoto, M. Suezaki, and M. Yokoyama, "Effect of thin gold interstitial-layer on the photovoltaic properties of tandem organic solar cell," Chem. Lett. **19**, 327–330 (1990).

[123] P. Peumans, V. Bulović, and S. R. Forrest, "Efficient photon harvesting at high optical intensities in ultrathin organic double-heterostructure photovoltaic diodes," Appl. Phys. Lett. **76**, 2650–2652 (2000).

[124] A. Yakimov and S. R. Forrest, "High photovoltage multiple-heterojunction organic solar cells incorporating interfacial metallic nanoclusters," Appl. Phys. Lett. **80**, 1667–1669 (2002).

[125] T. Zhang, C. An, P. Bi, Q. Lv, J. Qin, L. Hong, Y. Cui, S. Zhang, and J. Hou, "A thiadiazole-based conjugated polymer with ultradeep HOMO level and strong electroluminescence enables 18.6% efficiency in organic solar cell," Adv. Energy Mater. p. 2101705 (2021).

[126] G. Liu, R. Xia, Q. Huang, K. Zhang, Z. Hu, T. Jia, X. Liu, H.-L. Yip, and F. Huang, "Tandem organic solar cells with 18.7% efficiency enabled by suppressing the charge recombination in front sub-cell," Adv. Funct. Mater. **31**, 2103283 (2021).

[127] S. Shao, J. Liu, J. Bergqvist, S. Shi, C. Veit, U. Würfel, Z. Xie, and F. Zhang, "In situ formation of MoO_3 in PEDOT:PSS matrix: A facile way to produce a smooth and less hygroscopic hole transport layer for highly stable polymer bulk heterojunction solar cells," Adv. Energy Mater. **3**, 349–355 (2012).

[128] F. Liu, S. Shao, X. Guo, Y. Zhao, and Z. Xie, "Efficient polymer photovoltaic cells using solution-processed MoO_3 as anode buffer layer," Sol. Energy Mater. Sol. Cells **94**, 842–845 (2010).

[129] J. Jung, D. L. Kim, S. H. Oh, and H. J. Kim, "Stability enhancement of organic solar cells with solution-processed nickel oxide thin films as hole transport layers," Sol. Energy Mater. Sol. Cells **102**, 103–108 (2012).

[130] C.-K. Cho, W.-J. Hwang, K. Eun, S.-H. Choa, S.-I. Na, and H.-K. Kim, "Mechanical flexibility of transparent PEDOT:PSS electrodes prepared by gravure printing for flexible organic solar cells," Sol. Energy Mater. Sol. Cells **95**, 3269–3275 (2011).

[131] V. Shrotriya, G. Li, Y. Yao, C.-W. Chu, and Y. Yang, "Transition metal oxides as the buffer layer for polymer photovoltaic cells," Appl. Phys. Lett. **88**, 073508 (2006).

[132] K. Takanezawa, K. Tajima, and K. Hashimoto, "Efficiency enhancement of polymer photovoltaic devices hybridized with ZnO nanorod arrays by the introduction of a vanadium oxide buffer layer," Appl. Phys. Lett. **93**, 063308 (2008).

[133] D. Y. Kim, J. Subbiah, G. Sarasqueta, F. So, H. Ding, Irfan, and Y. Gao, "The effect of molybdenum oxide interlayer on organic photovoltaic cells," Appl. Phys. Lett. **95**, 093304 (2009).

[134] L. Yang, H. Xu, H. Tian, S. Yin, and F. Zhang, "Effect of cathode buffer layer on the stability of polymer bulk heterojunction solar cells," Sol. Energy Mater. Sol. Cells **94**, 1831–1834 (2010).

[135] Y. Liang, Z. Xu, J. Xia, S.-T. Tsai, Y. Wu, G. Li, C. Ray, and L. Yu, "For the bright future-bulk heterojunction polymer solar cells with power conversion efficiency of 7.4%," Adv. Mater. **22**, E135–E138 (2010).

[136] O. V. Mikhnenko, P. W. M. Blom, and T.-Q. Nguyen, "Exciton diffusion in organic semiconductors," Energy Environ. Sci. **8**, 1867–1888 (2015).

[137] L. Onsager, "Initial recombination of ions," Phys. Rev. **54**, 554–557 (1938).

[138] C. L. Braun, "Electric field assisted dissociation of charge transfer states as a mechanism of photocarrier production," J. Chem. Phys. **80**, 4157–4161 (1984).

[139] R. A. Marsh, J. M. Hodgkiss, and R. H. Friend, "Direct measurement of electric field-assisted charge separation in Polymer:Fullerene photovoltaic diodes," Adv. Mater. **22**, 3672–3676 (2010).

[140] D. Veldman, Özlem İpek, S. C. J. Meskers, J. Sweelssen, M. M. Koetse, S. C. Veenstra, J. M. Kroon, S. S. van Bavel, J. Loos, and R. A. J. Janssen, "Compositional and electric field dependence of the dissociation of charge transfer excitons in alternating polyfluorene Copolymer/Fullerene blends," J. Am. Chem. Soc. **130**, 7721–7735 (2008).

[141] I. A. Howard, R. Mauer, M. Meister, and F. Laquai, "Effect of morphology on ultrafast free carrier generation in Polythiophene:Fullerene organic solar cells," J. Am. Chem. Soc. **132**, 14866–14876 (2010).

[142] F. C. Jamieson, T. Agostinelli, H. Azimi, J. Nelson, and J. R. Durrant, "Field-independent charge photogeneration in PCPDTBT/$PC_{70}BM$ solar cells," J. Phys. Chem. Lett. **1**, 3306–3310 (2010).

[143] J. Guo, H. Ohkita, H. Benten, and S. Ito, "Charge generation and recombination dynamics in Poly($_3$−hexylthiophene)/Fullerene blend films with different regioregularities and morphologies," J. Am. Chem. Soc. **132**, 6154–6164 (2010).

[144] J. Liu, S. Chen, D. Qian, B. Gautam, G. Yang, J. Zhao, J. Bergqvist, F. Zhang, W. Ma, H. Ade, O. Inganäs, K. Gundogdu, F. Gao, and H. Yan, "Fast charge separation in a non-fullerene organic solar cell with a small driving force," Nat. Energy **1** (2016).

[145] S. Chen, Y. Liu, L. Zhang, P. C. Y. Chow, Z. Wang, G. Zhang, W. Ma, and H. Yan, "A wide-bandgap donor polymer for highly efficient non-fullerene organic solar cells with a small voltage loss," J. Am. Chem. Soc. **139**, 6298–6301 (2017).

[146] S. Chen, Y. Wang, L. Zhang, J. Zhao, Y. Chen, D. Zhu, H. Yao, G. Zhang, W. Ma, R. H. Friend, P. C. Y. Chow, F. Gao, and H. Yan, "Efficient nonfullerene organic solar cells with small driving forces for both hole and electron transfer," Adv. Mater. **30**, 1804215 (2018).

[147] X. Wan, C. Li, M. Zhang, and Y. Chen, "Acceptor–donor–acceptor type molecules for high performance organic photovoltaics – chemistry and mechanism," Chem. Soc. Rev. **49**, 2828–2842 (2020).

[148] V. Coropceanu, J. Cornil, D. A. da Silva Filho, Y. Olivier, R. Silbey, and J.-L. Brédas, "Charge transport in organic semiconductors," Chem. Rev. **107**, 926–952 (2007).

[149] T. Kietzke, "Recent advances in organic solar cells," Adv. OptoElectron. **2007**, 1–15 (2007).

[150] V. D. Mihailetchi, J. Wildeman, and P. W. M. Blom, "Space-charge limited photocurrent," Phys. Rev. Lett. **94** (2005).

[151] C. M. Proctor, M. Kuik, and T.-Q. Nguyen, "Charge carrier recombination in organic solar cells," Prog. Polym. Sci. **38**, 1941–1960 (2013).

[152] T. Kirchartz, B. E. Pieters, K. Taretto, and U. Rau, "Mobility dependent efficiencies of organic bulk heterojunction solar cells: Surface recombination and charge transfer state distribution," Phys. Rev. B **80** (2009).

[153] M. Azzouzi, J. Yan, T. Kirchartz, K. Liu, J. Wang, H. Wu, and J. Nelson, "Nonradiative energy losses in bulk-heterojunction organic photovoltaics," Phys. Rev. X **8**, 031055 (2018).

[154] R. A. J. Janssen and J. Nelson, "Factors limiting device efficiency in organic photovoltaics," Adv. Mater. **25**, 1847–1858 (2012).

[155] N. M.C.Scharber, "Efficiency of bulk heterojunction organic solar cells," Prog. Polym. Sci. **38**, 1929–1940 (2013).

[156] S. Goel, X. Luo, and R. L. Reuben, "Molecular dynamics simulation model for the quantitative assessment of tool wear during single point diamond turning of cubic silicon carbide," Computational Material Science **51**, 402–408 (2012).

[157] A. F. Voter, *Radiation Effects in Solids* (Springer, 2007).

[158] P. Kordt, S. Stodtmann, A. Badinski, M. Al Helwi, C. Lennartz, and D. Andrienko, "Parameter-free continuous drift–diffusion models of amorphous organic semiconductors," Phys. Chem. Chem. Phys. **17**, 22778–22783 (2015).

[159] J. R Norris, *Markov Chains* (Cambridge University Press, 1998).

[160] F. Schwabl, *Statistical Mechanics* (Springer, 2006).

[161] N. V. Kampen, *Stochastic Processes in Physics and Chemistry* (Elsevier, 2007).

[162] D. T. Gillespie, "A general method for numerically simulating the stochastic tim eevolution of couples chemical reactions," The Journal of Computational Physics **22**, 403–434 (1976).

[163] A. Bortz, M. Kalos, and J. Lebowitz, "A new algorithm for Monte Carlo simulation of ising spin systems," Journal of Computational Physics **17**, 10–18 (1975).

[164] W. M. Young and E. W. Elcock, "Monte Carlo studies of vacancy migration in binary ordered alloys: I," Proceedings of the Physical Society **89**, 735–746 (1966).

[165] B. Ries and H. Bässler, "Monte Carlo study of dispersive charge-carrier transport in spatially random systems with and without energetic disorder," Physical Review B **35**, 2295–2302 (1987).

[166] P. M. Borsenberger, E. H. Magin, M. D. V. Auweraer, and F. C. D. Schryver, "The role of disorder on charge transport in molecularly doped polymers and related materials," Phys. Status Solidi (a) **140**, 9–47 (1993).

[167] S. Baranovskii, I. Zvyagin, H. Cordes, S. Yamasaki, and P. Thomas, "Electronic transport in disordered organic and inorganic semiconductors," J. Non-Cryst. Solids **299-302**, 416–419 (2002).

[168] P. Peumans and S. R. Forrest, "Separation of geminate charge-pairs at donor–acceptor interfaces in disordered solids," Chem. Phys. Lett. **398**, 27–31 (2004).

[169] P. Peumans, S. Uchida, and S. R. Forrest, "Efficient bulk heterojunction photovoltaic cells using small-molecular-weight organic thin films," Nature **425**, 158–162 (2003).

[170] F. Yang and S. R. Forrest, "Photocurrent generation in nanostructured organic solar cells," ACS Nano **2**, 1022–1032 (2008).

[171] C. Groves, "Suppression of geminate charge recombination in organic photovoltaic devices with a cascaded energy heterojunction," Energy Environ. Sci. **6**, 1546–1551 (2013).

[172] C. Groves, J. C. Blakesley, and N. C. Greenham, "Effect of charge trapping on geminate recombination and polymer solar cell performance," Nano Letters **10**, 1063–1069 (2010).

[173] J. Nelson, "Diffusion-limited recombination in polymer−fullerene blends and its influence on photocurrent collection," Phys. Rev. B **67** (2003).

[174] C. Groves and N. C. Greenham, "Bimolecular recombination in polymer electronic devices," Phys. Rev. B **78** (2008).

[175] I. Maqsood, L. D. Cundy, M. Biesecker, J.-H. Kimn, D. Johnson, R. Williams, and V. Bommisetty, "Monte Carlo simulation of förster resonance energy transfer in 3d nanoscale organic bulk heterojunction morphologies," J. Phys. Chem. C **117**, 21086–21095 (2013).

[176] T. Offermans, S. C. Meskers, and R. A. Janssen, "Monte-Carlo simulations of geminate electron–hole pair dissociation in a molecular heterojunction: a two-step dissociation mechanism," Chem. Phys. **308**, 125–133 (2005).

[177] M. C. Heiber and A. Dhinojwala, "Dynamic Monte Carlo modeling of exciton dissociation in organic donor-acceptor solar cells," J. Chem. Phys. **137**, 014903 (2012).

[178] H. van Eersel, R. A. J. Janssen, and M. Kemerink, "Mechanism for efficient photoinduced charge separation at disordered organic heterointerfaces," Adv. Funct. Mat. **22**, 2700–2708 (2012).

[179] C. Groves, L. J. A. Koster, and N. C. Greenham, "The effect of morphology upon mobility: Implications for bulk heterojunction solar cells with nonuniform blend morphology," J. Appl. Phys. **105**, 094510 (2009).

[180] R. A. Marsh, C. Groves, and N. C. Greenham, "A microscopic model for the behavior of nanostructured organic photovoltaic devices," J. Appl. Phys. **101**, 083509 (2007).

[181] H. van Eersel, P. A. Bobbert, and R. Coehoorn, "Kinetic Monte Carlo study of triplet-triplet annihilation in organic phosphorescent emitters," J. Appl. Phys. **117**, 115502 (2015).

[182] H. van Eersel, P. A. Bobbert, R. A. J. Janssen, and R. Coehoorn, "Monte Carlo study of efficiency roll-off of phosphorescent organic light-emitting diodes: Evidence for dominant role of triplet-polaron quenching," Appl. Phys. Lett. **105**, 143303 (2014).

[183] C.-M. Yang, C.-H. Wu, H.-H. Liao, K.-Y. Lai, H.-P. Cheng, S.-F. Horng, H.-F. Meng, and J.-T. Shy, "Enhanced photovoltaic response of organic solar cell by singlet-to-triplet exciton conversion," Appl. Phys. Lett. **90**, 133509 (2007).

[184] D. M. González, V. Körstgens, Y. Yao, L. Song, G. Santoro, S. V. Roth, and P. Müller-Buschbaum, "Improved power conversion efficiency of p3ht:PCBM organic solar cells by strong spin-orbit coupling-induced delayed fluorescence," Adv. Ener. Mat. **5**, 1401770 (2015).

[185] W. Kaiser and A. Gagliardi, "Kinetic Monte Carlo study of the role of the energetic disorder on the open-circuit voltage in Polymer/Fullerene solar cells," J. Phys. Chem. Lett. **10**, 6097–6104 (2019).

[186] C. Groves, "Developing understanding of organic photovoltaic devices: kinetic Monte Carlo models of geminate and non-geminate recombination, charge transport and charge extraction," Energy Environ. Sci. **6**, 3202 (2013).

[187] F. Zhao, C. Wang, and X. Zhan, "Morphology control in organic solar cells," Adv. Energy Mat. **8**, 1703147 (2018).

[188] K. Weng, L. Ye, L. Zhu, J. Xu, J. Zhou, X. Feng, G. Lu, S. Tan, F. Liu, and Y. Sun, "Optimized active layer morphology toward efficient and polymer batch insensitive organic solar cells," Nat. Commun. **11** (2020).

[189] S. Pröller, O. Filonik, F. Eller, S. Mansi, C. Zhu, E. Schaible, A. Hexemer, P. Müller-Buschbaum, and E. M. Herzig, "Electrophoresis assisted printing: A method to control the morphology in organic thin films," ACS Appl. Mater. Interfaces **12**, 5219–5225 (2020).

[190] M. Q. Zhang, "A fast vectorized multispin coding algorithm for 3d Monte Carlo simulations using kawasaki spin-exchange dynamics," J. Stat. Phys. **56**, 939–950 (1989).

[191] M. C. Heiber and A. Dhinojwala, "Efficient generation of model bulk heterojunction morphologies for organic photovoltaic device modeling," Phys. Rev. Appl. **2** (2014).

[192] N. Madras and A. D. Sokal, "The pivot algorithm: A highly efficient Monte Carlo method for the self-avoiding walk," J. Stat. Phys. **50**, 109–186 (1988).

[193] P. P. Ewald, "Die berechnung optischer und elektrostatischer gitterpotentiale," Annalen der Physik **369**, 253–287 (1921).

[194] U. Wolf, V. I. Arkhipov, and H. Bässler, "Current injection from a metal to a disordered hopping system. i. Monte Carlo simulation," Phys. Rev. B **59**, 7507–7513 (1999).

[195] M. Langevin, "Recombinaison et diffusion des ions gazeux," Journal de Physique Théorique et Appliquée **4**, 322–333 (1905).

[196] C. G. Shuttle, B. O'Regan, A. M. Ballantyne, J. Nelson, D. D. C. Bradley, and J. R. Durrant, "Bimolecular recombination losses in polythiophene:Fullerene solar cells," Phys. Rev. B **78** (2008).

[197] L. J. A. Koster, V. D. Mihailetchi, and P. W. M. Blom, "Bimolecular recombination in polymer/fullerene bulk heterojunction solar cells," Appl. Phys. Lett. **88**, 052104 (2006).

[198] G. Juška, K. Arlauskas, J. Stuchlik, and R. Österbacka, "Non-langevin bimolecular recombination in low-mobility materials," J. Non-Cryst. Sol. **352**, 1167–1171 (2006).

[199] C. Deibel, A. Baumann, and V. Dyakonov, "Polaron recombination in pristine and annealed bulk heterojunction solar cells," Appl. Phys. Lett. **93**, 163303 (2008).

[200] A. Maurano, C. G. Shuttle, R. Hamilton, A. M. Ballantyne, J. Nelson, W. Zhang, M. Heeney, and J. R. Durrant, "Transient optoelectronic analysis of charge carrier losses in a Selenophene/Fullerene blend solar cell," J. Phys. Chem. C **115**, 5947–5957 (2011).

[201] G. F. A. Dibb, T. Kirchartz, D. Credgington, J. R. Durrant, and J. Nelson, "Analysis of the relationship between linearity of corrected photocurrent and the order of recombination in organic solar cells," J. Phys. Chem. Lett. **2**, 2407–2411 (2011).

[202] M. Gerhard, A. P. Arndt, M. Bilal, U. Lemmer, M. Koch, and I. A. Howard, "Field-induced exciton dissociation in PTB_7-based organic solar cells," Phys. Rev. B **95**, 195301 (2017).

[203] G. F. Burkhard, E. T. Hoke, and M. D. McGehee, "Accounting for interference, scattering, and electrode absorption to make accurate internal quantum efficiency measurements in organic and other thin solar cells," Adv. Mater. **22**, 3293–3297 (2010).

[204] L. A. A. Pettersson, L. S. Roman, and O. Inganäs, "Modeling photocurrent action spectra of photovoltaic devices based on organic thin films," J. Appl. Phys. **86**, 487–496 (1999).

[205] A. Köhler and H. Bässler, "Triplet states in organic semiconductors," Mater. Sci. Eng.: R: Reports **66**, 71–109 (2009).

[206] F. SCHAUFELE, I. DEMARCO, and R. N. DAY, "FRET imaging in the wide-field microscope," in "Mol. Imaging," (Elsevier, 2005), pp. 72–94.

[207] S. Günes, H. Neugebauer, and N. S. Sariciftci, "Conjugated polymer-based organic solar cells," Chem. Rev. **107**, 1324–1338 (2007).

[208] I.-W. Hwang, D. Moses, and A. J. Heeger, "Photoinduced carrier generation in P3HT/PCBM bulk heterojunction materials," J. Phys. Chem. C **112**, 4350–4354 (2008).

[209] R. Coehoorn, H. van Eersel, P. Bobbert, and R. Janssen, "Kinetic Monte Carlo study of the sensitivity of OLED efficiency and lifetime to materials parameters," Adv. Func. Mater. **25**, 2024–2037 (2014).

[210] M. Fahlman, S. Fabiano, V. Gueskine, D. Simon, M. Berggren, and X. Crispin, "Interfaces in organic electronics," Nat. Rev. Mater. **4**, 627–650 (2019).

[211] K. Vandewal, K. Tvingstedt, A. Gadisa, O. Inganäs, and J. V. Manca, "On the origin of the open-circuit voltage of Polymer−Fullerene solar cells," Nat. Mater. **8**, 904–909 (2009).

[212] K. Vandewal, K. Tvingstedt, A. Gadisa, O. Inganäs, and J. V. Manca, "Relating the open-circuit voltage to interface molecular properties of donor:acceptor bulk heterojunction solar cells," Phys. Rev. B **81**, 125204 (2010).

[213] M. B. Salim, R. Nekovei, and R. Jeyakumar, "Organic tandem solar cells with 18.6% efficiency," Solar Energy **198**, 160–166 (2020).

[214] H. Xu, F. Yuan, D. Zhou, X. Liao, L. Chen, and Y. Chen, "Hole transport layers for organic solar cells: Recent progress and prospects," J. Mater. Chem. A **8**, 11478–11492 (2020).

[215] Z. Yin, J. Wei, and Q. Zheng, "Interfacial materials for organic solar cells: Recent advances and perspectives," Adv. Sci. **3**, 1500362 (2016).

[216] D. Głowienka, D. Zhang, F. D. Giacomo, M. Najafi, S. Veenstra, J. Szmytkowski, and Y. Galagan, "Role of surface recombination in perovskite solar cells at the interface of HTL/$CH_3NH_3PbI_3$," Nano Energy **67**, 104186 (2020).

[217] S. Heo, G. Seo, K. T. Cho, Y. Lee, S. Paek, S. Kim, M. Seol, S. H. Kim, D.-J. Yun, K. Kim, J. Park, J. Lee, L. Lechner, T. Rodgers, J. W. Chung, J.-S. Kim, D. Lee, S.-H. Choi, and M. K. Nazeeruddin, "Dimensionally engineered perovskite heterostructure for photovoltaic and optoelectronic applications," Adv. Energy Mater. **9**, 1902470 (2019).

[218] S. S. Reddy, K. Gunasekar, J. H. Heo, S. H. Im, C. S. Kim, D.-H. Kim, J. H. Moon, J. Y. Lee, M. Song, and S.-H. Jin, "Highly efficient organic hole transporting materials for perovskite and organic solar cells with long-term stability," Adv. Mater. **28**, 686–693 (2015).

[219] H. Liu, L. Hu, F. Wu, L. Chen, and Y. Chen, "Polyfluorene electrolytes interfacial layer for efficient polymer solar cells: Controllably interfacial dipoles by regulation of polar groups," ACS Appl. Mater. Interfaces **8**, 9821–9828 (2016).

[220] M. Vasilopoulou, A. R. B. M. Yusoff, N. Kuganathan, X. Bao, A. Verykios, E. Polydorou, K.-K. Armadorou, A. Soultati, G. Papadimitropoulos, M. I. Haider, A. Fakharuddin, L. C. Palilis, S. Kennou, A. Chroneos, P. Argitis, and D. Davazoglou, "A carbon-doped tantalum dioxyfluoride as a superior electron transport material for high performance organic optoelectronics," Nano Energy **70**, 104508 (2020).

[221] J. Troughton, M. Neophytou, N. Gasparini, A. Seitkhan, F. H. Isikgor, X. Song, Y.-H. Lin, T. Liu, H. Faber, E. Yengel, J. Kosco, M. F. Oszajca, B. Hartmeier, M. Rossier, N. A. Lüchinger, L. Tsetseris, H. J. Snaith, S. D. Wolf, T. D. Anthopoulos, I. McCulloch, and D. Baran, "A universal solution processed interfacial bilayer enabling ohmic contact in organic and hybrid optoelectronic devices," Energy Environ. Sci. **13**, 268–276 (2020).

[222] A. Köhler and H. Bässler, *Electronic Processes in Organic Semiconductors* (Wiley-VCH Verlag GmbH & Co. KGaA, 2015).

[223] H. Bässler, "Charge transport in disordered organic photoconductors a Monte Carlo simulation study," Phys. Status Solidi B **175**, 15–56 (1993).

[224] J. O. Oelerich, D. Huemmer, and S. D. Baranovskii, "How to find out the density of states in disordered organic semiconductors," Phys. Rev. Lett. **108**, 226403 (2012).

[225] L. Shi, C. K. Lee, and A. P. Willard, "The enhancement of interfacial exciton dissociation by energetic disorder is a nonequilibrium effect," ACS Cent. Sci. **3**, 1262–1270 (2017).

[226] J. C. Blakesley and D. Neher, "Relationship between energetic disorder and open-circuit voltage in bulk heterojunction organic solar cells," Phys. Rev. B **84**, 075210 (2011).

[227] S. Baranovskii, "Theoretical description of charge transport in disordered organic semiconductors," Phys. Status Solidi B **251**, 487–525 (2014).

[228] A. Melianas, F. Etzold, T. J. Savenije, F. Laquai, O. Inganäs, and M. Kemerink, "Photo-generated carriers lose energy during extraction from Polymer−Fullerene solar cells," Nat. Commun. **6**, 1–8 (2015).

[229] S. Wilken, T. Upreti, A. Melianas, S. Dahlström, G. Persson, E. Olsson, R. Österbacka, and M. Kemerink, "Experimentally calibrated kinetic Monte Carlo model reproduces organic solar cell current–voltage curve," Sol. RRL **4**, 2000029 (2020).

[230] W. Pasveer, J. Cottaar, C. Tanase, R. Coehoorn, P. Bobbert, P. Blom, D. De Leeuw, and M. Michels, "Unified description of charge-carrier mobilities in disordered semiconducting polymers," Phys. Rev. Lett. **94**, 206601 (2005).

[231] N. K. Elumalai and A. Uddin, "Open circuit voltage of organic solar cells: An in-depth review," Energy Environ. Sci. **9**, 391–410 (2016).

[232] O. J. Sandberg, M. Nyman, and R. Österbacka, "Effect of contacts in organic bulk heterojunction solar cells," Phys. Rev. Appl. **1**, 024003 (2014).

[233] D. Scheunemann, S. Wilken, O. J. Sandberg, R. Österbacka, and M. Schiek, "Effect of imbalanced charge transport on the interplay of surface and bulk recombination in organic solar cells," Phys. Rev. Appl. **11**, 054090 (2019).

[234] M. Burgelman, P. Nollet, and S. Degrave, "Modelling polycrystalline semiconductor solar cells," Thin Solid Films **361-362**, 527–532 (2000).

[235] W. Tress, K. Leo, and M. Riede, "Influence of hole-transport layers and donor materials on open-circuit voltage and shape of i-v curves of organic solar cells," Adv. Funct. Mater. **21**, 2140–2149 (2011).

[236] A. Petersen, T. Kirchartz, and T. A. Wagner, "Charge extraction and photocurrent in organic bulk heterojunction solar cells," Phys. Rev. B **85**, 045208 (2012).

[237] A. Zampetti, A. H. Fallahpour, M. Dianetti, L. Salamandra, F. Santoni, A. Gagliardi, M. Auf der Maur, F. Brunetti, A. Reale, T. M. Brown *et al.*, "Influence of the interface material layers and semiconductor energetic disorder on the open circuit voltage in polymer solar cells," J. Polym. Sci., Part B: Polym. Phys. **53**, 690–699 (2015).

[238] G. A. Buxton and N. Clarke, "Predicting structure and property relations in polymeric photovoltaic devices," Phys. Rev. B **74**, 085207 (2006).

[239] C. Ahläng, O. J. Sandberg, and R. Österbacka, "Two-dimensional drift-diffusion study of mid-gap states and subsequent vacuum level shifts at interfaces in bulk-heterojunction solar cells," Phys. Rev. B **98**, 075306 (2018).

[240] L. Meng, Y. Shang, Q. Li, Y. Li, X. Zhan, Z. Shuai, R. G. E. Kimber, and A. B. Walker, "Dynamic Monte Carlo simulation for highly efficient polymer blend photovoltaics," J. Phys. Chem. B **114**, 36–41 (2010).

[241] A. Melianas, N. Felekidis, Y. Puttisong, S. C. Meskers, O. Inganäs, W. M. Chen, and M. Kemerink, "Nonequilibrium site distribution governs charge-transfer electroluminescence at disordered organic heterointerfaces," Proc. Natl. Acad. Sci. **116**, 23416–23425 (2019).

[242] A. Brigeman, M. Fusella, B. P. Rand, and N. Giebink, "Nonthermal site occupation at the donor-acceptor interface of organic solar cells," Phys. Rev. Appl. **10**, 034034 (2018).

[243] S. Athanasopoulos, S. Tscheuschner, H. Bässler, and A. Köhler, "Efficient charge separation of cold charge-transfer states in organic solar cells through incoherent hopping," J. Phys. Chem. Lett. **8**, 2093–2098 (2017).

[244] H. van Eersel, R. A. Janssen, and M. Kemerink, "Mechanism for efficient photoinduced charge separation at disordered organic heterointerfaces," Adv. Funct. Mater. **22**, 2700–2708 (2012).

[245] M. C. Heiber, C. Baumbach, V. Dyakonov, and C. Deibel, "Encounter-limited charge-carrier recombination in phase-separated organic semiconductor blends," Phys. Rev. Lett. **114**, 136602 (2015).

[246] A. Melianas and M. Kemerink, "Photogenerated charge transport in organic electronic materials: Experiments confirmed by simulations," Adv. Mater. **31**, 1806004 (2019).

[247] S. Dimitrov, B. Schroeder, C. Nielsen, H. Bronstein, Z. Fei, I. McCulloch, M. Heeney, and J. Durrant, "Singlet exciton lifetimes in conjugated polymer films for organic solar cells," Polymers **8**, 14 (2016).

[248] H.-C. Liao, C.-S. Tsao, Y.-T. Shao, S.-Y. Chang, Y.-C. Huang, C.-M. Chuang, T.-H. Lin, C.-Y. Chen, C.-J. Su, U.-S. Jeng, Y.-F. Chen, and W.-F. Su, "Bi-hierarchical nanostructures of donor–acceptor copolymer and fullerene for high efficient bulk heterojunction solar cells," Energy Environ. Sci. **6**, 1938–1948 (2013).

[249] J. Peet, J. Y. Kim, N. E. Coates, W. L. Ma, D. Moses, A. J. Heeger, and G. C. Bazan, "Efficiency enhancement in low-bandgap polymer solar cells by processing with alkane dithiols," Nat. Mater. **6**, 497–500 (2007).

[250] Y. Tamai, K. Tsuda, H. Ohkita, H. Benten, and S. Ito, "Charge-carrier generation in organic solar cells using crystalline donor polymers," Phys. Chem. Chem. Phys. **16**, 20338–20346 (2014).

[251] T. Fukuhara, Y. Tamai, I. Osaka, and H. Ohkita, "Bimolecular recombination and fill factor in crystalline polymer solar cells," Jpn. J. Appl. Phys. **57**, 08RE01 (2018).

[252] J. Hou, H.-Y. Chen, S. Zhang, G. Li, and Y. Yang, "Synthesis, characterization, and photovoltaic properties of a low band gap polymer based on silole-containing Polythiophenes and 2, 1, 3-Benzothiadiazole," J. Am. Chem. Soc. **130**, 16144–16145 (2008).

[253] G. Li, V. Shrotriya, J. Huang, Y. Yao, T. Moriarty, K. Emery, and Y. Yang, "High-efficiency solution processable polymer photovoltaic cells by self-organization of polymer bends," Nat. Mater. **4**, 864–868 (2005).

[254] C. Duan, W. Cai, B. B. Y. Hsu, C. Zhong, K. Zhang, C. Liu, Z. Hu, F. Huang, G. C. Bazan, A. J. Heeger, and Y. Cao, "Toward green solvent processable photovoltaic materials for polymer solar cells: The role of highly polar pendant groups in charge carrier transport and photovoltaic behavior," Energy Environ. Sci. **6**, 3022–3034 (2013).

[255] Y. Sun, C. J. Takacs, S. R. Cowan, J. H. Seo, X. Gong, A. Roy, and A. J. Heeger, "Efficient, air-stable bulk heterojunction polymer solar cells using MoOx as the anode interfacial layer," Adv. Mater. **23**, 2226–2230 (2011).

[256] Y. Zheng, G. Wang, D. Huang, J. Kong, T. Goh, W. Huang, J. Yu, and A. D. Taylor, "Binary solvent additives treatment boosts the efficiency of PTB7:PCBM polymer solar cells to over 9.5%," Sol. RRL **2**, 1700144 (2018).

[257] B. Ebenhoch, S. A. Thomson, K. Genevičius, G. Juška, and I. D. Samuel, "Charge carrier mobility of the organic photovoltaic materials ptb7 and $pc_{71}bm$ and its influence on device performance," Org. Electron. **22**, 62–68 (2015).

[258] Y. Tamai, "Delocalization boosts charge separation in organic solar cells," Polym. J. **52**, 691–700 (2020).

[259] G. Lastra, V. S. Balderrama, L. Resendiz, J. Pallarrs, L. F. Marsal, V. Cabrera, and M. Estrada, "Air environment degradation of a high-performance inverted PTB7-th:PC70bm solar cell," IEEE J. Photovoltaics **9**, 464–468 (2019).

[260] D. H. Wang, P.-O. Morin, C.-L. Lee, A. K. K. Kyaw, M. Leclerc, and A. J. Heeger, "Effect of processing additive on morphology and charge extraction in bulk-heterojunction solar cells," J. Mater. Chem. A **2**, 15052–15057 (2014).

[261] T. Liu and A. Troisi, "Absolute rate of charge separation and recombination in a molecular model of the P3HT/PCBM interface," J. Phys. Chem. C **115**, 2406–2415 (2011).

[262] W. C. Tsoi, S. J. Spencer, L. Yang, A. M. Ballantyne, P. G. Nicholson, A. Turnbull, A. G. Shard, C. E. Murphy, D. D. Bradley, J. Nelson *et al.*, "Effect of crystallization on the electronic energy levels and thin film morphology of P3HT:PCBM blends," Macromolecules **44**, 2944–2952 (2011).

[263] F. C. Jamieson, E. B. Domingo, T. McCarthy-Ward, M. Heeney, N. Stingelin, and J. R. Durrant, "Fullerene crystallisation as a key driver of charge separation in Polymer/Fullerene bulk heterojunction solar cells," Chem. Sci. **3**, 485–492 (2012).

[264] T. M. Burke, S. Sweetnam, K. Vandewal, and M. D. McGehee, "Beyond langevin recombination: How equilibrium between free carriers and charge transfer states determines the open-circuit voltage of organic solar cells," Adv. Energy Mater. **5**, 1500123 (2015).

[265] S. H. Park, A. Roy, S. Beaupré, S. Cho, N. Coates, J. S. Moon, D. Moses, M. Leclerc, K. Lee, and A. J. Heeger, "Bulk heterojunction solar cells with internal quantum efficiency approaching 100%," Nat. Photonics **3**, 297 (2009).

[266] S. Athanasopoulos, H. Bässler, and A. Köhler, "Disorder vs delocalization: Which is more advantageous for high-efficiency organic solar cells?" J. Phys. Chem. Lett. **10**, 7107–7112 (2019).

[267] V. Janković and N. Vukmirović, "Combination of charge delocalization and disorder enables efficient charge separation at photoexcited organic bilayers," J. Phys. Chem. C **122**, 10343–10359 (2018).

[268] S. N. Hood and I. Kassal, "Entropy and disorder enable charge separation in organic solar cells," J. Phys. Chem. Lett. **7**, 4495–4500 (2016).

[269] F. Suzuki, S. Kubo, T. Fukushima, and H. Kaji, "Effects of structural and energetic disorders on charge transports in crystal and amorphous organic layers," Scientific Reports **8** (2018).

[270] L. Pautmeier, R. Richert, and H. Bässler, "Poole-frenkel behavior of charge transport in organic solids with off-diagonal disorder studied by Monte Carlo simulation," Synthetic Metals **37**, 271–281 (1990).

[271] Z. He, B. Xiao, F. Liu, H. Wu, Y. Yang, S. Xiao, C. Wang, T. P. Russell, and Y. Cao, "Single-junction polymer solar cells with high efficiency and photovoltage," Nat. Photonics **9**, 174–179 (2015).

[272] M. Nam, J. Yoo, Y. Park, H. Y. Noh, Y. Park, J. Cho, J.-A. Kim, J. Kim, H. H. Lee, R. Chang, and D.-H. Ko, "Ternary blend organic solar cells with improved morphological stability," J. Mater. Chem. A **7**, 9698–9707 (2019).

[273] Z. He, C. Zhong, S. Su, M. Xu, H. Wu, and Y. Cao, "Enhanced power-conversion efficiency in polymer solar cells using an inverted device structure," Nat. Photonics **6**, 591–595 (2012).

[274] J. Yuan, Y. Xu, G. Shi, X. Ling, L. Ying, F. Huang, T. H. Lee, H. Y. Woo, J. Y. Kim, Y. Cao, and W. Ma, "Engineering the morphology via processing additives in multiple all-polymer solar cells for improved performance," J. Mater. Chem. A **6**, 10421–10432 (2018).

[275] X. Song, N. Gasparini, and D. Baran, "The influence of solvent additive on polymer solar cells employing fullerene and non-fullerene acceptors," Adv. Electron. Mater. **4**, 1700358 (2018).

[276] Y. Xie, Y. Bao, J. Du, C. Jiang, and Q. Qiao, "Understanding of morphology evolution in local aggregates and neighboring regions for organic photovoltaics," Phys. Chem. Chem. Phys. **14**, 10168–10177 (2012).

[277] R. Jasiūnas, A. Melianas, Y. Xia, N. Felekidis, V. Gulbinas, and M. Kemerink, "Dead ends limit charge carrier extraction from all-polymer bulk heterojunction solar cells," Adv. Electron. Mater. **4**, 1800144 (2018).

[278] P. Friederich, A. Fediai, S. Kaiser, M. Konrad, N. Jung, and W. Wenzel, "Toward design of novel materials for organic electronics," Adv. Mater. **31**, 1808256 (2019).

[279] L. Lu, T. Zheng, Q. Wu, A. M. Schneider, D. Zhao, and L. Yu, "Recent advances in bulk heterojunction polymer solar cells," Chem. Rev. **115**, 12666 (2015).

[280] J. Benduhn, K. Tvingstedt, F. Piersimoni, S. Ullbrich, Y. Fan, M. Tropiano, K. A. McGarry, O. Zeika, M. K. Riede, C. J. Douglas, S. Barlow, S. R. Marder, D. Neher, D. Spoltore, and K. Vandewal, "Intrinsic non-radiative voltage losses in fullerene-based organic solar cells," Nat. Energy **2**, 17053 (2017).

[281] Z. Tang, J. Wang, A. Melianas, Y. Wu, R. Kroon, W. Li, W. Ma, M. R. Andersson, Z. Ma, W. Cai, W. Tress, and O. Inganäs, "Relating open-circuit voltage losses to the active layer morphology and contact selectivity in organic solar cells," J. Mater. Chem. A **6**, 12574–12581 (2018).

[282] J. Popp, W. Kaiser, and A. Gagliardi, "Impact of phosphorescent sensitizers and morphology on the photovoltaic performance in organic solar cells," Adv. Theory Sim. **2**, 1800114 (2019).

[283] B. Yang, F. Guo, Y. Yuan, Z. Xiao, Y. Lu, Q. Dong, and J. Huang, "Solution-processed fullerene-based organic schottky junction devices for large-open-circuit-voltage organic solar cells," Adv. Mater. **25**, 572 (2013).

[284] K. Vandewal, J. Widmer, T. Heumueller, C. J. Brabec, M. D. McGehee, K. Leo, M. Riede, and A. Salleo, "Increased open-circuit voltage of organic solar cells by reduced donor-acceptor interface area," Adv. Mater. **26**, 3839 (2014).

[285] S. Sutty, G. Williams, and H. Aziz, "Fullerene-based schottky-junction organic solar cells: A brief review," J. Photonics Energy **4**, 040999 (2014).

[286] M. Zhang, H. Wang, H. Tian, Y. Geng, and C. W. Tang, "Bulk heterojunction photovoltaic cells with low donor concentration," Adv. Mater. **23**, 4960 (2011).

[287] Zhang, M. and Irfan, and Ding, H. and Gao, Y. and Tang, C. W., "Organic schottky barrier photovoltaic cells based on MoOx/C_{60}," Appl. Phys. Lett. **96**, 183301 (2010).

[288] B. Yang, Z. Xiao, and J. Huang, "Polymer aggregation correlated transition from schottky-junction to bulk heterojunction organic solar cells," Appl. Phys. Lett. **104**, 143304 (2014).

[289] X. Xiao, K. J. Bergemann, J. D. Zimmerman, K. Lee, and S. R. Forrest, "Small-molecule planar-mixed heterojunction photovoltaic cells with fullerene-based electron filtering buffers," Adv. Energy Mater. **4**, 1301557 (2014).

[290] D. Spoltore, A. Hofacker, J. Benduhn, S. Ullbrich, M. Nyman, O. Zeika, S. Schellhammer, Y. Fan, I. Ramirez, S. Barlow, M. Riede, S. R. Marder, F. Ortmann, and K. Vandewal, "Hole transport in low-donor-content organic solar cells," J. Phys. Chem. Lett. **9**, 5496–5501 (2018). PMID: 30187758.

[291] E. Collado-Fregoso, S. N. Pugliese, M. Wojcik, J. Benduhn, E. Bar-Or, L. Perdigón Toro, U. Hörmann, D. Spoltore, K. Vandewal, J. M. Hodgkiss, and D. Neher, "Energy-gap law for photocurrent generation in fullerene-based organic solar cells: The case of low-donor-content blends," J. Am. Chem. Soc. **141**, 2329–2341 (2019).

[292] J.-W. Seo, J. H. Kim, M. Kim, S.-M. Jin, S.-H. Lee, C. Cho, E. Lee, S. Yoo, J. Y. Park, and J.-Y. Lee, "Columnar-structured low-concentration donor molecules in bulk heterojunction organic solar cells," ACS Omega **3**, 929–936 (2018).

[293] W. Feng, C. Song, X. Hu, S. Liu, R. Yi, X. Yang, H. Yan, and X. Hou, "Highly efficient charge collection in bulk-heterojunction organic solar cells by anomalous hole transfer and improved interfacial contact," ACS Appl. Mater. Interfaces **10**, 28256–28261 (2018). PMID: 30117726.

[294] K. Ding, X. Liu, and S. R. Forrest, "Charge transfer and collection in dilute organic donor–acceptor heterojunction blends," Nano Lett. **18**, 3180–3184 (2018). PMID: 29684283.

[295] A. Yazmaciyan, M. Stolterfoht, P. L. Burn, Q. Lin, P. Meredith, and A. Armin, "Recombination losses above and below the transport percolation threshold in bulk heterojunction organic solar cells," Adv. Energy Mater. **8**, 1703339 (2018).

[296] L. Meng, Y. Shang, Q. Li, Y. Li, X. Zhan, Z. Shuai, R. G. E. Kimber, and A. B. Walker, "Dynamic Monte Carlo simulation for highly efficient polymer blend photovoltaics," J. Phys. Chem. B **114**, 36 (2010).

[297] F. Molina-Lopez, H. Yan, X. Gu, Y. Kim, M. F. Toney, and Z. Bao, "Electric field tuning molecular packing and electrical properties of solution-shearing coated organic semiconducting thin films," Adv. Funct. Mater. **27**, 1605503 (2017).

[298] F. Molina-Lopez, H.-C. Wu, G.-J. N. Wang, H. Yan, L. Shaw, J. Xu, M. F. Toney, and Z. Bao, "Enhancing molecular alignment and charge transport of solution-sheared semiconducting polymer films by the electrical-blade effect," Adv. Electron. Mater. p. 1800110 (2018).

[299] M. Elshobaki, R. Gebhardt, J. Carr, W. Lindemann, W. Wang, E. Grieser, S. Venkatesan, E. Ngo, U. Bhattacharjee, J. Strzalka *et al.*, "Tailoring nanoscale morphology of polymer:Fullerene blends using electrostatic field," ACS Appl. Mater. Interfaces **9**, 2678–2685 (2016).

[300] B. Xue, B. Vaughan, C.-H. Poh, K. B. Burke, L. Thomsen, A. Stapleton, X. Zhou, G. W. Bryant, W. Belcher, and P. C. Dastoor, "Vertical stratification and interfacial structure in P3HT:PCBM organic solar cells," J. Phys. Chem. C **114**, 15797–15805 (2010).

[301] D. Khatiwada, S. Venkatesan, Q. Chen, J. Chen, N. Adhikari, A. Dubey, A. F. Mitul, L. Mohammed, and Q. Qiao, "Improved performance by morphology control via fullerenes in PBDT−TBT−alkoBT based organic solar cells," J. Mater. Chem. A **3**, 15307–15313 (2015).

[302] D. Khatiwada, S. Venkatesan, E. C. Ngo, and Q. Qiao, "Versatile role of solvent additive for tailoring morphology in polymer solar cells for efficient charge transport," J. Nanosci. Nanotechnol. **15**, 7040–7044 (2015).

[303] Y. Wu, S. Schneider, C. Walter, A. H. Chowdhury, B. Bahrami, H.-C. Wu, Q. Qiao, M. F. Toney, and Z. Bao, "Fine-tuning semiconducting polymer self-aggregation and crystallinity enables optimal morphology and high-performance printed all-polymer solar cells," J. Am. Chem. Soc. (2019).

[304] J. Lederer, W. Kaiser, A. Mattoni, and A. Gagliardi, "Machine learning–based charge transport computation for pentacene," Adv. Theory Sim. **2**, 1800136 (2019).

[305] N. R. Tummala, C. Risko, C. Bruner, R. H. Dauskardt, and J.-L. Brédas, "Entanglements in P3HT and their influence on thin-film mechanical properties: Insights from molecular dynamics simulations," J. Polym. Sci., Part B: Polym. Phys. **53**, 934–942 (2015).

[306] A. Berretti and A. D. Sokal, "New Monte Carlo method for the self-avoiding walk," J. Stat. Phys. **40**, 483–531 (1985).

[307] M. Taherpour and Y. Abdi, "Monte Carlo simulation for investigation of morphology dependent charge transport in bulk-heterojunction organic solar cells," J. Phys. Chem. C **123**, 1527–1538 (2019).

[308] V. D. Christoph Brabec, Ullrich Scherf, *Organic Photovoltaics: Materials, Device Physics, and Manufacturing Technologies* (John Wiley & Sons, 2014), chap. 5, pp. 159–243, 2nd ed.

[309] Y. Wang, S. Gu, G. Liu, L. Zhang, Z. Liu, R. Lin, K. Xiao, X. Luo, J. Shi, J. Du, F. Meng, L. Li, Z. Liu, and H. Tan, "Cross-linked hole transport layers for high-efficiency perovskite tandem solar cells," Sci. China: Chem. (2021).

[310] J. Wang, Z. Zheng, Y. Zu, Y. Wang, X. Liu, S. Zhang, M. Zhang, and J. Hou, "A tandem organic photovoltaic cell with 19.6% efficiency enabled by light distribution control," Adv. Mater. **33**, 2102787 (2021).

[311] T. Leijtens, K. A. Bush, R. Prasanna, and M. D. McGehee, "Opportunities and challenges for tandem solar cells using metal halide perovskite semiconductors," Nat. Energy **3**, 828–838 (2018).

[312] J. Liu, S. Lu, L. Zhu, X. Li, and W. C. H. Choy, "Perovskite-organic hybrid tandem solar cells using a nanostructured perovskite layer as the light window and a PFN/doped-MoO3/MoO3 multilayer as the interconnecting layer," Nanoscale **8**, 3638–3646 (2016).

[313] X. Chen, Z. Jia, Z. Chen, T. Jiang, L. Bai, F. Tao, J. Chen, X. Chen, T. Liu, X. Xu, C. Yang, W. Shen, W. E. Sha, H. Zhu, and Y. M. Yang, "Efficient and reproducible monolithic perovskite/organic tandem solar cells with low-loss interconnecting layers," Joule **4**, 1594–1606 (2020).

[314] G. Li, W.-H. Chang, and Y. Yang, "Low-bandgap conjugated polymers enabling solution-processable tandem solar cells," Nat. Rev. Mater. **2** (2017).

[315] S. Liu, J. Yuan, W. Deng, M. Luo, Y. Xie, Q. Liang, Y. Zou, Z. He, H. Wu, and Y. Cao, "High-efficiency organic solar cells with low non-radiative recombination loss and low energetic disorder," Nat. Photonics **14**, 300–305 (2020).

[316] Y. Cui, H. Yao, J. Zhang, T. Zhang, Y. Wang, L. Hong, K. Xian, B. Xu, S. Zhang, J. Peng, Z. Wei, F. Gao, and J. Hou, "Over 16% efficiency organic photovoltaic

cells enabled by a chlorinated acceptor with increased open-circuit voltages," Nat. Commun. **10** (2019).

[317] C.-C. Chen, S.-H. Bae, W.-H. Chang, Z. Hong, G. Li, Q. Chen, H. Zhou, and Y. Yang, "Perovskite/polymer monolithic hybrid tandem solar cells utilizing a low-temperature, full solution process," Mater. Horiz. **2**, 203–211 (2015).

[318] S. Xie, R. Xia, Z. Chen, J. Tian, L. Yan, M. Ren, Z. Li, G. Zhang, Q. Xue, H.-L. Yip, and Y. Cao, "Efficient monolithic perovskite/organic tandem solar cells and their efficiency potential," Nano Energy **78**, 105238 (2020).

[319] Y.-M. Xie, Q. Xue, Q. Yao, S. Xie, T. Niu, and H.-L. Yip, "Monolithic perovskite/organic tandem solar cells: Developments, prospects, and challenges," Nano Select **2**, 1266–1276 (2021).

[320] L. Liu, Z. Xiao, C. Zuo, and L. Ding, "Inorganic perovskite/organic tandem solar cells with efficiency over 20%," J. Semicond. **42**, 020501 (2021).

[321] S. Qin, C. Lu, Z. Jia, Y. Wang, S. Li, W. Lai, P. Shi, R. Wang, C. Zhu, J. Du, J. Zhang, L. Meng, and Y. Li, "Constructing monolithic perovskite/organic tandem solar cell with efficiency of 22.0% via reduced open-circuit voltage loss and broadened absorption spectra," Adv. Mater. **34**, 2108829 (2022).

[322] X. Wu, Y. Liu, F. Qi, F. Lin, H. Fu, K. Jiang, S. Wu, L. Bi, D. Wang, F. Xu, A. K.-Y. Jen, and Z. Zhu, "Improved stability and efficiency of perovskite/organic tandem solar cells with an all-inorganic perovskite layer," J. Mater. Chem. A **9**, 19778–19787 (2021).

[323] K. O. Brinkmann, T. Becker, F. Zimmermann, C. Kreusel, T. Gahlmann, M. Theisen, T. Haeger, S. Olthof, C. Tückmantel, M. Günster, T. Maschwitz, F. Göbelsmann, C. Koch, D. Hertel, P. Caprioglio, F. Peña-Camargo, L. Perdigón-Toro, A. Al-Ashouri, L. Merten, A. Hinderhofer, L. Gomell, S. Zhang, F. Schreiber, S. Albrecht, K. Meerholz, D. Neher, M. Stolterfoht, and T. Riedl, "Perovskite–organic tandem solar cells with indium oxide interconnect," Nature **604**, 280–286 (2022).

[324] W. Chen, Y. Zhu, J. Xiu, G. Chen, H. Liang, S. Liu, H. Xue, E. Birgersson, J. W. Ho, X. Qin, J. Lin, R. Ma, T. Liu, Y. He, A. M.-C. Ng, X. Guo, Z. He, H. Yan, A. B. Djurišić, and Y. Hou, "Monolithic perovskite/organic tandem solar cells with 23.6% efficiency enabled by reduced voltage losses and optimized interconnecting layer," Nat. Energy **7**, 229–237 (2022).

[325] M. Zhang, L. Zhu, G. Zhou, T. Hao, C. Qiu, Z. Zhao, Q. Hu, B. W. Larson, H. Zhu, Z. Ma, Z. Tang, W. Feng, Y. Zhang, T. P. Russell, and F. Liu, "Single-layered organic photovoltaics with double cascading charge transport pathways: 18% efficiencies," Nat. Commun. **12** (2021).

[326] M. I. Hossain, W. Qarony, S. Ma, L. Zeng, D. Knipp, and Y. H. Tsang, "Perovskite/silicon tandem solar cells: From detailed balance limit calculations to photon management," Nano-Micro Lett. **11** (2019).

[327] G. E. Eperon, M. T. Hörantner, and H. J. Snaith, "Metal halide perovskite tandem and multiple-junction photovoltaics," Nat. Rev. Chem. **1** (2017).

[328] A. D. Vos, "Detailed balance limit of the efficiency of tandem solar cells," J. Phys. D: Appl. Phys. **13**, 839–846 (1980).

[329] A. Singh and A. Gagliardi, "Efficiency of all-perovskite two-terminal tandem solar cells: A drift-diffusion study," Sol. Energy **187**, 39–46 (2019).

[330] P. Peumans, A. Yakimov, and S. R. Forrest, "Small molecular weight organic thin-film photodetectors and solar cells," J. Appl. Phys. **93**, 3693–3723 (2003).

[331] M. Polyanskiy, "Refractive Index Database," `https://refractiveindex.info`. [Online; accessed 19-March-2021].

[332] K. Wang, J. Zhou, X. Li, N. Ahmad, H. Xia, G. Wu, X. Zhang, B. Wang, D. Zhang, Y. Zou, H. Zhou, and Y. Zhang, "A surface modifier enhances the performance of the all-inorganic CsPbI2Br perovskite solar cells with efficiencies approaching 15%," Phys. Chem. Chem. Phys. **22**, 17847–17856 (2020).

[333] W. Yan, Y. Guo, D. Beri, S. Dottermusch, H. Chen, and B. S. Richards, "Experimental determination of complex optical constants of air-stable inorganic $CsPbI_3$ perovskite thin films," Phys. Status Solidi RRL **14**, 2000070 (2020).

[334] M. S. Alias, I. Dursun, M. I. Saidaminov, E. M. Diallo, P. Mishra, T. K. Ng, O. M. Bakr, and B. S. Ooi, "Optical constants of $CH_3NH_3PbBr_3$ perovskite thin films measured by spectroscopic ellipsometry," Opt. Express **24**, 16586 (2016).

[335] D. D. C. Rasi, K. H. Hendriks, M. M. Wienk, and R. A. J. Janssen, "Quadruple junction polymer solar cells with four complementary absorber layers," Adv. Mater. **30**, 1803836 (2018).

[336] A. Rajagopal, Z. Yang, S. B. Jo, I. L. Braly, P.-W. Liang, H. W. Hillhouse, and A. K.-Y. Jen, "Highly efficient perovskite–perovskite tandem solar cells reaching 80% of the theoretical limit in photovoltage," Adv. Mater. **29**, 1702140 (2017).

[337] E. Raoult, R. Bodeux, S. Jutteau, S. Rives, A. Yaiche, D. Coutancier, J. Rousset, and S. Collin, "Optical characterizations and modelling of semitransparent perovskite solar cells for tandem applications," 36th European Photovoltaic Solar Energy Conference and Exhibition, 2019; 757-763 (2019).

[338] A. Gagliardi, M. A. der Maur, D. Gentilini, F. di Fonzo, A. Abrusci, H. J. Snaith, G. Divitini, C. Ducati, and A. D. Carlo, "The real TiO_2/HTM interface of solid-state dye solar cells: role of trapped states from a multiscale modelling perspective," Nanoscale **7**, 1136–1144 (2015).

[339] M. A. der Maur, G. Penazzi, G. Romano, F. Sacconi, A. Pecchia, and A. D. Carlo, "The multiscale paradigm in electronic device simulation," IEEE Trans. Electron Devices **58**, 1425–1432 (2011).

[340] F. Santoni, A. Gagliardi, M. A. der Maur, and A. D. Carlo, "The relevance of correct injection model to simulate electrical properties of organic semiconductors," Org. Electron. **15**, 1557–1570 (2014).

[341] A. H. Fallahpour, A. Gagliardi, F. Santoni, D. Gentilini, A. Zampetti, M. A. der Maur, and A. D. Carlo, "Modeling and simulation of energetically disordered organic solar cells," J. Appl. Phys. **116**, 184502 (2014).

[342] A. H. Fallahpour, D. Gentilini, A. Gagliardi, M. A. der Maur, P. Lugli, and A. D. Carlo, "Systematic study of the PCE and device operation of organic tandem solar cells," IEEE J. Photovoltaics **6**, 202–210 (2016).

[343] A. Gagliardi and A. Abate, "Mesoporous electron-selective contacts enhance the tolerance to interfacial ion accumulation in perovskite solar cells," ACS Energy Lett. **3**, 163–169 (2017).

[344] A. Singh, W. Kaiser, and A. Gagliardi, "Role of cation-mediated recombination in perovskite solar cells," Sol. Energy Mater. Sol. Cells **221**, 110912 (2021).

[345] R. Tagliaferro, D. Gentilini, S. Mastroianni, A. Zampetti, A. Gagliardi, T. M. Brown, A. Reale, and A. D. Carlo, "Integrated tandem dye solar cells," RSC Advances **3**, 20273 (2013).

[346] D. Gentilini, A. Gagliardi, A. A. Franco, F. Sauvage, and A. di Carlo, "A drift-diffusion study on charge unbalancing effects in dye-sensitized solar cells," J. Electrochem. Soc. **162**, H753–H758 (2015).

[347] C. Motta, F. El-Mellouhi, and S. Sanvito, "Charge carrier mobility in hybrid halide perovskites," Sci. Rep. **5** (2015).

[348] Y. He and G. Galli, "Instability and efficiency of mixed halide perovskites $CH_3NH_3AI_{3-ix}Cl_x$ (A = Pb and Sn): A first-principles, computational study," Chem. Mater. **29**, 682–689 (2016).

[349] J. N. Wilson, J. M. Frost, S. K. Wallace, and A. Walsh, "Dielectric and ferroic properties of metal halide perovskites," APL Mater. **7**, 010901 (2019).

[350] M. Samiee, S. Konduri, B. Ganapathy, R. Kottokkaran, H. A. Abbas, A. Kitahara, P. Joshi, L. Zhang, M. Noack, and V. Dalal, "Defect density and dielectric constant in perovskite solar cells," Appl. Phys. Lett. **105**, 153502 (2014).

[351] F. Arca, M. Loch, and P. Lugli, "Enhancing efficiency of organic bulkheterojunction solar cells by using 1,8-diiodooctane as processing additive," IEEE Journal of Photovoltaics **4**, 1560–1565 (2014).

[352] J. J. Kwiatkowski, J. M. Frost, and J. Nelson, "The effect of morphology on electron field-effect mobility in disordered C60 thin films," Nano lett. **9**, 1085–1090 (2009).

[353] A. Labrunie, J. Gorenflot, M. Babics, O. Aleveque, S. Dabos-Seignon, A. H. Balawi, Z. Kan, M. Wohlfahrt, E. Levillain, P. Hudhomme *et al.*, "Triphenylamine-based push–pull σ–C60 dyad as photoactive molecular material for single-component organic solar cells: Synthesis, characterizations, and photophysical properties," Chem. Mater. **30**, 3474–3485 (2018).

[354] A. K. Chilvery, A. K. Batra, B. Yang, K. Xiao, P. Guggilla, M. D. Aggarwal, R. Surabhi, R. B. Lal, J. R. Currie, and B. G. Penn, "Perovskites: transforming photovoltaics, a mini-review," J. Photonics Energy **5**, 057402 (2015).

[355] T. Leijtens, J. Lim, J. Teuscher, T. Park, and H. J. Snaith, "Charge density dependent mobility of organic hole-transporters and mesoporous TiO_2 determined by transient mobility spectroscopy: Implications to dye-sensitized and organic solar cells," Adv. Mater. **25**, 3227–3233 (2013).

[356] G. E. Eperon, T. Leijtens, K. A. Bush, R. Prasanna, T. Green, J. T.-W. Wang, D. P. McMeekin, G. Volonakis, R. L. Milot, R. May, A. Palmstrom, D. J. Slotcavage, R. A. Belisle, J. B. Patel, E. S. Parrott, R. J. Sutton, W. Ma, F. Moghadam,

B. Conings, A. Babayigit, H.-G. Boyen, S. Bent, F. Giustino, L. M. Herz, M. B. Johnston, M. D. McGehee, and H. J. Snaith, "Perovskite-perovskite tandem photovoltaics with optimized band gaps," Science **354**, 861–865 (2016).

[357] C. Wehrenfennig, G. E. Eperon, M. B. Johnston, H. J. Snaith, and L. M. Herz, "High charge carrier mobilities and lifetimes in organolead trihalide perovskites," Adv. Mater. **26**, 1584–1589 (2013).

[358] M. Yue, J. Su, P. Zhao, Z. Lin, J. Zhang, J. Chang, and Y. Hao, "Optimizing the performance of CsPbI3-based perovskite solar cells via doping a ZnO electron transport layer coupled with interface engineering," Nano-Micro Lett. **11** (2019).

[359] J. G. Simmons and G. W. Taylor, "Nonequilibrium steady-state statistics and associated effects for insulators and semiconductors containing an arbitrary distribution of traps," Phys. Rev. B **4**, 502–511 (1971).

[360] D. D. C. Rasi and R. A. J. Janssen, "Advances in solution-processed multijunction organic solar cells," Adv. Mater. **31**, 1806499 (2018).

[361] W. Kaiser, J. Popp, M. Rinderle, T. Albes, and A. Gagliardi, "Generalized kinetic Monte Carlo framework for organic electronics," Algorithms **11**, 37 (2018).

[362] D. T. Gillespie, "Exact stochastic simulation of coupled chemical reactions," J. Phys. Chem. **81**, 2340–2361 (1977).

[363] C. Stelling, C. R. Singh, M. Karg, T. A. König, M. Thelakkat, and M. Retsch, "Plasmonic nanomeshes: Their ambivalent role as transparent electrodes in organic solar cells," Sci. Rep. **7**, 1–13 (2017).

Acknowledgement

First and foremost, I would like to thank the Almighty ALLAH for giving me the opportunity, strength, patience and knowledge to work and write this thesis. This doctoral research has been a genuinely challenging experience for me, and I could not have completed it without the support and guidance from numerous individuals.

My unalloyed appreciation goes to my supervisor, Prof. Dr. rer. nat. Alessio Gagliardi for giving me the opportunity to work in his research group. I am really thankful for your ideas, and useful discussions throughout my doctoral research training. Thank you for all the freedom to express myself, and the motivation to undertake the challenges presented to me over the past few years. I want to again thank you for the wide experience that I have got from teaching tutorials to visiting different conferences and summer schools. I have grown and learned a lot during the past years working under your guidance.

I specially thank the German Academic Exchange Service (Deutscher Akademischer Austauschdienst, DAAD) and Higher Education Commission (HEC) of Pakistan for giving me a chance, and funding my doctoral research. I want to thank the management of Sukkur IBA University, for allowing me as their employee to avail this wonderful opportunity to carry out my PhD in Germany. I also want to thank other members of my examining committee: Assoc. Prof. Aldo Di Carlo, PhD for co-examining and the chair Prof. Dr. rer. nat. Bernhard Wolfrum and mentor Prof. Dr.-Ing. Christian Jirauschek. My sincere thanks to all the former and current SNE group members, with special thanks to Tim Albes, Waldemar Kaiser, Ajay Singh, Michael Rinderle, Felix Mayr and Barbara Asam for their help at various stages of my research journey. It was amazing working with you, sharing ideas and knowledge.

As per the saying, a person is known by the company he keeps. Anything is possible, when you have right people there to support you. A big thanks and gratitude to my close friends out of office, Sohail Ahmed, Muhammad Hafeez, Halar Haleem, and especially Hina Irshad for their unconditional support. Even though we were unable to see each other during the past few years, the emotional and moral support from your end meant all to keep me motivated at every step. Without you guys, this journey would not have happened. Thanks a lot for being great friends.

Last but not the least, nothing can outweigh the unconditional support, and sacrifices, my entire family have given for me. You have given me huge strength to pursue my dream far from you. Without you, I would have never achieved what I have achieved so far. Thank you for everything. This thesis is dedicated to you.